A study of air motion and combustion in the IDI diesel engine

Somerville, Berard

Award date:
1993

Awarding institution:
University of Bath

A STUDY OF AIR MOTION AND COMBUSTION IN THE IDI DIESEL ENGINE

submitted by Berard Somerville
for the degree of PhD
of the University of Bath
1993

BJGS September 1993

ProQuest LLC
789 East Eisenhower Parkway
P.O. Box 1346
Ann Arbor, MI 48106-1346

SUMMARY

This thesis describes a study of air motion and combustion in the Indirect Injection (IDI) diesel engine. In the IDI diesel engine, an auxiliary chamber is attached to the main chamber via a narrow throat. During the compression stroke air is forced into the auxiliary chamber forming a swirling and/or turbulent flow field into which fuel is injected. Engines of this type are used in the majority of passenger car diesel engines. With their superior fuel consumption compared with gasoline engines, they are well placed to expand further into the European marketplace. In order to meet EC exhaust emission legislation, as well as consumer demands for power and driveability, a greater understanding of the processes taking place within the engine is required.

A multi-dimensional model of the compression and expansion stroke air motion has been formulated using a general purpose computational fluid dynamic modelling package. Using the numerical model the effect of design changes on the non-combusting air flow has been investigated. An attempt has been made to relate the results of the computational investigation to published experimental results of overall engine performance. The sensitivity of the model to mesh density, differencing scheme and boundary conditions has been studied. Techniques for the full modelling of the combustion and exhaust gas formation processes are outlined and applied to a simple model.

In-cylinder non-combusting pressure and air flow have also been investigated experimentally. Laser Doppler Anemometry (LDA) measurements of velocity have been taken in the swirl chamber of an engine fitted with the standard Ricardo Comet Vb IDI auxiliary chamber. Optical access for the laser has been arranged to minimise changes to the internal geometry of the standard production engine. The experimental investigation has provided boundary conditions and validation data for the numerical model.

CONTENTS

CHAPTER 1 INTRODUCTION

1 Introduction I-2
2 The indirect injection (IDI) diesel engine I-2
3 Exhaust emission legislation I-4
3.1 Particulates and hydrocarbons I-5
3.2 Oxides of nitrogen I-5
4 Application of Fluid Dynamic Modelling I-6
5 Laser Doppler Anemometry I-7
6 The scope of this thesis I-7

CHAPTER 2 LITERATURE REVIEW

1 Introduction II-2
2 Experimental studies of air motion and combustion II-3
2.1 The mechanisms of IDI combustion II-8
2.2 In-cylinder applications of Laser Doppler Anemometry (LDA) II-9
3 Computational studies II-12
4 Summary of experimental and computational studies on IDI engines II-17
5 A brief history of the divided chamber diesel engine II-18
5.1 The Ricardo Comet head (Mks 1,2,3,5,5b) II-20
5.2 Pre-combustion chamber (pre-chamber) system II-23
5.3 Acro (Bosch-Acro) II-24
5.4 Lanova II-25
5.5 Later systems II-26

CHAPTER 3 EXPERIMENTAL INVESTIGATION

1 Introduction III-2
2 Experimental facilities III-2
2.1 The Ford diesel engine and drive III-2
2.2 Modifications made to the engine III-4
2.3 Instrumentation and Data acquisition III-8
2.4 Infra-red measurement of surface temperatures III-12
3 Experimental procedure III-13
4 Pressure data III-14
5 LDA measurements of swirl chamber air velocity III-19
5.1 Introduction III-19
5.2 The LDA system III-19
5.3 LDA measurements in the IDI engine III-21
5.4 Discussion III-25

CHAPTER 4 NUMERICAL STUDY OF IDI AIR MOTION

1 Introduction IV-2
1.1 Model Generation and set-up IV-3
2 Sub-models added to the code IV-4
2.1 Piston-in-cylinder motion IV-5
2.2 Variation of gas properties with temperature IV-6
2.3 Data processing routine IV-7

3 Baseline model and results IV-8
4 Data processing techniques IV-11
4.1 Swirl number IV-11
4.2 The validity of the assumptions of solid body rotation about a fixed centre of swirl IV-15
4.3 Throat discharge coefficient IV-16
4.4 Compression pumping losses IV-17
5 Effect of engine speed IV-18
6 Summary IV-21

CHAPTER 5 VALIDATING THE NUMERICAL MODEL

1 Introduction V-2
2 Thermodynamic validation V-2
3 Comparison with results of other authors V-4
4 Configuring the cfd model for experimental validation V-6
4.1 The sensitivity of the solution to mesh density V-6
4.2 The sensitivity of the solution to numerical differencing scheme V-8
4.3 The effect of using temperature dependent gas properties V-12
4.4 Wall boundary conditions V-13
4.5 Calculation of wall heat transfer coefficients V-16
5 Comparison with experimental results V-18
5.1 Pressure V-18
5.2 LDA results V-20
5.3 Discussion V-24
6 Summary V-26

CHAPTER 6 PARAMETRIC STUDIES

1 Introduction VI-2
2 Throat area study VI-3
3 Glow plug position VI-6
4 Downstream glow plug and a 5% throat area increase VI-8
5 Swirl Chamber Shape VI-8
5.1 Optimising exit flow from chamber VI-10
6 Discussion VI-16
7 Summary VI-18

CHAPTER 7 MODELLING DIESEL COMBUSTION

1 Introduction VII-2
2 Combustion modelling techniques VII-4
2.1 Injection and spray modelling VII-4
2.2 Kinetics controlled combustion VII-5
2.3 Auto-Ignition VII-5
2.4 Magnussen combustion model VII-6
2.5 Product formation VII-7
2.6 Studies of diesel combustion VII-7
3 Modelling IDI combustion VII-8
3.1 Formulating a combustion model VII-8
3.2 The combustion process VII-9
3.3 Discussion VII-14
4 Summary VII-15

CHAPTER 8 DISCUSSION, RECOMMENDATIONS & CONCLUSIONS

1 Introduction VIII-2
2 Experimental Study VIII-2
3 Numerical Modelling of IDI engine air flow VIII-3
3.1 Air flow in the IDI diesel engine VIII-4
3.2 Using numerical modelling for in-cylinder flow predictions VIII-5
4 Experimental validation of numerical modelling VIII-8
5 Recommendations for future work VIII-10
5.1 Experimental VIII-10
5.2 Experimental / Computational Interaction VIII-11
5.3 Flow modelling VIII-11
6 Conclusions VIII-15

LIST OF REFERENCES

APPENDICES

APPENDIX A THE BASIC THEORY OF FLOW MODELLING

1 Introduction A-2
2 Formulation of the basic Navier-Stokes equations A-2
3 Formulating the discretised equations A-9
3.1 Diffusion A-9
3.2 Convection A-11
3.3 Upwind differencing A-12
3.4 Hybrid and higher order schemes A-13
3.5 Discretising the pressure term A-13
3.6 Numerical diffusion A-15
3.7 Temporal discretisation A-15
3.8 Discretisation of the complete momentum equations A-16
3.9 Boundary conditions and wall modelling A-17
4 Obtaining a solution A-17
4.1 Solving the scalar variables A-17
4.2 Solving for the flow A-19
4.3 SIMPLE A-20
4.4 PISO A-22
4.5 Implementation of SIMPLE and PISO in STAR-CD A-23
5 Turbulence modelling A-24
5.1 Introduction A-24
5.2 The k-ε model A-26
5.3 Further stress models A-28

APPENDIX B The computational mesh

APPENDIX C The prostar environment

APPENDIX D Summary of all model parameters and boundary conditions

APPENDIX E Computing requirements

PUBLISHED PAPERS

Charlton, Cox, Somerville, Watts, Horrocks. (1992) *An investigation of the emission characteristics of the passenger car IDI diesel engine.* IMechE conference paper no C448/025

Somerville, Charlton, Nasseri. (1993) *CFD study of air motion in a passenger car IDI diesel engine.* IMechE conference paper no. C461/023/93

Somerville, Charlton, MacGregor, Nasseri (1993) *A study of air motion in an IDI passenger car diesel engine.* IMechE conference paper no. C465/002

ACKNOWLEDGMENTS

I want to thank Dr Steve Charlton for his supervision, encouragement and support during the project, and Dr Stuart MacGregor for his help towards the end of the project.

I am very grateful to George Bonwick for his help in constructing and maintaining the experimental equipment. I am grateful to Doug Greenwell, for operating the LDA acquisition equipment.

The financial and technical support of the Ford Motor Company is gratefully acknowledged.

This thesis has been produced using WordPerfect 6.0 (DOS) and printed on a (postscript) Apple Laserwriter NT, using a Times Roman 12pt typeface. Most graphs were generated using the UNIGRAPH package on a SUN workstation, and imported into the postscipt via eps. Graphics and other figures were created using the Coreldraw 3 package on a PC, and imported into the postscript via eps. The colour photos were taken by the University photographic unit.

NOMENCLATURE

γ	specific heat ratio (Cp/Cv)
ρ	density kg/m^3
τ	shear stress N/m^2
μ	fluid viscosity Ns/m^2
ω	angular velocity s^{-1}
$\dot{m}$	instantaneous mass flow rate through throat
p,P	pressure
p_0	total pressure
u_i,u_j,u_k	components of velocity
A_{throat}	throat area
C_d	throat discharge coefficient
C_v,C_p	specific heat of air at constant volume, and constant pressure
I	moment of inertia
R	Gas constant for specific gas
T_0	Stagnation temperature
S	source terms in momentum and energy equations

CHAPTER ONE
INTRODUCTION

1 Introduction I-2

2 The indirect injection (IDI) diesel engine I-2

3 Exhaust emission legislation I-4
3.1 Particulates and hydrocarbons I-5
3.2 Oxides of nitrogen I-5

4 Application of Fluid Dynamic Modelling I-6

5 Laser Doppler Anemometry I-7

6 The scope of this thesis I-7

1 Introduction

This thesis is concerned with the numerical modelling and experimental measurement of the air flow in a small high-speed indirect injection (IDI) diesel engine. In this introduction, the principles behind the IDI diesel engine are described and a justification for numerical modelling of in-cylinder flows presented.

2 The indirect injection (IDI) diesel engine

Diesel engines have been used in automotive applications since the mid 1930's and now form a significant part of the automotive market. Modern diesel engines are often divided into two distinct groups according to the type of combustion system. Direct Injection (DI) engines operate with the fuel injected directly into the compressed air charge in the cylinder. Depending on the type of engine, the charge may be swirling or quiescent. As the fuel / air charge is not pre-mixed, as in a gasoline engine, efficient combustion depends on all the fuel having sufficient oxygen to burn completely. In a DI engine, this requires high fuel injection pressures (possibly up to 1000bar), to ensure the fuel is dispersed throughout the combustion chamber. The Indirect Injection (IDI) engine uses a separate pre-chamber in the engine head, connected by one or more narrow passages to the main chamber. During the compression process a turbulent and/or swirling air motion is generated in the pre-chamber. Fuel at low pressure (300bar) is injected into the pre-chamber and the turbulent air motion promotes good air/fuel mixing. Direct Injection engines are used in the majority of truck, bus and power generation applications. Until recently all high speed diesel engines have used the IDI system because of its superior noise and emission performance, but recently a number of high speed direct injection (HSDI) engines have been used in production cars. The IDI combustion system remains the most widely used diesel engine for passenger car and light duty high speed applications.

Figure 1.1 shows the *Ricardo Comet Vb* combustion system used by the majority of diesel car manufacturers, the most notable exception being Mercedes who use a *pepperpot* configuration (Figure 1.2) [1][1]. In the Ricardo system, an intense swirling motion in the pre- or swirl- chamber is formed during the compression stroke, into which the fuel is injected. The mechanism of the combustion process is discussed more fully in Chapter 2. The glow plug shown in Figure 1.2 is a cold-starting aid, which provides a hot point to initiate ignition. Even with the high compression ratios used in IDI engines (typically 21:1), the convective heat transfer losses to the cylinder walls during compression mean that a glow plug is required when starting the engine from cold.

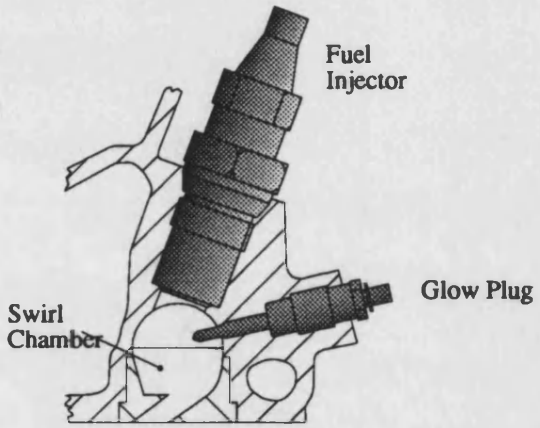

Figure 1.1
Ricardo Comet 5b Swirl Chamber

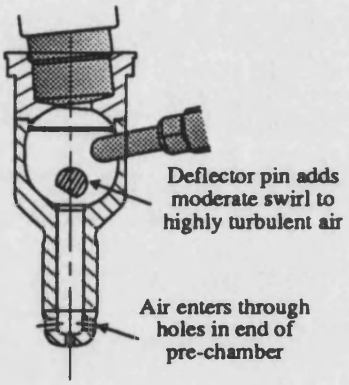

Figure 1.2
Mercedes "pepper-pot" turbulent pre-chamber

When compared with the DI engine, engines based on the IDI system are about 10% less efficient. This difference is due primarily due to the later heat release [2], but also to the additional heat losses over the larger surface area and increased pumping losses. The trend in passenger car diesel engines is towards the DI, and advances such as two-stage injection and controlled exhaust gas recirculation have improved noise and emission levels. It is likely that within the next decade, most manufacturers will switch to the more efficient DI engine.

---

1 Throughout this thesis, numbers in square brackets refer to the list of references at the end of the thesis.

3 Exhaust emission legislation

The primary driving force behind technological development is currently exhaust emission legislation, although manufacturers cannot lose sight of 'traditional' requirements such as cost and performance. The principal exhaust emissions from diesel and gasoline engines are Nitrogen Oxides NO and NO_2 (NO_x), Carbon Monoxide (CO) and a range of hydrocarbons from burnt, partially burnt and unburnt fuel. Other emissions include sulphates (from sulphur in the fuel), and wear material from the engine itself. Emissions may be gaseous (eg CO and NO_x) or particulate (eg carbon, soot and some hydrocarbons). Solid hydrocarbon materials may themselves absorb further organic compounds. Carbon Dioxide CO_2 is a product of combustion, but is not generally regarded as an 'emission'.

The first exhaust emission legislation for diesel powered cars was introduced in the early 70s (BS Au 141a:1971; EC Directives 70/220/EEC; 72/306/EEC), limiting visible smoke, carbon monoxide (CO) and hydrocarbon (HC) emissions [3,4]. The limits on the invisible emissions (CO, HC) were not incorporated into UK national law until 1976. The most recent directive (91/441/EEC - an amendment to the original directive 70/220/EEC) is binding throughout the EC. Stage 1 applies to vehicles entering service after 31 December 1992, and Stage 2 for 1995/6. Stage 3 is a proposed standard for the year 2000. Table 1 summarises the legislation.

Directive 91/441/EEC	Date	CO g/km	HC + NOx g/km	Particulates g/km
Stage 1	31/12/92 (new registrations)	2.72	0.97	0.14
Stage 2 -IDI Engines	1996	1.0	0.7	0.08
DI Engines until 1999		1.0	0.9	0.1
Stage 3 (proposed)	2000	0.5	0.5	0.04

Table 1. Summary of forthcoming European Exhaust Emission Standards for Light Duty Diesel Vehicles (ECE -15 drive cycle)

The requirements for Stage 1 apply to all light duty vehicles (under 3.5 tonne) both gasoline and diesel. The Stage 2 diesel requirements listed in the table are stricter

on CO and more lenient on NOx than the gasoline levels, reflecting the strengths and weaknesses of the two engines. To encourage the development of the high speed Direct Injection (DI) engine, the Stage 1 limits for HSDI engines have been deferred until 1994, and full Stage 2 requirements until 1999. The current generation of diesel engines have been designed to meet the 91/441/EEC Stage 1 requirements, and the technology exists to met the Stage 2 regulations (1996). Engine research and development is being undertaken to reduce exhaust emissions to the levels required for Stage 3, which is likely to be binding from 2000.

3.1 Particulates and hydrocarbons

Particulate exhaust matter originates primarily from unburnt and partially burnt fuel and oil, and sulphates from the sulphur in the fuel. Particulates are formed when there is insufficient oxygen available for complete combustion, which often occurs during the diffusion mixing stage of the combustion process. Fuel sprays impinging on the combustion chamber walls are another source of particulates and HCs, as combustion depends on the fuel evaporation rate from the wall. The primary methods available for reducing HC and particulate emissions are optimisation of the air motion and fuel injection, minimisation of dead volume in the combustion chamber and use of oxidising catalysts. Particulate traps in the exhaust pipe have been widely investigated as a method of reducing particulate emissions, but serious problems with in-service maintenance, size and cost have so far restricted their use.

3.2 Oxides of nitrogen

Nitrogen oxides are a direct result of the high temperature mixing of oxygen and nitrogen (ie air), so that as the efficiency of the combustion process is improved (and hence particulates and hydrocarbons reduced), the peak combustion temperature and NO_x levels are raised. There is therefore a trade off between NO_x and hydrocarbons. NO_x can be controlled with Exhaust Gas Recirculation (EGR) in which exhaust gases are passed back into the intake charge, reducing the oxygen available during the combustion process and increasing the charge specific heat capacity, further reducing flame temperatures. Although EGR can only be used when the engine is operating

at part load, it allows NO_x reduction in most suburban driving conditions. As diesel combustion is inherently lean (operates with excess oxygen), no similar technology to the three-way catalytic convertor, which both oxidises hydrocarbons and CO and reduces NO_x in a gasoline engine exists, although two-way NO_x reduction catalysts are available that, providing the exhaust mixture is sufficiently rich, use the CO, hydrocarbons and hydrogen in the exhaust to reduce the NO. A second stage oxidation catalyst is required to remove the remaining hydrocarbons. On a turbocharged engine, intercooling - without increasing the total power output of the engine -reduces the mean and peak cycle temperatures and thus NO_x formation.

4 Application of Fluid Dynamic Modelling

Engine development has traditionally been based on prototype building and engine testing. With the development of finite element modelling, some degree of structural and thermal optimisation of the engine block and head is possible before machining a prototype engine. Fluid Dynamic modelling offers the same potential for optimising flow and combustion. Given the appropriate flow domain and boundary conditions (eg initial pressure, wall temperatures), a numerical algorithm calculates flow, pressure, temperature and fuel concentration either in steady-state, or varying with time (transient). The technology has already been used for predicting over-body and under-bonnet flows, but in-cylinder applications have yet to find a place in mainstream development. Various organisations have published results of numerical modelling applied to the IDI combustion system, but there appears to have been no systematic appraisal of the strengths and weaknesses of the technology, and no attempts made to validate the predicted data through comparison with experimental results.

Applied to in-cylinder flows, numerical modelling offers the potential of providing a technique for examining in detail the processes occurring in the combustion chamber. The solution can be extended to model fuel injection and combustion, given the appropriate numerical sub-models. The ultimate aim of this process would be a complete model of the engine combustion system, such that given intake and fuel injection conditions the numerical model could predict the combustion processes and exhaust emission formation. In theory, such a model could be used

to optimise the engine for minimum exhaust and maximise power, before building the first prototype.

Modelling of in-cylinder flows presents a number of difficulties. The piston-in-cylinder motion defines a moving flow domain, the flow is unsteady, highly turbulent and three-dimensional. It is only recently that the general purpose codes necessary for simulating complex piston-in-cylinder flows have become available, and research is continuing into more appropriate techniques for modelling turbulence, fuel sprays and combustion. Very little experimental data is available for validation of flow predictions, especially in the complex geometries that define real cylinder flows and computing power continues to place a limit on the complexity of numerical models.

5 Laser Doppler Anemometry (LDA)

In-cylinder velocity measurement and visualisation techniques such as hot-wire anemometry and high speed photography are established engine research tools. With the advances in laser Doppler anemometry (modular optical equipment allowing relatively easy set-up and optical alignment; advanced *black-box* signal processing) application of LDA to internal engine flow measurement has become more widespread. Although a number of organisations have used LDA techniques for flow measurement in *research* and *modified production* Direct Injection (DI) engines, there appear to be no published LDA studies of IDI engine auxiliary chamber flows in realistic geometries. LDA is an excellent experimental tool for validating computational fluid dynamic (cfd) models. Although in the present study, interaction between cfd and LDA has been limited to comparing single component velocity measurements, full three-dimensional velocity and turbulent shear-stress comparisons are possible when multi-component laser systems are used.

6 The scope of this thesis

This thesis is intended as a contribution to the development of fluid dynamic modelling techniques for the internal combustion engine. The primary area of investigation is a study of the air motion in a small IDI diesel engine during the

compression and expansion strokes using numerical modelling and experimental measurement. For the numerical modelling, a general purpose proprietary package has been configured to simulate the compression and expansion flow fields in a small IDI diesel engine. Experimental measurements of in-cylinder pressure and air velocity have been taken in a modified production engine. The experimental measurements are useful in their own right, and as a source of validation data for the numerical modelling.

The main objectives can be summarised as being

- to investigate the air motion in a small IDI diesel engine during the compression and expansion strokes using numerical modelling and experimental measurement
- to validate the numerical results against experimental data obtained from a modified production engine
- to assess the capabilities of a general purpose proprietary code for modelling complex in-cylinder flows

In Chapter 2, literature concerning numerical and experimental investigations of IDI diesel engine air flow and combustion is reviewed. The use of laser Doppler anemometry in engine research is discussed, and a brief history of the IDI diesel engine presented. Chapter 3 presents the experimental apparatus and results. Chapter 4 introduces the numerical modelling techniques and the results obtained. In Chapter 5, methods of validating the numerical model are discussed and the computational and experimental results compared. Having established the validity of the numerical modelling technique, Chapter 6 presents the results of a number of parametric studies involving swirl chamber throat area and the effect of relocating the glow plug within the engine. An attempt is made to relate the effect that such changes have on air motion, to published results on overall firing engine performance. Although the primary aim of this study has been an investigation of cold-flow, Chapter 7 extends the numerical model to include heat release and combustion. The theory of numerical modelling of diesel combustion is presented, and its implementation to the IDI case discussed. The remaining Chapters discuss the application of numerical modelling to engine flows and outline recommendations for future work. Appendix

A presents the theory of numerical modelling of air flow, drawn from a number of fluid mechanics text books and CFD lecture notes. The remaining Appendices present further details of the numerical modelling.

CHAPTER TWO
REVIEW OF LITERATURE

1 Introduction II-2

2 Experimental studies of air motion and combustion II-3
2.1 The mechanisms of IDI combustion II-8
2.2 In-cylinder applications of Laser Doppler Anemometry (LDA) II-9

3 Computational studies II-12

4 Summary of experimental and computational studies on IDI engines II-17

5 A brief history of the divided chamber diesel engine II-18
5.1 The Ricardo Comet head (Mks I,II,III,V,Vb) II-20
5.2 Pre-combustion chamber (pre-chamber) system II-23
5.3 Acro (Bosch-Acro) II-24
5.4 Lanova II-25
5.5 Later systems II-26

1 Introduction

Since small divided combustion chamber diesel engines were introduced to road vehicles in the 1920s and 30s, manufacturers and designers have been investigating the mechanisms of air flow and combustion in the engine. Most of these have been experimentally based, often using high speed photography. In the last decade there has been an increasing use of mathematical modelling of in-cylinder processes. The first of these used zero-dimensional models of the engine. More recently, multi-dimensional computational fluid dynamic models have provided a technique for visualising the details of engine flows. Although swirl chamber engines have been produced for many years now, motor manufacturers are continually seeking to improve the combustion system, and as new techniques become available (eg laser sheet visualisation), further studies are undertaken.

In this section, some of the published techniques used to investigate air motion and combustion in divided combustion chamber engines are presented. These are broken down into experimental and computational models. In general, only applications to IDI engines have been included, although researchers can also draw from the extensive literature relating to the testing of DI Diesel and Spark Ignition engines. Although quantitative comparison of results from different studies is difficult, as engine geometry, and testing conditions vary between investigations, useful qualitative comparisons can be made.

Frequent reference will be made to *swirl number* or *swirl ratio*. This is a measure of the angular velocity of the swirling flow in the swirl chamber, and is defined as

$$N_s = \frac{\textit{Angular velocity of swirling flow}}{\textit{Engine speed}}$$

The method used to calculate an effective angular air velocity varies between researchers, but is often based on velocity measurements at a single location, or the average of a few points in the flow.

2 Experimental studies of air motion and combustion

There have been many studies of the processes occurring in divided combustion chamber engines. These have included studies of air motion (motored and firing), fuel injection, combustion and exhaust gas formation. Most investigations have used one or more of the following techniques:

High Speed Photography using

Schlieren

Shadowgraph

Back-illumination

A marker in the flow (eg plasma traces, fixed cotton tufts)

Hot wire anemometry

Photographic techniques usually require extensive modifications to the combustion chamber to allow a flat optical window to be fitted. This is often done by using a cylindrical swirl chamber, where the two ends of the cylinder are replaced with quartz windows (Figure 1). Such configurations are generally kept as simple as possible, and often do not include glow plugs or fuel injection ports. *Schlieren* and *Shadowgraph* techniques produce images corresponding to changes in fluid density, for instance due to fuel injection, or combustion. In shadowgraph

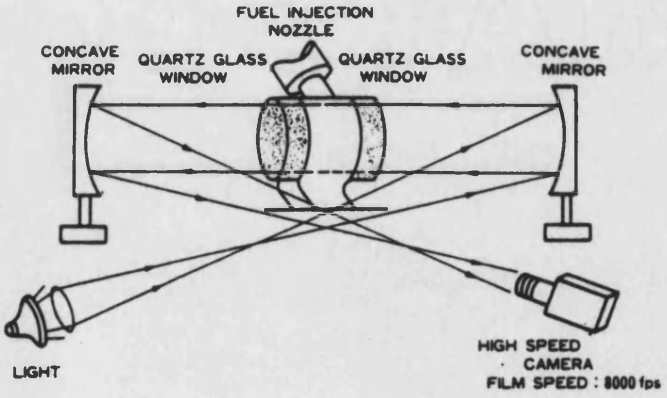

Figure 1
Typical cylindrical swirl chamber for photographic study (Tanaka)

photography, light from a source passes through the flow onto a screen. Density gradients in the flow refract the light forming light or dark bands on the screen. In Schlieren visualisation, a knife edge is used to cut off part of the image formed when light passes through the flow. Density gradients cause light and dark patches on the screen. Very few photographic techniques exist that allow air velocity measurements to be made directly. A marker in the flow may be used and the velocity determined by comparing consecutive photos, but particles, large enough to be photographed, are quickly thrown out of the swirling air by the centrifugal force. Qualitative information about flow has been obtained by placing mini wind-vanes in the flow (eg cotton tufts) to record the direction of the air motion. Laser sheet techniques may provide researchers with a further tool in swirl chamber flow visualisation.

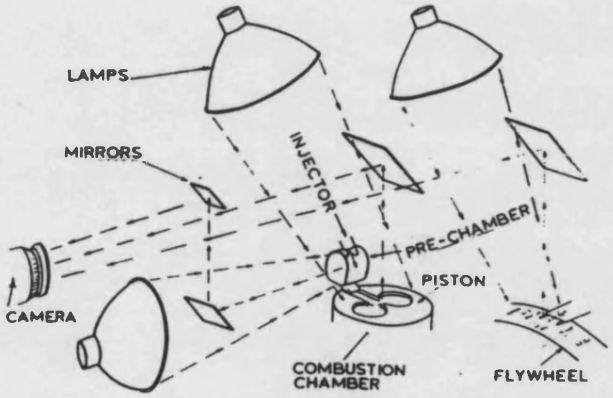

Figure 2.2
Optical system layout (Alcock)

In one of the first colour studies, Alcock [7] photographed air motion and combustion in Ricardo Comet V and other combustion systems. The set-up (Figure 2.2) allowed the flame structure in the swirl-chamber and piston trough to be recorded simultaneously. Alcock found that the swirl peaked before 10° btdc, falling to half its peak value at around 20° atdc, and took the form of a 'semi-free' vortex: the linear velocity perpendicular to the chamber radius was roughly constant.

Broome [8] photographed the movement of cotton tufts mounted on stalks of hypodermic tubing spigotted into a side wall of the swirl-chamber. As this technique was not able to provide quantitative information, Broome mounted a 1/6 gram vane at the centre of the swirl chamber, and recorded swirl ratios of 40 at tdc. Nagao [9-(1967)] used a free-surface *water* model with aluminium powder tracer in a 1.01 rpm

engine (ie a piston pushing water at 1.01rpm) to simulate air motion in a 1500rpm engine. The study also photographed mixture formation and combustion in a cylindrical swirl chamber.

Nakajima [10-(1968)] used high speed photography of plasma discharges to observe motored engine air-motion in low compression ratio (7:1) Comet III, Comet V and flat bottomed pre-chambers. Back-illumination was used to study fuel spray and combustion processes. The combustion chambers were fitted with two flat parallel sides, of heat resistant glass to allow observation. Nakajima found that engine performance improved when the level of swirl in the chamber was reduced by moving the connecting throat from a tangential to a radial position. This improvement is attributed to unburnt fuel being able to transfer more easily from the swirl to the main chamber.

Schlieren techniques are useful for recording the air/fuel mixing and combustion following fuel injection. Meintjes [11] used the technique to study air/fuel mixing in a flat sided dual throat pre-chamber. Nakakita [12] applied Schlieren (Figure 3), Back-illumination and Shadowgraph techniques in a study of

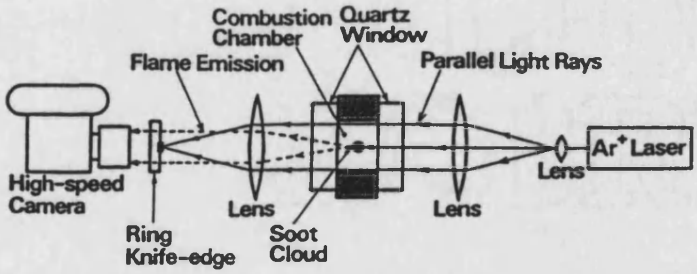

Figure 3
Apparatus used for Schlieren photography (Nakakita)

soot formation in the swirl chamber. Back-illumination was especially suitable for visualising soot clouds as the technique is unaffected by density gradients in the gases. Tanaka [13] at Nissan, used high speed photography to investigate the effect of adding a second ('sub') throat to a standard swirl chamber. Aluminium tufts (Figure 4) were attached to shafts fixed into a quartz window at the end of a

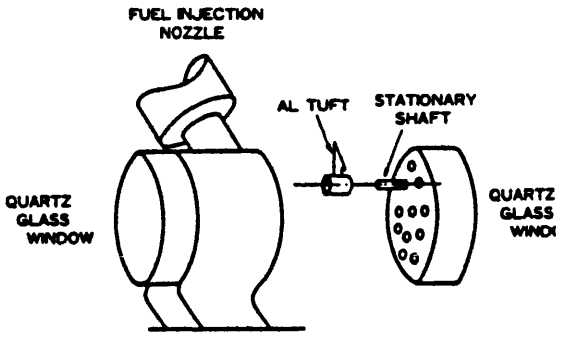

Figure 4
Aluminium tufts used for measuring air motion (Tanaka)

cylindrical swirl chamber, such that the tufts could rotate freely on the shaft. High speed photography of the tufts allowed the direction of air flow during the cycle to be observed. The same investigation used shadowgraph photography to investigate the fuel spray and flame structure in the dual throat engine.

As part of a study of the Diesel soot formation process, Nakakita 12] in Toyota Central Research used a number of photographic techniques to study air motion and combustion in a cylindrical swirl chamber. Nakakita found that back-illumination was necessary to visualise in-cylinder soot clouds, as shadowgraph and schlieren techniques are sensitive to shadows generated by gas density gradients and soot. Schlieren visualisation was used to study fuel-air mixing and flame structure.

Nishida [14] used high speed photography to characterise the combustion processes taking place in both the main and swirl chamber, and the effect on the structure of combustion of injection timing, throat area, injector location and the presence of a piston recess. Figure 5 shows a diagrammatic representation of the combustion process following fuel injection in a baseline case. The results from this study are discussed in a later section.

Photographic techniques cannot be used to measure directly local time-dependent air velocity. *Hot wire anemometry* uses the heat losses from a thin hot wire placed in the flow to calculate instantaneous flow temperature or velocity. The technique can be used with little modification to engine geometry, but as an intrusive technique may affect the flow. Researchers have experienced a number of problems in applying hot wire anemometry to internal combustion engines: the wires themselves are at risk of physical damage from solid particles in the flow and the

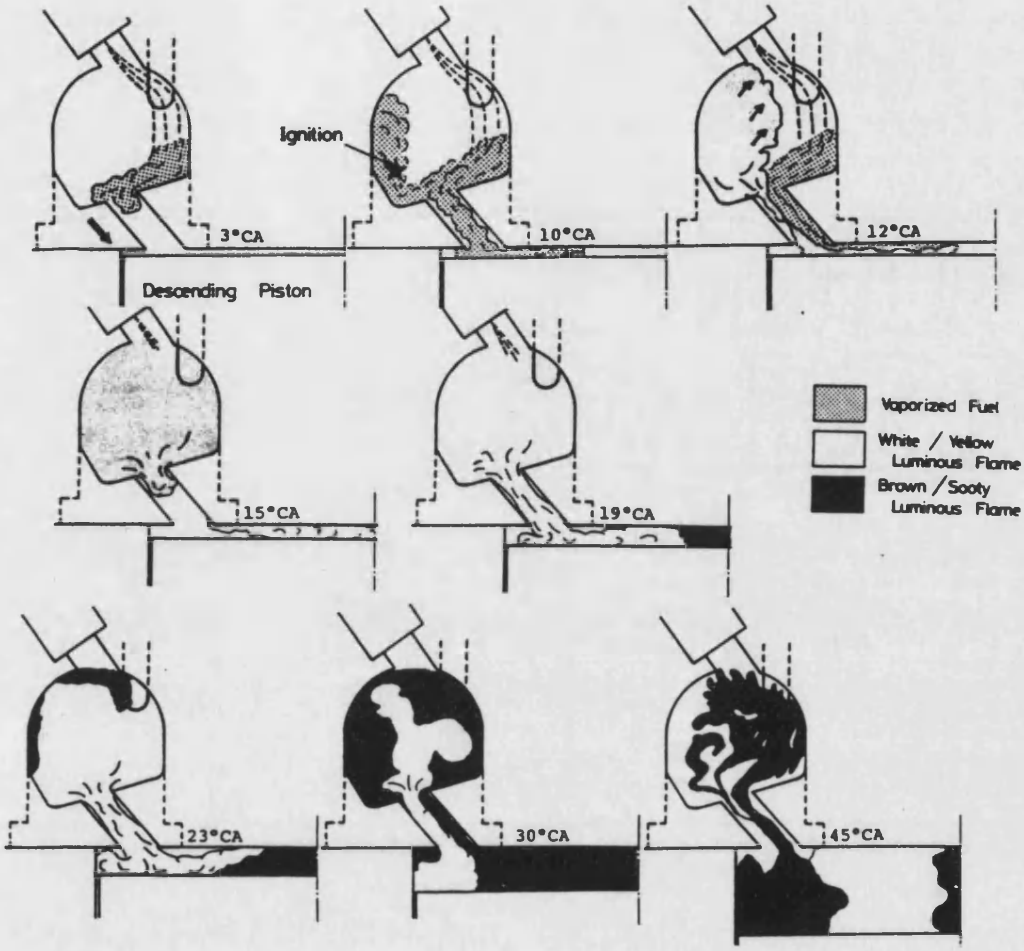

Figure 2.5
Diagrammatic representation of combustion processes following injection at 2°btdc (Nishida)

temperatures associated with high compression ratios reduce the sensitivity of the wire (as the air temperature approaches the wire temperature). Calibration can be difficult for varying density flows.

Hassan [15] used hot wire anemometry to measure air velocity across a simplified swirl chamber. In work undertaken at the University of Bath, Tawfig [16] used hot-wire anemometry and a rotating paddle wheel to measure non-firing air motion in a geometrically correct swirl-chamber. The results were compared with analytical results from a zero-dimensional model. Tawfig found that swirl number reached a peak of around 80x engine speed between 15° and 5° btdc. Subramaniya

[17] used hot wire techniques to calculate velocity and turbulence in a low compression ratio, 400rpm engine swirl chamber engine.

2.1 The mechanisms of IDI combustion

Many experimental studies have attempted to determine the mechanisms of IDI air motion, fuel injection and combustion. Many of these studies attempt to relate changes in overall engine performance (bmep, sfc, emission levels etc.) to changes in engine design (eg Charlton [18]), while others using the experimental techniques presented above have investigated the direct effect of design changes on in-cylinder air motion and combustion. Both techniques are valuable: detailed investigations can provide information about how design changes are able to improve overall performance. This section attempts briefly to summarise the mechanisms of IDI combustion.

During compression, air is forced through the auxiliary chamber throat into the body of the chamber, forming a swirling motion in the auxiliary chamber. The heat losses to the throat wall during compression when the engine is cold, force manufacturers to use a cold starting aid (*glow plug*) in the auxiliary chamber to act as a point of ignition [19]. When running at normal operating temperature, during much of the compression stroke, the auxiliary chamber insert heats the incoming air. Early studies (Dicksee [20]) showed that high thermal conductivity inserts gave better performance than low conductivity inserts, as it was believed they allowed heat to flow in and out of the insert. Most experimental investigations have found the swirling air motion produced in the auxiliary chamber to be of solid body rotation type reaching a peak swirl number around 15° btdc. Fuel is injected as a relatively coarse spray, which travels in the swirling air flow and wets the bottom surface of the swirl chamber (Figure 2.6). The combustion process (based on fuel injection at 2° btdc) is characterised in Figure 2.5. Nishida found that advancing fuel injection (to 7° and 12° btdc at 1000rpm) increased smoke and NO_x emissions. Nishida attributes this to the reduction in fuel drawn into the main chamber before ignition, increasing the fuel burnt in the swirl chamber, reducing air utilisation in the main chamber. Additionally the earlier flame transfer from the swirl chamber impinges on the piston when it is close to the cylinder head, quenching more of the flame.

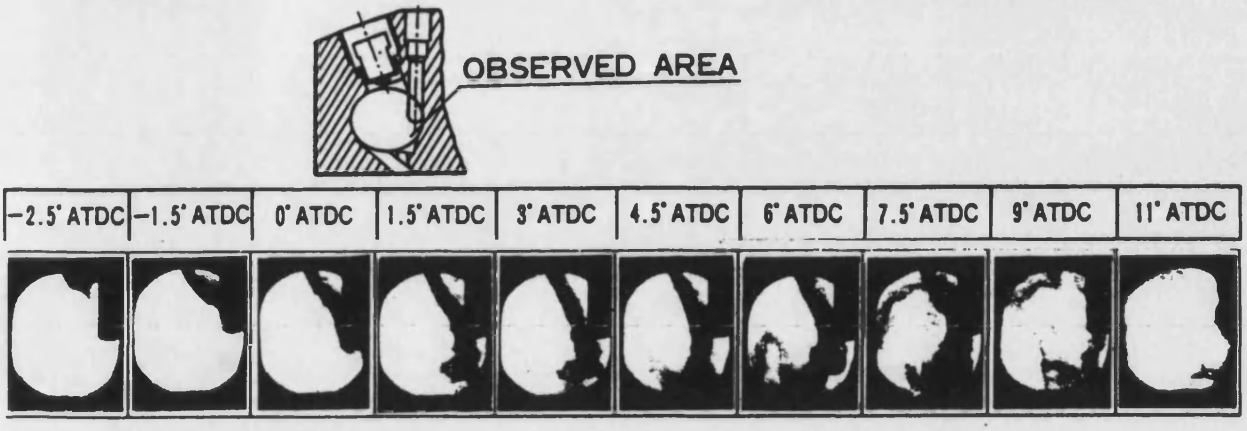

Figure 2.6
Shadowgraphs showing fuel injection and combustion (Tanaka)

Similar results relating NOx levels to injection timing have been obtained by other studies [21,22]. Following ignition in the auxiliary chamber, the burning fuel / air mixture is forced through the throat into the main chamber, with the considerable heat losses associated with the dual chamber combustion system. The gases from the throat split into two vortices, drawing the air in the main chamber into the combustion process. Nishida found that combustion completely finished in the swirl chamber around 50° atdc and between 90 and 100° atdc in the main chamber. The shape of the piston recess is important in obtaining good levels of air utilisation in the main chamber [13,23].

2.2 In-cylinder applications of Laser Doppler Anemometry (LDA)

LDA works on the principle that the light reflected from a particle contains a Doppler shift, proportional to the particle's velocity. The interference between the Doppler shift from two coherent light beams incident on the particle, produces a 'beat' that can be measured, and from which the particle velocity can be can be calculated. It is generally necessary to introduce the particles into the fluid ('seeding'). LDA allows accurate measurements to be made of local air velocity and turbulence, without disturbing the flow, although modifications may have to be made to the engine to allow optical access. Wigley [24] provides an excellent introduction to many of the problems and procedures in applying LDA to in-cylinder measurements.

Although LDA techniques were first developed in the 60s, it is only in recent years that they have become a useful engine research tool. Most of the studies published on in-cylinder flow relate to manifold (eg [28]), valve or combustion chamber flows in motored direct injection (DI) engines. Applications of LDA to in-cylinder flows generally fall into two categories:

- Studies in production or research engines, modified to allow optical access [25-27]
- Studies in purpose built model engines [29,30]

Modified research / production engines generally limit the area to which optical access can be obtained. Zur Loye (27) inserted 4 quartz windows in a spacer ring

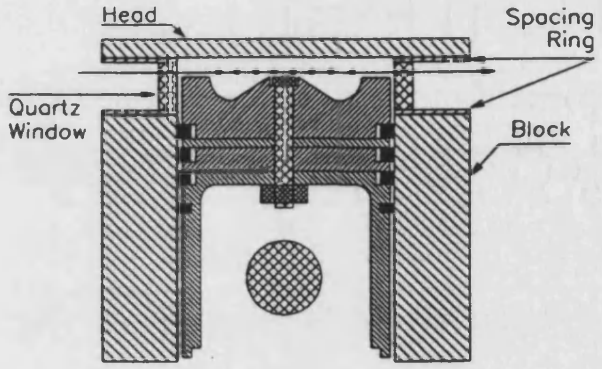

Figure 2.7
Modifications made to cylinder block to allow optical access (Zur Loye)

between the cylinder head and the block (Figure 2.7). Wigley placed a quartz window in the cylinder head of a Perkins engine in a study of swirl velocity in motored and firing engines. [26,31]

Model engines may use transparent cylinders and/or heads to allow total optical access, but are often limited to running at reduced speeds and compression ratios. Arcoumanis [32] studied the effect of intake swirl in a low compression, 200rpm engine manufactured from plexiglass. Kamimoto [33] built a 5:1 compression ratio

quartz model engine with tetrafluroethylene piston rings for laser flow visualisation and velocity measurements (Figure 8).

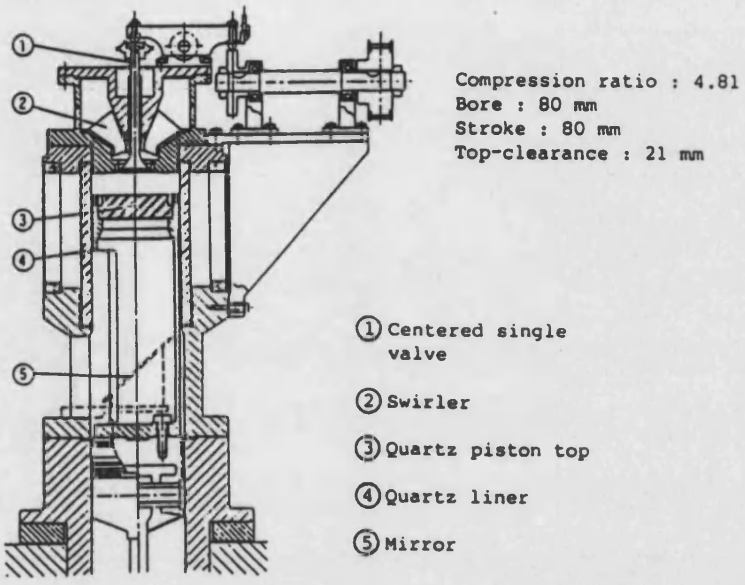

Figure 8
Transparent cylinder engine to allow optical access to main chamber (Kamimoto)

Researchers have used in-cylinder LDA for a number of different types of investigation. Most in-cylinder studies have investigated some aspect of intake or compression air flow. In one of the first studies, Rask [25] used backscatter LDA to measure instantaneous velocity in a two cylinder DI type engine. Recent work undertaken at Imperial College has investigated inlet valve flow and swirl levels during compression in model and research motored DI engines [34,35]. A number of LDA studies have been used to validate numerical models of fluid flow. Pinchon [28] compared LDA results with those obtained from the CONCHAS code. Zur-Loye [27] compared LDA measured turbulence with values calculated using the KIVA code. Some LDA studies in firing engines have been undertaken [26], but problems with optical access, fouling of windows, and signal/noise ratios limit the data that can be obtained from such studies.

2.3 LDA studies in divided combustion chamber engines

Very little has been published on experimental studies using LDA in swirl-chambers of indirect injection IDI engines. Zimmerman in 1983 [36] used a forward scatter LDA configuration to measure air flow in a motored engine with a dual-throat pre-chamber. Comparisons were made with a five-zone numerical model. To allow optical access, the author used a cylindrical pre-chamber with the same volume as the production chamber, allowing quartz windows to be placed at both ends of the chamber. Zimmerman justifies this modification to the chamber by noting that visualized gross flow in a 5x-size model shows little difference to that in a spherical chamber. Talcum powder was used to seed the flow, and measurements were taken at two points in the pre-chamber, one near the main throat, the other adjacent to the injector. The results presented suggest that the air in the pre-chamber rotates as a solid body with a maximum swirl ratio of about 20 at the three engine speeds tested: 600, 1340 and 1780rpm. Zimmerman notes that the swirl decays rapidly after the maximum at around 15° btdc.

3 Computational studies

The earliest mathematical model of swirl chamber flow is probably that by Alcock [37-(1934)] who used the principles of conservation of angular momentum to calculate throat velocity and swirl number in the auxiliary chamber. More recent numerical models of IDI Diesel engine flows can be broken into two basic categories:

1 zero dimensional thermodynamic (phenomenological) models

2 Multidimensional solutions of fluid flow equations

Phenomenological models consist of a number of control volumes representing cylinders, manifolds, pipes etc. They can be called *zero-dimensional*, as little or no geometric information is associated with the control volumes. Each control volume possesses thermodynamic properties, can transfer heat and work, and is connected to further control volumes. The governing equations are based on the principles of conservation of mass, momentum and energy and determine mass and energy flow

between the control volumes. Starting from a particular point (often bdc) in the cycle at which sufficient properties (eg temperature, pressure, equivalence ratio) are known for each control volume, the equations are solved over a series of time steps (eg every 1 degree CA). Sub-models may be used to calculate additional functions such as dependence of gas properties on temperature, combustion heat release, wall heat loss, often based on empirical data. Phenomenological models are ideally suited to studying the interaction of processes occurring in different parts of an engine such as the effect of adding a turbocharger to an engine. Such models have become a standard tool of engine designers and are routinely used to analyze energy losses and predict engine efficiency.

Watson [2] used a four zone (main & swirl chambers, inlet & exhaust manifolds) zero-dimensional model to compare low speed (2200rpm) DI and IDI engines. Of the 14% difference in thermal efficiency at full load between the two combustion systems, Watson found that 70% is due to the later heat release in the IDI engine. The Institut Français du Pétrole has undertaken a series of studies, both zero- and multi-dimensional, in mathematical modelling of swirl chamber flow and combustion. Pinchon [38] used a zero dimensional model to investigate IDI engine efficiency and found that the principal reason for reduced IDI efficiency over the DI was swirl chamber heat loss. The multi-dimensional studies are discussed below. Kouremenos [39] at the University of Athens, undertook an analysis of pre-chamber (*pepper-pot* see Figure 1.2) engine thermodynamics and obtained good agreement from the model with experimental results. This research group went on to apply the model to swirl chamber engines [40], and prediction of soot and NO_x formation [41]. Tawfig [16] at the University of Bath used the framework of the SPICE package to model a swirl chamber engine, using conservation of angular momentum considerations to predict swirl number and compared the results with experimental data, obtaining reasonable agreement. The investigation studied the effect on swirl number and pumping losses of changing the swirl chamber throat area. Phenomenological engine models are now available to designers as off-the-shelf packages that can be configured to analyze most engine configurations, given the appropriate inputs.

Multi-dimensional modelling is based on breaking the flow domain into *cells* and calculating fluid (air) flow by solving the fundamental equations that govern fluid flow for each cell. These equations are known as the Navier-Stokes equations. The terms *two-dimensional* and *three-dimensional* are used to define the number of dimensions in which the exact geometry of the flow boundaries are defined, and in which the equations are to be solved. Additional equations may be solved to model temperature distribution, fuel injection, combustion reactions etc. The early applications of multi-dimensional modelling techniques to in-cylinder flows were mainly to relatively simple geometries [42,43]. Table 1 traces the development of IDI engine applications of flow modelling. Many of the applications to divided combustion chamber engines have used the codes developed at the Los Almos National laboratory. Development of this family of codes began in the seventies with the 2-d RICE code, and was subsequently developed through CONCAS [44] to KIVA [45] and TurboKIVA [46]. Meintjes [11] used RICE to validate the zero-dimensional model previously described, feeding boundary conditions from the phenomenological model to the CFD model. Pinchon (IFP) [47] used the CONCAS-SPRAY model to investigate air flow in a Ricardo type swirl chamber, investigating the effect on swirl chamber air flow of increased swirl-chamber insulation. A later study by the IFP [38] extended the modelling to a fully three-dimensional geometry and included combustion modelling using the KIVA code. The same code was used by Zellat at Renault [48] who investigated the effect of injection timing on swirl and main chamber heat release.

The SPEED Diesel Combustion code of Imperial College [49] has also been used to simulate IDI engine air flow and combustion. Boretti [50] at Fiat used the code to study the effect of geometrical changes on swirl chamber cold-flow. This study highlighted mesh generation as a time-consuming feature of CFD, and added an automatic mesh generation facility to allow meshes for parametric studies to be generated quickly. Boretti notes that the results obtained from the combustion model must be treated with care, due to the sensitivity of the model to empirical constants.

Of the multi-dimensional studies listed, only Nakakita and Komatsu compare the predictive model with experimental data. In a study of the soot formation process, Nakakita obtained good qualitative agreement between predicted soot concentration, and back-illumination photography. Komatsu, working with a very

coarse mesh, found that the model underpredicted air velocities. Attempts to compare results from predictive models, with experimental results from a different study (eg. the LDA results of Zimmerman) are useful for *qualitative* comparisons, but unless identical engine geometries, boundary conditions, engine speeds etc. have been used in both studies, *quantitative* comparisons can be misleading.

Table 1: Multi-dimensional models of IDI engine air flow and combustion

Author-	Code 2d / 3d	Application	No. Elements in swirl chamber	Features of engine cycle modelled	Combustion model
Meintjes 1982	RICE 2-d	Oldsmobile type Ricardo V	54 x 41 = 2214		
Pinchon 1985	CONCAS -SPRAY 2-d	Ricardo V	18 x 16 = 288	Fuel injection / air fuel mixing	
Pinchon 1989	KIVA 3-d	Ricardo V with / without glow plug	12 x 15 x 6 = 1080	Fuel injection / combustion	Ignition: Zellat Combustion :Magnussen
Nakakita 1990	3-d	Sphere with tangential throat		Fuel injection / combustion / soot formation & oxidation	Ignition: 1 eq Arrhenius Comb: Magnussen Soot: Tesner / Nagel
Zellat 1990	KIVA 3-d	Ricardo with glow plug	12 x 18 x 6 = 1296	Fuel injection / combustion / soot formation	ditto Soot formation: Tesner
Komatsu 1991	3-d	Spherical swirl chamber	820	Air motion only	
Boretti 1992	SPEED 3-d	Ricardo Comet type	8000 (estimated) 15000 - total	Fuel injection / combustion	Ignition: Shell model Combustion: Magnussen
Somerville 1992	STAR-CD 3-d	Ricardo Comet type	25 000 / 90 000	Air motion	

4 Summary of experimental and computational studies on IDI engines

Author	Year	Experimental technique	Computational technique
Alcock	1962	High-speed photography	
Lyn	1962	Schlieren	
Broome	1966	Cotton tufts to visualise flow direction, swirl vane	
Nagao	1967	High-speed photography	
Nakajima	1968	Plasma as a tracer for air motion Back illumination in firing engine	
Hassan	1970	Hot wire anemometry	
Watson	1979		two zone 0-d model (thermodynamic efficiency evaluation of IDI engine)
Ajakaiye	1981	Hot wire anemometry	Zero-dimensional model
Meintjes	1982	Schlieren photography	Two-dimensional non-bodyfitting mesh
Pinchon	1985		zero and 2-dimensional models
Tanaka	1986	Aluminium tufts, Shadowgraph	
Nishida	1986	Photographic study of combustion	
Kouremenos	1988		zero-dimensional model
Pinchon	1989		3-d modelling of combustion (KIVA)
Kouremenos	1990		zero-dimensional model (NOx formation)
Tawfig	1990	Hot wire anemometry / paddle wheel	zero-dimensional model
Zellat	1990		3-d modelling of combustion and soot formation (KIVA)
Nakakita	1990	Schlieren, Back Illumination, Shadowgraph	
Aoyama	1990	High Speed photography (investigating NOx formation)	
Nakakita	1990		3d simulation of soot formation
Subramaniya	1991	Hot wire anemometry	
Komatsu	1991		Spherical pre-chamber
Boretti	1992		3-d modelling (KIVA)

5 A brief history of the car diesel engine

The history of the Compression Ignition engine dates back to the early 1890s. Steam engines were well established in railway, marine and stationary engine applications, and spark ignition (petrol) engines were being developed for automotive applications. [20,51-58]

Credit for the conception and development of the early Compression Ignition engine can be given to two men. In 1890, the British engineer Herbert Akroyd Stuart (1864-1937) patented an engine in which, as a method of eliminating pre-ignition, pure air was compressed, and only then fuel injected (Figure 2.9). About the same time, the German engineer Dr Rudolf Diesel (1858-1913) applied for a patent (1892) in which he laid out the framework of a constant pressure cycle, achieved by introducing fuel *gradually* into the combustion chamber towards the end of the

1, bedplate ; 2, fuel tank ; 3, cylinder ; 4, piston ; 5, connecting rod ; 6, crank ; 7, crankshaft ; 8, countershaft ; 9, 2-to-1 gears ; 10, air valve ; 11, exhaust valve ; 12, cam ; 13, valve lever ; 14, vaporizor ; 15, fuel pump ; 16, sprayer ; 17, cam for fuel pump ; 18, governor.

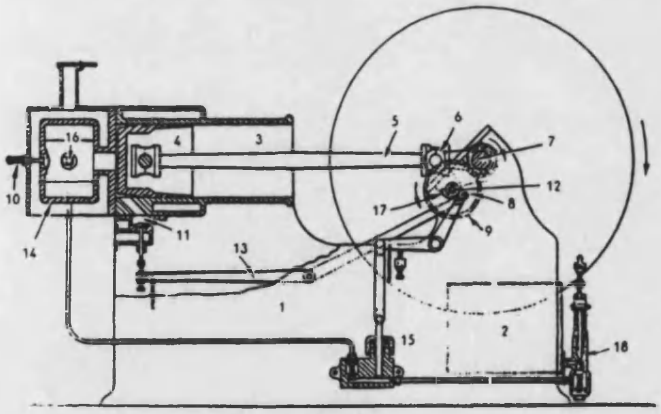

Figure 2.9
Akroyd Stuart patent engine

1, single-acting cylinder ; 2, piston ; 3, guide ; 4, connecting rod ; 5, crank ; 6, flywheel shaft ; 7, gears ; 8, vertical shaft ; 9, horizontal distribution shaft ; 10, cam ; 11, fuel valve ; 12, valve spring ; 13, coal hopper ; 14, governor ; 15, solid fuel shut-off cock.

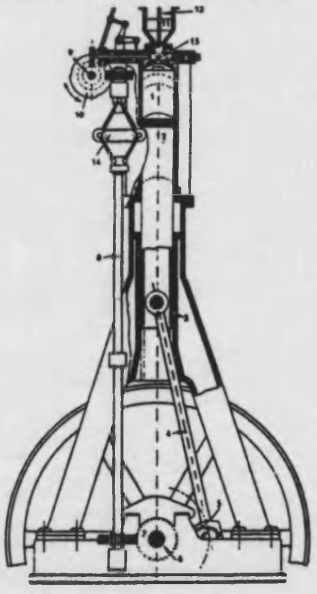

Figure 2.10
Rudolf Diesel patent engine

compression stroke (Figure 2.10). The use of the term 'Diesel' for Oil engines became a subject of much controversy in the first decades of the century among

(mainly British) engineers, who believed too much credit was given to Dr Diesel, at the expense of the development work of Akroyd-Stuart.

The early applications of the Diesel engine were mainly for low speed (800rpm) stationary engines and marine applications, where the better fuel economy, relatively simple design, and low volatility of the fuel, made the Diesel engine especially attractive. The shortage of petrol during the War forced Germany to adapt petrol engines to run on heavy oil and companies such as Benz (Mannheim), Mercedes (Stuttgart), M.A.N (Augsburg), and Saurer (Arbon, just over the border in Switzerland) quickly became involved in Diesel engine development. The early engines developed on the continent were almost exclusively based on *pre-combustion chamber* and *ante-chamber* systems, where the fuel is injected, and combustion starts into a partially separate chamber (usually in the head, occasionally in the piston), from which the burning gases pass back to the main chamber. In some engine designs, the separate chamber was used as an *air-cell*, storing fresh air during the compression stroke, and releasing it during expansion to support the combustion process. Development of the engine progressed quickly in Germany, and by the 1930s the pre-chamber systems in large applications (lorries, buses etc.) were being replaced by Direct Injection systems.

The plentiful supplies of petrol in the UK and America during the War meant that UK and US manufacturers were slower to see the advantages of converting their engines to Diesel. The first attempts to apply C.I. to transport in the UK came in the mid 20s. By 1927, the Associated Equipment Company (AEC at Southall), using an Acro combustion system was fitting Diesel engines to heavy lorries, and in 1930 to London buses. Ricardo Ltd was formed in 1927, and 4 years later patented the Comet combustion system (Mks I,II and later III). Whereas almost all German manufacturers used pre-combustion systems, British engine-builder used both ante-chamber systems (few used pre-combustion chambers) and *open-chambers* (DI), and the trend ever since has generally been away from the auxiliary chamber system towards DI combustion.

By the late 1930s the main types of auxiliary chamber combustion systems in use were the pre-combustion, Acro, Lanova, and Ricardo types. Many variations on each of these existed, and many more were to follow.

As development work on high speed diesels progressed, the Ricardo combustion system became more widely adopted, with most other designs disappearing. This was probably due to the superior fuel economy and performance of the Ricardo system. Today the Ricardo design dominates the car diesel engine market (it is used, among others, by Peugeot, Renault, VW, BMW, Ford, and most of the Japanese companies). Several attempts to modify the Ricardo system have been made, for instance introducing a secondary throat [13], and using a vertical (downstream) glow plug. In the last five years, Direct Injection engines have been used in some passenger cars: The Perkins *Prima* engine has been fitted to a range of British produced cars with promising results. The main problems with the car DI engine are noise and emission levels, although technology such as two stage injection and Exhaust Gas Recirculation (EGR) is being used to improve these aspects. It is almost certain that within the next decades, the proportion of DI passenger car Diesel engines being produced will increase, eventually replacing the IDI in many applications.

5.1 The Ricardo Comet head (Mks I,II,III,V,Vb)

Following its introduction in the early thirties, the Ricardo Comet head, designed by Sir Harry Ricardo, quickly became the most widely used small high speed Diesel engine design. Mks I,II & III were all patented in two patents in 1931 and 1934, presumably to stop competitors using any of the designs.[1]

---

[1] The 1936 proceedings of the Institution of Automotive Engineers provides some interesting background to the early development of the Comet head. Following a reading of a paper by two members of Ricardo's staff, Freeman-Saunders accused Ricardo of stealing his own design, claiming to have patented the *Lister-Saunders combustion chamber* in 1928. Ricardo reported in a written reply to the accusation that the Comet head was a modification of an old 'Laurin' type, dating back to 1907 (on which Ricardo had worked). The principal *new* feature of the Ricardo Comet design was the insulated hot plug [insert]

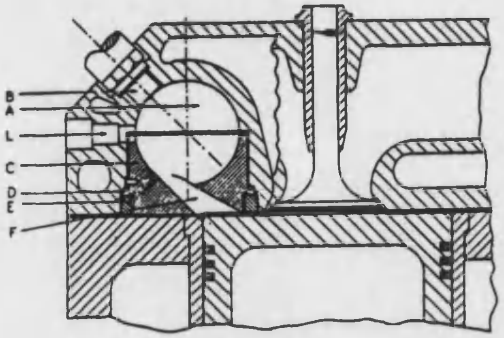

Figure 2.11
Ricardo Comet Mk I chamber

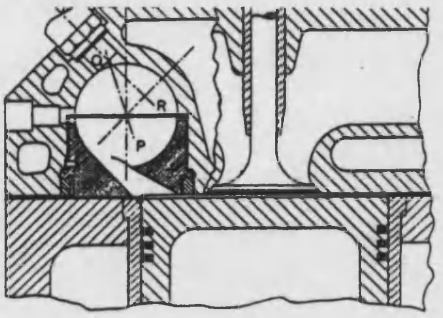

Figure 2.12
Comet Mk II Chamber

The *Mk I chamber* is shown in Figure 2.11. This original Comet chamber was spherical, connected to the main chamber by a tangential throat with up to 80% of the air being transferred to the swirl chamber. The fuel injector injects fuel *towards the centre of the sphere*. The key feature of the Comet design is the heat resisting insert, insulated from the cylinder head by a thin air layer. This insert has two main purposes: 1) to keep the insert at a temperature high enough to prevent flame quenching when fuel hits it and; 2) to store heat during combustion, thus heating incoming air on the following compression cycle, and reducing ignition delay as a function of engine speed. The offset combustion chamber meant that large (recessed) valves could be used. A feature of all the Comet designs is the need for a cold starting aid: Heat losses to the cold insert are such that even with the high compression ratio, a hot point is needed to initiate combustion. The cold starting aid is known to operate not by heating the incoming air, but by providing a point of ignition for the air/fuel mixture.

The *Mk II chamber* (Figure 2.12) was very similar to the Mk I, but the direction of the spray is moved in relation to the sphere centre, so that it becomes approximately tangential to a circle around half the diameter of the sphere. This increased the delay slightly, but ensures that the exhaust gases are carried away from the injector, so that in the final stages of combustion, fuel is still injected into fresh air. This allowed more fuel to be injected without air starvation.

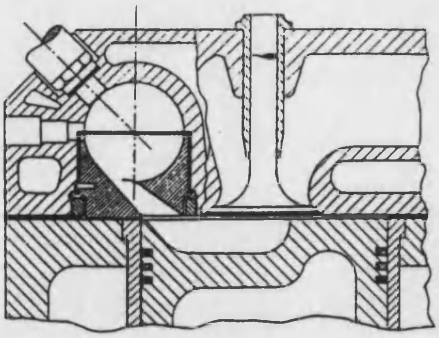

Figure 2.13 (Glyde)
Comet Mk III Chamber

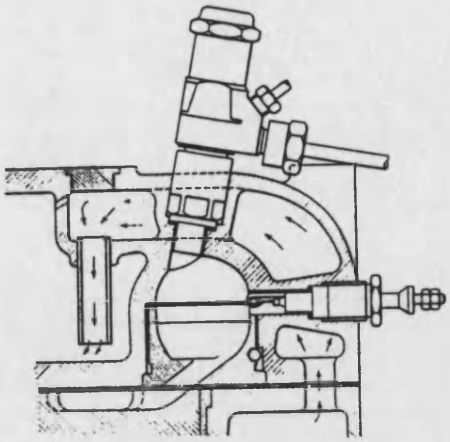

Figure 2.14 (Pounder)
Comet Mk V Chamber

The *Mk III chamber* (Figure 2.13) was the system that was put into production in almost all the engines that used the Ricardo system, and was used with modifications until the late 50s. The original Mk III (as in the 1931/34 patents) was similar to the Mk II with the important difference that a cavity and two hemispherical depressions were machined into the piston crown, reducing the tdc volume ratio from around 80% to 50%. The swirling motion formed in the piston cavity by gases leaving the swirl chamber brought the air in the main chamber into contact with the burning air/fuel mixture, greatly increasing air utilisation. The reduction in the amount of air transferred to the swirl chamber also reduced pumping and heat transfer losses. Later versions of the Mk III, modified the design slightly: the spherical shape was elongated slightly by addition of a short cylindrical section between them to increase the distance for fuel penetration before impinging on the hot insert. The figures shown for Mks I,II & III, all use tapered throats. From quite early on, some companies using the design opted for a constant cross-section throat to reduce machining costs.

The Mk V chamber[2] (Figure 2.14) was developed in the late 50s to meet the growing requirement of high-speed Diesels for small commercial vehicles and taxis. Whereas the Mk III used a spherical (and later elongated) chamber, the insert of the Mk V was modified so that the side of the insert, opposite the throat entry took the form of a cone, (ie straight edged). This modification apparently increased the air

---

[2] The Mk IV was a Ricardo experimental engine

utilisation in the chamber, possibly by increasing the distance the fuel could travel before impinging on the insert wall. Changes were also made to the piston crown design, moving from the hemispherical depressions towards the *clover-leaf* shape. The Mk Vb was developed by Ricardo together with Ford in the late 60's, and has been used without substantial modification by most diesel engine manufacturers since.

5.2 Pre-combustion chamber (pre-chamber) system

Developed in Germany, it was widely used on the continent and in some imported engines in the UK. It was still used in some British Rail locomotives until the 70s when it was superseded by the high speed DI. The combustion system is still used in the form of the Mercedes pepper-pot engine.

During the compression stroke, air is forced through a number of small holes into a separate chamber in the cylinder head. Shortly before top dead centre, all the fuel is injected into the turbulent air in the pre-chamber. Following ignition, the expanding gases force the burning air/fuel mixture back into the main chamber. Whereas the Comet system uses an ordered swirling mechanism to aid air/fuel mixing, the original pre-combustion chamber relied solely on the turbulence generated to mix the air and fuel. Figure 2.15 shows a recent development of the Mercedes prechamber design in which a degree of ordered swirl is given to the incoming air.

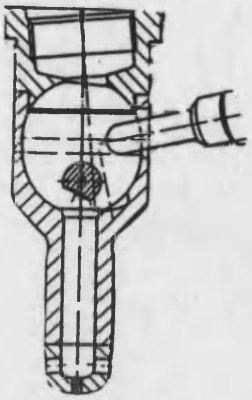

Figure 2.15
1989 Mercedes
pre-chamber design

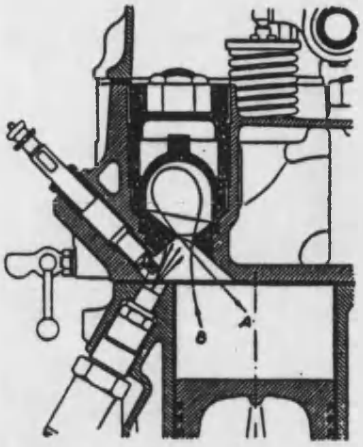

Figure 2.16 (Judge)
Acro chamber

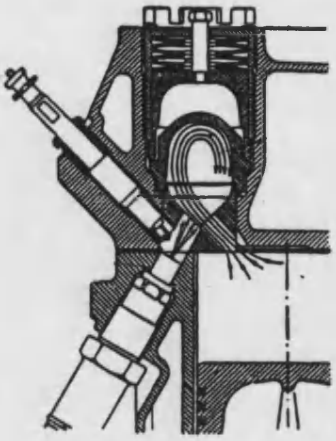

Figure 2.17 (Judge)
Kreuzstrom chamber

5.3 Acro (Bosch-Acro)

Developed by Saurer, the system was produced by the company from 1928 and fitted to heavy lorries, and later used by a number of other companies. The basic outline is shown in Figure 2.16, but each application of the system modified it. A narrow cone of fuel spray is injected into the throat venturi, and the turbulence generated in the throat gave reasonable air/fuel mixing. The Acro system lacked both the ordered swirling motion of the Ricardo system, and the intense turbulence of the pre-combustion chamber system, and was modified by Saurer in 1932 to the *Kreuzstrom* ('cross-stream') (Figure 2.17), which does give a degree of ordered swirl. Reports vary as to whether combustion actually took place in the chamber, or whether its principal purpose was as an air cell, supplying air to sustain combustion, as the exhaust gases escaped back into the main chamber.

5.4 Lanova

Developed by the German engineer Lang, this design was first used by Henschel in the early thirties, and became popular in Germany and the US. The Lanova was probably the most widely used air-cell engine. (Figure 2.18) Shortly before top dead centre, fuel is injected (from the left-hand side) into the air-cell (on the right). Ignition takes place in the air-cell, and as the pressure in the air cell becomes greater than that in the cylinder, air is forced from the air cell. The air leaving the air cell hits and atomises the incoming fuel spray carrying it round in two annular paths (figure of eight), although late versions (sixties) used a single offset lobe. An interesting feature of some models of the Lanova was a screw (on the right-hand side of Figure 2.18) which allowed the volume of the air cell to be reduced, increasing the compression ratio to improve cold starting. Some variations of the engine had a profiled air cell, to form a series of air cells along the same axis, with a slight restriction between them. One of the disadvantages of the Lanova, is that the swirling motion formed is very dependent on combustion, and therefore difficult to optimise over a range of engine speeds (cf the Ricardo where the swirl is proportional to engine speed).

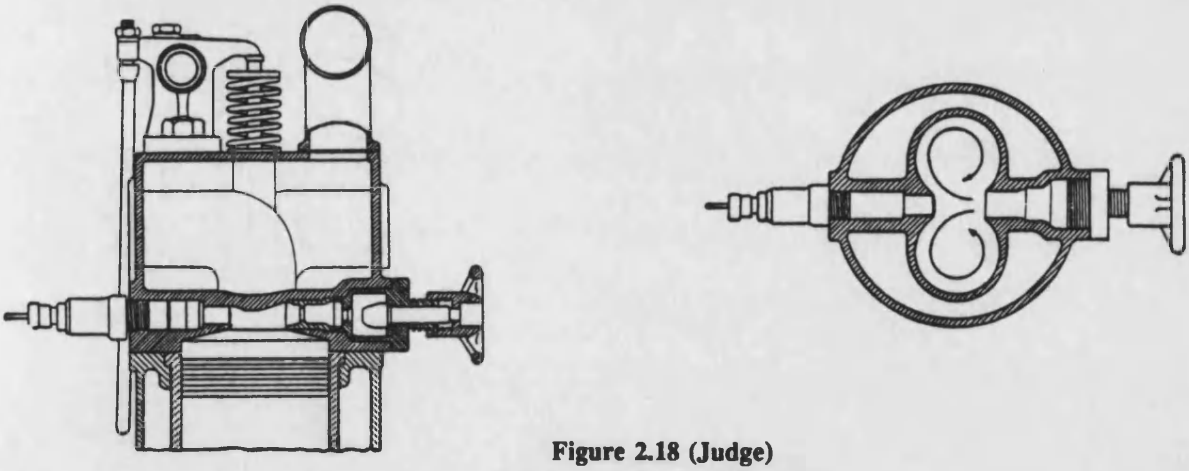

Figure 2.18 (Judge)
Lanova combustion chamber

5.5 Later systems

The Lanova was modified and developed in many different directions, by various companies in Europe and the US. The *Perkins Aeroflow* (Figure 2.19) was

successfully used by the company for many years. The *Omo* head (Figure 2.20), was also popular on the continent and in the States. Other interesting designs include the *clerestory* chamber (Figure 2.21), with the valves in the chamber itself.

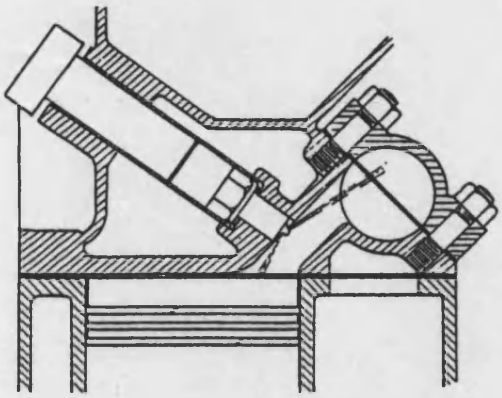

Figure 2.19
Aeroflow

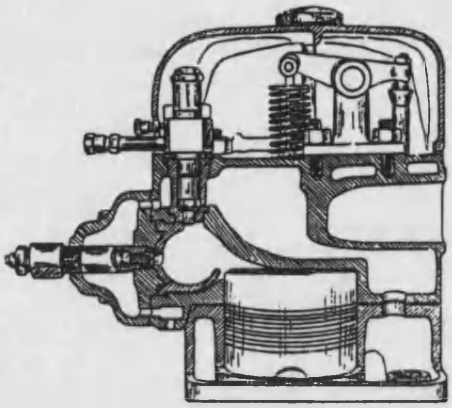

Figure 2.20
Omo

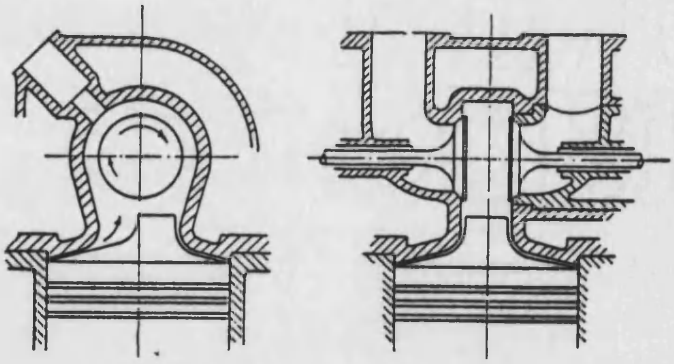

Figure 2.21
Clerestory pre-chamber

CHAPTER THREE
EXPERIMENTAL INVESTIGATION

1 Introduction III-2

2 Experimental facilities III-2
2.1 The Ford diesel engine and drive III-2
2.2 Modifications made to the engine III-4
2.3 Instrumentation and Data acquisition III-8
2.4 Infra-red measurement of surface temperatures III-12

3 Experimental procedure III-13

4 Pressure data III-14

5 LDA measurements of swirl chamber air velocity III-19
5.1 Introduction III-19
5.2 The LDA system III-19
5.3 LDA measurements in the IDI engine III-21
5.4 Discussion III-25

1 Introduction

This Chapter describes an experimental investigation of the in-cylinder pressure and air motion during the compression and expansion strokes in a motored Ford 1.8l IDI passenger car diesel engine. Swirl chamber air velocity measurements have been made using laser doppler anemometry (LDA), although very few results were obtained. Modifications to a standard production engine have been made to allow optical access to the swirl chamber, while preserving the regular internal geometry.

In Chapter 4, results obtained from the computer simulations of the same process will be presented and the results compared in Chapter 5.

2 Experimental facilities

2.1 The Ford diesel engine and drive

All test data presented here have been taken from a standard Ford 1.8l IDI diesel engine. This type of engine is currently in production and is used in the Fiesta and Escort passenger cars and vans. A number of modifications have been made to the research engine, and these are discussed below. The experimental work has been undertaken on a motored engine - instead of injecting fuel into the engine, it is driven from an external electric motor. Both the diesel engine and electric motor are mounted on a large cast iron bed plate. Figure 3.1 shows the rig, set up for laser doppler anemometry measurements.

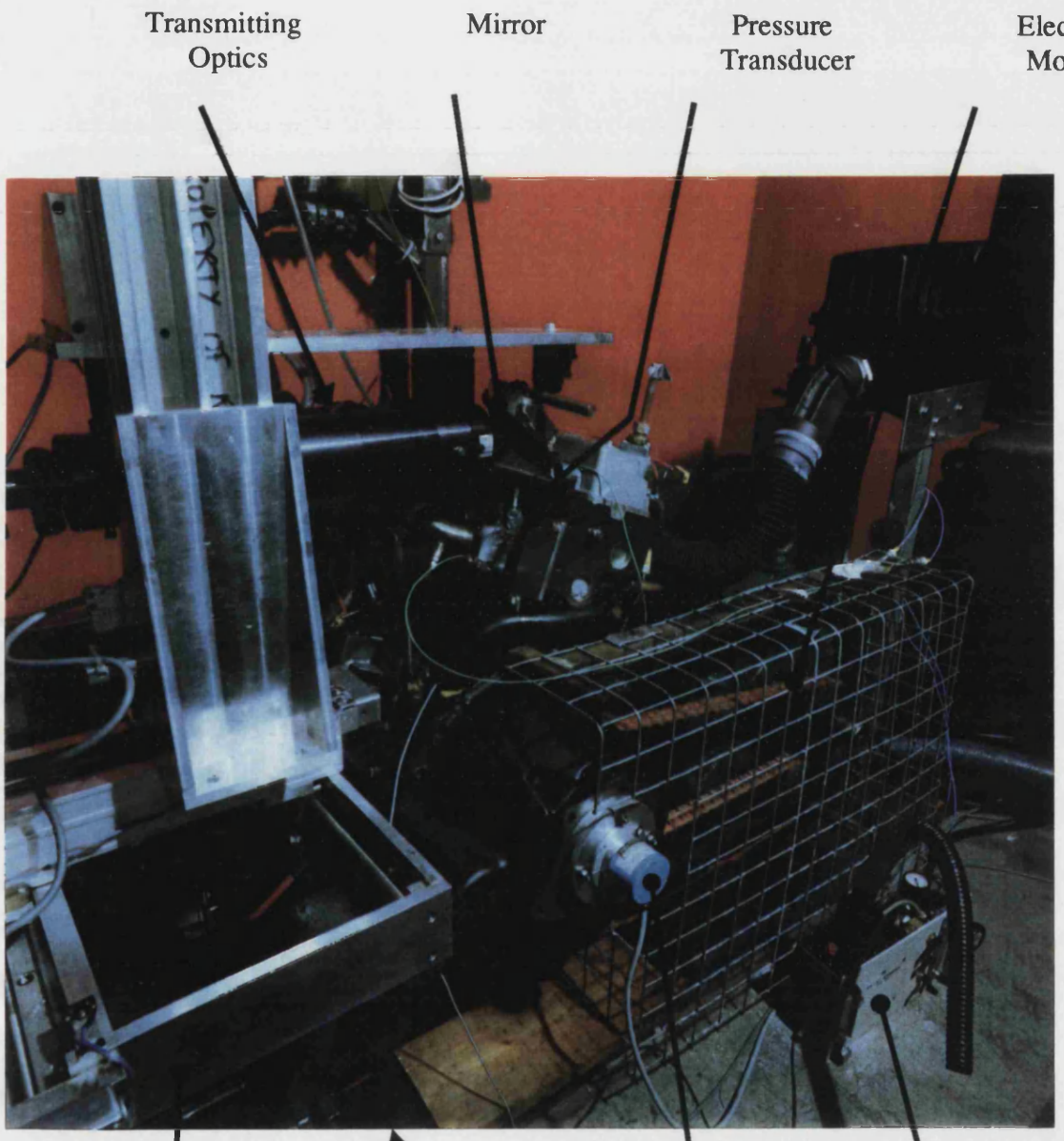

Figure 3.1
Experimental Test Rig

The size of electric motor required to turn the engine at a given speed can be estimated as follows.

Assuming a friction mean effective pressure (fmep) of around 3.5bar at 3000rpm (Heywood figures for small IDI engines), then

$$Power = \frac{Work(J)}{time\ per\ two\ revs\ (s)}$$

$$Power = \frac{1.8\times10^{-3}m^3 \times 3.5\times10^{5}Pa}{2\times60/3000\ \text{sec}}$$

$$\rightarrow Power \approx 16\ kW$$

Thus a 16kW motor should have the power to turn the engine at 3000rpm. For this study, a fixed speed 17kW (23hp) 440V 1500rpm motor was used. Pulleys on the motor and engine shaft were changed to vary the engine speed. Although fitted with a star-delta starting mechanism, the low speed torque of the electric motor was insufficient to start the diesel engine unaided. Activating the engine starter motor for a short period however allowed the electric motor to reach a speed where the torque was sufficient to drive the engine. Using this starting technique, the motor ran with speeds up to 1500rpm. With higher gear ratios, the starter motor speed, when referred back to the motor was not sufficient to overcome the low speed torque restriction. Although the motor has the *power* to drive the engine at 3000rpm, it does not have sufficient *torque* at low speed. Using a combination of pulleys, the engine could be driven at 900,1200 & 1500 rpm.

2.2 Modifications made to the engine

The production 1.8l IDI diesel engine has been mounted to allow it to be motored on a test bed. The engine has been modified to reduce frictional losses and to provide optical access to the swirl chamber. Additionally, to increase the scope for comparisons between the experimental and computational studies, the swirl chamber

insert in one cylinder has been replaced with a specially constructed *reduced throat area* insert.

Running a motored engine on the test bed

The diesel engine can be externally motored without any major modifications. The fuel pump has been removed, and a pulley fitted to the crankshaft, in place of the gearbox. The engine bell-housing has been machined to allow a belt to drive the pulley.

Reducing frictional losses

To reduce the power needed to turn the engine (or for a given power, to increase the speed at which the engine can be run) the pistons in cylinders 1 and 2 have been removed, leaving the balancing pair 3 and 4 (nearest flywheel) in the engine. The cam-followers on the cylinders 1 and 2 have been removed, keeping the valves permanently closed. To maintain the correct lubrication pressure to the remaining pistons, the crankpin bearing shells in cylinders 1 and 2 have been retained, secured by Jubilee clips. The vacuum pump (supplying a vacuum to the servo unit) has also been removed.

Providing optical access to the swirl chamber

Optical access for the laser system to the swirl chamber is provided by replacing the fuel injector in one of the cylinders with a fused quartz window (Figure 3.2)[1]. Quartz is suitable for providing optical access in motored engines as it is optically transparent to visible light, has a low thermal expansion coefficient (0.6×10^{-6} °C^{-1} compared to 12×10^{-6} °C^{-1} for cast iron), and a high melting point (1700°C). The arrangement shown in the photo in Figure 3.2 severely limits the useful field of vision within the swirl chamber but preserves the internal geometry of the engine. Increasing the window size to increase optical access would require extensive machining of the cylinder head, and probably involve re-sealing the coolant jacket. Various methods of sealing the quartz window in the engine were considered. The technique adopted must physically secure the lens against a 50bar pressure, allow

[1] £40 per window (1992). Supplied by Spanoptic Ltd, Glenrothes

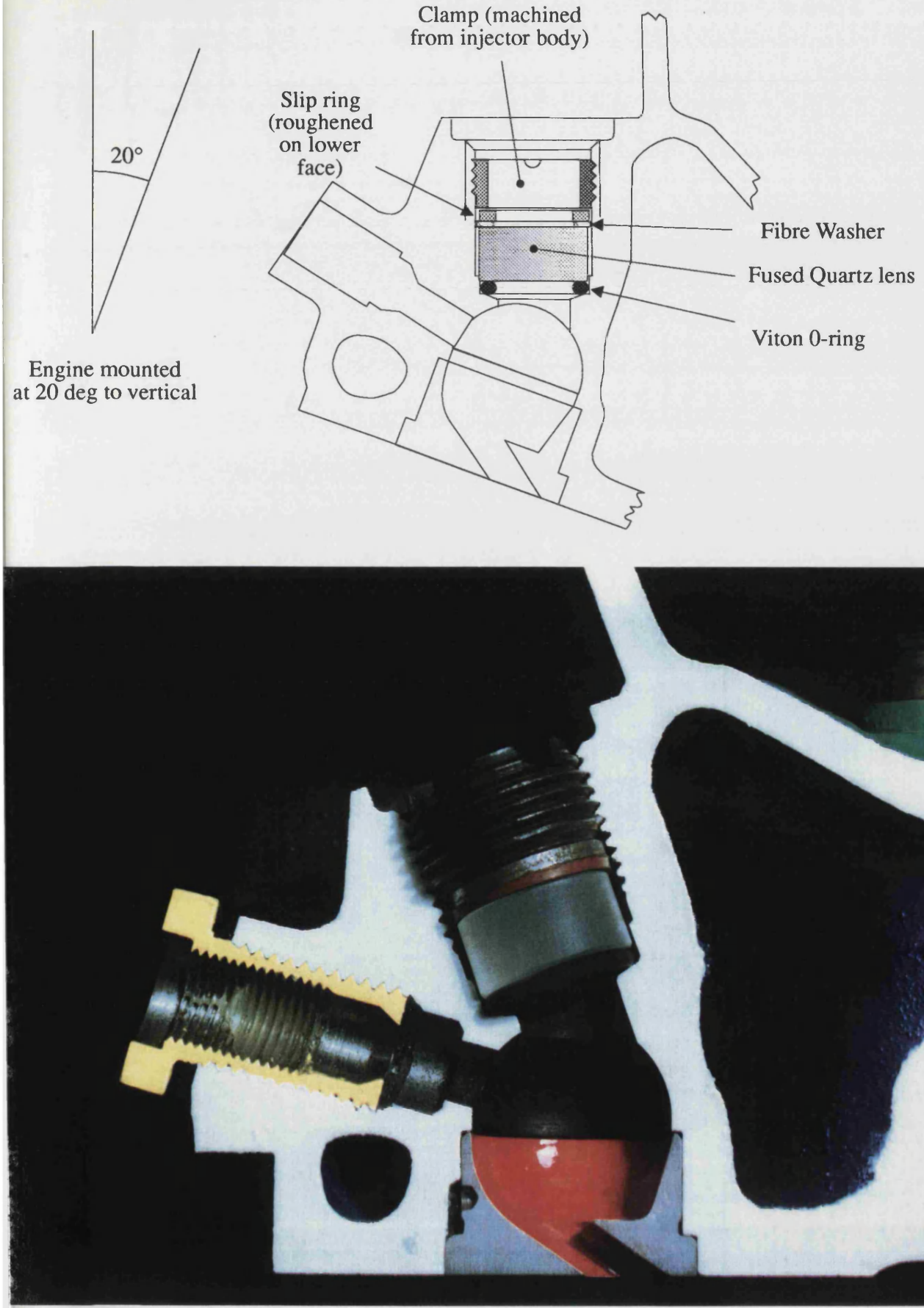

Figure 3.2
Arrangement for securing quartz window in engine for lda measurements

for thermal expansion of the lens, and prevent air leakage. The diagram in Figure 3.2 shows the arrangement used: A viton (heat resistant rubber) seal is placed in between the cylinder head and the lens, and the lens secured by a screw clamp, machined from the outer casing of the fuel injector. Removing, cleaning, and inserting the lens takes about 5 minutes. The quartz lens moves the effective measurement point within the swirl chamber by about 3mm.

Reduced throat area insert

Previous work undertaken (Charlton) has investigated the changes in engine performance due to an increase or decrease in the cross-sectional area of the swirl chamber throat. These studies have been undertaken on engines with throat sizes from 90% to 110% of the standard Ricardo swirl chamber throat area. A numerical parametric study of the effect of the insert throat area on swirl chamber air velocities (Chapter 6) showed that the change in swirl chamber air motion and pressure due to a 10% change in throat area was small, especially at low engine speeds. To allow comparisons between experimental and computational results for two differing cases to be made, a special swirl chamber insert was manufactured with a throat area of

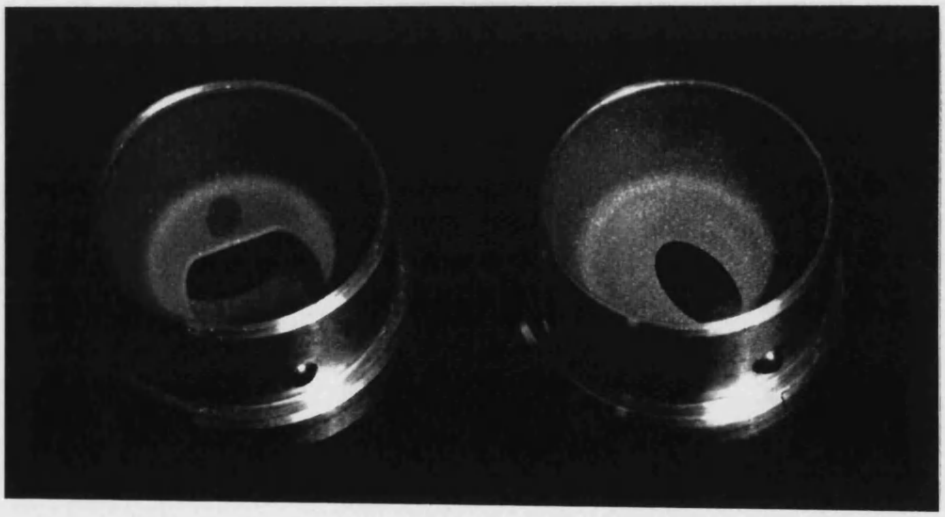

Figure 3.3
Left: Standard Ricardo insert
Right: 50% area throat insert

50% of the standard Ricardo insert (Figure 3.3). After pressure data had been obtained from cylinder 4 with the standard insert, the insert was changed, and the engine run with the new insert in cylinder 4 and the standard insert in cylinder 3. Laser measurements can be made in both chambers by replacing the appropriate fuel injector with the quartz window assembly.

2.3 Instrumentation and Data acquisition

The test rig was configured to measure in-cylinder pressure and swirl chamber air velocity. To support these readings, manifold and coolant temperatures, 'blow-by' and shaft crank angle were also recorded. This section describes the instrumentation used to record all data except that for the laser system, which is discussed in section 5.

2.3.1 Pressure transducers

In-cylinder pressure is measured by pressure transducers. Piezo-electric transducers are used to measure pressure variations over a wide pressure and temperature range. A change in the external force (pressure) applied to the transducer generates an electric charge in a quartz element in the transducer. This charge is amplified and integrated in a charge amplifier which converts the signal to an analogue signal directly proportional to pressure. Piezo-resistive transducers measure pressure directly over a limited pressure and temperature range (0-80°C).

In this study, an absolute pressure piezo-resistive transducer has been placed at the bottom of the main chamber (through a cylinder wall tapping) to give an accurate pressure measurement at the start of the compression process. (Figure 3.4) This information is an important boundary condition for the numerical model. Piezo-electric transducers have been used to measure swirl chamber and main chamber pressure throughout the cycle.

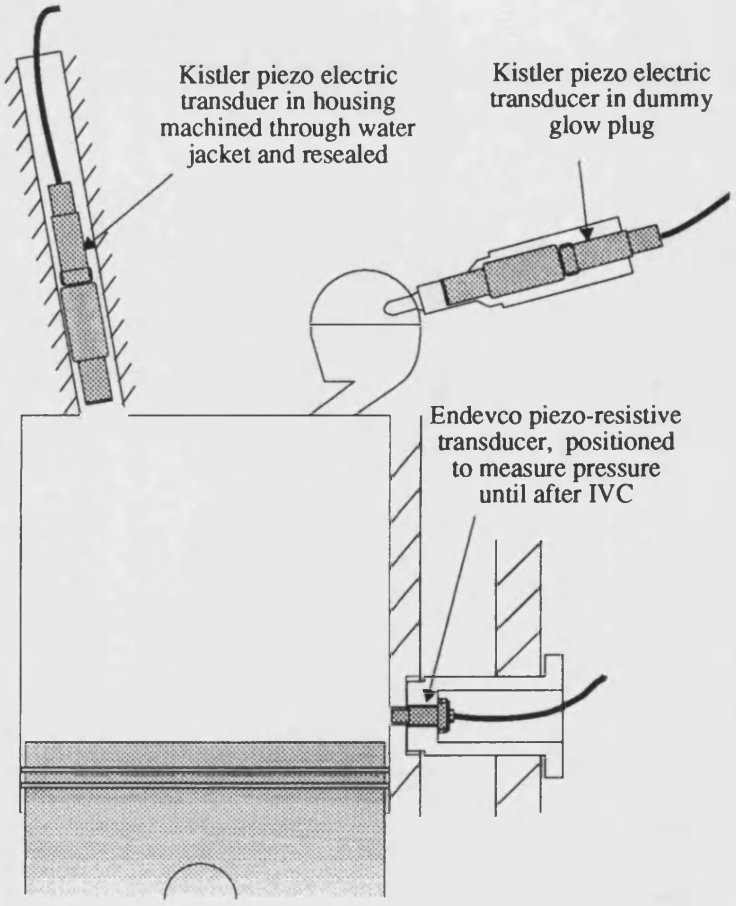

Figure 3.4
Pressure transducer arrangement

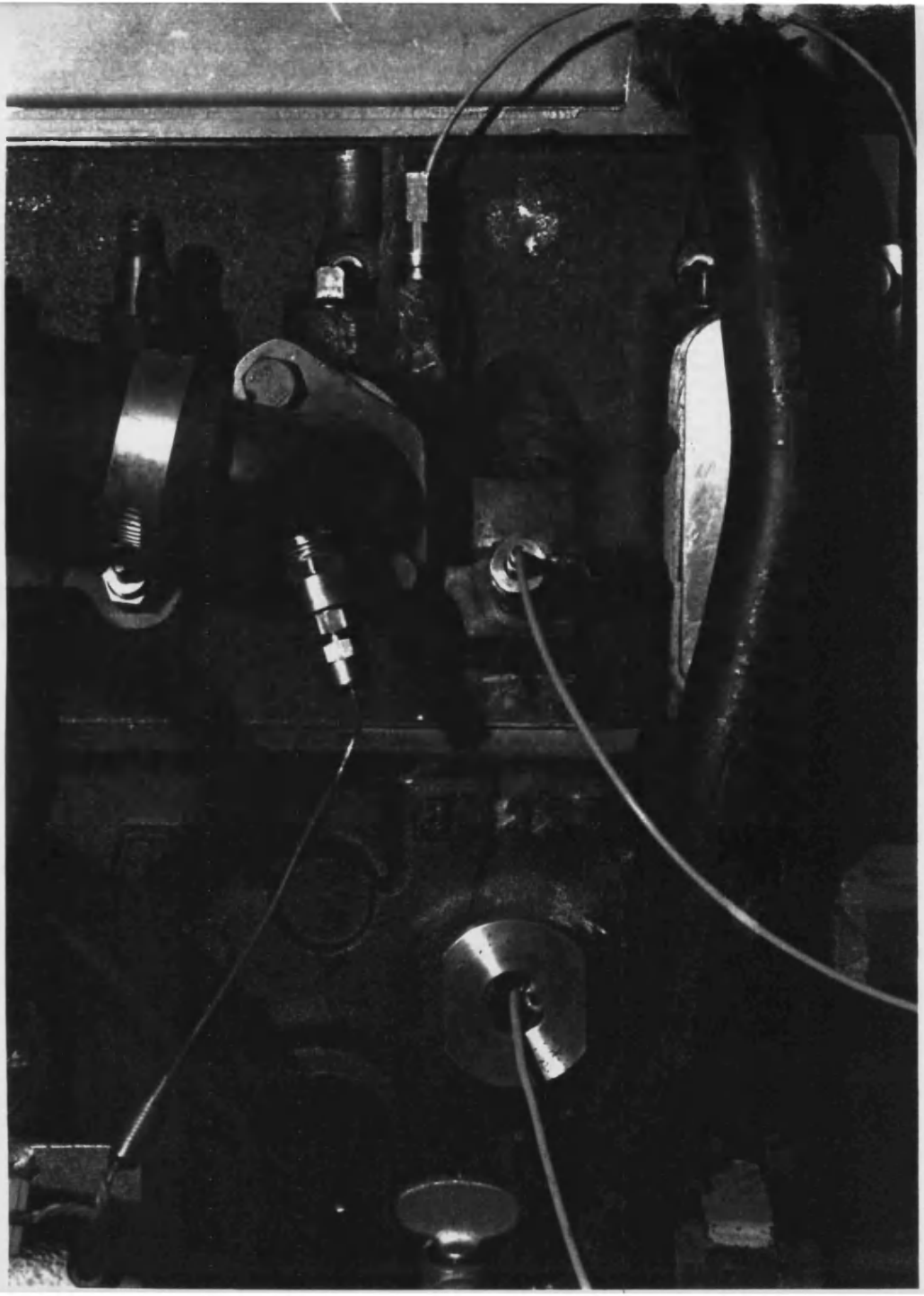

Data acquisition

The three pressure channels are recorded on a 'Computerscope' 1 MHz data acquisition board fitted to a PC. Proprietary software on the computer controls and interrogates the board. The transient data can be displayed varying with time on the screen, and is stored on the computer hard disk. The pressure data acquisition system has been set up to start acquiring data following a trigger supplied (see shaft encoder below) once every two cycles. The instantaneous value of each of the three pressure channels is recorded when a clock signal (configurable to every 2,3,or 4 degrees crank angle) is supplied. Data is then acquired until all or a part of the 64K buffer on the board is full. Figure 3.5 shows a typical 'screen dump' from the Computerscope, showing main and swirl chamber pressures (the lines appear coincidental), absolute pressure (on a different scale) and the encoder once per cycle pulse.

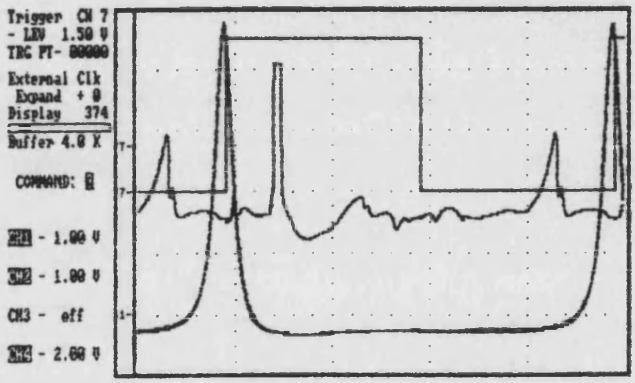

Figure 3.5
Computerscope screen dump

Piezo-electric transducers

Two Kistler piezoelectric transducers (both Type 6121 0-250bar range) are used to measure pressure in the swirl and main chambers. The swirl chamber transducer is fitted inside a dummy glow plug. The main chamber transducer in a tapping through the cylinder head. This tapping is machined through the head, and the water jacket

resealed with 'plastic metal'. The transducers were calibrated using a dead-weight tester, in which a known pressure is applied to the transducers, and the sensitivity of the charge amplifier, adjusted to read the same pressure. The charge amplifier must be switched to the 'long' time setting so that the reading does not decay before the reading is taken. Accurate calibration proved difficult. When calibrated to measure accurately (within 1%) 50bar, an error of up to 5% at 10bar was recorded. Even with the long time setting, the signal corresponding to *zero* pressure, changed by up to 0.5 bar after the 50 bar was applied and released. These problems could be due to errors in any of the calibration, transducer or amplification equipment. The sensitivity setting on the charge amplifier was such that very small adjustments gave significant changes in the output signal, making accurate adjustment tricky. Given the problems experienced in calibrating the piezo-electric transducers, the pressure traces presented below may have an error of upto ±2 bar at peak pressure.

When in the engine, the relative calibration of the two transducers could be checked by swopping the main and swirl chamber channels (ie transducer and charge amplifier). Assuming that the engine conditions did not change between the two tests, after calibration the two transducers gave readings within 1bar of each other at peak pressure.

Piezo-resistive transducer

To measure main chamber pressure at the start of the compression process, an Endevco (Type 8530C) absolute pressure transducer (0-3bar absolute) was placed in a tapping at the bottom of the main chamber. The transducer was placed (70mm below the top surface of the block) to measure pressure from bottom dead centre until after inlet valve closure, before being covered by the piston. Using this arrangement, the transducer was protected from the high temperature and pressure of the full compression stroke. The transducer requires a 10V constant voltage supply, and generates a millivolt signal, which is amplified to provide a 0-5V signal.

2.3.2 Shaft Encoder

A 1000 line optical shaft encoder was fitted to the crankshaft. This provided a once per revolution signal and 1000 pulses per rotation. The once-per-rev signal drives

an engine speed meter and provides the *trigger* for the data acquisition board and the LDA processor. The 1000 per rev signals were filtered to reduce the signal to 500, 333 or 250 pulses per revolution and used to provide the data acquisition board with *clock* signals.

2.3.3 Temperature measurements

Thermocouples were fitted to measure the temperature of the coolant flowing out of the cylinder head, and inlet and exhaust manifold air temperatures. The primary purpose of these readings was to monitor engine conditions. The temperatures were displayed, but not automatically recorded.

2.3.4 Measurement of piston blow-by

Blowby is the term given to loss of charge past the piston rings to the crankcase. The amount of charge leakage is primarily a function of in-cylinder pressure and engine speed, but is also influenced by the state of the piston rings and cylinder lubrication. Blowby in a motored engine is likely to be very different to blowby in a firing engine due to the different mep in the cylinder. The effect in a motored engine of the loss of charge is to reduce the peak pressure. Instantaneous measurement of blowby is difficult, however by attaching a flow meter to the crank case, a time averaged value can be obtained. With one piston only in the engine (the second piston was later added to improve the engine balancing) running at 3000rpm, blowby was measured at 8l/min with the engine cold and 9l/min with the engine hot. This is equivalent to about 2% of the swept volume and a 1 bar reduction in peak pressure.

2.4 Infra-red measurement of surface temperatures

As optical access to the engine had been arranged for the LDA testing, the possibility of using an infra-red thermometer to measure swirl chamber surface temperature was investigated. Black body radiation at 70°C has a wavelength of 8450nm, and at 300°C, 4300nm (Wien's displacement law - [59]). The quartz window is not transparent to light at this wavelength [60]. Calcium Fluoride is suitable for infra-red

measurements in this range, but its high coefficient of expansion probably makes it unsuitable for engine work. Other materials proved too expensive.

3 Experimental procedure

A 3kW coolant heater was attached to the engine to reduce the time needed to reach reasonably steady conditions. After 30 minutes of heating with the engine stationary, the coolant temperature leaving the head was raised to around 60°C - oscillating as the heater switched on and off under thermostat control. When the electric motor is switched on, the temperature falls immediately to around 50°C, and rises slowly. All test data has been taken with the coolant temperature out of the head between 55° and 65°C. When running at 900rpm, the steady state temperature is around 55°C. At 1500rpm, the steady state temperature is in excess of 70°C - reached after 60 minutes. Without the engine heater, the engine takes over an hour to reach 60°C.

4 Pressure data

Figure 3.6 shows the 1500rpm pressure trace taken from the absolute pressure transducer placed towards the bottom of the main chamber (See Figure 3.4). The shaded areas represent the cycle windows where the piston is covering the transducer. Following firing tdc (on left hand side of the plot), pressure in the main chamber falls to 0.85bar absolute (ie sub-atmospheric). As the exhaust valve opens, the pressure

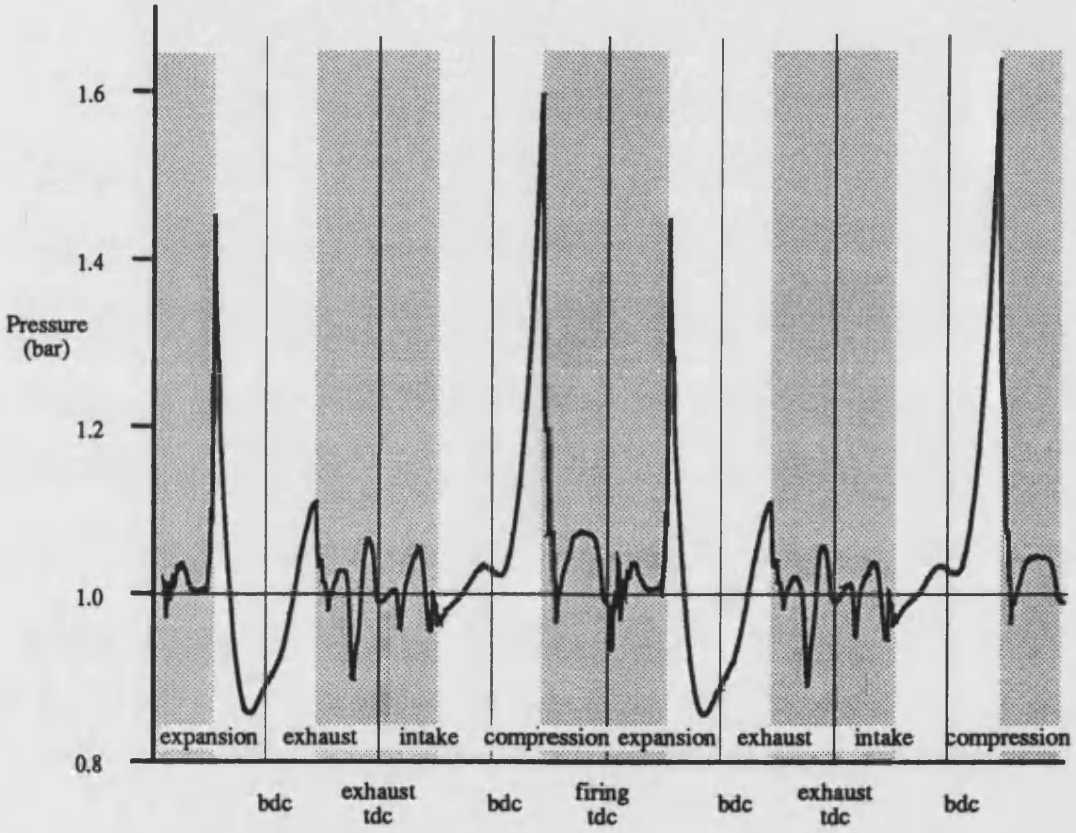

Figure 3.6
Pressure Trace from absolute (piezo-resistive) transducer
Shaded areas represent parts of cycle where piston covers transducer

rises as air is sucked into the cylinder. As the piston changes direction at bdc, the rate of increase of pressure changes as air is pumped out of the chamber. On the intake stroke, the piston uncovers the transducer when the chamber pressure is sub-atmospheric. As the air is pulled into the cylinder, the pressure rises. The manifold tuning appears to lift the chamber pressure above atmospheric - as the intake stops,

the reduction in pressure around intake bdc suggests that the charge leaks out until the intake valve (at 37°abdc). The piston covers the transducer again during the early stages of the compression stroke.

Processing the piezo-electric transducer data

The figures on the next page show the main and swirl chamber pressure traces taken at two engine speeds. The pressure traces are ensemble averaged over around 12 cycles (the maximum number of cycles is limited here by the 64kByte acquisition board memory limit). To ensemble average the data, the trace is first broken down into a series of 720°cycles. Within each cycle, the main and swirl chamber pressure at bottom dead centre before compression are shifted to match the absolute pressure *at this point* - the piezo-electric transducers measure rate of change of pressure and can drift from cycle-to-cycle. An ensemble-averaged trace is calculated by averaging the corresponding points within each cycle. Figure 3.7 compares the raw *point data* with the averaged data from 12 consecutive cycles. Over this period there is very little variation in the measured pressure, and the trace from any one 720° cycle would be a good representation of the *average* cycle.

Although the research engine is fitted with an optical shaft encoder, it was not

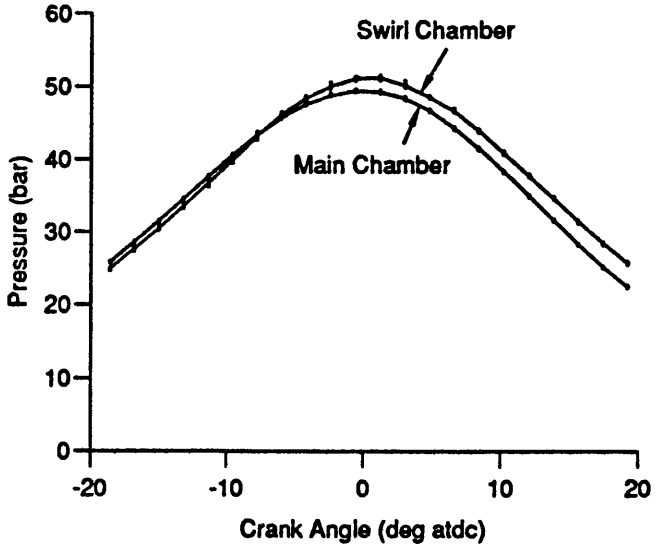

Figure 3.7
Comparison of point and ensemble averaged pressure

possible to set the encoder top dead centre pulse to mark accurately (to within 0.5°degree) tdc. For all pressure results presented here, the pressure curves have been shifted along the crank angle axis so that tdc occurs at the point of maximum main chamber pressure. If it were possible here to plot pressure against the real crank angle axis, a speed dependent delay between peak pressure and tdc of up to 1°CA at 1000rpm (0.6°at 4500rpm) would be recorded. [Pinchon-47].

Figures 3.8 and 3.9 plot the ensemble averaged pressure trace for engine speeds of 920 and 1470rpm. During the compression process, the pressure in the main chamber leads the swirl chamber. At both speeds, the swirl chamber pressure rises above the main chamber pressure before top dead centre. From the two piezo-electric pressure transducers, it should be possible to calculate the pressure difference across the throat. This parameter is useful as it is proportional to the compression pumping loss in the engine, and can be directly compared with the computational results. The peak pressure difference between the two chambers is proportional to engine speed: peak pressure differences predicted by the numerical study (Chapter 4) are 1 bar at 1500rpm rising to 9 bar at 4500rpm.

With the engine running at the maximum obtainable speed of 1500rpm however, it was impossible to measure reliably the pressure difference between the two chambers. If the peak pressure difference is around 1 bar (as suggested by the numerical model), a 0.5% error in each of the transducers can result in the apparent

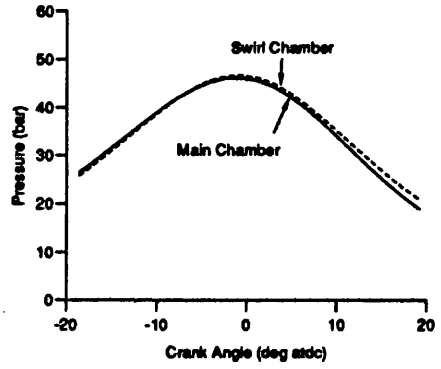

Figure 3.8
Main and Swirl chamber pressures at 920rpm

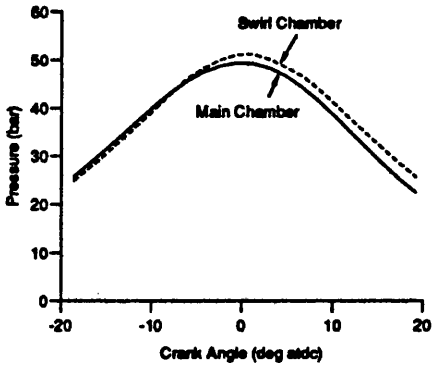

Figure 3.9
Main and Swirl Chamber pressures at 1470rpm

pressure differences being eliminated or doubled, depending on the direction of the error. Errors in the transducer readings are expected due to:

- relative calibration errors (the two transducers are not identically calibrated) - Confirmed by interchanging the two transducers (around 1 bar difference at peak pressure)
- readings can be changed by up to 0.5 (at peak pressure) by adjusting tightening torque and transducer mounting

From Figures 3.8 and 3.9 however, the variation of pressure difference with engine speed can be seen. The pressure difference across the throat is significantly greater at 1470rpm than 920rpm. Peak pressure also varies with engine speed. Peak swirl chamber pressure at 920rpm is around 46bar, and around 52bar at 1470rpm. This difference is probably due to increased heat losses at the lower engine speed (the faster the engine, the closer to adiabatic the cycle) and more time for piston blow-by.

The expansion stroke pressure difference plotted in Figures 3.8 and 3.9 is unrealistic. Although the trend is correct - the main cylinder pressure trails the swirl chamber pressure, the difference between the two pressures should diminish towards bottom dead centre, as the piston (and air motion) slows down. In the Figures shown, the pressure difference remains significant until well past bdc. The same results are obtained if the transducer channels (transducer, cables and charge amplifier) are interchanged. These results may be due to charge loss in the cabling from the transducer to the charge amplifier. Changes in pressure on the transducer create a charge. If the insulation in the cabling is deficient (perhaps due to the mounting arrangements), the final *apparent* pressure following an adiabatic compression / expansion cycle will be below the initial pressure. A more likely explanation may be thermal effects on the transducers (which do have integral temperature compensation). Figure 3.10 shows the comparison between the *absolute* pressure and the piezo-electric pressures (main and swirl) at the bottom of the pressure range. The three pressures match closely at the beginning of the compression stroke. At the end of the expansion stroke however, both piezo-electric transducers are giving unrealistically low readings (traces occasionally indicate sub-zero absolute pressures). If thermal effects are the cause of the discrepancies, it would be expected that the main chamber transducer would be more greatly affected -

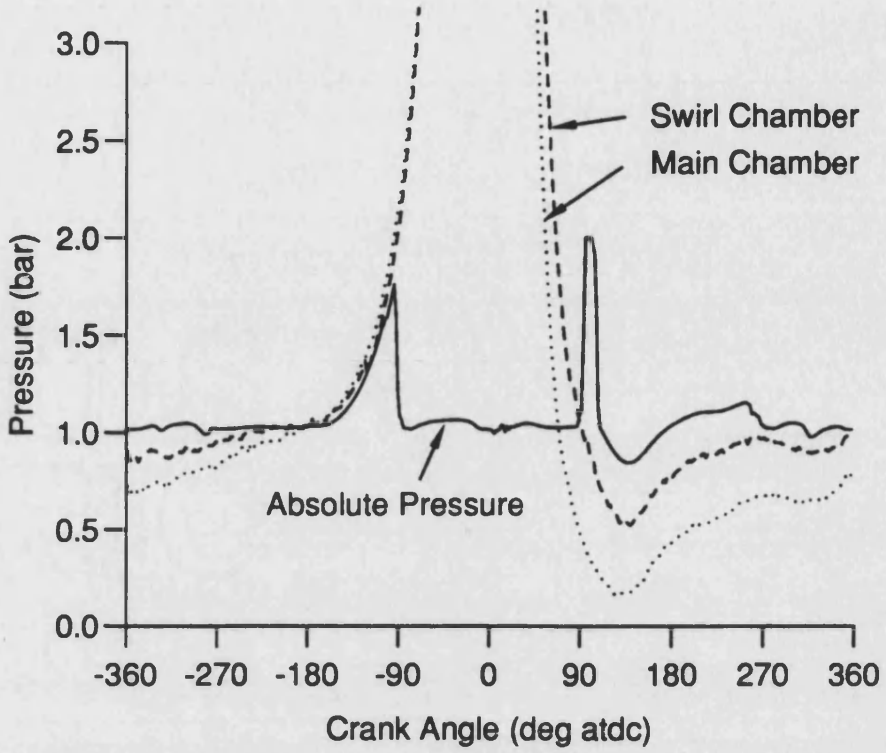

Figure 3.10
Ensemble averaged pressure comparison at beginning of compression and end of expansion strokes (920 rpm)

the swirl chamber transducer is totally enclosed in the dummy glow plug, and is therefore better protected from thermal load. From Figure 3.10 it is clear that although both piezo-electric traces are unrealistically low, the main chamber trace is the worse of the two.

Although the technique used in this study to measure the main and swirl chamber pressures is an established procedure, it is generally used in firing engines, where (genuine) pressure differences between the traces during the expansion stroke are a much larger percentage of the peak pressure. Additionally, it is unlikely that in the absence of the *absolute* pressure transducer, the *over-expansion* at the end of the expansion stroke would be noticed.

5 LDA measurements of swirl chamber air velocity

5.1 Introduction

Laser Doppler Anemometry works on the principle that when the Doppler shift from two (coherent) beams incident on a particle interact, a beat frequency is produced, proportional to the particle velocity component normal to the plane of the beams. Receiving optics feed the scattered light to a photomultiplier, which amplifies and filters the signal. From the photomultiplier the signal is analyzed in a signal processor. As the flow velocity varies, particles with a range of velocities produce a series of Doppler bursts, from which the varying flow velocity can be determined.

Laser Doppler Anemometry has a number of advantages for in-cylinder velocity measurement: the technique itself is non-intrusive, although in allowing optical access, modifications may have to be made to the engine geometry; velocity measurements are spatially resolved and independent of local fluid properties (eg temperature and pressure); given suitable seeding particles, the technique is fast enough to measure very high frequency fluctuations. The principal disadvantages of LDA are the initial cost of a system, and the expertise required to operate the equipment.

5.2 The LDA system

Early laser systems relied on careful alignment of a series of lenses and mirrors. More recent commercial laser systems use modular units which significantly reduces set up time, and enhances the reliability of the system. Figure 5.20 shows diagrammatically the laser system used in this study. A fibre optic link carries the output from a 1W Argon-Ion laser to the transmitting optics, mounted alongside the engine. The transmitting optics module is mounted on a x,y,z electrically driven traverse unit. The back-scattered Doppler signals are passed through a photo-multiplier into the signal processor, which is interrogated by a PC-based software package. Accurate alignment of the modular components in the system (eg laser into the fibre optic) is important. In setting up the laser, allowance must be made for refraction of the light passing through the quartz window.

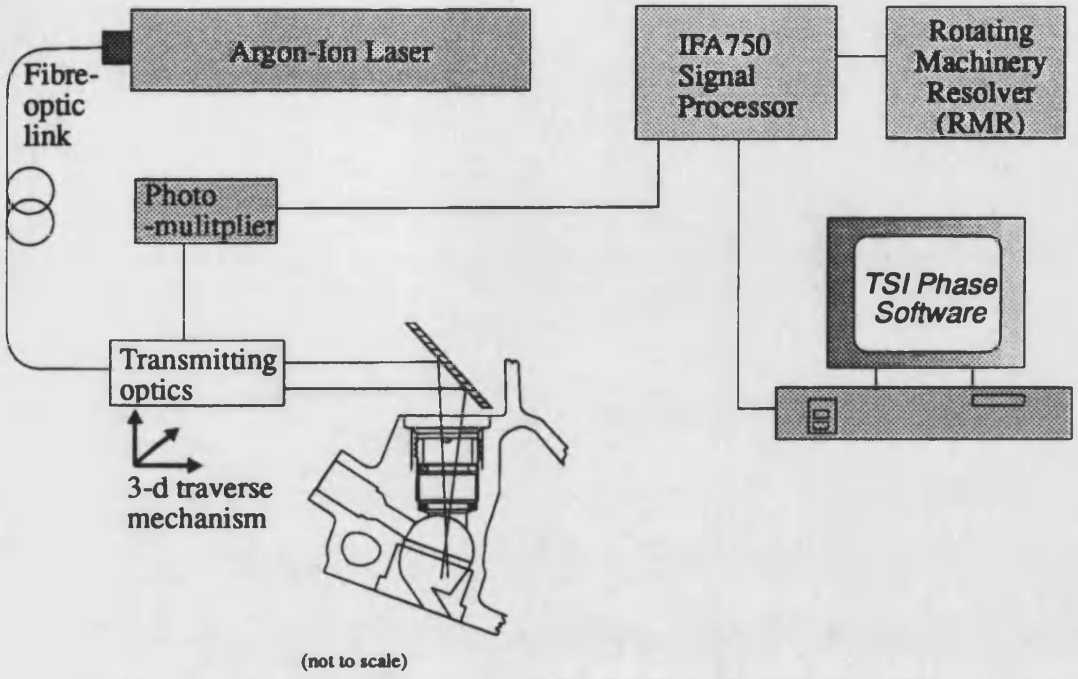

Figure 3.11
Schematic of LDA system

To provide particles to generate the Doppler bursts, the flow must be seeded. Seeding particles must be small and light enough to follow the flow, whilst being big enough to provide an acceptable data rate. In this study, 1.2μm quartz spheres, suspended in an ethanol solution have been atomised in a TSI 6-jet blast atomizer. The blast atomizer produces a cloud of particles which are fed into the engine inlet manifold.

The signal processing equipment consists of a TSI 'rotating machinery resolver' (RMR), and a TSI IFA750 single channel processor. The RMR is fed with the shaft encoder signal and resolves the signal into cyclic information. The RMR has been set up to resolve a 720° cycle, split into *bins* of x° crank angle, where x can be set as required (generally 3.6°). Over any one cycle, the data rate is not sufficient to produce a complete velocity profile for the cycle. Instead, over a series of consecutive cycles, any velocity data collected over the duration of the (x°) bin is stored in it. The velocity data from each bin is then averaged to provide an ensemble

averaged velocity for that bin. Given sufficient data in each bin, it is possible to plot velocity and turbulence levels over the cycle.

5.3 LDA measurements in the IDI engine

The LDA study of swirl chamber air motion proved disappointing. Although it was anticipated that it would be difficult to obtain comprehensive data from the study, the extent of these difficulties was not foreseen, and in spite of numerous attempts, it was not possible to obtain data over the whole of the compression and expansion strokes. The main problems arose from the very low data rate obtained from the engine. The TSI signal processing equipment provides a range of control settings which allow the sensitivity of the equipment to be increased, at the expense of accuracy. Even with the most lenient settings, background noise (which shows up as constant random velocity 'measurements') was significant over most of the cycle, and very few genuine Doppler bursts were detected, especially at higher air velocities. At a number of points within the limited field of view, background noise swamped *all* real data. A range of filter settings are available to limit data acquisition over certain velocity ranges. Through careful filter selection, the background noise could be reduced to a level where low velocity (-20 to 20 m/s) readings could be taken.

Given sufficient running time, even with the limited data obtained during any one cycle, it *should* be possible to build up a velocity profile of the cycle where data is obtainable: the photo-multiplier which amplifies the Doppler signal is set to a low level to cut out the background noise, and the signal processing equipment simply waits until each bin (set to 3.6° or 7.2°) is full, however long is necessary. In practice, after around 15 minutes operation, the quartz window became fouled with a thin coating of oil and seeding particles, and had to be cleaned. It was not therefore possible to run the test for long enough for a full data set to be taken. For most of the results shown below, the engine was run for around 4 minutes at 920rpm (=1800 720° cycles).

To generate a Doppler burst, some form of seeding is required. The TSI jet atomizer was used to provide a cloud of 1.2μm spheres which were fed into the intake manifold. When the engine was run without the seeding, Doppler bursts were still measured over some of the cycle. This may be due to residual particles within

the manifold being dislodged, dust particles in the intake charge, or oil droplets from within the engine. When the atomizer was activated, data rate increased during, and following the high velocity part of the cycle (shortly before and after compression top dead centre). High data rates were occasionally obtained during the engine expansion stroke, primarily when the engine was cold. This is likely to be due to water droplets forming within the engine towards the end of the expansion stroke. This effect appeared (subjectively) more marked on humid days. It is possible that some of these water droplets remain in the swirl chamber during the gas transfer part of the cycle and seed the following compression stroke air flow.

Figure 3.12 shows the cyclically resolved velocity profile obtained from the standard Ricardo Comet V swirl chamber. Each dot on the plot represents one bin of data: straight lines have been drawn in connecting consecutive bins. The velocities shown in Figure 3.12 must be analysed with reference to the plot of *number of data points per bin*, Figure 3.13. Very few readings were taken in the period between 30°btdc and 5°atdc, and in some cases the velocity measurements in the region are taken from one or two Doppler readings per bin. Given the extremely low data rate, the velocity data in this region cannot be considered significant. Figure 3.14 illustrates this point by removing from the plot, all bins containing 5 or fewer velocity measurements. Over most of the cycle, the two curves are identical, as every bin contains sufficient data. None of the bins in the region from 30°btdc to 5°atdc contain more than 5 readings.

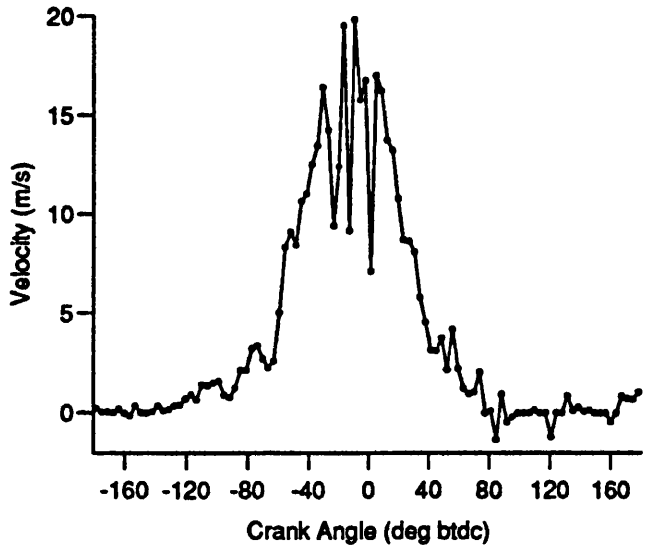

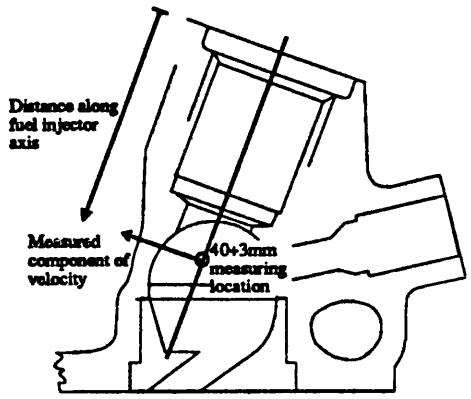

Figure 3.12
Cyclically averaged LDA data @ 920 rpm

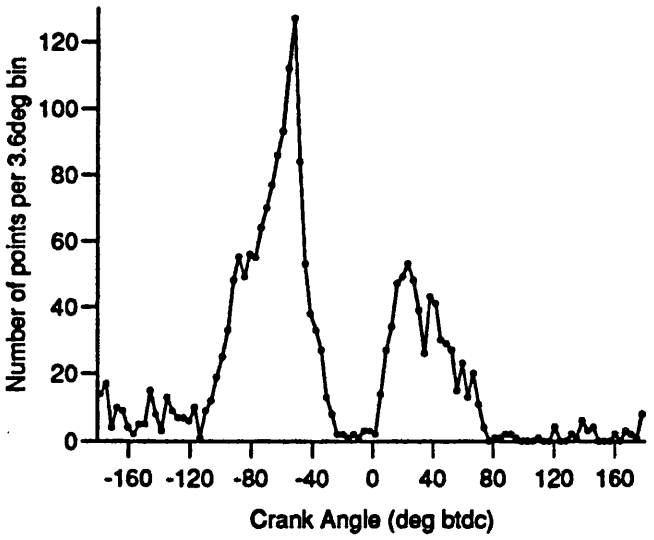

Figure 3.13
LDA velocity measurement data rate over cycle

Figure 3.15 compares the effect of bin size on the velocity profile. During two consecutive runs, bin sizes of 3.6° and 7.2° crank angle were defined. Over the whole cycle, an average 23 'good' data points per bin were recorded for the 3.6° bin size cycle, and 43 points per bin for the 7.2° cycle. For most of the cycle, where data rate is adequate, there is little difference between the two curves. In the high

velocity region around top dead centre, where data rate falls to a very low level, increasing the bin size averages out peaks in the data.

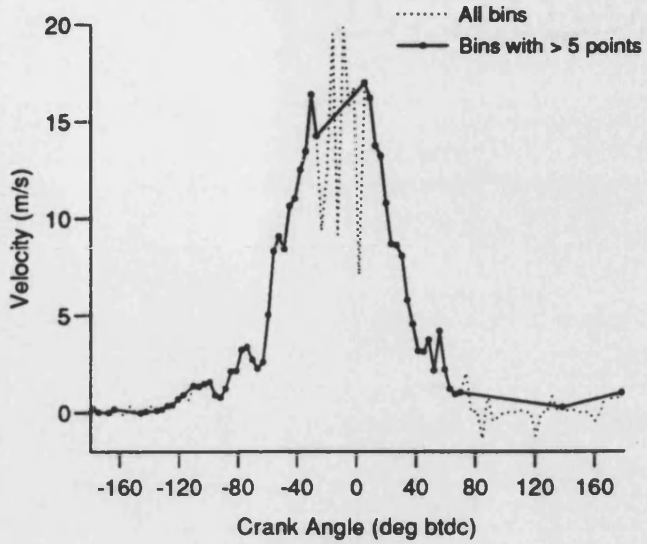

Figure 3.14
Effect on velocity profile of removing bins 5 or fewer velocity measurements

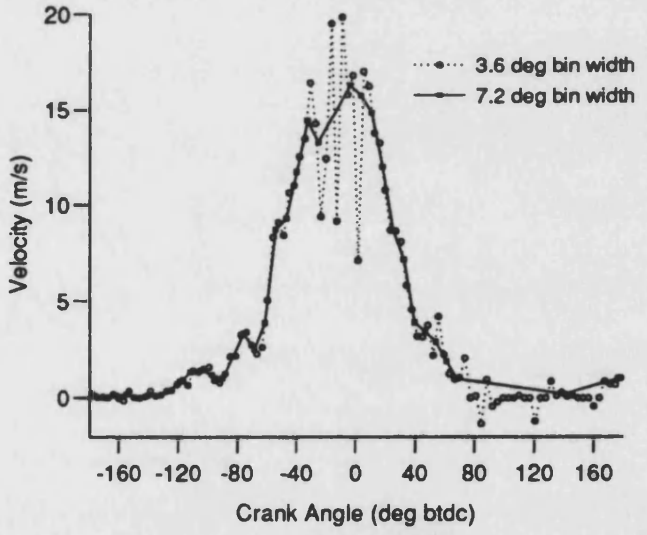

Figure 3.15
Effect on velocity profile of changing the acquisition bin width

Figure 3.16 compares the LDA measurements of velocity at 3 points in the flow field. The component of velocity measured is that crossing perpendicular to the axis of the fuel injector, and the results follow the expected profile of velocity increasing away from the centre of the swirl chamber. The markers indicate the bins,

and the data has been filtered to remove those bins which contain no or one data point only, thus no data is plotted for 37mm location in the period 40°btdc until shortly before tdc. Each of the curves has a similar *points per bin* profile to that shown in Figure 3.13: very little data is recorded around tdc.

Although the filter settings used to reduce background noise will tend to remove data readings over 20m/s, Figure 3.16 shows that these settings were probably not the cause of the lack of data in the high velocity area: Data rate drops over the 40°btdc to tdc region, not just at the high velocity positions but at each of measurement locations.

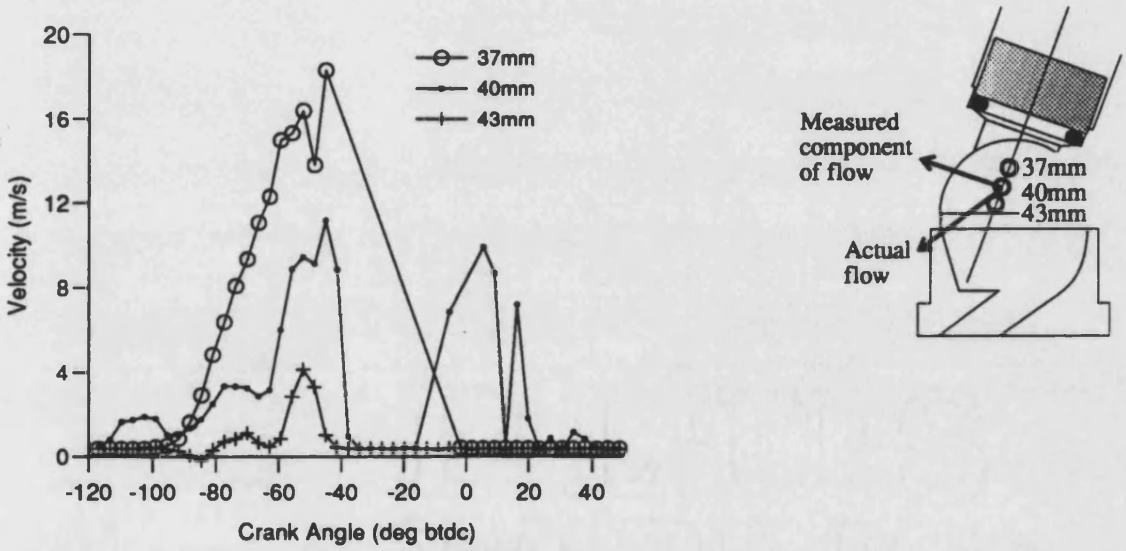

Figure 3.16
Velocity measurements at three locations in the swirl chamber

5.4 Discussion

Although it was not possible to record data over the complete compression & expansion strokes, the results shown illustrate that velocity measurements within the swirl chamber are possible, and that the technique can be used to investigate the variations in velocity over the chamber. An increase in the quantity and quality (ie reducing noise) of data captured by the signal processing equipment will be necessary to fill in the detail in the high velocity regions and if the technique is to be extended to higher engine speeds. Backscatter mode, where the beam source and detector are

on the same axis, and same side of the particle, is the most difficult type of operation, but without extensive changes to the engine geometry - which have been minimised in this study - this remains the only means of optical access.

Given that the seeding particles are incompressible, and that the air charge is compressed through a volume ratio of 21.5:1, the data rate would be expected to increase significantly towards top dead centre. One possible reason for the very low date rate is that the 1.2μ particles were not able to follow the flow. This theory is supported by the fact that even fewer velocity data were obtained when the engine speed was increased from 920rpm to 1470rpm. Smaller particles (0.5μ & 0.7μ) are available, but as data rate varies as the cube of the diameter, using yet smaller particles is unlikely to greatly increase the data available, without reductions in the background noise levels.

Data acquisition was also impeded by the lack of repeatability. A location within the engine which on one occasion provided an acceptable data rate over part of the cycle, might not give any signal the following day, under apparently the same operating conditions This may be due to inconsistency in the seeding, slight variations in the engine temperature or changes in ambient conditions (eg relative humidity).

In this study, a relatively large bin width has been used, to maximise the number of points per bin. Ensemble averaging calculates the average velocity of all the data points falling inside the bin, and from the spread (standard deviation) of the data about the mean, turbulence levels can be calculated. As the velocity over the duration of the bin is changing, the bin size should be kept as small as possible to minimise errors in the turbulence calculations. Cycle-to-cycle variation, and changes in the bulk mean flow (for instance due to slight changes in engine speed) will increase the velocity spread within the bin. This increased spread will appear as increased 'turbulence'.

CHAPTER 4
NUMERICAL MODELLING OF IDI ENGINE FLOW

1 Introduction IV-2
1.1 Model Generation and set-up IV-3

2 Sub-models added to the code IV-4
2.1 Piston-in-cylinder motion IV-5
2.2 Variation of gas properties with temperature IV-6
2.3 Data processing routine IV-7

3 Baseline model and results IV-8

4 Data processing techniques IV-11
4.1 Swirl number IV-11
4.2 The validity of the assumptions of solid body rotation about a fixed centre of swirl IV-15
4.3 Throat discharge coefficient IV-16
4.4 Compression pumping losses IV-17

5 Effect of engine speed IV-18

6 Summary IV-21

1 Introduction

From a consideration of basic fluid mechanics and thermodynamics, it is possible to derive a set of equations, which given appropriate boundary and initial conditions, will completely determine the movement and state of a fluid in a given geometry. These are the well-known Navier-Stokes equations. The solution of these equations has proved extremely complex and it is only in recent years that techniques for using these equations to determine fluid flows in useful geometries have become available.

CFD was first applied to in-cylinder flows in the early eighties, and used two-dimensional codes and simplified geometries. References 38,48 & 50 are recent applications of CFD to divided combustion chamber engines which use full three-dimensional fluid flow modelling.

Appendix A contains a summary of the derivation of the fundamental equations, discretisation, solution techniques and turbulence modelling. Written in tensor notation, the momentum equations may be written as

$$\frac{\partial(\rho u_i)}{\partial t} + \frac{\partial}{\partial x_j}(\rho u_j u_i - \tau_{ij}) = -\frac{\partial p}{\partial x_i} + S_{u_i}$$

$$\tau_{ij} = \mu\left(\frac{\partial u_i}{\partial x_j} + \frac{\partial u_j}{\partial x_i} - \frac{2}{3}\frac{\partial u_k}{\partial x_k}\delta_{ij}\right)$$

All the simulations in this study have used the k-ε turbulence model. This model was first derived from empirical data by Launder and Spalding (1975) and has since been modified and applied to a wide range of turbulent flows. The k-ε model is generally regarded as a compromise between simplicity and complexity. It is widely known to predict incorrectly the detail of a number of common flows, including swirling, separating and recirculating fluid motion. All the previous applications of CFD to divided combustion chamber flows have used the k-ε model, but future studies are likely to attempt to use Reynolds Stress Modelling (RSM), which

overcomes some of the drawbacks of the k-ε model, but at the expense of computational time. Turbulence modelling is discussed in greater detail in Appendix A, section 5.

1.1 Model Generation and set-up

All mesh generation for the models used in this study was undertaken using the PATRAN Release 2.5 mesh generator. PATRAN is a geometric modelling package, developed for finite element modelling, but is equally suitable for generating finite volume meshes. Around 30 models have been constructed during the study, with varying geometries and numbers of cells. Details of the mesh generation process and views of many of the meshes generated are presented in Appendix B. Boundary conditions and control parameters are set in the STAR pre-processor (Prostar). Appendix C lists Prostar commands used to set up a typical solution run. Initial conditions are defined for bottom dead centre before compression (*bdc*). The solution algorithm then calculates a solution at each time step, starting with 1.5° crank angles, reducing to 0.4° before top dead centre (tdc). The solutions have generally been terminated around 20° after top dead centre (*atdc*).

Boundary conditions

The compression and expansion processes following bdc before compression are modelled as closed cycles, the only boundary to the flow being the chamber walls. As mentioned in the previous Chapter, in a motored engine, some charge is lost during the compression process past the piston rings (blow-by). This *outflow boundary* has not been included in most models. To reduce the computational effort, the geometry has generally been assumed to be symmetric about the central plane, which is defined as a *symmetry plane boundary*. In practice the inlet valve recess is slightly bigger than the exhaust valve. Solid walls can be defined as adiabatic, fixed temperature, fixed heat flux, or any combination of the three via a subroutine. The SPICE engine simulation package developed by Charlton at the University of Bath has been configured to provide wall boundary conditions.

Initial conditions

Initial conditions must be specified for each variable at bdc. Except where stated, quiescent initial conditions are assumed, with pressure = 1 bar, and temperature = 293K.

Moving Mesh

At the beginning of each time step, a routine (see below) defines the position of the mesh. At bdc 15 layers of cells are used to model the main chamber flow domain. During the compression cycle, cell layers are successively removed to maintain acceptable cell aspect ratios. At tdc four cell layers remain in the main chamber.

2 Sub-models added to the code

The STAR-CD package, developed originally at Imperial College is a general framework for solving the fundamental equations defining fluid motion in steady-state and unsteady flows. The package consists of two modules: *prostar* for model development, setting boundary conditions, and post-processing; and *star* - the main solver. The capability exists within the package to add code to a series of (otherwise empty) subroutines which are linked to the main solution code. These subroutines allow most aspects of the solution phase to be changed to meet the requirements of the user, for instance to code different turbulence models, or define complex initial and boundary conditions on a cell-by-cell basis. During this study sub-models have been added to the code to:

- allow the main chamber mesh to vary with time to simulate a piston-in-cylinder motion
- define gas properties as a function of temperature
- add a data-processing routine to perform a degree of post-processing *during* the solution phase to reduce the data storage requirements
- model heat release and combustion (described in Chapter 7)

2.1 Piston-in-cylinder motion

The driving force behind the air motion in an engine is the movement of the piston. To model this motion, the position of the mesh in the main chamber is made to vary with time. At the beginning of each time step, the time into the simulation is passed to a subroutine, which defines the position of the mesh as follows

Consider the crank-slider mechanism shown

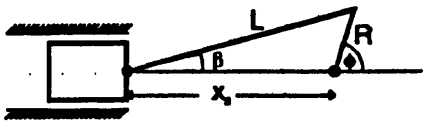

Now

$$x_s = L\cos\beta - R\cos\phi$$

and

$$L\sin\beta = R\sin\phi$$

$$\sin\beta = R/L\sin\phi$$

Now

$$\cos\beta = \sqrt{(1-\sin^2\beta)}$$

$$= \sqrt{(1-(R/L)^2\sin^2\phi)}$$

So

$$x_s = L\sqrt{1-\left(\frac{R}{L}\right)^2\sin^2\phi} - R\cos\phi$$

Thus the position of the top surface of the piston, relative to the bottom surface of the cylinder head can be calculated as a function of time. At each time step, the routine compresses or expands the layers of cells in the main chamber (excluding those in the piston crown and valve recesses). The routine allows cell layers to be evenly distributed from top to bottom, (if no piston recess is being modelled), or

allows the cell layers to gradually increase in thickness away from the top or bottom (ie thin layers near piston and cylinder head, thick layers in the middle). This last option is required to form an acceptable transition region from the thin layers in the piston trough to thicker layers in the main chamber.

By adjusting the top-dead-centre clearance, the engine compression ratio can be adjusted. This is necessary for models where the piston recess has been omitted (in order to reduce computational time).

For each solution, the subroutine reads a data file containing the relevant input to the program (eg engine speed and top-dead-centre clearance).

2.2 Variation of gas properties with temperature

By default, the solver assumes that the working fluid (air) is a perfect gas, whose specific heat capacities (Cv and Cp) do not vary with temperature. For a real gas Cv and Cp change significantly during the compression. This variation with temperature can be modelled by defining Cv as a function of temperature in the *UCP* subroutine.

Heywood [64] lists a series of polynomials taken from the JANAF [65] tables defining Cp as a function of temperature for a number of gases. Cv for the air mixture is calculated:

1. For given temperature, calculate Cp for Nitrogen and Oxygen individually, based on tables by JANAF
2. Calculate Cp for air with Nitrogen / Oxygen ratio 0.7809: 0.2095 (volumetric ratio)
3. Hence calculate Cv as (Cp -R)

The calculated values of Cv were checked for agreement with tables (Rogers & Mayhew [66])

2.3 Data processing routine

In a transient simulation such as piston-in-cylinder motion, the values of all the parameters being solved change at every time step. The *prostar* environment allows the user to define those parameters to be written to a transient data file. The transient data file is read during post-processing and the data plotted in the form of contour plots (pressure, temperature etc) or vector plots (for velocities). As results have to be stored for every cell in the model, a large quantity of data must be written to the file. The frequency at which data may be written is determined by the size of data file which can be handled.

Most of the post-processing routines (described below) require data values for those cells in the swirl chamber (ie not the main chamber). A subroutine (called once per time step[1]) controls the output of transient data to a data file. This subroutine accesses the data through COMMON blocks and generates an ASCII data file, to allow the file to be moved between computers. The procedure can be compared to taking readings from an experimental rig: no attempt is made to record all the parameters at all positions on the rig, rather only those parameters which are required for further analysis are stored. This technique allows a degree of *post*-processing to be undertaken *during* the solution phase: for instance an average main chamber pressure is stored, instead of storing the pressure in 20000 main chamber cells.

The user sub-routine writes out the following parameters:

1. The x,y,z coordinates (cell-centres) for all the cells in the swirl chamber, including the throat
2. The volume of all cells in the swirl chamber and throat
3. The u,v,w velocity components of velocity for all the cells in 1.
4. Average main chamber static pressure and average swirl chamber static pressure
5. Average main chamber static temperature and average swirl chamber static temperature

---

[1] Called from the NEWXYZ routine at the beginning of every time step.

6. Average air density in the swirl chamber
7. Mass weighted average turbulence
8. Change in internal energy of system since previous pass

Items [1] and [2] are written once only, the remaining items are written every x time steps, where generally x = 2. The data-acquisition subroutine is called at the beginning of the time step, before a solution has been obtained. The results stored at time step N, are therefore those calculated for the time step (N-1), and this must be compensated for.

3 Baseline model and results

Figure B.1 in Appendix B shows the baseline model - that of the Ricardo Comet Vb combustion system shown in Figure 1.1, using around 40000 cells {case 13}[2]. Figure 4.1 (a-c - at end of Chapter) presents an overview of the velocity, pressure, turbulence in the swirl chamber over a series of crank angles. In section 4, techniques for processing and interpreting this data will be presented.

Velocity

Shortly after the beginning of the compression stroke, an ordered swirling motion is seen to form in the swirl chamber, with a centre of rotation, near the throat exit (4.1a - 120°btdc). As the cycle progresses, the air velocity in the swirl chamber increases, and the centre of the swirling flow moves towards the geometric centre of the swirl chamber. By 2°btdc, the piston face is included in the enlargement. Swirl number plotted in Figure 4.2 {case 3}, is the ratio of swirl velocity to engine speed, calculated about the geometric centre of the swirl chamber. Swirl reaches a peak around 14° before top-dead-centre (btdc), before decaying rapidly. *The rate of decay of swirl (the gradient of the curve) can be seen to decrease slightly at top dead*

[2] Throughout this thesis, {case} numbers refer to the Appendix D summary of geometry and boundary conditions

centre: in the period from peak swirl until top-dead-centre, slow moving air passing through the throat acts as a brake on swirl in the auxiliary chamber. At top-dead-centre this brake is removed, and the swirling motion is aided by air flowing back through the throat. *The rate of decay of swirl is greater than the rate of production.* During compression, swirl changes from 50 - 100% of its peak value in 35° CA. and decays to 50% again in 8° CA.

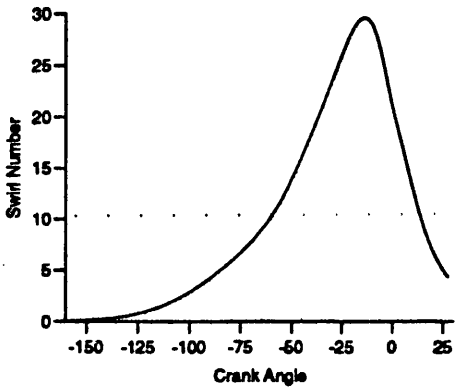

Figure 4.2
Swirl number

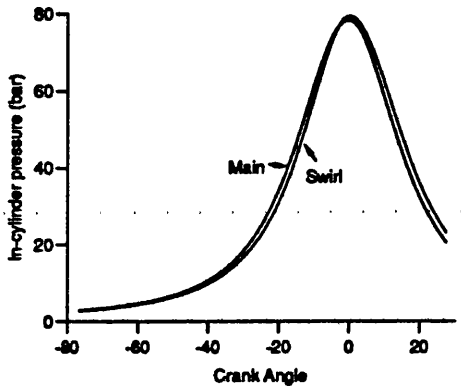

Figure 4.3
In-cylinder Pressure

Pressure and temperature

Figure 4.3 plots the in-cylinder pressure against crank angle, averaged over each chamber from an adiabatic 3000rpm simulation {case 3}. During the compression stroke, the swirl chamber pressure lags behind the main chamber pressure. During the expansion stroke the main chamber lags behind the swirl chamber pressure. It is interesting to note that the swirl chamber pressure exceeds that in the main chamber *before* tdc. Although the piston is moving more slowly, the momentum of the air in the throat and swirl chamber, continues to draw air into the swirl chamber, against the pressure gradient. The contour plots in Figure 4.1b show the pressure distribution over the central plane of the swirl chamber from the 1500rpm case. The pressure drop across the throat is seen to have reversed by 2° btdc. Figure 4.4 plots chamber averaged static temperatures from the 1500rpm simulation.

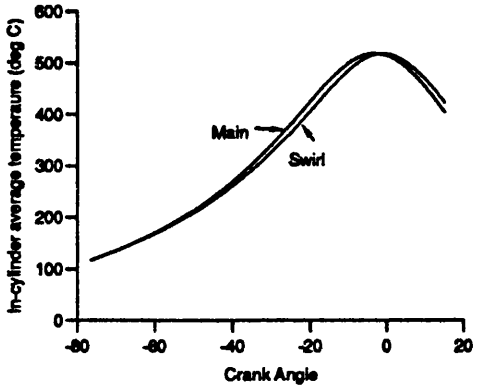

Figure 4.4
Main and swirl chamber averaged temperature

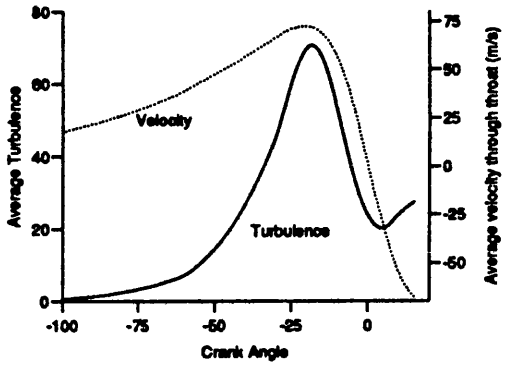

Figure 4.5
Swirl Chamber Turbulence. Throat average velocity

Turbulent kinetic energy and dissipation

Figure 4.5 shows the variation of turbulence in the swirl chamber over time {case 3}. From the contour plots of turbulence, it is seen that turbulence is generated primarily by the shear layers in the swirl chamber throat. The turbulence distribution in the swirl chamber is plotted in Figure 4.1c. The turbulence is carried into the chamber by the flow and gradually dissipated. The glow plug is also seen to be a source of generation of turbulence (the effect of removing the glow plug from the chamber is discussed in Chapter 6). Average turbulence in the swirl chamber reaches a peak at 18° btdc, as the throat air velocity passes its maximum value. As the piston slows down towards tdc, dissipation of turbulence exceeds its generation, and the overall turbulence level falls. After tdc, as air is drawn out of the throat, turbulence generation increases, peaking for a second time after 15° atdc. The parameter plotted in Fig 4.5 is based on swirl chamber turbulence only, so turbulence convected into the main chamber is not shown.

4 Data processing techniques

This section discusses the analysis of the flow-simulation data. A number of parameters which vary with crank angle have been selected to characterise the processes occurring during the compression and expansion strokes.

4.1 Swirl number

Auxiliary chamber swirl number, defined as

$$Swirl\ number = \frac{Angular\ velocity\ of\ air\ in\ swirl\ chamber}{Crank\ shaft\ speed}$$

has been calculated and plotted as a function of crank angle by many researchers investigating IDI engine air flows. Engine developers have known for a long time that swirl number is generally independent of engine speed: if the engine speed is doubled, the swirl velocity doubles. This is an important feature of the Ricardo combustion system, as the reduced ignition delay caused by the increase in velocity and turbulence at high speeds, ensures that ignition and combustion take place more quickly, thus allowing the injection timing to be kept within a relatively narrow band over a range of engine speeds. The swirl calculations presented in this Chapter are taken from cold-flow models, ie there is no fuel injection or combustion. Researchers and engine designers are primarily interested in swirl levels because of the importance of air / fuel mixing during combustion. The swirling flow supplies oxygen to the burning fuel and removes exhaust gases (Chapter 7). Low levels of swirl reduce the efficiency of combustion in the swirl chamber by delaying the complete mixing of fuel and hence burning. Very high levels of swirl increase the rate of combustion, but probably increase peak combustion temperature and hence NOx levels.

The techniques used to calculate the swirl number (or swirl ratio) vary depending on the experimental or computational data available. Direct measurements of swirl are difficult. A vane may be fixed in the centre of the swirl chamber, (eg. [8,16]) but the method suffers from many drawbacks. Most experimental calculations of swirl number are based on extrapolating swirl number from velocity measurements

at one or more points in the flow field, or simply quoting an effective swirl number at each point. Such calculations of swirl number make the assumptions that *the centre of the swirl is in the geometric centre of the swirl chamber*, and in the case of calculations based on more than one point, that *the rotation is of a solid body type*. Multi-dimensional studies allow the mechanism of swirl in the chamber to be investigated more fully, and these assumptions to be assessed.

In this study, swirl number has been calculated as follows:

$$S_N = \frac{\textit{Angular velocity } (\omega)}{\textit{Engine Speed}}$$

where

$$\omega = \frac{\textit{Angular momentum of air mass}}{\textit{Moment of inertia of air about centre of rotation}}$$

$$= \frac{I\omega}{I} = \frac{\Sigma\, m\, V_r\, k}{\Sigma\, m\, k^2}$$

where m = mass of air in cell
V_r = tangential velocity component
k = distance to centre of rotation

The summations are over all cells in the swirl chamber, except those in the throat and near the injector, and the calculation is performed at each time step for which a data set is stored, thus giving the variation of swirl number with crank angle. The swirl number calculated is that which would be given by a solid body rotation with the same angular momentum as the swirling flow.

Location of swirl centre

Almost all previous studies of swirl chamber flow have assumed that the centre of rotation of swirl lies in the geometric centre of the swirl chamber.

Figure 4.6 compares swirl number *calculated about the geometric centre of the swirl chamber* with a calculation based on the *instantaneous position of the centre of swirl*, computed on a high density mesh without a glow plug {case 8}. The position of this free centre of swirl is determined by locating the cell at which the velocity is nearest to zero - the centre jumps from cell to cell, creating the slightly uneven curve shown. For a true solid body rotation, it is expected that the swirl number calculated about the actual centre of swirl would be *greater* than that calculated about any other (arbitrary) point. Figure 4.6 shows, however, that using the actual centre of swirl gives a *lower* swirl number than that calculated about the geometric centre. During the compression stroke, the piston continues to compress air until top-dead-centre. Thus for air of a given velocity in the swirl chamber, that entering the chamber later during the compression stroke is denser - has a higher momentum, and influences the swirl calculation proportionally more. Moving the centre of swirl, away from the throat (during the compression stroke), increases the moment arm to the denser, high velocity air entering from the throat, increasing the swirl number.

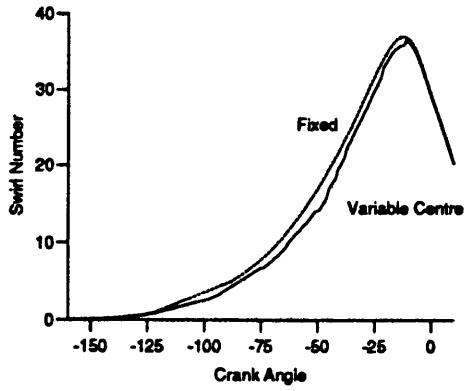

Figure 4.6
Swirl Number calculated about fixed and variable centre

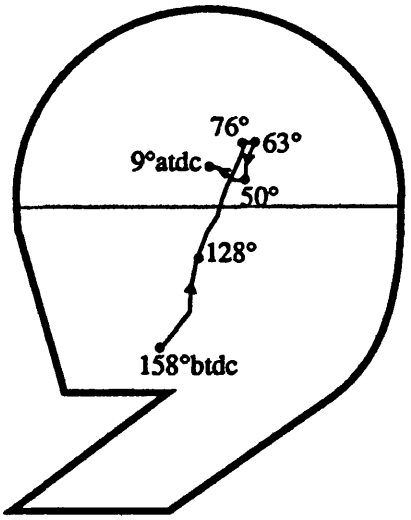

Figure 4.7
Precession of swirl centre with crank angle

Figure 4.7 shows the path of the centre of swirl. The figures show crank angle. By around 100° btdc, the actual swirl centre is very close to the centre of the

swirl chamber, and it remains close during the critical fuel injection period - in the period from 20° btdc to beyond tdc, both swirl curves in Figure 4.6 are virtually identical.

Calculation of swirl ratio based on velocity magnitude at a point

Figure 4.8 shows swirl number {case 3} based on velocities at a number of individual points in the central plane of the chamber, calculated as

$$\omega = \frac{V_{mag}}{r}$$

where V_{mag} = Velocity magnitude of cell

r = distance to the geometric centre of the swirl chamber

This calculation is similar to that used to obtain swirl number from experimental point-velocity measurements. The figure shows the wide range of swirl values which may be calculated, depending on the location of the measuring point. By comparing Figure 4.8 with Figure 4.2, the relationship between a point swirl measurement - for instance an experimental reading - and the global swirl number can be estimated.

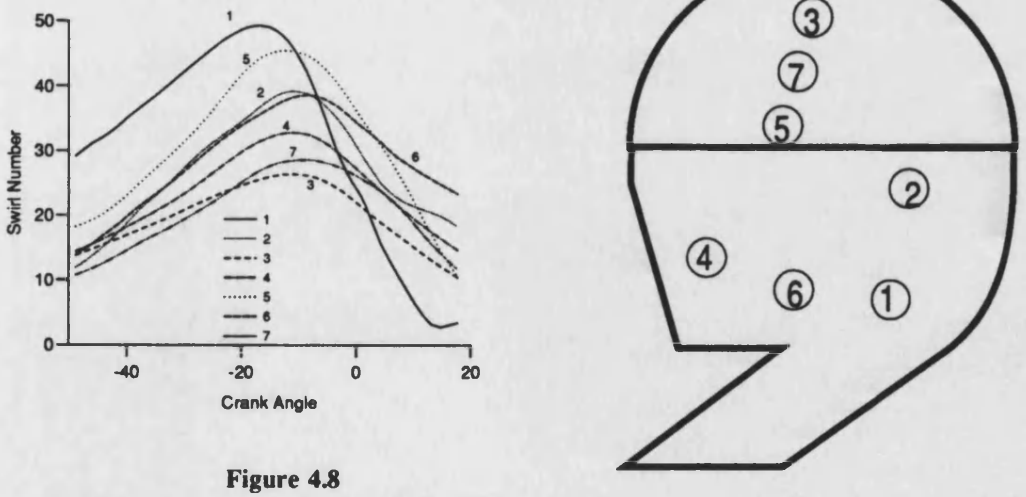

Figure 4.8
Swirl number calculations based on point measurements

4.2 The validity of the assumptions of solid body rotation about a fixed centre of swirl

Figures 4.9 and 4.10 show a number of velocity profiles taken across the horizontal line passing through the geometric centre on the central plane of the swirl chamber from a model without a glow plug {case 3}. For perfect solid body rotation, each profile would be a straight line. If the rotation was about the centre of the swirl chamber, each profile would pass through the 0,0 origin. Although a non-slip (zero velocity) condition *must* exist at the walls, the velocity profiles do not reflect this: In all the results presented here, the *law-of-the-wall* (see Appendix A) is used to avoid detailed calculations of near wall flows.

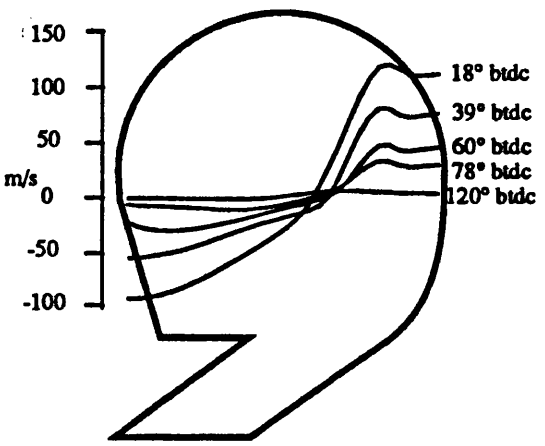

Figure 4.9
Velocity profiles BEFORE peak swirl

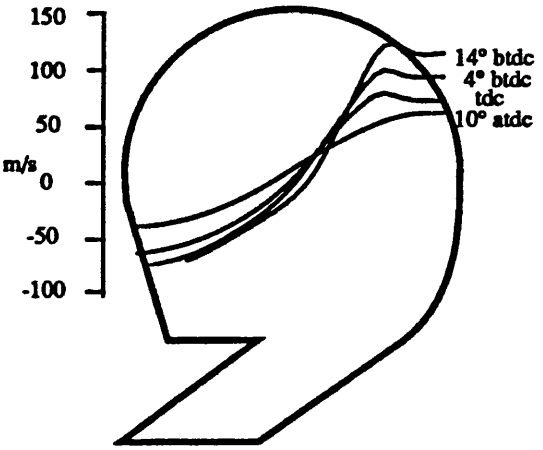

Figure 4.10
Velocity Profile AFTER peak swirl

It has already been shown that the assumption that the centre of the swirling flow is fixed in the centre of the swirl chamber is reasonable: In the period following fuel injection (15° btdc and later), the swirl centre is close to the geometric centre. Figures 4.9 and 4.10 show that on either side swirl centre, a region of solid body rotation exists. During the compression stroke, the velocities on the right hand side of the chamber however are greater than those on the left. Two factors account for this. As the air is compressed into the swirl chamber, a bulk 'upward' movement of air is superimposed on the swirling flow. Secondly, a three-dimensional effect exists. The jet from the throat covers under half the depth of the chamber. As the

progresses around the chamber, the entrained air reduces the peak velocity. An assumption of solid body rotation in the swirl chamber is a useful technique for understanding the flow but is an approximation to the actual transient, three-dimensional flow field which exists.

4.3 Throat discharge coefficient

Most non-multidimensional IDI models use the concept of a throat discharge coefficient to calculate the flow into (and out of) the swirl chamber:

$$\text{Actual mass flow} = C_d \,.\, \text{Ideal mass flow}$$

Ideal mass flow is calculated from details of the geometry and pressure difference, while the value of C_d is often assumed to be constant - Tawfig [16] used a value of 0.6. The CFD model allows an accurate calculation of throat discharge coefficient.

Based on compressible flow theory, the *ideal* mass flow through the throat is given by

$$\dot{m} = \frac{A_{throat} p_0}{\sqrt{RT_0}} \left(\frac{p_{throat}}{p_0}\right)^{\frac{1}{\gamma}} \left(\frac{2\gamma}{\gamma-1}\left[1-\left(\frac{p_{throat}}{p_0}\right)^{\frac{\gamma-1}{\gamma}}\right]\right)^{\frac{1}{2}}$$

where the subscript 0 refers to stagnation conditions. To allow C_d to be calculated, a number of assumptions have been made:

1. Stagnation conditions are taken to be average main chamber static values while $P_{main} > P_{swirl}$, and average swirl chamber values while $P_{swirl} > P_{main}$. The first of these conditions (ie during compression) is reasonable as average flow velocities in the main chamber are very low. As the swirl chamber velocities are not negligible, the second of these conditions (during expansion) results in a slight error.
2. Throat static pressure is taken to be the swirl chamber average value during compression and main chamber average value during expansion. This is justified by examining the pressure contour plots presented above: the pressure at the throat exit (where the velocity plots have shown the contracta effect to be greatest) is almost identical to the downstream value.

3. At each time step, a steady-state condition is assumed to exist: no attempt is made to include transient or momentum effects in the calculation.

Figure 4.11 shows the throat discharge coefficient calculated using the method described (case 3). The pressure difference across the throat is also plotted. During the compression stroke C_d increases very gradually from just under 0.5 to 0.7. Shortly before tdc, the concept of discharge coefficient changes, as air continues to flow into the swirl chamber against a pressure gradient - hence values of C_d greater than 1. C_d after tdc is plotted as a negative value for clarity.

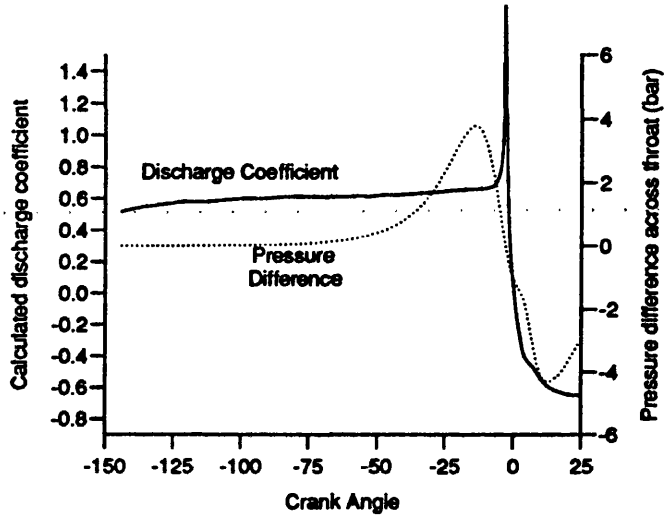

Figure 4.11
Throat discharge coefficient

4.4 Compression pumping losses

During an engine compression stroke, the piston acts on the fluid in the cylinder to compress it. This process requires work, given by $\int p dv$. In the indirect injection diesel engine, additional work is required to pump the charge through the swirl chamber throat, during the compression and expansion strokes. *Pumping loss* is the term given to this additional work. In the frictionless system being modelled here, the total compression work is given by:

Total compression piston work = Work to compress gas + pumping work

The total piston work can be calculated as

$$\sum_{N=1,tdc} (average\ pressure\ over\ time\ step) \times (change\ in\ volume\ over\ step)$$

where the summation is over all time steps from bottom to top dead centre (tdc). As an adiabatic, constant γ compression process is being modelled, the *work to compress gas* term can be calculated as $\sum_{all\ steps} p_{adiab} \Delta v$, where p_{adiab} is the pressure calculated at a given time step given pv^{γ} = constant. For a real cycle, the *work to compress gas* term could be calculated by modelling an open (DI type) quiescent cylinder with the same compression ratio as the IDI. Experimental measurements of throat pumping losses have constructed such *equivalent* compression ratio open cylinder engines for comparison with the IDI.

The pumping work is given by the difference between *total piston* work, and *work to compress gas.*

Compression work and pumping losses can usefully be expressed as mean effective pressures (mep), where

$$mep\ (Pa) = \frac{Work(J)}{Swept\ volume(m^3)}$$

For the 3000rpm simulation {case 1}, compression mep is 6.61bar, of which 0.14bar (2%) is pumping losses.

5 Effect of engine speed

Figures 4.12 and 4.13 show the variation of swirl and turbulence with engine speed. Simulations have been run at 1500, 3000 and 4500 rpm {cases 7,3,9}. The peak swirl number is independent of engine speed, but the crank angle at which the peak occurs is retarded at higher engine speeds. Figure 4.14 plots throat mass flow against crank angle. During the early stages of the compression, the higher the engine speed,

the lower the mass flow per crank angle. As the total mass transfer across the throat is the same in all cases (given enough time to stabilise, it is defined by the geometry), the mass transfer continues longer (in terms of crank angle) for the higher engine speeds, causing the later peak in swirl number. Peak throat Mach numbers given by $\frac{v_{throat}}{\sqrt{\gamma RT}}$ for the 1500, 3000 and 4500 cases are 0.12, 0.24 and 0.35 respectively, so throat flow never becomes choked. The average turbulence in the swirl chamber is greatly increased at higher engine speeds due to the increased shear generated by the higher velocities in the throat. Figure 4.15 shows throat pumping losses during compression for each of the simulations. For each engine speed, the work required to compress the gas remains constant (it is a function of compression ratio only). At the higher engine speeds, additional work is required to pump the air through the swirl chamber throat at a higher velocity.

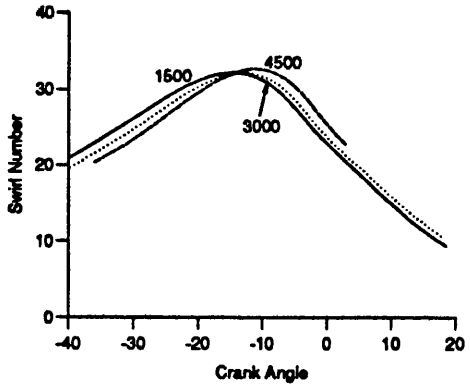

Figure 4.12
Effect of engine speed on swirl number

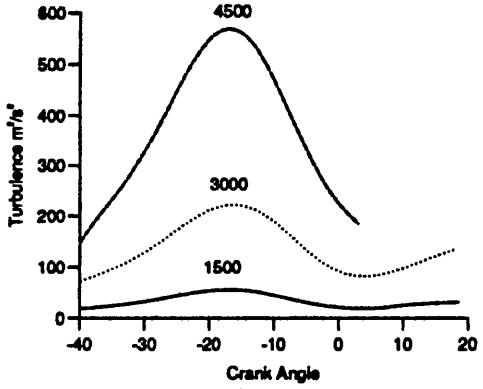

Figure 4.13
Effect of engine speed on average turbulence

In later Chapters, the problems of achieving mesh independent solutions when using multi-dimensional modelling will be discussed. Since the basic mesh used in the comparison of engine speeds is identical for each case - the only difference in the solution being the engine speed, any changes in the solution (for instance those mentioned) can be attributed solely to the effect of the engine speed change.

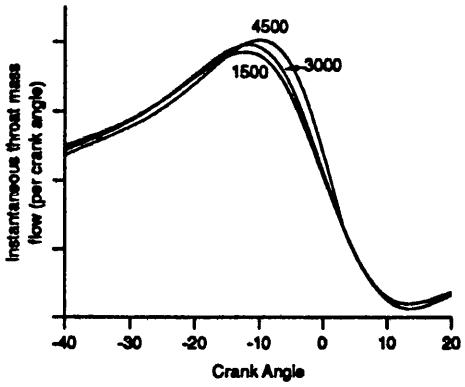

Figure 4.14
Mass flow through throat

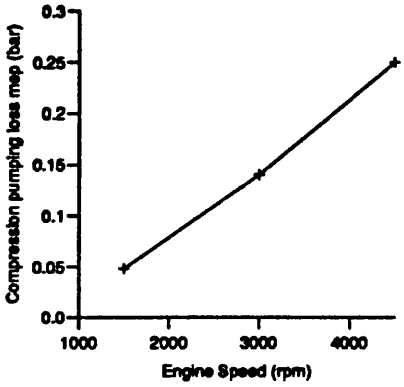

Figure 4.15
Throat pumping losses during compression

6 Summary

1 A CFD multi-dimensional modelling package has been configured to solve the transient, compressible three-dimensional equations governing fluid flow in a typical IDI Diesel engine geometry. To achieve this, submodels have been added to define piston movement, to account for changing air properties with temperature and to allow extensive post-processing of the results.

2 Results have been presented from a number of models showing the development of flow, turbulence and other parameters from bottom dead centre before compression to part way through the expansion stroke.

3 As a method of interpreting the simulation results, the parameter swirl number has been calculated over the cycle. The assumption that the flow rotates about the geometric centre of the swirl chamber is shown to be reasonable, but the assumption that the flow is a true solid body rotation is only a rough approximation to the actual flow field. The magnitude of the swirl number is dependent on the method used to calculate it - and if calculated from single point velocity measurements is very sensitive to the location of the measuring point.

4 The assumption of a throat discharge coefficient of 0.6 during compression is generally valid.

5 Swirl number is independent of engine speed over the range studied, but the crank angle at which the peak swirl occurs is retarded at higher engine speeds.

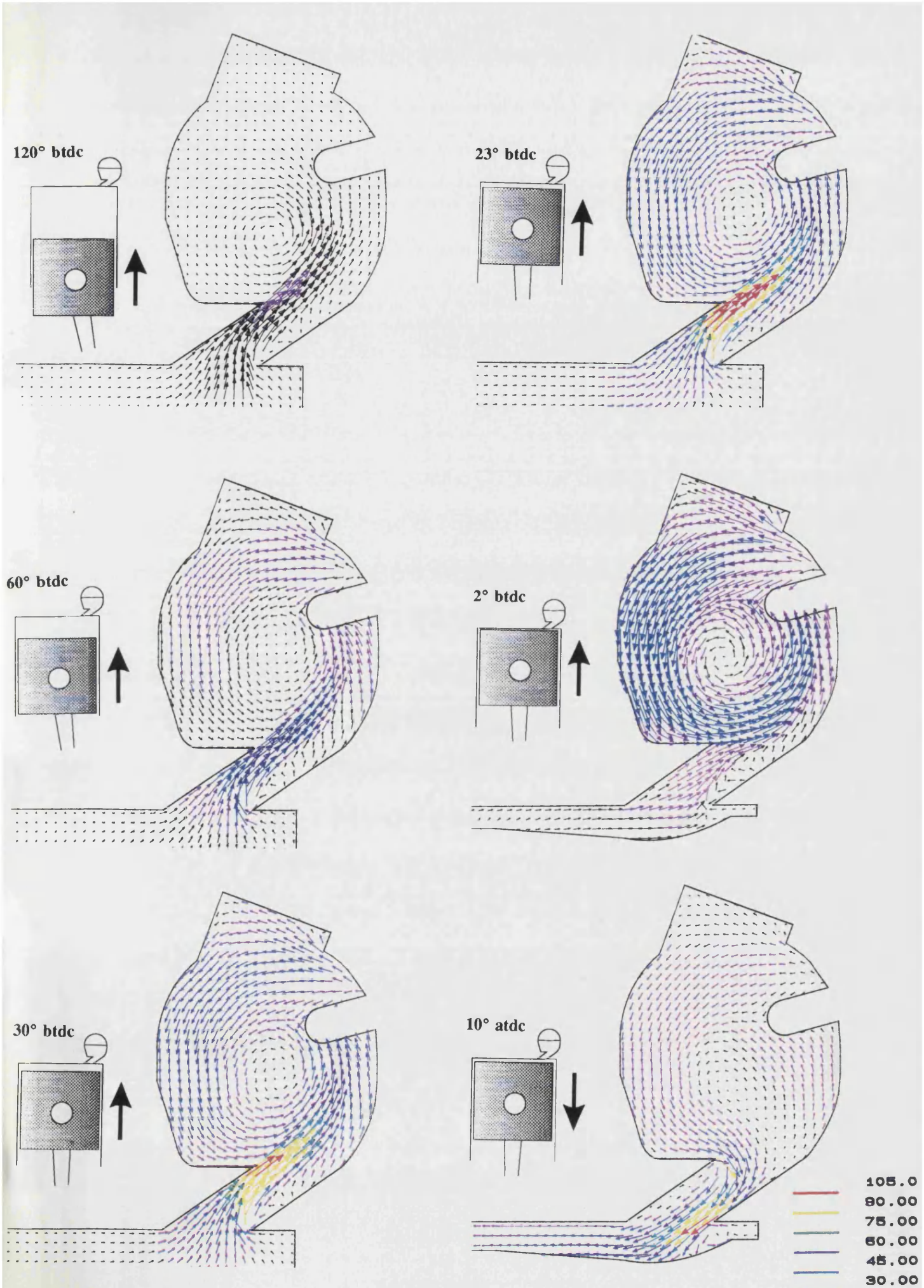

Figure 4.1a
Velocity vector plots in central plane

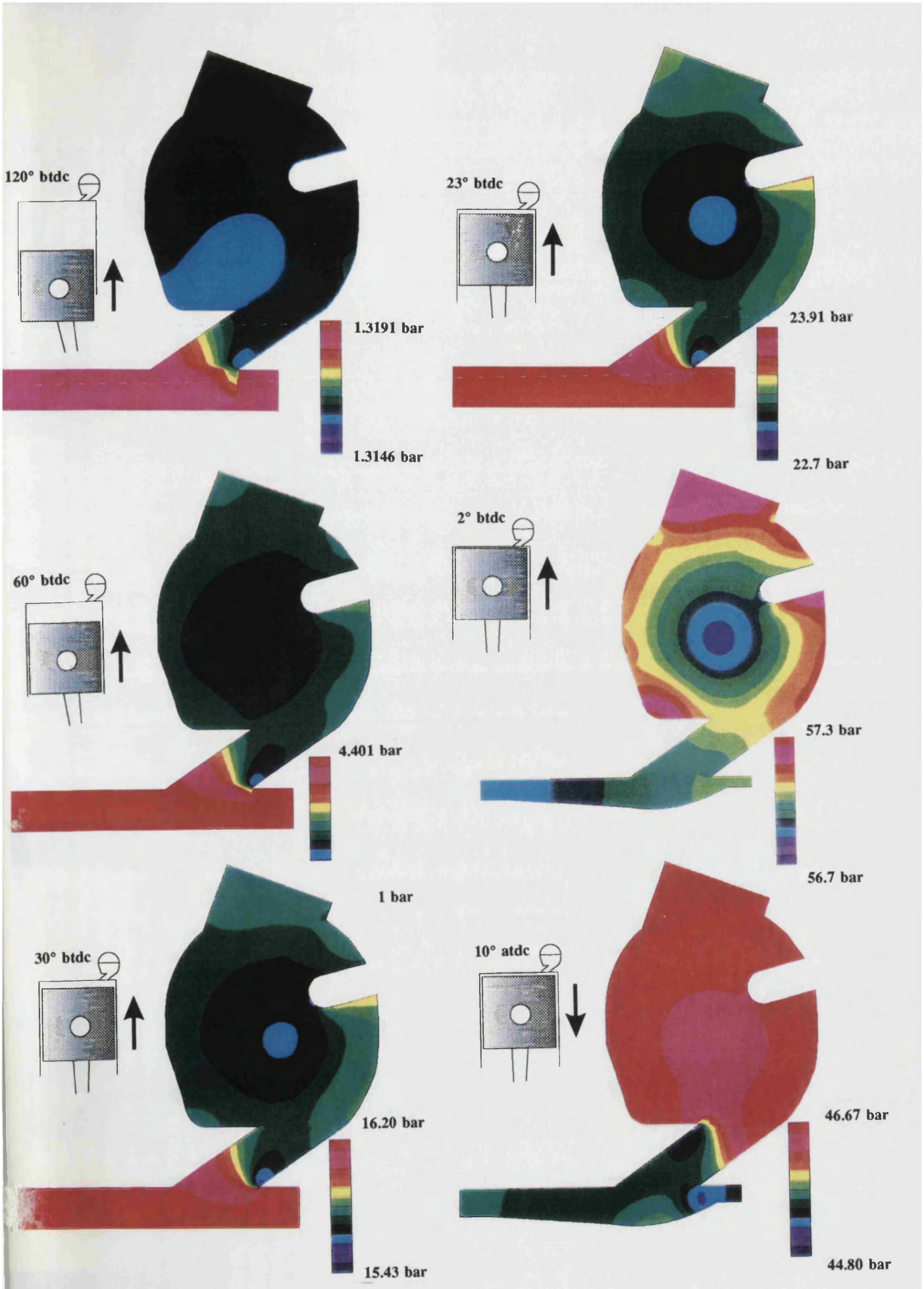

Figure 4.1b
Pressure distribution in central plane
(note varying scale)

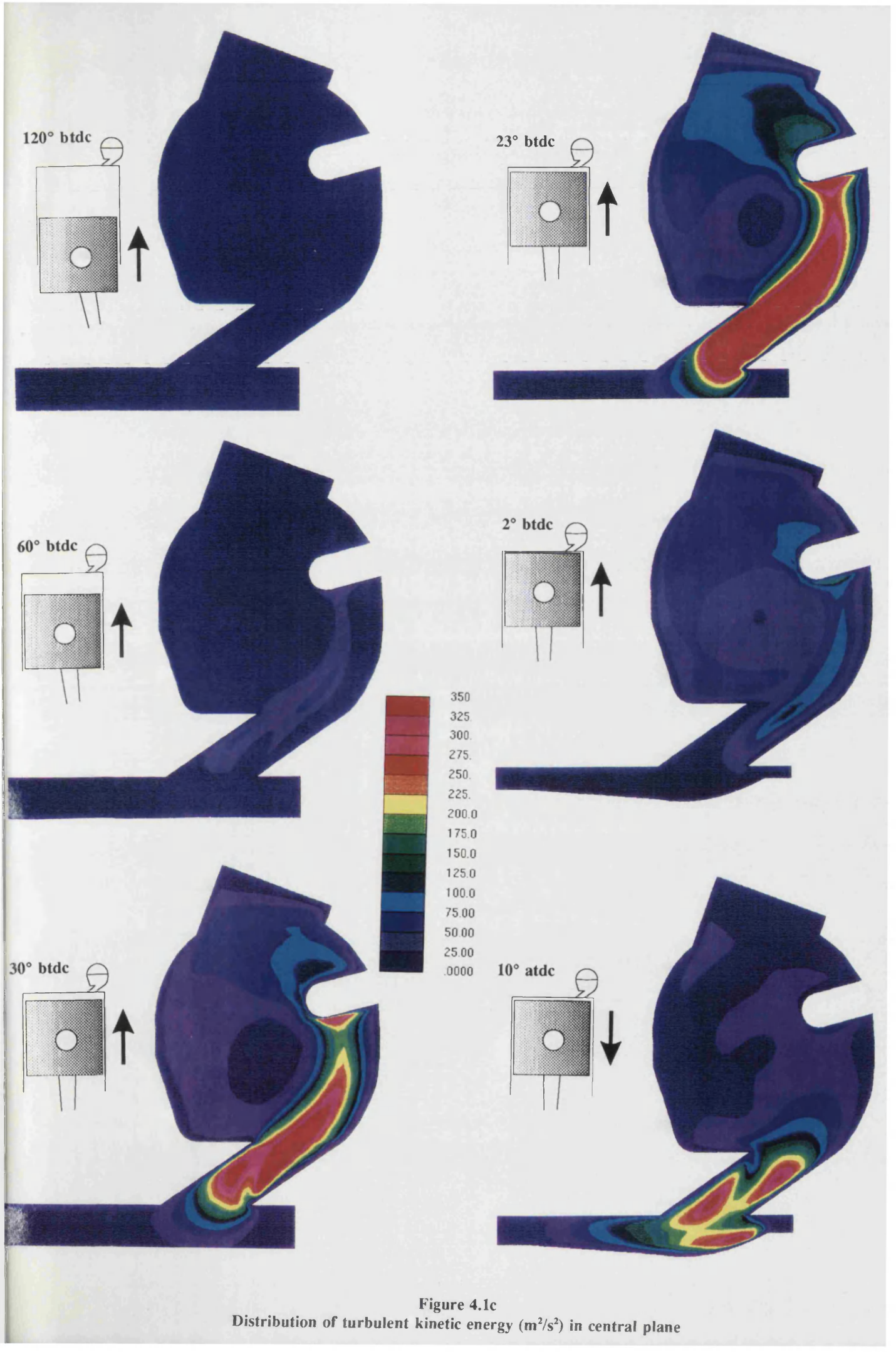

Figure 4.1c
Distribution of turbulent kinetic energy (m^2/s^2) in central plane

CHAPTER FIVE
VALIDATION OF THE NUMERICAL MODEL

1 Introduction V-2

2 Thermodynamic validation V-2

3 Comparison with results of other authors V-4

4 Configuring the cfd model for experimental validation V-6
- 4.1 The sensitivity of the solution to mesh density V-6
- 4.2 The sensitivity of the solution to numerical differencing scheme V-8
- 4.3 The effect of using temperature dependent gas properties V-12
- 4.4 Wall boundary conditions V-13
- 4.5 Calculation of wall heat transfer coefficients V-16

5 Comparison with experimental results V-18
- 5.1 Pressure V-18
- 5.2 LDA results V-20
- 5.3 Discussion V-24

6 Summary V-26

1 Introduction

In the previous Chapter, results from a number of computer simulations of IDI Diesel engine flow were presented. This Chapter discusses techniques for validating the CFD results and compares the results with theoretical relationships, similar computational / experimental studies undertaken elsewhere and the experimental work presented in Chapter 3.

Given a physical geometry, boundary and initial conditions (which define a unique flow field), the numerical techniques used to obtain the flow solution involve a number of approximations. As part of the validation study, the sensitivity of the solution to mesh density (cells per volume) and numerical differencing scheme has been investigated. Both these factors influence the results obtained from the numerical model.

The CFD model used in this study is limited to a small section of the overall engine. No attempt has been made to predict manifold air flow, intake and exhaust strokes, or the mechanism of heat transfer through the cylinder walls to the coolant. It is therefore necessary to impose the relevant boundary conditions on the CFD model. Good agreement between experimental and predicted results cannot be obtained without accurate data for boundary conditions.

2 Thermodynamic validation

The simplest boundary conditions assume adiabatic cylinder walls, no variation of gas properties with temperature, and initial quiescent conditions. Under these conditions, the compression and expansion processes should follow a pv^{γ}= constant relationship. Thus the pressure for a given volume can be obtained from

$\frac{P}{P_{initial}} = \left(\frac{V_{initial}}{V}\right)^{\gamma}$. Combining the equation of state (pv=mRT) with pv^{γ} gives the relationship between temperature and volume $\frac{T}{T_{initial}} = \left(\frac{V_{initial}}{V}\right)^{\gamma-1}$.

Figures 5.1 and 5.2 plot p-v and T-v diagrams for the compression stroke and part of the expansion stroke. As the contour plots plotted in Chapter 4 show, variations exist in the values of temperature and pressure over the cylinder. The values plotted in Figures 5.1 and 5.2 are averaged over the main and swirl chamber. Although the values plotted are strictly static values, the difference between dynamic and static pressures / temperature is negligible compared with the total pressure / temperature distribution. The good agreement between the two parameters indicates that the computational technique is following basic thermodynamic principles.

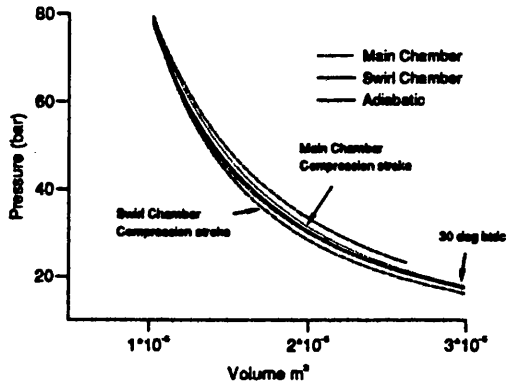

Figure 5.1
p-v diagram for adiabatic compression 30° btdc to 27°atdc. Note positions of main chamber curves relative to adiabatic curve, either side of top-dead centre

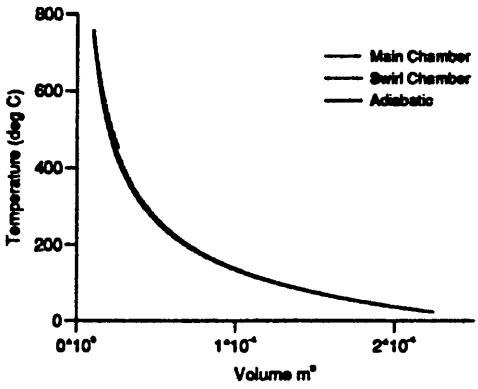

Figure 5.2
t-v diagram for adiabatic compression Bottom-dead-centre to 27°atdc. The three lines are almost coincident over most of the cycle

3 Comparison with results of other authors

Direct quantitative comparison of both numerical and experimental in-cylinder flow measurements with those of other authors is difficult. Each organisation bases their investigation on different engines, with unstated geometries, compression and volume ratios. Numerical models apply unknown boundary conditions, and experimental data is not generally presented in a format from which comparisons can be easily made. Whereas code developers can access a series of standard test cases (backfacing step, flow in a cavity etc.) where extensive experimental data for the exact case exists, once the numerical model is extended to realistic geometries, there is little scope for experimental validation against published data. Qualitative comparisons are however possible and useful.

Figure 5.3 is taken from Pinchon [47] and shows a *2-dimensional model* predicted swirl number based on point measurements at the locations shown. The general trend in Figure 5.3 - swirl rising gradually to a peak of around 30° before tdc - is similar to the results predicted by the present study, the major differences being the magnitude of the swirl (up to 40 x engine speed), the crank angle at peak swirl (between 10° and 5°btdc as opposed to 15°) and the secondary peak that Pinchon predicts after tdc.

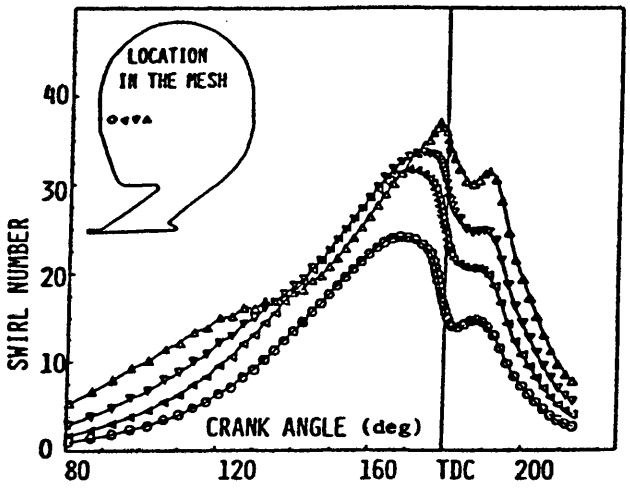

Figure 5.3
Swirl number from a 2-dimensional CFD model [Pinchon]

In a study of swirl in the Ford 1.6l engine, Tawfig [16,67] measured peak

swirl numbers of around 80 using hot wire anemometry and 25 using a paddle wheel. With a zero-dimensional model, Tawfig predicted a peak swirl number of 70. Figure 5.4 shows the *hot wire anemometry* and *predicted* swirl number comparisons. Swirl numbers around 70 / 80 are much higher than those predicted by other authors.

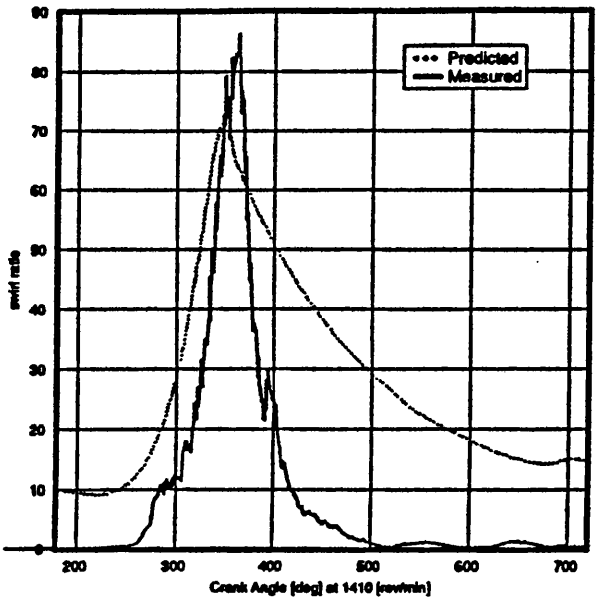

Figure 5.4
Comparison of predicted (SPICE) and measured (hot wire) swirl [Tawfig]

Zimmerman [36] used Laser Doppler Anemometry to measure air velocity in a 5x scale model cylindrical pre-chamber. Figure 5.5 is a figure taken from the paper showing swirl velocity against engine velocity. Zimmerman is showing that the peak swirl number is constant at around 20 x engine speed, at the three engine speeds presented. The cylindrical swirl chamber used, is significantly different to the Ricardo Comet Vb design (it has an auxiliary throat), so direct comparisons between the results can not be made. The results show however that the magnitude of the swirl is comparable, and that swirl number is independent of engine speed.

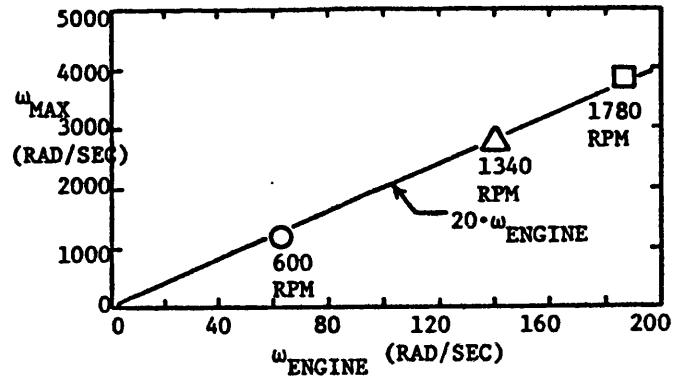

Figure 5.5
Maximum angular velocity at one point in flow field.
LDA study by Zimmerman

4 Configuring the cfd model for experimental validation

When applying computational fluid dynamic modelling to an engine flow, it might be expected that for a given set of physical conditions (engine geometry, boundary and initial conditions etc) the numerical technique would predict a single flow field. The predicted flow field could then be compared with experimental data. However, additional factors can affect the predicted solution. In attempting to validate the computational solution against experimental data, factors which affect the numerical solution must be considered.

4.1 The sensitivity of the solution to mesh density

Mesh density is a (normally qualitative) description of the number of computational cells in a given geometry. Starting from a 'coarse' mesh, it is known that as the mesh density (ie number of cells) is increased, the solution obtained changes. Eventually a *mesh-independent* solution is obtained, where any further increase in the number of cells in the mesh, does not change the solution. The recognised test of mesh independency is no significant change in the solution, when the cell length is halved.

Very few studies of the effect of mesh density on realistic in-cylinder flows have been undertaken. For a useful study, at least three or four models with identical

geometries with different mesh densities are required. To reduce the computing time, this study of the effect of mesh density has used a series of five meshes with a uniform depth (2½ dimensional) as shown in Appendix B, Figure B4. The overall geometry, and all initial and boundary conditions are identical for each model. As the effect of varying the mesh density is greatest in regions of high velocity gradients, the number of cells in the main chamber (where the flow is relatively uninteresting) has been kept approximately constant in each model. The mesh density has been increased in the swirl chamber from cells of characteristic length of just under 1mm down to 0.15mm, where

$$l_{char} = \sqrt[3]{\frac{Swirl\ Chamber\ Volume}{Number\ of\ Cells\ in\ Swirl\ Chamber}}$$. In a fully three dimensional mesh halving the characteristic length (l_{char}) implies a 2^3 increase in the total number of cells[1].

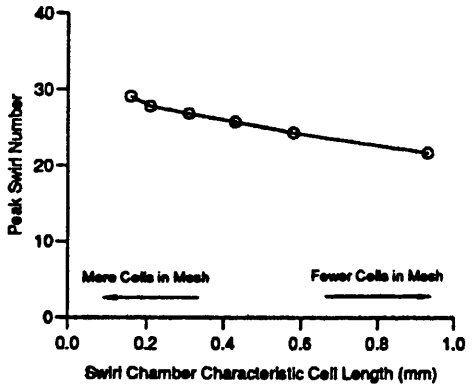

Figure 5.6
Dependency of swirl number on mesh density

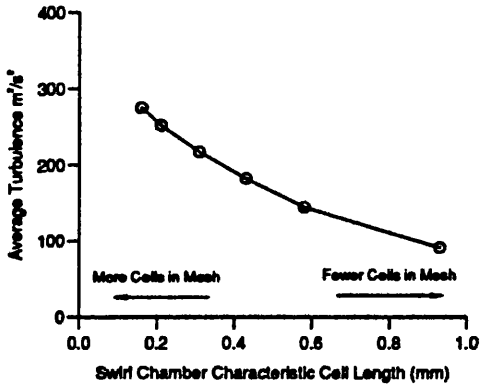

Figure 5.7
Dependency of turbulence on mesh density

[1] Computational time varies ≈ (No. Cells)^2

Figure 5.6 plots the variation of the *peak* swirl with l_{char} {cases 40-45}. As the length is reduced, the peak swirl increases. The finer mesh better resolves the velocity gradients - especially in the throat, leading to higher velocities and swirl. Turbulence is generated by shear layers in the flow, and would be expected to increase with the higher velocities associated with the finer meshes. It is clear that even with the finest mesh (l_{char} = 0.15) a mesh independent solution has not been obtained - rather than flattening off, the curve is continuing to increase as l_{char} is reduced. The associated peak turbulence level plotted against l_{char} in Figure 5.7 confirms the trend. A l_{char} of 0.15 is equivalent to a model of around 1.5 million cells in a three-dimensional mesh of the full geometry. Obtaining a solution from a model of this size is well beyond present computing power.

The majority of CFD studies published in the literature have used relatively coarse meshes - primarily because of limitations in computing hardware. The following Table summarises a number of recent IDI multi-dimensional investigations.

Study	Estimated characteristic length of swirl chamber cell (mm)	Estimated no of swirl chamber cells
Pinchon (1989)	1.7	1080
Zellat (1990)	1.6	1296
Komatsu (1991)	1.9	820
Boretti (1992)	0.9	8000
'standard' validation mesh	0.6	25000

4.2 The sensitivity of the solution to numerical differencing scheme

The numerical differencing scheme refers to the techniques used to discretise the convection terms in the momentum equations. These techniques are discussed in greater detail in Appendix A. The differencing scheme defines how the flow in a computational cell influences the flow in its neighbours. With Upwind Differencing (UD) the convection term is determined only by the flow in the cell immediately upstream. In a high Reynold's number flow, with the flow streamlines aligned with

the mesh, this has been shown to be a reasonable assumption. In a swirling flow however, with the flow streamlines crossing the mesh lines, the upwind differencing scheme is known to underpredict angular velocity. The central differencing scheme is more accurate as the cell convection terms are influenced by neighbouring cells both upstream and downstream but the solution is prone to become unstable. In one implementation of the Central Differencing provided by the STAR package, instabilities in the CD are detected and UD blended in. This Self-Filtered Central Differencing has been used for all CD results presented here. This scheme is expected to be more accurate than the UD scheme, and to be less affected by numerical diffusion (Appendix A, section 3.6). Models run using a filtered CD scheme require slightly more computing time than those run using the UD scheme.

Figures 5.8 and 5.9 plot predicted swirl number and turbulence against crank angle for six configurations {cases 1,2,3,6,8,10}. At each of three mesh densities, the two Upwind UD and Central CD schemes are compared. It must be emphasised that each curve is a prediction of the **same** actual flow - the engine speed, geometry, initial and boundary conditions are identical in each case. For a given mesh density, The CD schemes predict higher levels of swirl and turbulence. The following table summarises the results:

Mesh Density	l_{char} (mm)	UPWIND Peak Swirl Peak Turbulence	CENTRAL Peak Swirl Peak Turbulence	% age increase CD over UD
Low	1.0	30.0 146.7	35.7 209.1	19.0 42.5
Medium	0.7	32.1 223.6	37.4 314.8	16.5 40.8
High	0.4	37.0 288.5	41.8 435.3	13.0 50.9

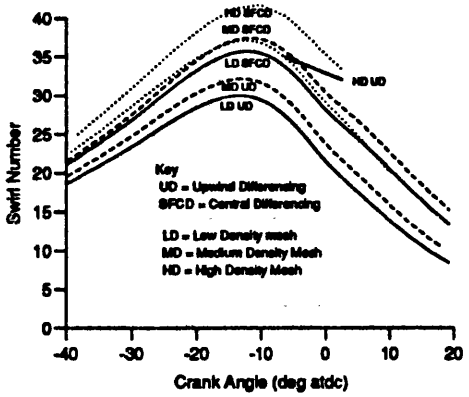

Figure 5.8
Effect of differencing scheme on swirl number

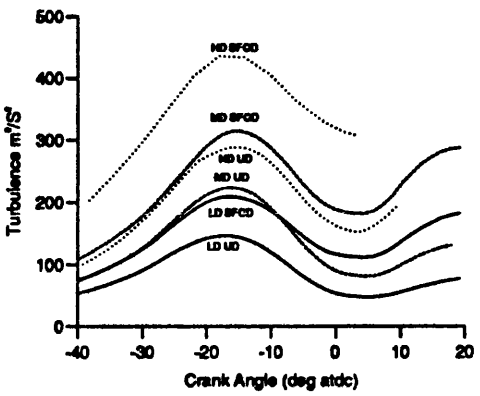

Figure 5.9
Effect of differencing scheme on turbulence

Peak swirl calculated with a CD scheme is up to 10% higher than that calculated with an UD scheme. From the Table, it is seen that as l_{char} is reduced (mesh density is increased), the percentage difference between the two schemes is reduced (19% on the low density mesh to 13% on the high density mesh). It is likely that even if a mesh independent solution were obtained, the UD and CD schemes would still predict a slightly different solution as a different set of underlying (discretised) equations are being solved.

Figures 5.6 and 5.7 above present the results of a mesh density study calculated on a 2 dimensional model with unit depth (see Appendix B, Figure B4). These cases were run with an UD differencing scheme. Figures 5.10 and 5.11 show the peak swirl and turbulence from the same meshes, but calculated with the filtered Central Differencing scheme {cases 50-55}. The previous (UD) results are included for comparison. The turbulence parameter plotted is now the level of turbulence at peak swirl (ie at around 12deg btdc). Whereas with the UD cases, a *peak* in the turbulence levels occurred at this point (Figure 5.12 showing turbulence from an UD and a high density CD scheme {cases 44/54}), with the CD scheme on the finer meshes, the turbulence rises through the whole compression stroke, giving only an *inflection* at the point of peak swirl (=peak throat velocity).

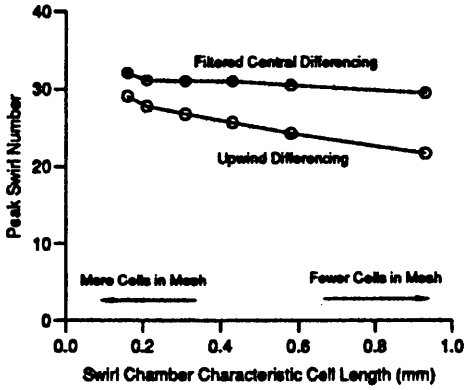

Figure 5.10
Effect of mesh density and differencing scheme on swirl number

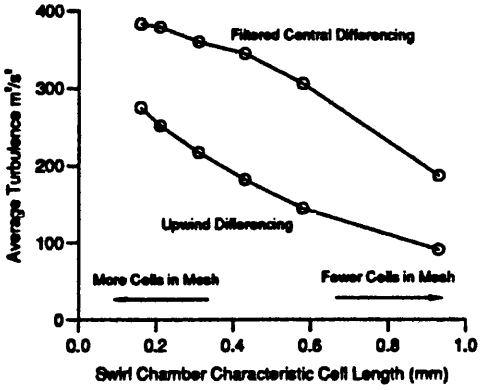

Figure 5.11
Effect of mesh density and differencing scheme on average turbulence

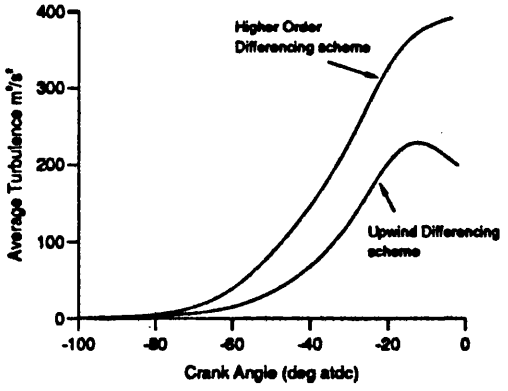

Figure 5.12
Turbulence trends calculated on fine mesh with Upwind and Central differencing

Referring to Figures 5.10 and 5.11, the overall swirl and turbulence levels calculated by the filtered CD scheme are higher than those predicted by the UD scheme, with the difference between the two being reduced as the mesh density is

increased. Unlike the UD scheme results, swirl and turbulence calculated by the filtered CD scheme appears to be reaching a plateau as l_{char} is reduced - indicating that mesh independency is probably being reached.

In all cases, increasing the model mesh density increases the swirl and turbulence levels. From consideration of the predicted results alone, it is therefore likely that the numerical model is underpredicting flow velocities. Switching from an Upwind Differencing scheme to the filtered Central Differencing scheme appears, for this class of flow, to improve the accuracy of the results, and allows a mesh independent solution to be obtained with a lower density mesh.

4.3 The effect of using temperature dependent gas properties

The p-v curve plotted in Figure 5.1 is based on adiabatic wall boundaries and assumes that the properties of air do not change with temperature (ie Cp =1.005 kJ/kgK, γ = 1.4). In order to model the compression and expansion processes accurately, the specific heat of air must vary as a function of temperature: as T increases, Cp increases, so that for a given compression ratio, the peak temperature and pressure are reduced. In the model, this is calculated on a cell-by-cell basis. Figure 5.13 shows the effect on predicted pressure of activating the gas property

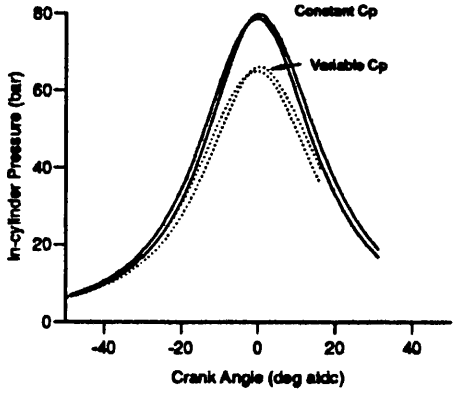

Figure 5.13
Effect on predicted pressure of varying Cp as a function of temperature

subroutine outlined in Chapter 4. Both results have been obtained from adiabatic models {cases 1,12}.

4.4 Wall boundary conditions

During any in-cylinder process, where a temperature difference exists between the cylinder walls and gas, heat will be transferred to or from the gas. The rate of heat transfer is a function of the temperature difference ΔT between the wall and the bulk fluid temperature, and the local heat transfer coefficient, which itself is a function of local gas velocity. In an engine cycle, the overall effect of wall heat transfer is a net transfer of heat to the engine coolant, and a reduction in the peak cylinder temperature and pressure. A number of possibilities exist for specifying wall boundary conditions in the numerical model.

1. Adiabatic walls.
2. Prescribed temperature. The solver calculates heat transfer coefficients and hence heat fluxes.
3. Prescribed heat flux.
4. Full modelling of the cylinder walls. The energy equation being solved (see Appendix A, Eq 16) is equally valid in solid materials (where the advection terms are zero). If the mesh is extended to include the cylinder walls, the solver can calculate the transient temperature distribution in the walls and hence heat transfer to the coolant.

An assumption of adiabatic conditions at the walls is obviously unrealistic, although the adiabatic case provides a useful datum and has been used for the studies of mesh dependency and differencing scheme presented above. Full modelling of heat transfer to the coolant requires an accurate mesh of the engine block and head from the cylinder wall to coolant. Such a model would involve extensive additional mesh generation and computational power, and still require accurate coolant boundary condition data.

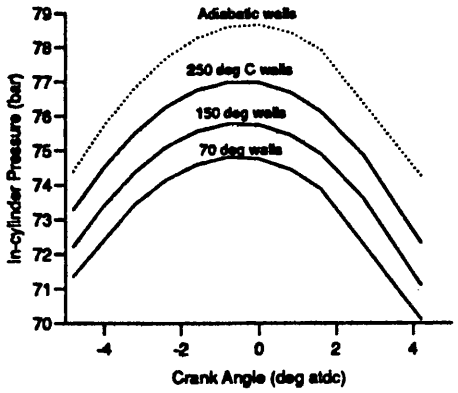

Figure 5.14
Effect of wall heat transfer on in-cylinder pressure

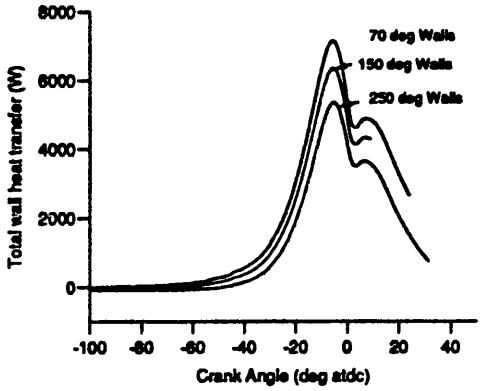

Figure 5.15
Variation of heat flux as function of wall temperature

Both the prescribed temperature and prescribed heat flux (both of which can be time dependent) options are simple to implement but accurate data are difficult to obtain. Specifying heat fluxes presumes a knowledge of the heat transfer coefficients that as a function of local gas velocity are to be determined as part of the solution. Figure 5.14 shows the predicted in-cylinder pressure for four cases {cases 20-23}, with each model having a prescribed wall temperature throughout the cycle. In a real cycle, the wall temperature varies widely over the cylinder, with the highest temperatures expected in the (insulated) swirl chamber insert. Figure 5.14 shows that the effect of moving from adiabatic conditions to the extreme case in which the cylinder walls are at the experimentally measured coolant temperature (70°C @ 3000rpm) is to reduce peak pressure by 4 bar. Peak temperature is reduced by around 40°C. In each case, gas velocities and swirl number changed by under 1% between the two extremes.

Figure 5.15 shows the predicted rate of heat transfer summed across the entire wall boundary. As expected the heat flux is greatest in the case where the walls are held at 70°C. Variation of heat transfer coefficients over the cycle is discussed in section 4.5.

Heat loss to the walls also varies as a function of engine speed. The shorter the time for compression / expansion (ie the faster the engine), the nearer adiabatic the cycle becomes - as there is less time for heat transfer. As the engine speed is increased however, the heat transfer coefficients increase (as a function of velocity). Figure 5.16 plots the in-cylinder pressure as predicted by the numerical model for engine speeds of 1500, 3000 and 4500rpm {cases 21,24,25}. In each case the wall temperature has been held constant throughout the cycle at 70°C. Figure 5.17 plots total heat transfer per degree crank angle for each case. The cumulative heat release over the cycle is the area under each curve. The case at 3000rpm has the lowest heat transfer per cycle. This is confirmed by Figure 5.16 which shows that the 3000rpm model has the highest peak pressure. As the engine speed is increased to 4500rpm, the heat transfer coefficients increase, total heat transfer is increased, and peak pressure is reduced. As the engine speed is lowered to 1500rpm, the reduction in heat transfer due to *lower heat transfer coefficients* is exceeded by the increase in heat transfer due to the *longer period for heat transfer*: Heat transfer increases and peak pressure falls. In a real engine switched from 3000rpm to 4500rpm however, the wall temperature would quickly rise, reducing the temperature difference, and hence the rate of heat transfer. In a real engine, higher engine speeds would result in higher peak pressures. Figure 5.16 also shows the variation with speed of the lag between tdc and the point of peak pressure mentioned in Chapter 3.

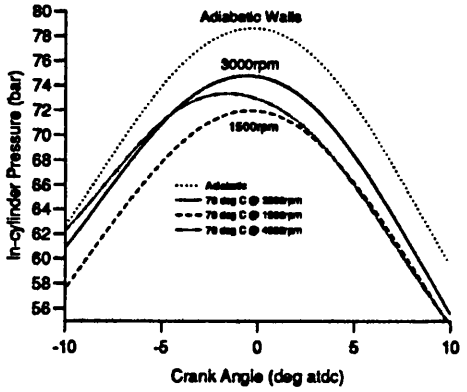

Figure 5.16
Effect of engine speed on peak pressure, when cylinder walls are fixed at 70°C

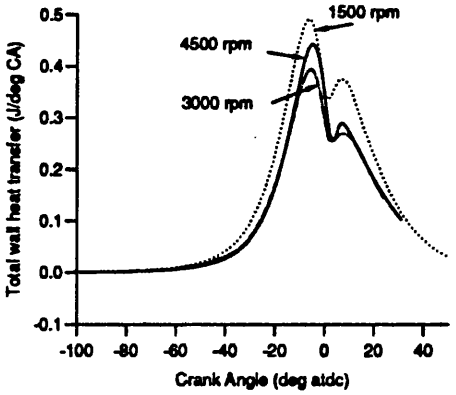

Figure 5.17
Effect of engine speed on wall heat transfer, when cylinder walls are fixed at 70°C

4.5 Calculation of wall heat transfer coefficients

Figure 5.18 shows calculated wall heat transfer coefficients, taken from the 'validation' model (described in section 5.1 of this Chapter), at an engine speed of 3000rpm and wall temperature held constant at 75°C. The spatial variation of heat transfer coefficient over the swirl chamber is displayed by breaking the swirl chamber into 3 zones:

1. Dome: the top half of the swirl chamber
2. Insert: the bottom half of the swirl chamber, excluding throat
3. Swirl chamber throat

Over each region, the heat transfer coefficients are spatially averaged, and plotted against crank angle.

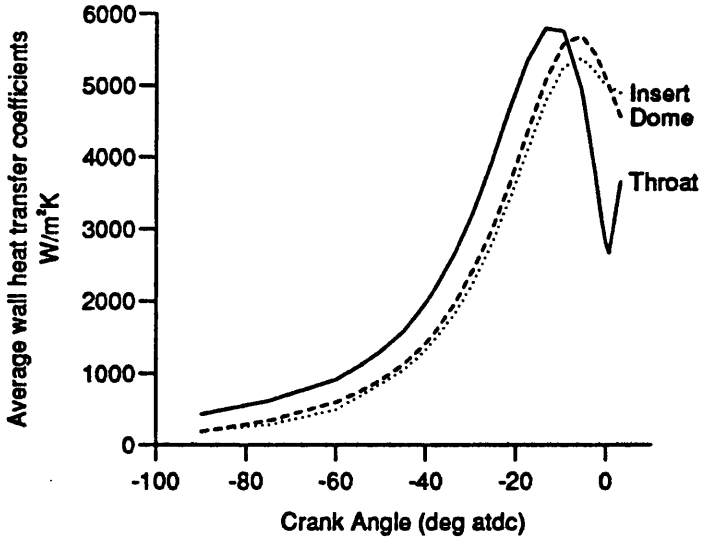

Figure 5.18
Predicted swirl chamber heat transfer coefficients (motored engine)

Heat transfer coefficients vary as a function of local gas velocity, and are highest in the swirl chamber throat. Throat heat transfer coefficients fall towards top dead centre as flow through the throat changes direction, and increase as the velocity increases. The maximum *local* (ie over a small area) heat transfer coefficient in the throat is 14500 W/m^{2}K, however the large areas of the swirl chamber throat where the velocity is low, reduce the average in the throat.

These results are taken from a motored engine. The *compression stroke* flow field in a motored engine is very similar to that in a firing engine, and the gas velocities and heat transfer coefficients will be the same. Following ignition in a firing engine, throat gas velocity and hence heat transfer coefficients are likely to be greater.

The 'law of the wall' relationships employed by the flow solver to calculate the near-wall velocities (see Appendix A) make assumptions about the nature of the flow next to the walls. While these assumptions are usually acceptable for flow modelling, the lack of velocity information within the near wall boundary layer, reduces the accuracy of the heat transfer coefficient calculations. For more accurate information, a model with a very fine mesh adjacent to the wall and without 'wall laws' would have to be solved.

5 Comparison with experimental results

5.1 Pressure

Figure 5.19 shows the pressure trace comparison from the reduced throat area insert on the experimental rig (1470rpm) and the numerical model (1450rpm {case 15}). To simulate the real cycle as closely as possible, the model is run with:

- correct geometry (including piston crown, compression ratio and volume ratio)
- wall boundaries set to 100°C constant throughout cycle. Coolant temperature (out of the head) at this speed stabilises around 75°C. The SPICE zero-dimensional IDI model developed by Tawfig [16] suggests that at 1500rpm, mean swirl chamber insert temperature is just over 100°C.
- variable specific heat (varies with temperature)
- simple valve modelling: the real engine is not a closed cycle from bdc to bdc. The inlet valve closes fully around 37°abdc, and the exhaust valve opens around 40°bbdc. To simulate the effect of the inlet valve closure, an atmospheric pressure boundary is defined for the first 35° abdc.

All the experimental pressure results presented in this Chapter are *ensemble averaged* over 10 to 15 cycles. It was shown in Chapter 3 that any significant cycle-to-cycle variations that existed could not be detected by the pressure transducers. Even if cyclic variations were significant, the numerical model as formulated will predict *the same* results each time for any given set of boundary conditions. Thus, even in cases where cycle-to-cycle variation is significant, it is the ensemble-averaged results that should be used for comparison with the numerical simulations.

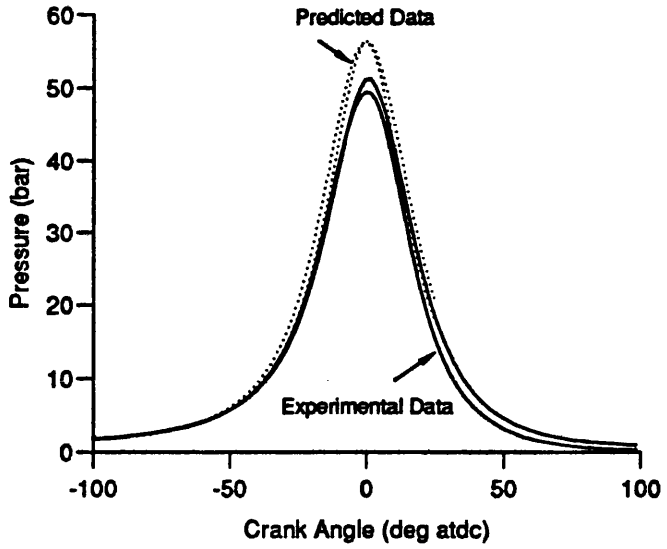

Figure 5.19
Comparison of predicted and experimental pressure at 1450rpm

From Figure 5.19, the model appears to be modelling the compression and expansion process correctly, except that the predicted peak pressure is too high. This may be due to the model underpredicting wall heat transfer (the 100°C wall temperature over the whole stroke may be too high), but is probably mainly due to piston blow-by. It is obviously possible to impose a mass outlet on the numerical model to simulate blow-by, and thus reduce the peak pressure to the required level, but unless the correct boundary conditions (ie mass flow per crank angle) are known at each engine speed, an arbitary value (which appears to give correct results) must be imposed, reducing the *predictive* capability of the model.

Figure 5.20 compares the low pressure (ie start of compression stroke) absolute pressure reading, piezo-electric transducer measurements and predicted values. The modelling of pressure at inlet valve closure (around 35°abdc) is important, as it indicates whether the trapped mass at the start of the compression stroke is correct. A 0.1 bar error in initial pressure will lead to a peak pressure error of $0.1 \times 21.5^{1.3} \approx 5$ bar. The error in main chamber pressure at 40° after bottom dead centre when inlet valve closure is not modelled (ie the cylinder is sealed at bdc) is around 0.1 bar. Figure 5.20 shows that the predicted main chamber pressure is very close to the absolute pressure reading taken from the piezo-resistive transducer. At

this low pressure, main chamber and swirl chamber predicted pressures are expected to be identical: the piezo-electric readings are taken at the very bottom of their range, and are not calibrated for precise measurement over this part of the pressure range.

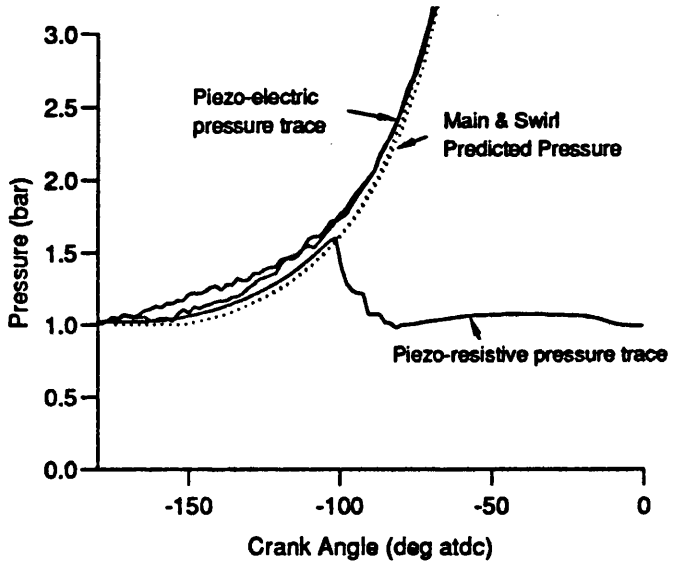

Figure 5.20
Comparison of predicted and experimental pressure at start of the compression stroke.

5.2 LDA results

The results from the LDA study presented in Chapter 3, provide only limited data for comparison with the flow predictions. The main limitation is the lack of LDA data in the high velocity (high swirl) region of the cycle. The compression-stroke low velocity measurements do however provide sufficient data for a useful comparison to be made between the flow model and the LDA measurements. The flow model results presented here are taken from a 1000rpm simulation {case 17}, and scaled (920/1000) to match the experimental engine speed. In Chapter 4, section 5, it was shown that predicted air velocity was directly proportional to engine speed.

Figures 5.21, 5.22 and 5.23 present comparisons of the LDA and the predicted flow data at three points on a traverse along the fuel injector axis.[2] The predicted values of velocity are resolved to give the component perpendicular to the fuel injector axis. Figure 5.21 shows the numerical model underpredicting the measured velocity by a maximum of around 30%. After 40°btdc, the laser data rate drops, and no further comparisons can be made. Figure 5.22 shows the modelled and the measured data indicating similar trends in the flow during the compression stroke: A fall and rise in the velocity data between 80° and 60° btdc is recorded by both techniques, as is a short reduction in the rate of increase of velocity (a plateau) at 55°btdc. This suggests that the qualitative predictions of the flow model are correct. The maximum flow model underprediction is around 70% at 55°btdc. Although the air speed at the measurement location in Figure 5.23 is of the same order of magnitude as that of Figure 5.22, the component being measured by the LDA system is almost perpendicular to the direction of flow, giving a low measured velocity. In the region for which reliable LDA is available, the predicted model matches the experimental data reasonably well, until around 85° btdc when the two velocity predicts diverge sharply. This may indicate error in the measurement location (in either technique), as a relatively small error along the traverse will have a greatly magnified effect in the resolved component of velocity. Following the divergence, the model matches the qualitative trend of the experimental data, but significantly underpredicts the velocity.

Figures 5.24, 5.25 and 5.26 compare the measured and predicted velocity profiles along part of the fuel injector axis, at three stages during the cycle. The most useful comparison for validation would be in the high swirl area of the cycle (15°btdc), but as has been discussed, no LDA data was obtained in this region. Comparisons are therefore made at 80°, 58° and 48° btdc. Over this period sufficient LDA data was obtained to have reasonable confidence in the results. In each of these figures, the trend along the axis is the same, indicating that the structure of the modelled flow is the same as that measured experimentally. At each of the comparison points, the model is significantly underpredicting the flow velocities.

---

[2] The 37,40 and 43mm distances are absolute coordinates from along the axis from the lip at the top of the injector bore. Refraction at the window moves the actual point of measurement further into the swirl chamber. The predicted flow values are plotted at the *effective* point of measurement.

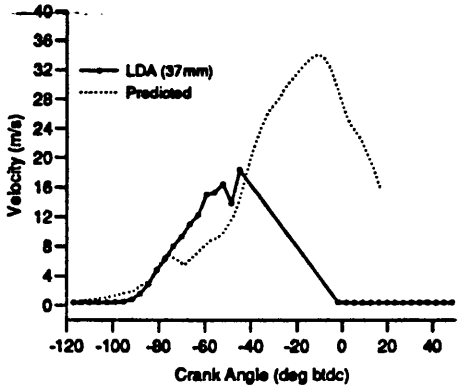

Figure 5.21
Comparison of predicted and experimental velocity data at 920rpm at 37+3mm along fuel injector axis

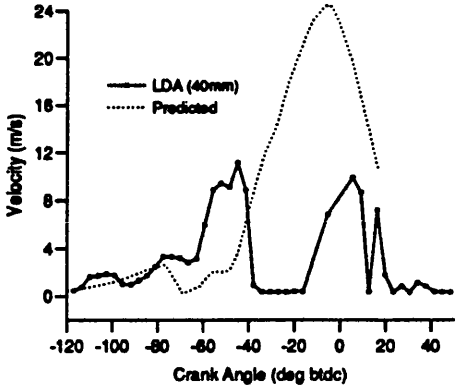

Figure 5.22
Comparison of predicted and experimental velocity data at 920rpm at 40+3mm along fuel injector axis

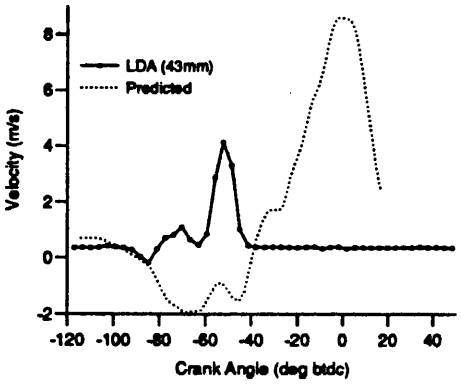

Figure 5.23
Comparison of predicted and experimental velocity data at 920rpm at 43+3mm along fuel injector axis

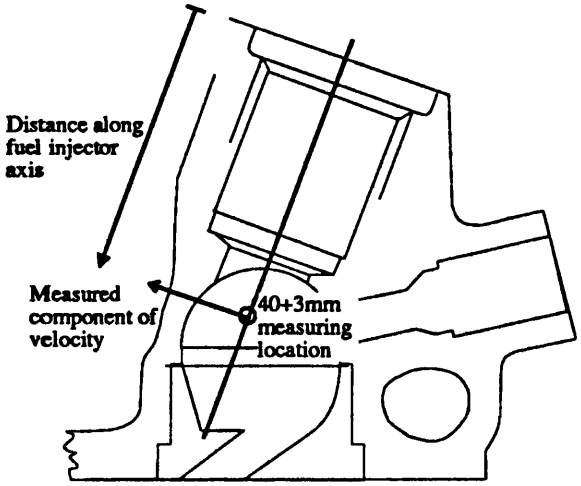

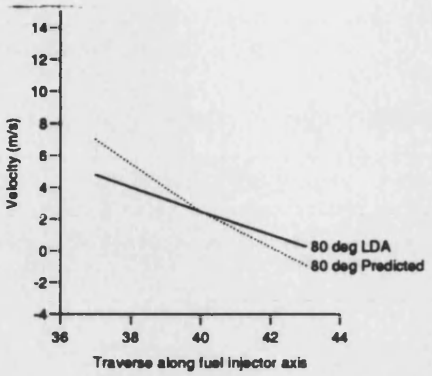

Figure 5.24
Comparison of predicted and experimental velocity data at 920rpm at 80°btdc

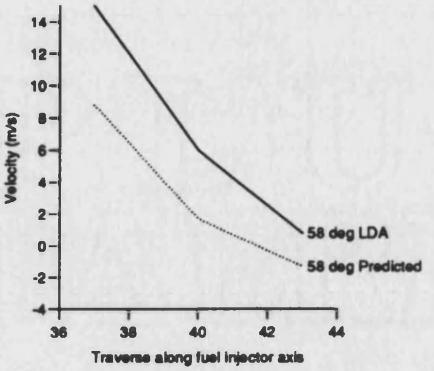

Figure 5.25
Comparison of predicted and experimental velocity data at 920rpm at 58°btdc

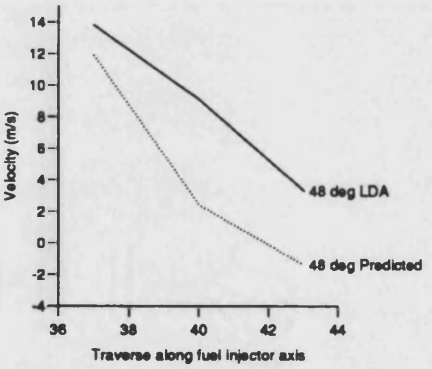

Figure 5.26
Comparison of predicted and experimental velocity data at 920rpm at 48°btdc

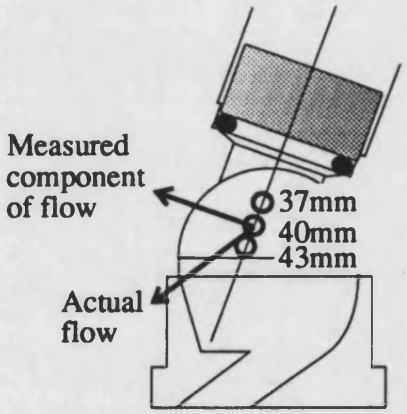

5.3 Discussion

One of the principal aims of this study, has been to determine to what extent numerical modelling can be used to simulate the flow field in a realistic automotive combustion chamber. In this Chapter, the steps involved in formulating a flow model have been outlined, and the sensitivity of the flow predictions to non-physical parameters examined. The results from this study have been incorporated into the 'validation' model: fine mesh, higher differencing scheme, realistic boundary conditions etc.

Although experimental velocity validation data was limited, the results presented suggest that the numerical model is underpredicting the flow velocities. Correcting the overprediction of pressure (for instance by adding a blow-by model) is likely to *increase* the difference between the flow model and velocity measurement. The results presented in Figure 5.8 indicate that if the number of cells in the mesh were increased (further reducing artificial diffusion), the predicted velocities would be expected to rise (+12% from the MD CD to the HD CD - table on page V-9), although the central differencing plot in Figure 5.8 suggests that the validation mesh (cell length 0.4mm) is within 15% of a mesh independent solution. From the results presented, the flow model appears to be capable of modelling the qualitative detail of the flow accurately: had the flow model alone recorded the peaks and troughs in Figure 5.22, they may have been dismissed as a numerical error. As both techniques record the same flow phenomena at the same location and point in the cycle, the modelled flow is probably genuine.

Possible sources of error

FLOW MODEL	LDA MEASUREMENT
Numerical errors due to mesh dependent solution, turbulence modelling etc	What is the exact measurement point? Measurement location is determined by an automatic traverse, with no direct frame of reference on the engine. Does engine vibration affect the measurement location?
Insufficient data for full specification of boundary conditions	Does the seed follow the flow? If the flow is self-seeding, do these secondary particles follow the flow? If the particles are thrown out of the swirling flow, is an additional radial component measured?
Geometric errors in modelling the combustion chamber	Operator error during data acquisition. LDA processing equipment is complex to operate. Errors in data are often not immediately apparent.
Results processing and interpretation	Results processing and interpretation

The Table above lists some of the possible sources of error in both the flow modelling and the experimental measurement. The velocity field up to 40°btdc is useful for model validation, but of only minor interest in the overall flow field within the engine. Given that a flow field exists within the engine, and that it is within the field of vision of the laser beams, it is reasonable to assume that techniques will be developed, possibly in the short term, to enable the velocity variation over the whole cycle to be measured experimentally. Once this data is available, it will be easier to quantify the extent to which the flow model predicts the actual flow.

6 Summary

1. When adiabatic boundary conditions are specified, the flow model conforms to basic thermodynamic principles.
2. The results from the swirl chamber flow model are in qualitative agreement with those of other researchers. Direct quantitative comparison is not possible, as there is insufficient detail available to replicate their work.
3. The flow model is sensitive to the level of mesh refinement, numerical differencing scheme and boundary conditions imposed on the model.
4. Comparison with experimental results suggests that the numerical model is underpredicting the air velocity in the swirl chamber in the low velocity region of the cycle, but is fully capable of predicting the structure of the flow.
5. Further experimental data is required to validate the numerical model in the important high swirl region around top dead centre.

CHAPTER SIX
PARAMETRIC MODELLING OF ENGINE PERFORMANCE

1 Introduction VI-2

2 Throat area study VI-3

3 Glow plug position VI-6

4 Downstream glow plug and a 5% throat area increase VI-8

5 Swirl Chamber Shape VI-8
5.1 Optimising exit flow from chamber, without reducing chamber swirl level VI-10

6 Discussion VI-16

7 Summary VI-18

1 Introduction

The previous Chapter attempted to establish the validity of numerical flow modelling, through comparison of the predicted data with theoretical relationships and experimental measurement. In this Chapter, the flow model is used to undertake a number of parametric studies of air motion in the engine: For each of a series of cases, the effect on air motion of changing one parameter (eg swirl chamber throat area, rate of heat transfer) has been investigated. It is in parametric studies, that numerical fluid modelling techniques are of the greatest use when investigating the processes occurring within an engine. Whereas geometry changes in a prototype engine are expensive and time-consuming to implement, once the geometry for a numerical model has been formulated, changes can often be made relatively easily. By comparing the results from the parametric study, the direct effect of the design change or change of boundary condition etc. on air motion and combustion can be determined. A number of parametric studies have already been presented. In Chapter Four, the effect of engine speed on swirl and turbulence was investigated by running the same model at 1500, 3000 and 4500rpm. In Chapter Five, the effect of wall heat transfer on in-cylinder pressure was examined by running the same model with wall temperatures of 70,150 and 250°C, and with adiabatic conditions. In this Chapter the results from parametric studies of engine geometry are presented.

From the results presented in Chapter 5, it is clear that the solutions obtained from the numerical modelling are sensitive to mesh size: reducing the cell size increases swirl and turbulence. This characteristic of the solutions is important, if accurate conclusions are to be drawn from parametric studies. Throughout this Chapter, it will be assumed that although it is known that the solutions will change were a finer mesh to be devised, comparisons between meshes with similar cell sizes are valid. This assumption is discussed in greater detail in Chapter 8.

Recent work undertaken at the University of Bath has investigated the effect on overall engine performance of changing the geometry of the engine swirl chamber (summarised in Charlton, Cox, Somerville et al.)[1] [18]. For each geometry, Charlton

---

[1] This paper, which also contains results from the numerical modelling study is appended at the end of the thesis for reference.

modified the insert and/or head for all four cylinders, and performed a steady-state test over the full range of load/speed combinations. Various configurations have been tested, including enlarged and reduced throat area; moving the engine cold-starting aid (glow plug); and including an extra *air cell* in the swirl chamber, as an additional source of oxygen in the later stages of combustion.

In an attempt to explain further the results obtained from these studies, numerical air flow models have been formulated for a number of different swirl chamber geometries. The results from these studies are presented in this Chapter. An attempt is made to make a connection between the observed change in air motion as predicted by the model, with the actual effect on engine performance as observed by Charlton.

2 Throat area study

During the compression stroke, air is forced from the main chamber through the swirl chamber throat into the swirl chamber. The angular velocity of the swirling motion set up in the swirl chamber depends on the swirl chamber throat area. Charlton found that when the area of the swirl chamber throat was increased, low load characteristics remained constant, while fuel consumption increased and NO_x levels were reduced at higher loads. These are indications of reduced combustion efficiency: fuel consumption is increasing, but peak combustion temperature is reduced, hence lower NO_x levels. The increase in high load fuel consumption and smoke may be due to the decreased jet penetration from the swirl chamber into the main chamber following ignition, reducing main chamber air utilisation. At part load, less oxygen is required for complete combustion, and the effect of main chamber jet penetration is reduced.

To investigate the cold-flow effects of throat area, a series of simulations using models of varying throat area have been run. To reduce the required computational effort, a two dimensional model with unit depth has been used (2½ dimensional model). Maintaining the exact symmetry plane cross section geometry (ie the vertical plane dividing the swirl chamber in two), the cross section has been given a uniform depth (Appendix B, Figure B5). The cell depth in the main and swirl chambers have been chosen to preserve the correct compression and volume ratio. Using this 2½ dimensional model greatly reduces model formulation time and the reduction in solver

computational time increases the number of cases that can be simulated. A similar mesh was used for the mesh dependency study in Chapter 5. Although the 2½ model is not able to simulate the full complexities of the (3-dimensional) swirl chamber flow, it can provide qualitative and quantitative data on the effect of throat area on the in-cylinder flow.

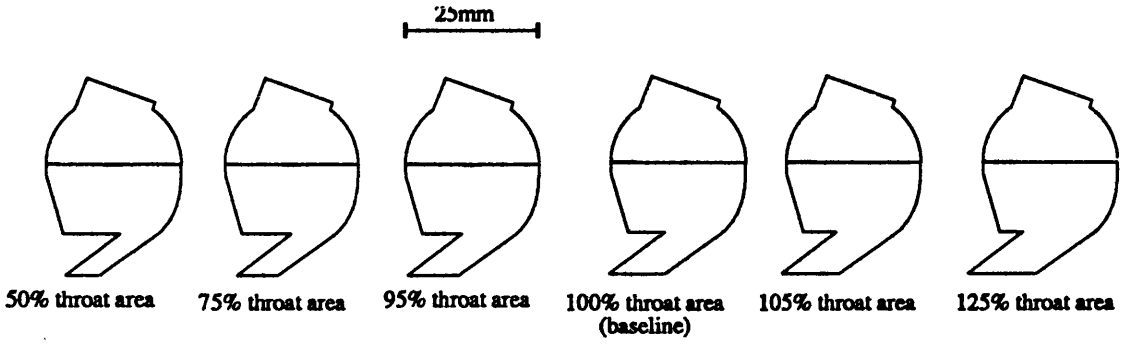

Figure 6.1
Swirl Chamber throat area study
Geometry profiles

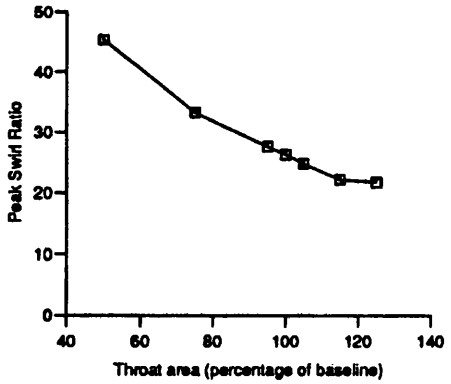

Figure 6.2
Effect of throat area on peak swirl

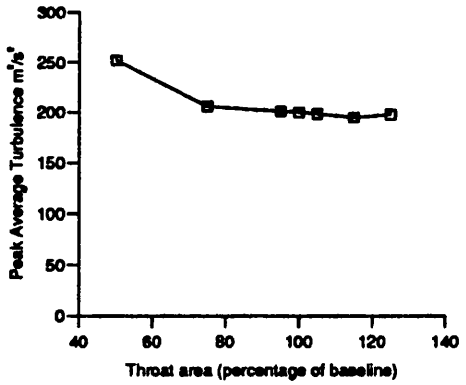

Figure 6.3
Effect of throat area on peak turbulence

Figure 6.1 summarises the model geometries. Six models have been generated with throat areas from 50% to 125% of the baseline (100%) case. As the study uses

a 2-d model with constant depth, it is not possible to change the throat dimension *into the paper*. The area has therefore been varied by altering the throat width. To preserve the correct compression and volume ratios (allowing direct comparisons of swirl and turbulence parameters), slight changes have been made to the length of the injector passage. The models do not include a glow plug or the piston crown.

Figures 6.2 and 6.3 plot the peak swirl and turbulence for the models as a function of throat area. Peak swirl number is a function of throat area (quadratic curve fit: $S = 0.008A - 0.38A^2 + 57$ where A = the percentage of baseline throat area 50-125%) while average swirl-chamber turbulence is approximately constant over the 75% to 125% throat area range. Reducing the throat area, increases the *pumping losses* - the work required to pump the air into the swirl chamber. Pumping losses account for (a small) part of the reduced efficiency of the IDI combustion system compared to DI diesel engines. Figure 6.4 shows calculated compression pumping mean effective pressure (pmep) (calculated as in Chapter 4) against throat area. The pmep has been non-dimensionalised (mep / $mep_{100\%}$).

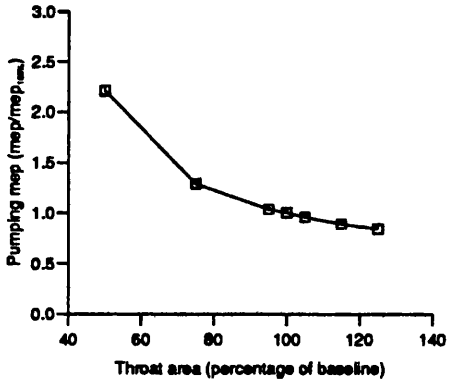

Figure 6.4
Effect of throat area on pumping losses

This study was also used to determine an appropriate size of swirl chamber insert for the second throat insert used in the experimental work: A 50% throat area insert was chosen as it produced a 100% increase in peak swirl.

3 Glow plug position

The experimental work of Charlton highlighted the advantages of moving the glow plug from its baseline (crossflow) position (Figure 6.5), to a position downstream of the injector (Figure 6.6). In the experimental study, Charlton found that engine fuel consumption improved over the whole cycle, particulate emissions were improved, but NO_x levels increased significantly. These are indications of a more efficient combustion process - the increased NO_x levels a result of higher combustion temperatures. To investigate the effect of the glow plug on air motion, the results from three 3-dimensional models have been compared: crossflow (baseline); downstream; and no glow plug (Appendix B, Figure B2). The volume of the injector bore in each model has been altered to compensate for the change in compression and volume ratio caused by the geometry changes. The models simulate a 3000rpm engine speed with adiabatic boundary conditions.

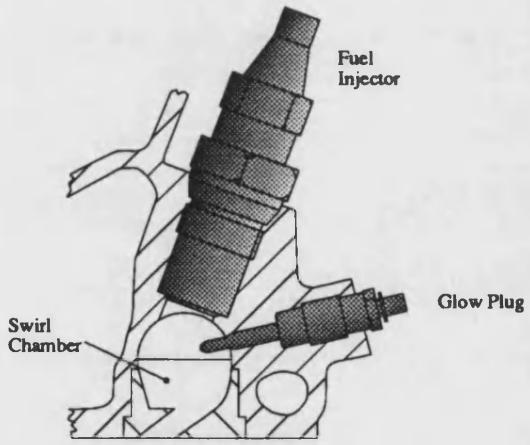

Figure 6.5
Swirl Chamber with Crossflow glow plug

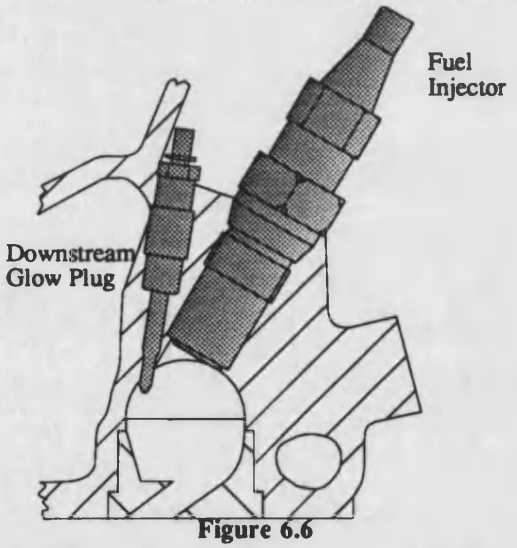

Figure 6.6
Swirl Chamber with Downstream glow plug

Figure 6.7 shows that the standard cross-flow glow plug is acting as a significant restriction to the flow, giving a peak swirl of around 28 x engine speed, compared with around 32 x engine speed for the downstream and no glow plug cases. The downstream glow plug, in a region of lower average velocity than in the cross-

flow position has hardly any effect on swirl levels - the downstream and the no glow plug swirl lines are almost coincident. An average swirl number of 30 in the period between fuel injection and top dead centre indicates that the swirling air in the auxiliary chamber will complete one full revolution of the chamber in (360/30 = 12) degrees of crankshaft rotation. Figure 6.8 compares the turbulence levels corresponding to the three geometries. The primary source of turbulence generation turbulence is the connecting passage between the two combustion chambers which is identical in each model. The cross-flow glow plug case, where the glow plug is placed in a region of high air velocity, generates the highest average turbulence. It is interesting that although the downstream case had a similar swirl number curve to the case without a glow plug, the associated turbulence levels are significantly higher: the downstream glow plug appears to be causing increased air turbulence, without significantly affecting overall swirl.[2]

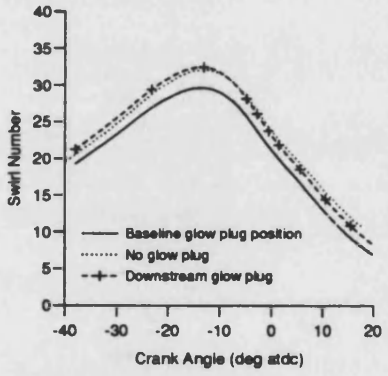

Figure 6.7
Effect of glow plug position on peak swirl

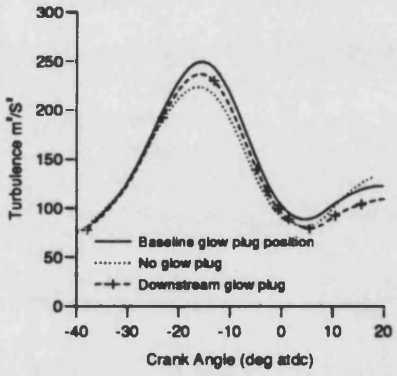

Figure 6.8
Effect of glow plug position on average turbulence

The increased air velocities will increase the rate of air/fuel mixing in the swirl chamber following injection and may explain the more efficient combustion measured experimentally.

---

2 It should be noted that this increase in turbulence in the downstream glow plug case *may* be a numerical and not a physical effect. As has been shown in the Chapter 5, the solutions obtained are not mesh independent - it is known that turbulence levels increase if mesh density is increased. The basic mesh for each of the models is identical, but local mesh refinement is required in the regions around the glow plug.

4 Downstream glow plug and a 5% throat area increase

Charlton [18] notes that whilst moving the glowplug to a downstream position increased NO_x and reduced smoke, increasing the throat area had the opposite effect - lowering NO_x and increasing smoke. When an engine with a downstream glow plug and a 5% increase in area was tested, Charlton found that although there were considerable part load improvements for smoke and particulates, NO_x levels were worse than for the downstream case. From the numerical modelling presented above, an increase from 100% to 105% throat area produces a 5% decrease in swirl. The swirl increase due to the downstream glow plug is around 10%. A combination of the two might therefore be expected to lead to around a 5% increase in swirl levels. The numerical solution appears to offer no explanation for the increased NO_x levels compared to the downstream standard throat case.

5 Swirl Chamber Shape

The air flow predictions presented in previous Chapters and above have been based on models of the standard Ricardo Comet Vb combustion chamber. In all of these cases the model is being used to predict the change in flow field *magnitude* due to the change in the parameter being investigated. The underlying flow *structure*, being defined by the geometry remains the same in all cases. In this section, the flow modelling technique will be used to predict the flow in four radically different geometries, with the aim of studying the feasibility of modifying the swirl chamber geometry to improve the flow.

The velocity vector plots at the end of Chapter 4 show that during both the compression and expansion strokes, the effective area of the swirl chamber throat is significantly less than the actual area of the throat. During the compression stroke, the *vertical* component of the air velocity forms a recirculation zone behind the sharp lip at the bottom of the throat. The hindrance to the flow could be removed by using a vertical entry to the throat. During the expansion stroke (10°atdc plot in Figure 4.1a), the *horizontal* component of the velocity forms a recirculation zone under the sharp lip at the top of the throat, as the flow turns through almost 90° to enter the throat. At the throat exit, the burning gases must leave with an angle close to the horizontal

to ensure that the jet entrains as much main chamber air as possible, and to reduce gas impingement on the piston.

Figure 6.9 shows the geometry used in a first attempt to improve the flow. The cut away bottom lip allows near vertical entry to the throat increasing the effective area of the throat, reducing pumping losses. The tapered flow passage should increase the jet velocity into the chamber increasing swirl. The bell shaped top lip will reduce the flow separation that occurs in the baseline design.

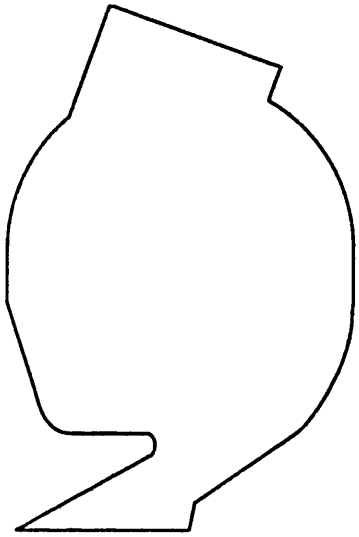

Figure 6.9
Modified throat geometry

The predicted flow fields shown in Figure 6.10 show that none of the expected improvements in the flow were realised. Flow into the chamber is improved, but by changing the angle of the jet into the chamber during compression, a secondary swirling vortex is formed on the right of the swirl chamber, reducing the overall level of swirl in the chamber. The secondary vortex, in a region outside the line of fuel spray injection, is unlikely to improve air/fuel mixing, while the reduction in main swirl magnitude will reduce the efficiency of the mixing process. Removing the bottom lip of the throat increases gas burning gas impingement on the piston (poor fatigue life) and will reduce main chamber air utilisation.

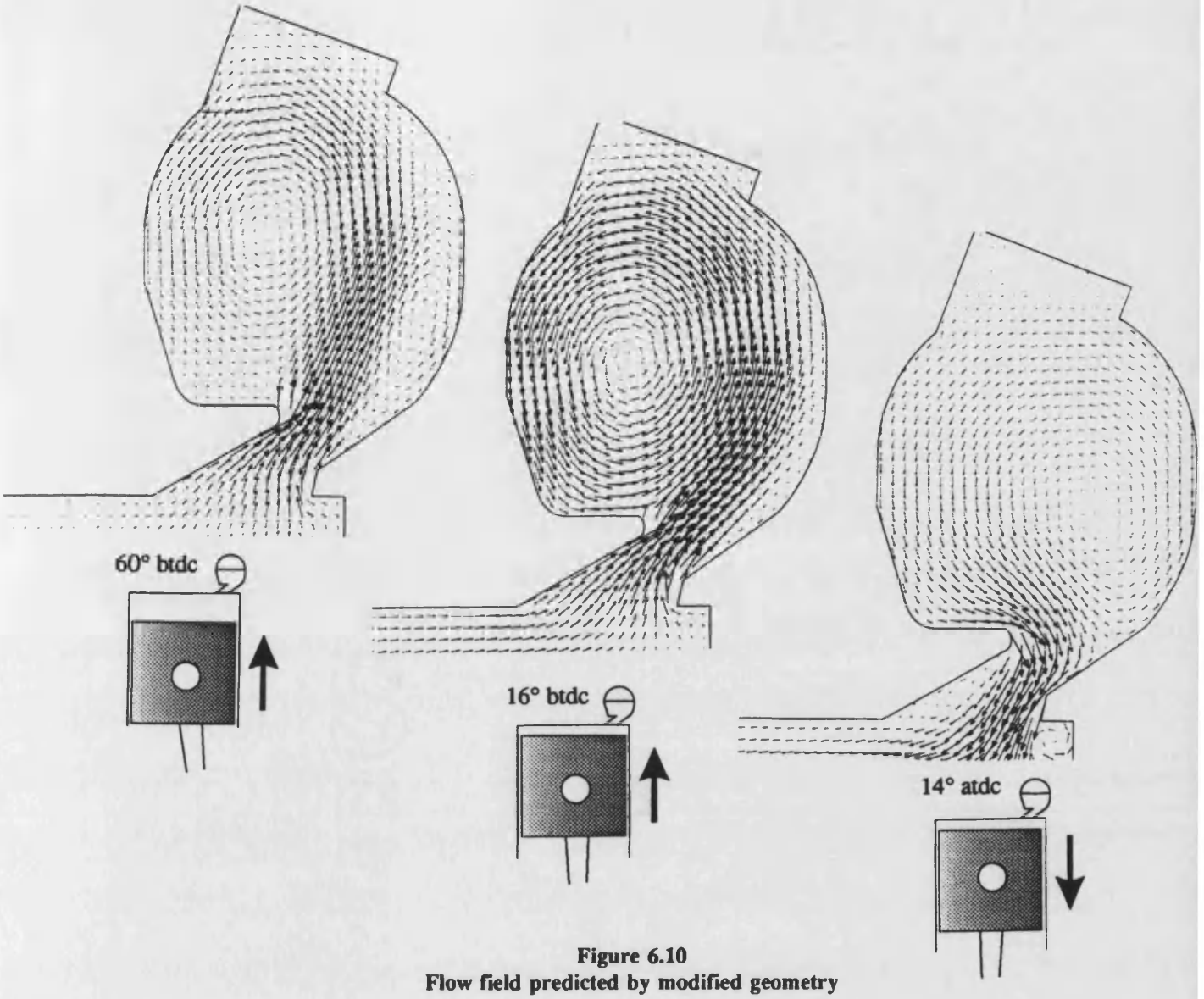

Figure 6.10
Flow field predicted by modified geometry

5.1 Optimising exit flow from chamber, without reducing chamber swirl level

The next series of geometry modifications show an attempt to improve the flow *out* of the swirl chamber. To maintain the existing levels of swirl, the standard Ricardo Comet Vb swirl chamber throat has been retained. The geometry shown in Figure 6.11 (*shape 1*) has a bell shaped entrance into the chamber. During the expansion stroke this will allow the burning gases to flow through a greater area of the throat.

To maintain the correct compression and volume ratio, the swirl chamber has been slightly elongated.

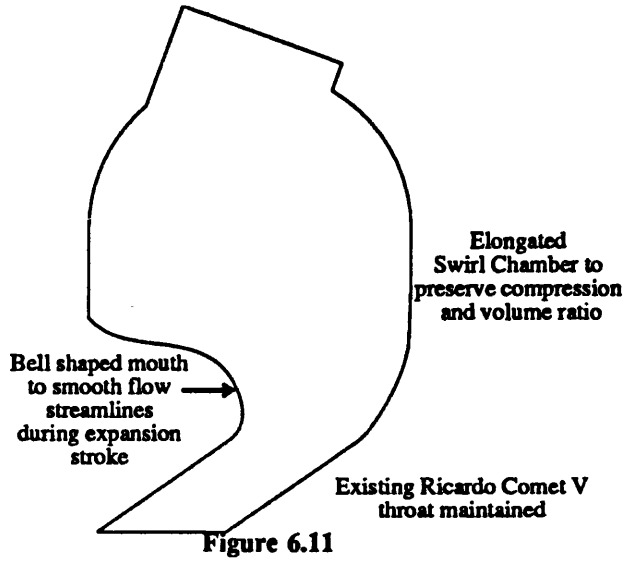

Figure 6.11
Geometry of 'shape 1' model

The predicted flow field for this geometry is shown in Figure 6.12. The effect of the bell entrance is to eliminate flow separation from the throat, setting up a reverse swirling motion in the chamber[3]. The clockwise swirling flow is ideal for smooth flow out of the chamber, but not for fuel/air mixing following fuel injection. From this flow field, it is clear that a sharp lip at the entrance to the swirl chamber is required to form the gas jet which will produce the required clockwise flow field.

[3] The degree of attachment to the wall is likely to be accentuated by the mesh structure used in this region.

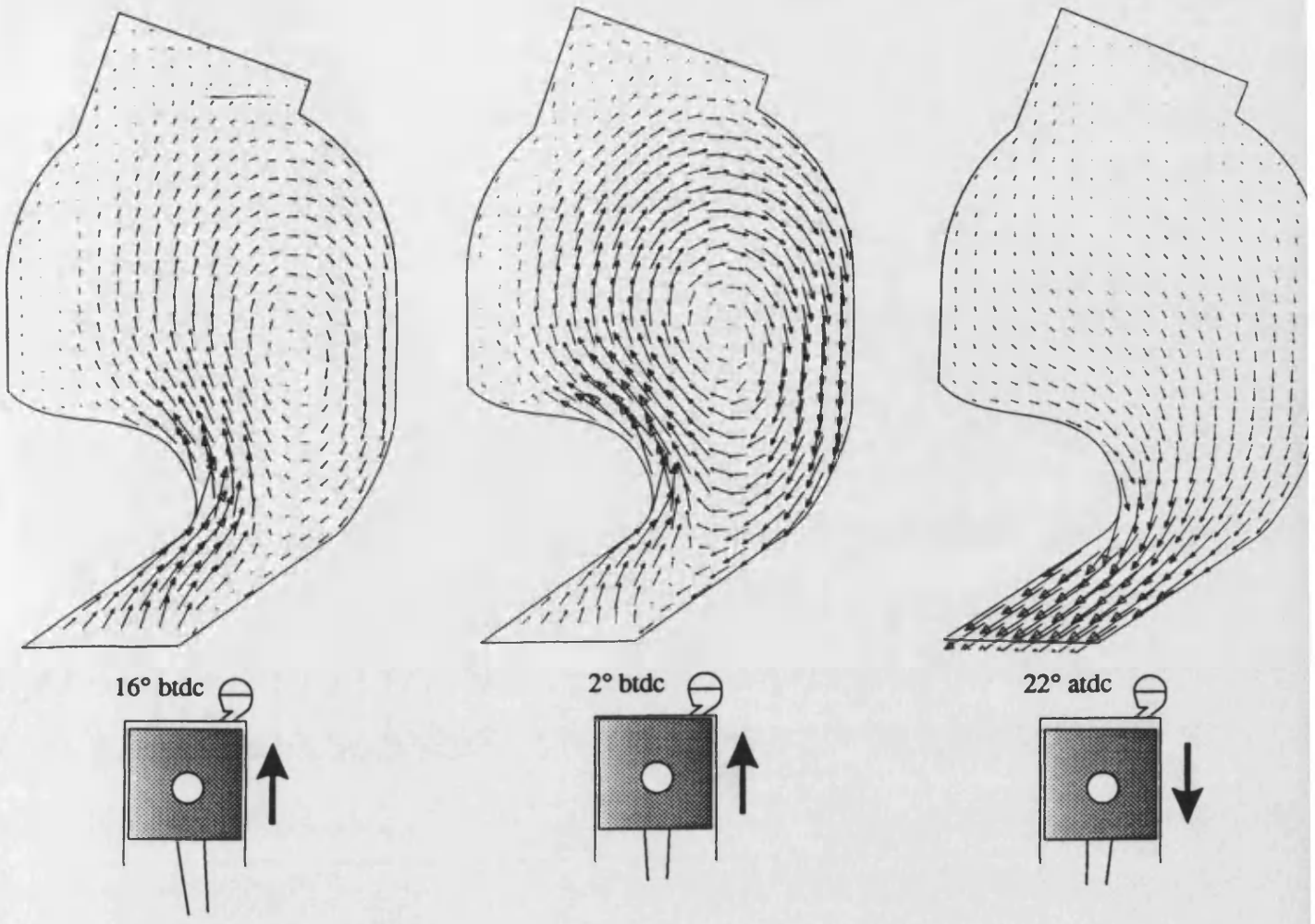

Figure 6.12
Predicted flow field for 'shape 1' geometry

Figure 6.13 shows a swirl chamber geometry (*shape 2*) in which the sharp lip at the top of the throat is retained, but in which the bottom left hand corner of the chamber is modified to reduce the angle through which the flow must 'turn' when flowing out of the chamber. The calculated peak swirl is 2% greater than the baseline (Ricardo Comet V) case. The angled approach to the throat exit (bottom left corner) does appear (Figure 6.14, 22°atdc) to be increasing the effective area of the throat during the expansion stroke, when compared with the flow field following tdc in Figure 4.1a.

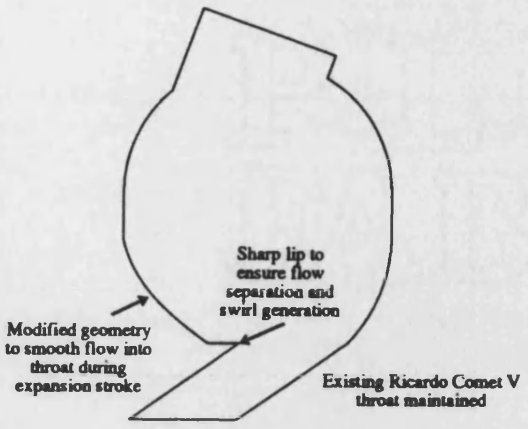

Figure 6.13
Geometry for 'shape 2' model

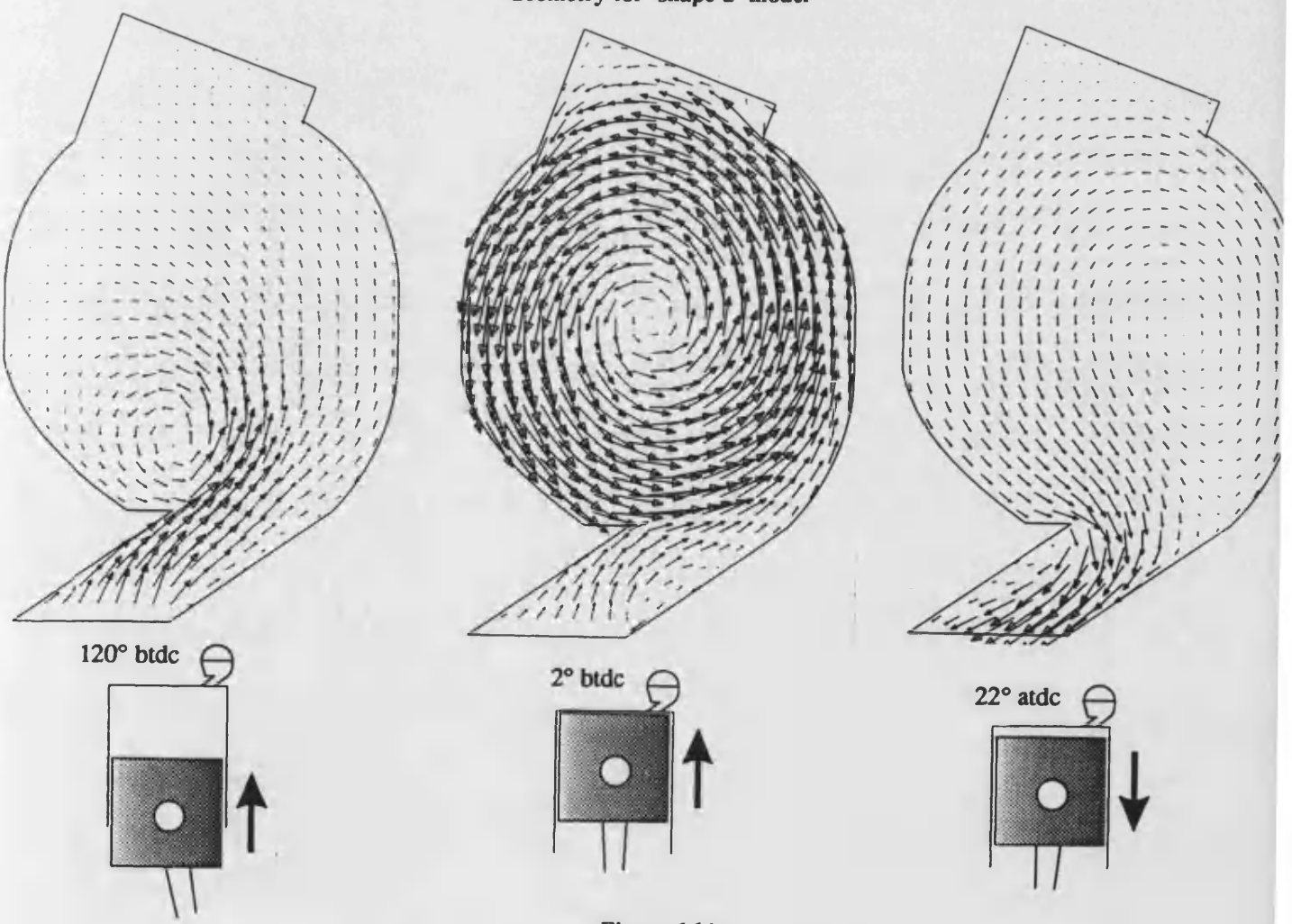

Figure 6.14
Flow field predicted by 'shape 2'model

Geometry shape 2 (Figure 6.13) maintains the roughly spherical form of the swirl chamber - in Figure 6.13, the radius from the centre to the wall is constant around the entire chamber. The geometry in Figure 6.15 further modifies the chamber wall in the bottom left hand corner of the chamber, reducing the swirl chamber radius, but further smoothing the expansion flow field (Figure 6.16). Peak swirl for this case falls by 6%, probably as a result of the obstruction presented by the modified wall.

The change in the expansion flow field due to each of the geometries can be quantified by plotting the pressure drop over the throat around top dead centre. Figure 6.17 shows that the compression pressure drop across the throat is similar for all three geometries. This is expected as the Ricardo Comet Vb throat has been incorporated in each design. The expansion stroke pressure drop (proportional to pumping losses) is greatest for the baseline Ricardo Comet Vb chamber: the flow following tdc has been improved in the each of the modified designs. Shape 1, in which a reversed flow field was set up, has the lowest pressure drop, reflecting the very smooth flow out of the chamber. Shape 2, with a sharp lip to ensure 'correct' swirl generation, produces a pressure drop slightly less than the baseline case - the modifications made to the wall to smooth the streamlines approaching the throat have had some effect. Shape 3, reduces the overall swirl, but produces a flow field with a 50% reduction in pressure drop across the throat during the expansion stroke.

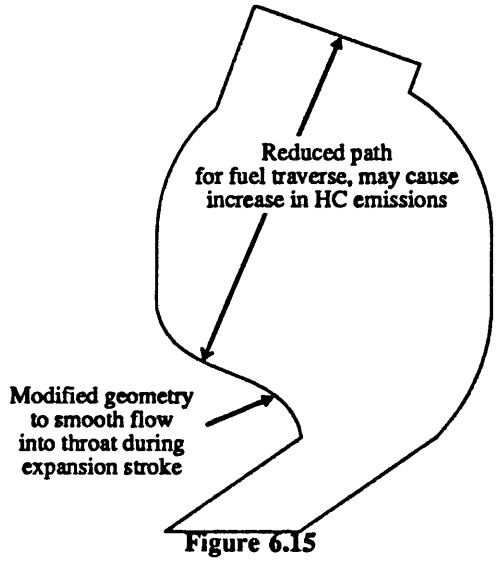

Figure 6.15
Geometry for 'shape 3' model

It will be shown in the following Chapter that the underlying flow structure is

not changed by the combustion process. It is likely therefore that the changes predicted in the expansion stroke flow field will apply to the firing case, as well as to a motored engine, but to a greater extent. This study has shown that simple modifications to the swirl chamber geometry could significantly streamline the flow in the chamber. A more detailed study would be required to establish the benefits of similar modifications on fully three dimensional meshes, although as the 2½ dimensional mesh of the baseline case has been shown to be an acceptable approximation to the 3-d case, the conclusions are probably the same.

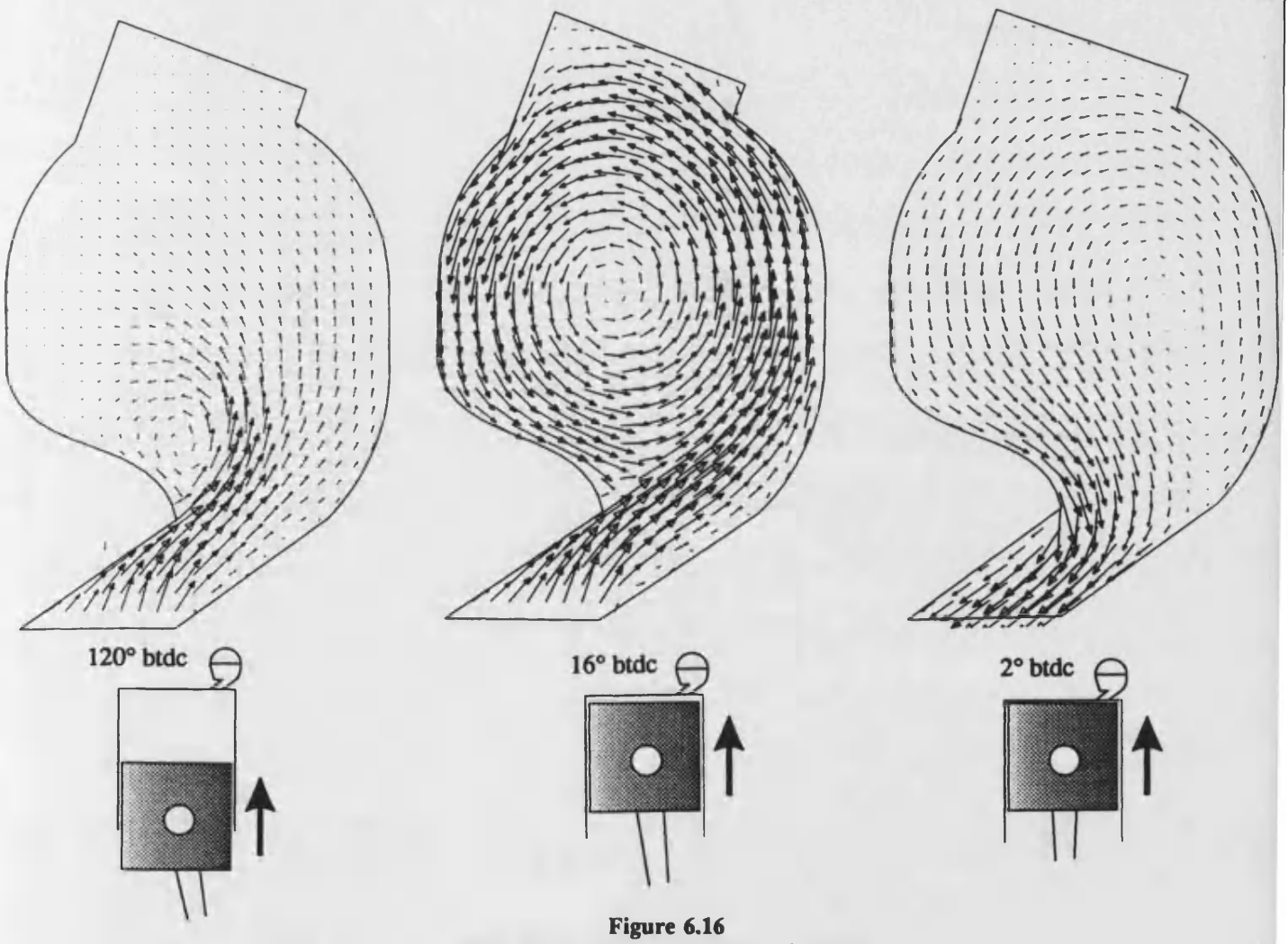

Figure 6.16
Flow field predicted by 'shape 3' model

Shapes 1, 2 & 3 have been elongated, to preserve the volume of the swirl chamber. Even with the elongation, the distance of fuel penetration from injector to

wall has been reduced. The Ricardo Comet **Mk III** chamber used a cylindrical type chamber (Figure 2.13 on page II-22), but this was changed to the current design (similar to Figure 2.14) to increase the distance of fuel penetration before impinging on the wall. The existing fuel traverse could probably be restored by further elongating the chamber, and at the same time reducing the depth (into the paper) in the three-dimensional geometry. When applied to shape 3 (which appears to be the best of the modified designs), this would also probably increase the level of swirl in the chamber. The next stage in this design process would be to use the numerical modelling to optimise the geometry (including combustion), before testing a prototype in a test-bed engine.

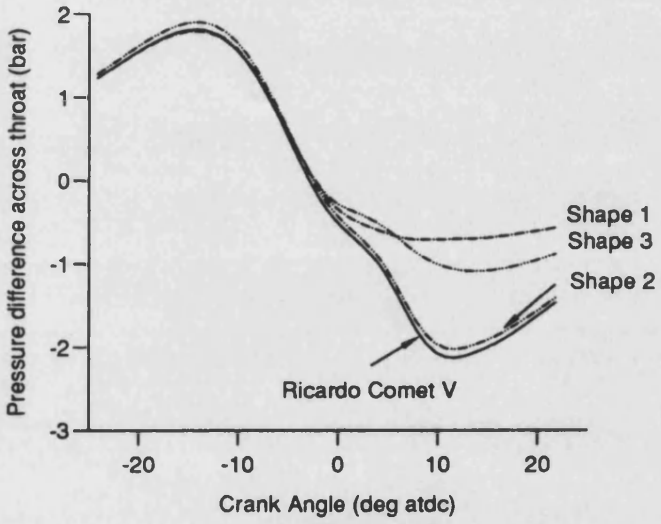

Figure 6.17
Pressure drop across throat for modified geometries

6 Discussion

The studies presented both above and in previous Chapters have presented simulations of cold-flow air motion only. Fuel injection and combustion have not been included in the model. Although it is not possible to make a *direct* connection between the

numerical modelling results presented and engine performance data, an attempt can be made to draw links between the air motion and the mechanisms of combustion.

It has been shown that moving the glow plug to a downstream position and reducing the throat area increase swirl generation. Increasing the swirl level in the chamber at the point of fuel injection, sweeps the evaporating fuel around the swirl chamber more quickly, so that at the point of ignition, more pre-mixed fuel/air mixture exists. The increased atomization of the fuel may reduce ignition delay. Following ignition the flame will develop more quickly in the premixed reactants, and lead to higher NO_x levels. The increased breakup and mixing reduces the localised mixture richness (fuel excess), so that at part load, when the swirl chamber contains sufficient oxygen for complete combustion, smoke and particulates are reduced. At higher loads, it is important that the air in the main chamber is available for combustion. Improved mixing in the swirl chamber increases the proportion of unburnt fuel drawn into the main chamber before combustion (more fuel is contained in the air near the throat), improving main chamber air utilisation, and reducing smoke and particulate formation. Thus in summary, increased swirl is likely to raise NO_x levels and reduce particulate and smoke formation. This is supported by the results of Charlton [18].

NO_x can be controlled in the engine at part load conditions by recirculation of exhaust gases and over the whole load / speed map by retarding injection timing. Retarding the injection timing reduces the time for mixture formation before ignition and delays the heat release timing, thus reducing NO_x formation.

The study of throat area examined the effect on swirl, turbulence and throat pressure drop of varying the throat area. One important factor not examined was the extent to which the throat area affects the penetration of the jet of burning fuel/air into the main chamber following ignition. An increase in throat area is likely to reduce the exit velocity, and thus reduce air/fuel mixing in the main chamber. At high loads therefore, when main chamber air utilisation is important, an increased throat area is thus expected to increase smoke and particulates. There is likely to be a trade-off between increased main chamber jet penetration and increasing pumping losses: a narrow throat may aid fuel/air mixing in both chambers, but will increase the pumping losses during both compression and expansion strokes.

7 Summary

1 Numerical modelling is an effective technique for undertaking parametric in-cylinder air motion studies, allowing the effect of single design parameters on in-cylinder flow to be investigated. Simplified (2 dimensional) models can quickly be formulated and solved to provide relationships between the proposed design change and flow.

2 By combining the predictions of air flow with experimental data on overall engine performance, tentative conclusions can be drawn about the link between the design change and the change in performance. Modelling of the fuel injection and combustion processes will greatly enhance this capability.

3 Numerical flow modelling is a useful tool for analysing the effect on air flow of radically differing designs.

CHAPTER SEVEN
DIESEL COMBUSTION MODELLING

1 Introduction VII-2

2 Combustion modelling techniques VII-4
- 2.1 Injection and spray modelling VII-4
- 2.2 Kinetics controlled combustion VII-5
- 2.3 Auto-Ignition VII-5
- 2.4 Magnussen combustion model VII-6
- 2.5 Product formation VII-7
- 2.6 Studies of diesel combustion VII-7

3 Modelling IDI combustion VII-8
- 3.1 Formulating a combustion model VII-8
- 3.2 The combustion process VII-9
- 3.3 Discussion VII-14

4 Summary VII-15

1 Introduction

Combustion in engines is a highly complex process. Fuel contains a range of hydrocarbons, each of which combust slightly differently. Fuel requires a charge of air to burn, and as has been shown in the previous Chapter, slight changes in the engine internal geometry, and hence air motion, can have significant effects on combustion. Additionally, combustion characteristics change with load and speed.

Engine combustion has been studied experimentally for many years, both in terms of overall performance and in detail using in-cylinder visualisation techniques such as high speed photography. The information obtained from experimental investigations has provided thermodynamic (zero-dimensional) models with heat release and combustion data allowing the models to be configured to provide a predictive capability over a range of engine conditions. Given sufficient *fundamental* knowledge about the mechanisms of combustion, it should be possible to formulate a truly *predictive* combustion model, in the same way that the Navier-Stokes equations allow the prediction of fluid motion. This potential however is unlikely to be realised for a considerable time: Firstly the fundamental knowledge about the mechanisms of the processes must be determined ('the theoretical model'). This may be derived from theory (for instance the Navier Stokes equations), experimental results, or most often a combination of the two. This model must then be formulated in method that can be handled using existing computer codes and hardware ('the code'). This normally involves linking the new model with an existing technique, for instance a fluid flow solver. It must be possible to obtain a stable solution in a finite time. Having been developed and coded, a new model can only be said to be useful, when it is shown to *predict* trends in realistic applications in accordance with known (generally experimentally measured) trends ('implementation').

The computer simulations of air flow formulated in previous Chapters, have demonstrated that the pre-combustion flow field can be modelled with confidence. As stated in Chapter One, the ultimate aim of such in-cylinder fluid modelling is a complete predictive model of engine combustion, such that given the engine geometry and appropriate inputs (valve timing, fuel injection timing), accurate predictions of power output and exhaust emissions can be made. The next step towards achieving this goal is combustion modelling.

In this Chapter, techniques for modelling diesel combustion are discussed and the results from a simulation of the combustion process presented.

The modelling of Diesel Combustion can be broken in to the following main stages:

1. *Fuel injection.* Fuel is injected as a liquid jet (which may contain cavities), which is progressively atomised through interaction with the moving, turbulent air. Spray droplets break up, coalesce, and evaporate (cooling the air). Some of the fuel impinges on the cylinder walls, where it may rebound, cling or evaporate
2. *Auto-ignition.* After an ignition delay, auto-ignition of the fuel starts, in one or more places in the chamber. Ignition delay is generally a function temperature and concentration.
3. *Combustion.* Following ignition, combustion proceeds. Combustion modelling leads to a heat release term dependent on the local concentrations of fuel and air. The two main modes of combustion are *pre-mixed* and *diffusion.* [64,68] During the ignition delay, fuel and air in some regions have become thoroughly mixed (pre-mixed). The flame spreads quickly through this mixture following ignition causing a rapid increase in pressure and temperature. Where no pre-mixing has occurred, and when the premixed combustion is exhausted, combustion proceeds as diffusion burning. Fuel and air (oxygen) are separated by hot, product containing eddies which are mixed by the turbulence in the air. Because of the high temperatures, when a combustible mixture is prepared (by the turbulent mixing), combustion occurs very quickly (kinetic time scale is small). The rate of combustion is thus governed by turbulent mixing. In regions of low temperature, or excessively lean or rich mixing, combustion may become kinetics controlled.

   Ignition — *kinetics controlled (reaction time scale is large compared to the turbulent time scale)*

   Combustion — *turbulence controlled (turbulent time scale is large compared to the reaction time scale).*

4. *Product formation* During the combustion process, fuel and air react, releasing heat and forming products. Diesel combustion is extremely complex: each hydrocarbon in the fuel reacts, combines and breaks-up in a vast series of chemical reactions. The products of combustion are primarily steam (H_2O) and carbon dioxide (CO_2), but also include unburnt hydrocarbons, soot, NO, NO_2 and other products from the combustion of trace species in the fuel (eg sulphur). Hydrocarbons and particulates are formed when, on a molecular level, fuel burns with insufficient oxygen, or at too low a temperature for complete combustion. NO and NO_2 are formed when the local temperature of combustion causes a reaction between atmospheric nitrogen and oxygen.

2 Combustion modelling techniques

Once an air motion model has been formulated, submodels for fuel injection, auto-ignition and combustion may be added. The following sections present techniques used to model combustion.

2.1 Injection and spray modelling

Fuel is injected into the swirling air mass as a continuous jet or a discontinuous spray. The jet breaks down into a spray which is progressively atomised by the turbulent air mass. The fuel spray is deflected by the swirling air and may impinge on the cylinder wall. As the fuel droplets evaporate, the surrounding air is cooled.

Once the fuel has evaporated it may be treated as a gas concentration and solved using the same technique as temperature, turbulence etc (*a scalar*). This scalar is created via fuel evaporation, is convected / diffused around the combustion chamber, and destroyed in combustion. A simple method for modelling the fuel spray is therefore as injection of a dense gas. This however is unrealistic as the gaseous entrainment and mixing is very different to that of a liquid and a gas. Modelling of individual fuel droplets as full two phase flow is well beyond the current and

foreseeable computing capabilities, as to resolve the spray surface detail requires an extremely fine mesh. The fuel spray may however be treated as a statistical sample of discrete droplets which are tracked through the mesh (a Lagrangian description) [42,43]. Each fuel droplet modelled represents a sample of real droplets. The modelled fuel droplet interacts with the flow, via momentum, heat and mass transfer, and these interactions are assumed to be representative of the sample. As the fuel evaporates, gaseous *scalar* is created.

2.2 Kinetics controlled combustion

Basic chemical theory states that rate of reaction $\propto kC_1^{\alpha}C_2^{\beta}$, where C_1 and C_2 are molar concentrations of the reactants, and k is a constant. In many cases, where the reaction is temperature (T) dependent, the constant takes the *Arrhenius* form $e^{\frac{-E_A}{TR}}$, where E_A is an (experimentally determined) activation energy constant. Thus in its simplest form, rate of reaction R_f is given by

$$R_f = -A\rho^2 m_{fuel} m_{oxygen} e^{\frac{-E_A}{RT}} \qquad (1)$$

This will be referred to as the single equation Arrhenius rate of reaction model.

2.3 Auto-Ignition

Kinetic rate of reaction expressions form the basis of autoignition modelling. Following fuel injection, a model is required to predict when and where auto-ignition occurs. At the time of injection, the conditions in the chamber are already sufficient to ignite the fuel, and the ignition delay results from firstly the time needed for the fuel to evaporate and form a combustible mixture (physical delay) and secondly the time needed for the reaction to take place (chemical delay). In a multi-dimensional simulation, the physical delay is accounted for by the spray and scalar (fuel vapour) modelling. An auto-ignition model is used to simulate the chemical delay. Some studies of ignition have directly used the rate equation given above [12,43]. The ignition process is not however a result of the direct reaction between fuel and

oxygen, but rather a range of reactions. The Shell model [69] breaks the ignition process into a series of *pseudo-reactions* for which reaction coefficients have been experimentally determined. Each reaction, which is dependent on the previous, then proceeds according to the rate reaction given above with the appropriate coefficients. The Shell model, modified for diesel combustion has been used in most of the recent multi-dimensional studies. In modelling ignition, it is assumed that the characteristic time for the chemical reaction is much greater than that for the turbulent mixing, thus the ensemble-averaged (ie not the turbulent variations) can be used in the rate reactions.

2.4 Magnussen combustion model

Once ignition has started, the temperature rises quickly and the characteristic time of combustion as predicted by the ignition model (exponential with temperature) is greatly reduced. The rate of combustion is now controlled not by how quickly the chemical reaction takes place, but by how quickly the fuel and oxygen can be mixed together by the turbulent eddy structures. Magnussen [70] proposed a single step equation which is now used as the standard model for turbulence controlled combustion. The rate of reaction is given by:

$$R_f = -A\rho\frac{\epsilon}{k}\ \min\left(m_{fu}, \frac{m_{fu}}{\gamma}, \frac{Bm_{pr}}{1+\gamma}\right) \qquad (2)$$

where **min** is an operator finding the minimum of the three terms and γ is oxygen/fuel ratio. The first and second terms in the brackets state that combustion is limited by the amount of fuel and oxygen respectively. The third term accounts for the need for a minimum amount of hot (product containing) gas to be present to provide the activation energy for combustion to proceed. Values for constants A and B were suggested by Magnussen, but these have subsequently been altered to fit better to experimental data. Rather than trying to simulate every single reaction in the combustion process, the overall heat release action is modelled (rate of reaction × calorific value of the fuel), and fitted to experimental data by selection of the

constants A and B. The model assumes that as the chemical kinetics are much faster than the turbulent mixing, the reaction rate is controlled by the decay of turbulence eddies, and when the fuel and air are mixed, the reaction occurs instantly.

2.5 Product formation

Because the Magnussen model does not attempt to model the component reactions of the combustion process, there is no simple way of directly predicting product formation. In a real combustion reaction, fuel and air do not need to be at stoichiometric ratio to react. At the molecular level, the hydrocarbons in the fuel will begin to form radicals which will react with oxygen molecules, but in rich (excess fuel) regions, will not completely react to form H_2O and CO_2. If these part-burnt hydrocarbons are not combusted later in the cycle, they will form exhaust emissions. NO_x formation is conceptually easier to predict, as it is a function of local air temperature, and, unlike hydrocarbons, does not affect subsequent combustion.

2.6 Studies of diesel combustion

A number of organisations have attempted to extend studies of air motion in diesel engines, both DI and IDI to include combustion. Early work (1982) of Gosman [43,47] used a single equation Arrhenius kinetics equation model and Magnussen's turbulent combustion model to simulate ignition *and* combustion. The switch from a kinetic to a turbulence model is made when the ratio $\frac{kinetic\ time\ scale}{turbulent\ time\ scale} = \frac{A\rho e^{-E_A/(RT)}}{k/\epsilon}$ is less than 1. In the most recent work of Gosman [42,50-an application of the code], ignition is modelled by the modified Shell model, and combustion by Magnussen. Ishiguro [71] used the Arrhenius equation to *prepare* mixture which was then consumed by the Magnussen model. This approach allows mixture build up following injection, and during combustion the turbulence Magnussen model to control the reaction. Pinchon [38] and Zellat

[48] used the modified Shell ignition model and the Magnussen combustion model for diesel combustion simulation.

3 Modelling IDI combustion

The STAR flow modelling package which has been used for the flow predictions of IDI engine flow, contains a number of tools which can be applied to the full modelling of combustion in an engine. The package has been used to construct a simple model of combustion in the engine. This model has been used to study the basic flow and combustion phenomena in a firing engine. To reduce the computational requirement, the study uses a relatively coarse 4000 cell, 2 dimensional mesh with unit depth.

3.1 Formulating a combustion model

The fuel spray is modelled using a Lagrangian technique that tracks representative fuel drops through the flow domain. As the fuel droplets pass through the mesh, they undergo heat transfer, mass transfer (evaporate), break up into smaller droplets and are deflected by the flow. The injection process also influences the in-cylinder air flow. At walls, droplets may either stick to the wall, rebound, or evaporate immediately. Each of the heat, mass transfer processes is governed by one or more constants. For this study constants have been chosen to replicate approximately, experimentally measured spray phenomena. The engine is assumed to be operating at medium load (50:1 air/fuel ratio) at 3000rpm.

As the fuel spray evaporates, it is converted to a gaseous fuel concentration ('scalar'). Transport equations are solved for both fuel and mixture fraction. Mixture fraction is a passive variable, which defines how much fuel would be present at any location had no combustion taken place. The difference between these two scalars allows the concentrations of oxygen and products to be calculated algebraically, (ie without solving full transport equations for each species).

Combustion is modelled using a simple Arrhenius rate equation and the Magnussen combustion model described above. The model with the lowest rate of reaction in

a given cell is used to defined the local rate of reaction. Gosman who used this approach [43] notes that the abrupt transition from one rate of reaction equation to another, cannot be correct, but that the approach is justified in view of the many other uncertainties in the modelling process. The Magnussen equation (Eq 2 above) constants have been set to A=20 and B=2.5 as used by Gosman [43]. Pinchon [38] found that A=16 and B=2 gave very similar results. Previous studies of diesel combustion suggested that the Arrhenius equation (Eq 1 above) constants should be set to $A=1x10^{12}$ and $E=1.0x10^{8}$ to $1.25x10^{8}$. In this study, it was found that these values of E resulted in ignition almost immediately following injection. To delay the ignition process, constant E was set to $1.3x10^{8}$ or $2.0x10^{8}$, depending on the point of injection (12°btdc or 7°btdc respectively). The fuel is assumed to be a hydrocarbon of formula $C_{14}H_{30}$, molecular weight 198 (M for diesel is in range 180-200).

The following sections show the results from this model of IDI combustion.

3.2 The combustion process

Fuel is injected towards the bottom left hand corner of the swirl chamber into the flow field some time after the point of peak swirl. The air velocity is thus falling. Although the behaviour of the fuel spray can be specified by appropriate setting of the spray model coefficients, with realistic settings, the fuel spray path appears to be largely unaffected by the swirling air motion. As the droplets evaporate the resulting fuel vapour is swept round by the swirling flow field. Figure 7.1 shows the droplet flow field at 9°btdc following injection at 12.3°btdc. The radius of each droplet is proportional to its mass. Each droplet plotted is a representative sample of a number of real fuel droplets. Figure 7.2 shows the concentration of fuel vapour at the same point with the bulk of the fuel is in the left half of the chamber.

In the simulations of combustion, the point of ignition is very dependent on the constants assigned to the fuel spray model - how much fuel evaporates, and how quickly after fuel injection. The model is not able to predict exact ignition delay following fuel injection, as depending on the value assigned to the activation energy constant (E), ignition can be advanced or retarded. Ignition may occur at more

than one place in the chamber. In all the simulations run, ignition has been close to the vertical centre line of the swirl chamber, at the interface between the fuel vapour and the hotter air flowing into the chamber. Following ignition, combustion quickly spreads to those areas where fuel vapour has already been mixed with air. Figure 7.3 shows the temperature field in the swirl chamber at 3.7°atdc, following fuel injection at 5°btdc. No allowance is made for the variation of specific heat with temperature, and the temperature field predicted is expected to be too high. By this stage the premixed combustion has been completed, and combustion is now being controlled by the rate at which the swirling motion supplies oxygen to the fuel, which is still concentrated on the left hand side of the chamber. Figure 7.4 plots oxygen concentration at the same time (3.7°atdc). The supply of oxygen has now been depleted in the left hand side of the chamber. The swirling motion mixes the oxygen rich gas (top right hand corner of chamber) with the fuel rich gas in the region of the fuel injector, allowing combustion to continue.

In-cylinder pressure and calculated (cumulative) heat release for this simulation (injection at 5°btdc) are shown in Figure 7.5. Following injection at

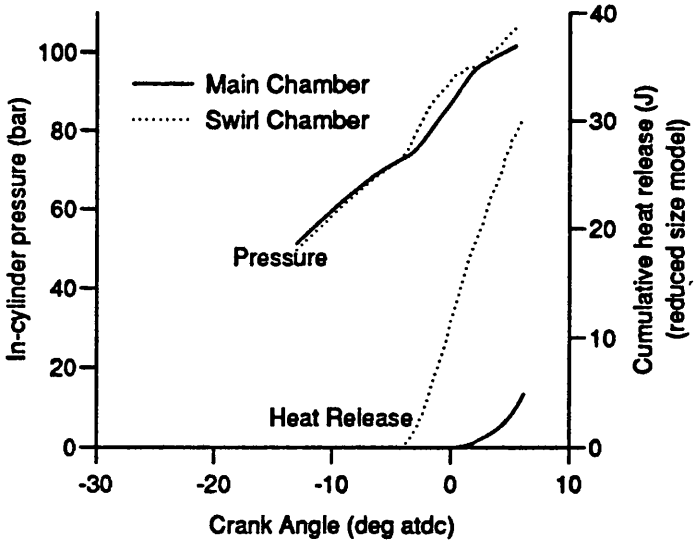

Figure 7.5
In-cylinder pressure and cumulative heat release for combustion simluation with fuel injection at 5°btdc

5°btdc, swirl chamber heat release starts within a few degrees crank angle, and main chamber heat release, shortly after top dead centre. Pressure rises immediately in

both chambers. The numerical solver, which was not designed for engine combustion, became unstable at 7°atdc. For the low A/F ratio employed (50:1), there is sufficient oxygen in the swirl chamber for complete combustion. However, as the pressure rises in the swirl chamber following ignition, fuel rich gases are forced into the main chamber. From the fuel and oxygen concentration plots (Figures 7.3 and 7.4) it is clear that fuel is being forced in the main chamber, before the oxygen in the upper half of the swirl chamber has been burnt. As the cycle continues, and the swirling motion decays, this oxygen will remain unburnt. This suggests that one effect of increasing the level of swirl in the chamber is to increase the proportion of oxygen that can be utilised by the combustion process.

Figure 7.6 shows in-cylinder pressure and heat release for a case where ignition starts at 12°btdc, but combustion is artificially inhibited *until top dead centre.* By top dead centre, the fuel has been distributed through most of the chamber, with the exception of the upper right quadrant (if the average swirl ratio in the period is 15, then it would be expected that over 12° crankshaft rotation, then the fuel vapour from the first fuel droplets injected would travel 12x15=180°). Following ignition, the swirl chamber pressure rise forces a large proportion of the fuel near the throat into the main chamber, and heat release is equally divided between the two chambers. The late pressure increase leads to the constant pressure combustion shown in Figure 7.6.

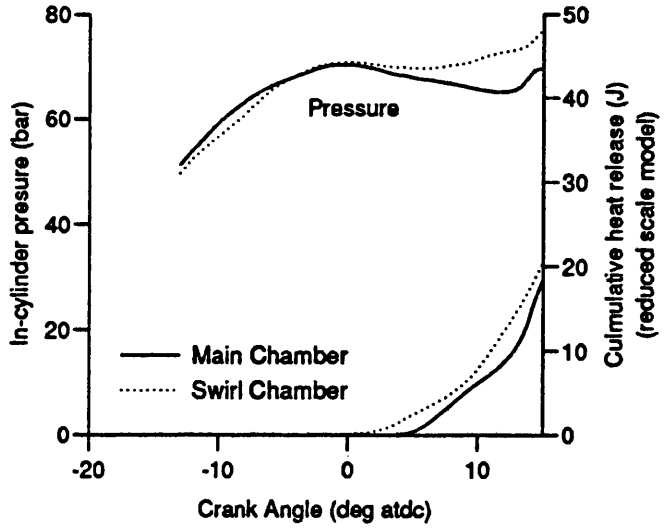

Figure 7.6
In-cylinder pressure and culmulative heat release for combustion simulation with early injection, and combustion inhibited until tdc

Figure 7.7 plots swirl ratio over the injection and combustion stage in the cycle, for the late combustion case (Figure 7.7). The effect of density change over the chamber, which is now significant, is included in the calculation. Following the point of peak compression generated swirl at around 15°btdc, swirl is further increased due to the additional momentum of the injected fuel droplets. The lower of the two lines after tdc represents the swirl ratio without combustion, the higher line, swirl ratio with combustion. Combustion slightly reduces the rate of decay of the swirling motion, but the overall swirling structure of the flow is unchanged.

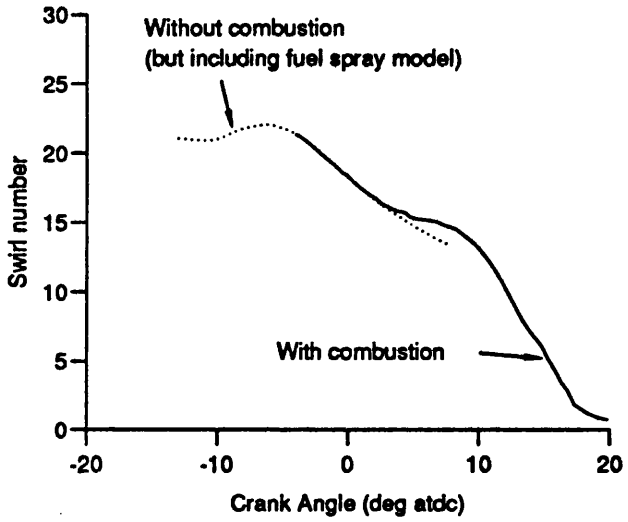

Figure 7.7
Effect of combustion on swirl number

Figure 7.1
Droplet traverse at 9°btdc, following injection at 12°btdc. Each droplet represents a sample of 'real' droplets.

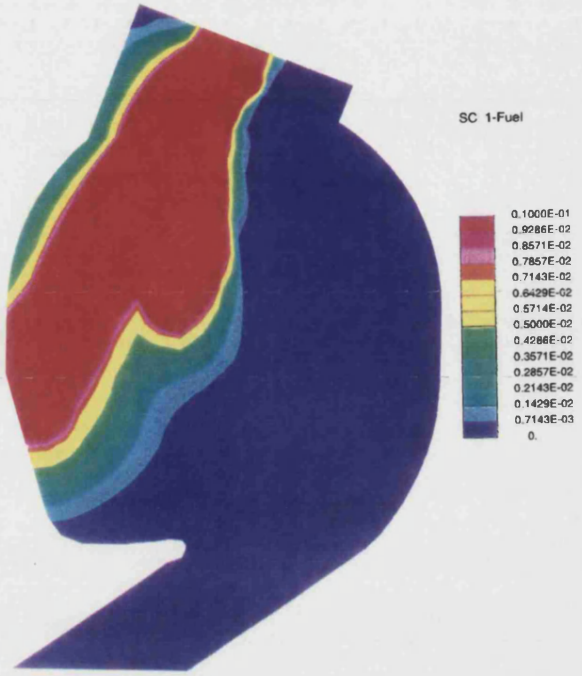

Figure 7.2
Fuel concentration field at 9°btdc following injection at 12°btdc.

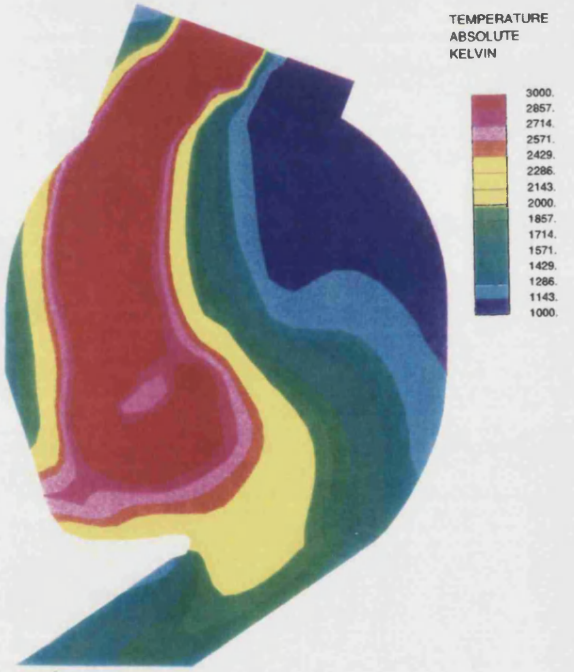

Figure 7.3
Temperature distribution in swirl chamber at 3.7°atdc, following injection at 5°btdc

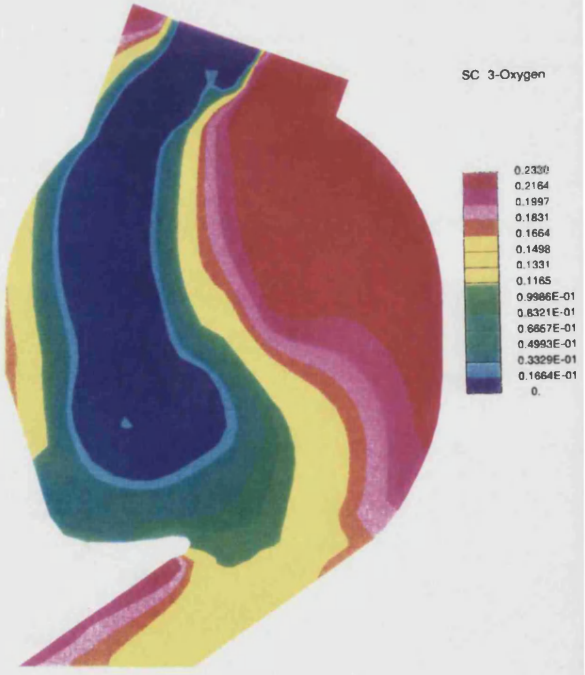

Figure 7.4
Oxygen concentration in swirl chamber at 3.7°atdc following fuel injection at 5°btdc

3.3 Discussion

The combustion results presented above are simple representations of highly complex phenomena. The simulations used coarse 2 dimensional meshes, crude representations of the fuel sprays, and simple ignition and combustion models. Real engine combustion is a three-dimensional process, and the mechanisms of ignition and combustion cannot be simulated by one or two equations. The results from this study however show that even the limited combustion simulation undertaken does provide further information about the mechanics of combustion. Even at a simple level, combustion simulation is computationally intensive, requiring very small time steps to capture the fast developing flow, and intensive computation within the time step to resolve the coupling between fuel sprays, evaporation and combustion.

One aspect of multi-dimensional combustion modelling which appears often overlooked, is the need, not only for realistic combustion models, but accurate predictions of the underlying air motion. Fuel vapour distribution is directly dependent on the velocity of the bulk air motion, and the Magnussen combustion model -the dominating rate equation for diesel combustion- assumes the rate of combustion is directly proportional to the (k/ε) value predicted by the turbulence model. Previous Chapters have demonstrated that both velocity and turbulence are dependent on the underlying mesh and numerical differencing schemes. Turbulence levels are also known to vary according to the turbulence model employed for the simulation. For any given model, it will always be possible to select coefficients for the combustion models that enable heat release rate to be matched to experimentally derived data. This tuning process however needs to be undertaken for each new engine speed and load simulated, and hence removes the *predictive* capability of the model. Accurate, predictive models of the detailed mechanism of combustion, as necessary for NOx predictions for instance, require solutions which are mesh independent, and reliable turbulence models.

4 Summary

1. Models for simulating multi-dimensional diesel combustion are available. These models are derived from experimental data, and must be 'tuned' to a particular application by appropriate selection of coefficients.
2. Full modelling of diesel combustion requires sub-models for fuel injection and evaporation, ignition and combustion. Further models would be required to predict exhaust product formation.
3. A simple model of diesel combustion has been formulated using a combination of an Arrhenius rate equation and the Magnussen combustion model. This study suggests that high swirl levels are needed to promote full air utilisation in the swirl chamber.

CHAPTER EIGHT

DISCUSSION, RECOMMENDATIONS FOR FUTURE WORK, & CONCLUSIONS

1 Introduction VIII-2

2 Experimental Study VIII-2

3 Numerical Modelling of IDI engine air flow VIII-3
- 3.1 Air flow in the IDI diesel engine VIII-4
- 3.2 Using numerical modelling for in-cylinder flow predictions VIII-5

4 Experimental validation of numerical modelling VIII-8

5 Recommendations for future work VIII-10
- 5.1 Experimental VIII-10
- 5.2 Experimental / Computational Interaction VIII-11
- 5.3 Flow modelling VIII-11

6 Conclusions VIII-15

1 Introduction

Previous Chapters of this thesis have presented results from an experimental and computational study of air motion in the IDI diesel engine. In this Chapter, the results and the conclusions from each of the Chapters are brought together and summarised, to give an overview of the study as a whole. At the end of the Chapter, possibilities for future work in the field are discussed.

2 Experimental Study

In Chapter 3, experimental measurements of in-cylinder pressure and single component, point measurements of swirl chamber velocity measured by LDA were presented. Measurement of in-cylinder pressure variation by piezo-electric transducers is an established experimental technique. To improve and add to the information provided by the piezo-electric transducers, a more precise piezo-resistive transducer was placed at the bottom of the main chamber. Shielded from the high temperature and pressure of the compression cycle by the piston, this transducer provided an absolute measurement of main chamber pressure at the beginning of the compression stroke, and the end of the expansion stroke. With the signal from the piezo-resistive transducer the high pressure measurements, which tend to drift and for which 'zero' calibration during the cycle is not possible, could be fixed at the beginning of each cycle. The absolute pressure measurement at the beginning of the compression stroke also confirmed the important initial boundary conditions for the numerical model.

The restriction on the low speed torque developed by the electric motor limited the maximum engine speed to 1500rpm. Various techniques for 'decompressing' the engine were examined, but proved either to be ineffective (eg. spraying the pulleys with oil to allow the belts to slip) or were considered unsuitable (eg simply removing a fuel injector). The most satisfactory way of increasing the engine speed would be the acquisition of a frequency control ac power supply unit, which would also allow variable speed control of the engine. With the engine running at its maximum speed (1500rpm), the pressure drop across the swirl chamber

throat (≈ 1 bar) was too small to be measured reliably. The results at 920 and 1470rpm in Figures 3.8 and 3.9 however, show the trend of increasing pressure difference with increasing engine speed. At higher engine speeds, or if in-cylinder pressure during a firing cycle were measured, the difference between the main and swirl chamber would become more statistically significant.

The ability to run the engine at ultra-low speeds (eg 100rpm) would allow the reasons for the low LDA data rates to be investigated. If the lack of data over the high velocity region of the cycle is due to seeding particles being unable to follow the bulk air flow at 920rpm, then as the engine speed is reduced, the centrifugal forces acting on the particles will decrease, and it will be possible to measure velocity over the whole cycle.

3 Numerical Modelling of IDI engine air flow

The process of formulating a numerical model of IDI diesel engine air flow was presented in Chapter 4. In Chapter 5, the factors which affect the accuracy of the solution were discussed and techniques for validating the model presented. In Chapter 6, the numerical model was used to investigate the effect of design changes on the engine. The results from the numerical model were compared with data taken from engine performance testing.

The numerical modelling process can be split into a number of main phases. Mesh generation is the process of creating the mathematical representation of the geometry. Mesh generation is time consuming - the models used for this study (Appendix B Figure B1) would take one to two weeks to generate from technical drawings. Once a basic model has been created however, changes to the geometry can often be made relatively quickly. During this pre-processing stage, appropriate boundary conditions must be defined. In constructing the computational mesh, attention must be given to the size of the model that is being built. This is discussed below.

The next stage in the modelling process is determining the information required from the solution. Storing each variable at each time step is not a realistic option for complex transient in-cylinder flows, so the data must be filtered and

selected. *Run time* post-processing - where post-processing steps are performed during the solution phase (for instance averaging of main and swirl chamber pressures at each time step) proved to be an effective technique for greatly reducing the computer storage requirements. Calculations for other parameters (such as swirl number) could also be made during the run, but unless it is known that no further post-processing will be required, this approach is too restrictive. Storing a selected sub-set of data allows the later calculation of further parameters (for instance re-calculation of swirl number about another point) without re-running the main solution. After the main solution phase, the stored data are processed and analysed. Although vector and contour plots are useful for showing a snapshot of the flow, they are limited as to the extent they can show time varying and three-dimensional trends. For in-cylinder analyses, plotting parameters against crank angle provides the most information about the developing flow.

3.1 Air flow in the IDI diesel engine

The modelling of the pre-combustion air flow in the Indirect Injection diesel engine has allowed parameters to be calculated that would be very difficult or impossible to measure using current experimental techniques. Previous experimental studies of swirl chamber air flow have either involved intrusive techniques, or required a significantly modified geometry. Numerical modelling has been shown to be a successful technique for predicting the differences in air flow between similar designs.

The model has been used to

- confirm that swirl number is independent of speed over the engine speed range studied
- predict the variation of throat discharge coefficient through the compression stroke (useful for zero-dimensional studies)
- predict the variation of pumping losses with throat area
- model the effect on swirl and turbulence of moving or removing the glow plug
- investigate the form of the swirling flow within the engine
- calculate spatially averaged heat transfer coefficients in the swirl chamber

3.2 Using numerical modelling for in-cylinder flow predictions

The primary aim of using numerical techniques for modelling in-cylinder flow is as a method of determining the processes occurring within the engine. The accuracy of the modelling is determined by a number of factors: the computational mesh, numerical differencing scheme, boundary conditions. For each of these factors, the extent to which they affect the solution is important.

Mesh Dependency

In Chapter 5, the effect of changing mesh density on the flow predictions was investigated. It was found that starting from a mesh (itself finer than that used by many other researchers), the predicted velocities could be significantly increased by increasing the mesh density (number of cells in the mesh). For a mesh with any given cell size, the *relative* trends obtained by changing engine speed, boundary conditions, glow plug position are the same. However, the *absolute* value of the results does vary with mesh density. When undertaking a multi-dimensional investigation of in-cylinder flow, it is important to realise that the solution *may* be mesh dependent and where possible for this dependency to be quantified by increasing the number of cells in the mesh and noting any change in the solution. If three or more cases of varying mesh density can be investigated, it may be possible to extrapolate the results to indicate how close the results are to a mesh independent solution. Reducing the cell size over the whole flow domain is often unnecessary. In regions where the flow is relatively uniform, a coarse mesh may be acceptable, and attention should be given to refining the meshing in regions of sharp velocity gradients. The requirement for coherent, continuous meshes may make this process difficult. In the IDI diesel engine case for which results are presented in this thesis, the critical areas of the flow are the swirl chamber and connecting passage. In the mesh dependency tests presented in Chapter 5, the swirl chamber and throat mesh has been refined to a much greater extent than the main chamber.

Differencing scheme

The choice of numerical differencing scheme influences the solution. The results presented in Chapter 5 suggest that for a given mesh density, a central differencing scheme is more accurate than an upwind scheme, and that mesh independency can be achieved with a coarser mesh. Providing stable solutions can be obtained with a central differencing scheme, switching to this higher order scheme is probably a more effective technique for increasing the accuracy of the results than reducing the average mesh cell size.

If it is accepted that for realistic in-cylinder geometries, mesh independent solutions are beyond current computing capabilities, great care must be paid to investigations that attempt to model design changes, especially where the design changes have a small effect on the overall flow pattern: Having changed the geometry, it is not then known whether the observed change in the solution, (which should correspond to the change in geometry), is the direct result of this design change, or related to the change in the mesh structure. This uncertainty can be reduced by maintaining, as far as possible, the commonality between the two cases. Thus when the effect on engine swirl of removing the glow plug was investigated (Chapter 6), the computational mesh was only changed in the immediate area of the glow plug. The same underlying mesh structure (see Appendix B, Figure 2) was used for both cases - the mesh remaining identical in the main chamber and throat - the only modifications being made in the immediate area of the glow plug. It was shown in Chapter 5 that increasing the computational mesh density increased both flow velocities and turbulence. The two are related: the higher flow velocities create larger shear layers that lead to higher turbulence. If a design change increases flow velocity without increasing turbulence (or vice versa), it is likely that the effect is physical rather than due to a change of mesh structure. If however both flow velocity and turbulence increase or decrease, and mesh density sensitivity tests show that slight changes to mesh density can lead to changes in the solution of the same order of magnitude as that observed, then a finer mesh is required to resolve accurately the flow in the two cases. Using an experimental analogy, the change in the solution can be imagined to be lying within the experimental error bars.

The modelling of turbulence has not been assessed in this study. For all the numerical simulations the k-ε turbulence model has been used. This model is known not to model recirculating and separating flows correctly, but is used in the absence of a better alternative. Gosman however [72], notes that some of the criticisms of the k-ε model may actually have arisen from numerical errors (such as mesh dependency), and such models may be *better* than is generally thought.

Boundary conditions

The in-cylinder flow processes are a small, but important, part of the IC engine cycle. Air enters the cylinder through manifolds and valves that may heat the intake charge, and mix the fresh intake with exhaust products remaining from the previous cycle. During the compression and expansion strokes, convective heat transfer to the walls and the coolant reduces the charge temperature. Some charge is lost past the piston to the crankcase. Boundary conditions must be specified to represent the interface between the flow model and the rest of the engine. In specifying the initial and boundary conditions, decisions must be taken about the relative importance of each. If an important boundary condition (such as wall heat transfer) is omitted (adiabatic conditions assumed), then the solution obtained - however 'correct' it appears - will not be complete. Other conditions (such as initial turbulence) have little effect on the overall solution, and are better omitted completely than given an otherwise arbitrary value (the turbulence generation in the throat swamps any intake induced turbulence). Specifying accurate initial and boundary conditions is often not possible, the values specified must however be considered when examining the results obtained. In this study the major boundary conditions for which accurate data were unavailable were wall heat fluxes and piston blow-by. Wall heat transfer was estimated by specifying a uniform and constant wall temperature - the solver calculating the appropriate heat transfer coefficients based on the local gas velocity. Piston blow-by was not modelled, and this probably accounts for the over prediction of in-cylinder pressure.

4 Experimental validation of numerical modelling

It is clear that the ability of numerical modelling to predict engine air flow and combustion is a valuable tool in engine design. The sensitivity of the solution to the parameters discussed above however indicates the need for validation of the predicted solutions.

In most realistic flow cases, it is not possible to use a mesh independent model. If good agreement between predicted and experimental results is obtained from a coarse mesh, then it is known that the concordance will be lost if a 'more accurate' solution from a finer mesh is calculated. In general, if the experimental measurements are correct, then where mesh dependent solutions are obtained, it would be expected that the velocities predicted by the numerical solution would be lower than those measured experimentally.

Pressure validation

In a firing engine, peak in-cylinder pressure is an important parameter for defining allowable stresses in the engine block and head. From the pressure trace, the rate of heat release and mean effective pressure (mep) can be calculated. When applied to motored engine simulation, engine pressure has less importance in its own right. It is however necessary for the model to predict pressure accurately as it forms one part of the overall modelling process: if the in-cylinder pressure is not correct, it is less likely that the predicted velocities and turbulence will be correct.

The validity of pressure predictions must be calculated on two levels. Firstly the solver is required to predict the in-cylinder pressure of an adiabatic, reversible compression - expansion process. Figure 5.1 and 5.2 show that the agreement between the theoretical and the predicted solutions is high - although a direct comparison is not possible because of the different pressures in the main and swirl chamber. Having established that global pressure calculations are correct, two further validity checks are required. Firstly does the solution predict the correct overall peak pressure? Secondly, is the pressure distribution - in this case the pressure drop across the throat - correct? Results presented in Chapter 5 showed that the peak cylinder

pressure was a function of the boundary conditions - wall heat transfer having the greatest effect. With the most realistic boundary conditions, the peak predicted pressure was higher than that measured experimentally. This is likely to be due to the lack of *blowby* boundary condition. Blowby varies from engine to engine and cylinder to cylinder - depending on the state of the piston rings, bore and engine lubrication, and is difficult both to measure and model.

Pressure distribution over the cylinder is predicted by the flow model with a high degree of resolution, but is difficult to measure experimentally. The small difference between two high, varying pressures could not be measured reliably using the two piezo-electric transducers, but the trend of increasing pressure difference with increasing engine speed was recorded by experimental measurement and numerical modelling.

Velocity validation

The low data rate obtained from the LDA study limited the comparisons between the LDA and flow model results to the low velocity region of the cycle. When compared with the corresponding flow model results, the model appears to be capable of resolving the structure of the flow, but is underpredicting the magnitude of the velocity. Further experimental data is required to determine the extent of the underprediction in the high velocity (high swirl) part of the cycle. If the seeding particles are being thrown out of the swirl flow, then it is possible that the LDA measurements are not those of the bulk air motion, but of particles with an additional radial component - ie the LDA is measuring too high a velocity.

The ability to predict accurately point air velocities is important if the modelling technique is to be fully validated. Given sufficient data however, the most useful means of comparison will be through calculation of global parameters such as swirl number, and average velocity. Such averaging will tend to reduce errors associated with individual measurements (eg incorrect positioning within the swirl chamber), and reveal the extent to which the flow modelling can be used to represent the flow field as a whole.

5 Recommendations for future work

This study of IDI diesel engine air flow and combustion has taken two relatively new and developing engine research tools, computational fluid dynamics (CFD) and laser doppler anemometry (LDA) and applied them to the complex swirl chamber flow field. The numerical model of the engine has involved formulating a geometry model, and within a general solution framework (STAR), obtaining a flow prediction. The experimental work involved modifying a standard FORD 1.8l production engine to allow optical access. The results from the experimental and computational techniques have been compared.

Both fluid modelling and the LDA have been successfully applied to the engine flow being investigated, but there is considerable potential for further development in the IDI engine and other engine applications. The principal aim of the research is to increase understanding of the processes occurring in the engine, which in turn will aid engine design and improve performance, fuel economy and reduce exhaust emissions. The numerical modelling can directly contribute to this development, while the LDA can provide vital validation data for the engine modelling process and additionally for sub-model (eg turbulence) validation. The potential for further work in each of these areas will now be examined in detail.

5.1 Experimental

The LDA measurements taken during this study are a very small section of the potential data available from the engine. Providing the date rate over the high velocity regions of the cycle can be increased then, without changing the optical access, LDA measurements can be taken at higher engine speeds and at a greater number of points. By moving the transmitting optics, a second component of velocity can be obtained, from which the three-dimensional nature of the flow, for instance around the glow plug can be obtained. Adding a quartz window to the side of the swirl chamber is possible, but involves extensive modification to the swirl chamber (the same modification can also be made to the numerical model). Such a vertical window in the swirl chamber would allow the third (and perhaps most revealing) component of velocity (the vertical component) to be measured. As

optical access would now be independent of the fuel injector, LDA studies of gas velocity in a firing engine could also be made. Although the presence of combustion makes the task of the LDA processing system more difficult, there is no reason why successful measurements of gas velocity in a firing engine cannot be made.

5.2 Experimental / Computational Interaction

Experimental measurement of in-cylinder pressure and velocity is useful in its own right, and as a source of validation data and boundary conditions for the flow modelling. As well as providing validation of flow velocities, there is enormous potential for application of LDA for turbulence model validation. The main obstacle to accurate experimental measurement of in-cylinder turbulence is likely to be the high data rate required. Optimising the particle seeding may allow the data rate over parts of the cycle to be increased. Reducing the size of the seeding particles will permit a greater response to high frequency fluctuations in the flow, but may further reduce the data rate.

5.3 Flow modelling

1. Combustion Modelling

Having established the validity of the engine air flow model, the next stage in the modelling process is the inclusion of combustion modelling. The basic theory behind combustion modelling, and a simple example of its implementation has been presented in Chapter 7. There is a wealth of published and unpublished data available on rates of heat release, firing in-cylinder pressure and engine performance, taken from test work on a range of IDI engine geometries (eg the downstream glow plug engine). Once the structure of the spray, ignition and combustion models has been implemented and optimised, these models can be developed so that the predicted flow / pressure development matches the experimentally obtained results. Although

at one level this implies 'tuning' of constants (which tends to reduce the truly predictive capability of the model), the application will also serve to highlight the strengths and weaknesses of the various sub-models, and indicate the extent to which the sub-models are themselves valid for diesel combustion.

In Chapter 6, results were presented for air motion studies of the effect of moving the glow plug and/or changing the throat area. The resulting changes in flow field were related to the observed changes in overall engine performance, as reported in the literature. Although tentative links can be made between the cold flow field, and overall engine performance in terms of fuel consumption and exhaust formation, no direct cause and effect was established. The addition of spray and combustion modelling to the cold flow model will allow these effects to be examined in more detail. In Chapter 6, possible connections between the flow field and combustion were proposed. Combustion modelling should provide results to support or reject these relationships. In particular, the following areas could be addressed:

- Does higher levels of swirl lead to more fuel being pulled into the main chamber before ignition (increasing air utilisation in the main chamber). What affect does this have on main chamber heat release?
- How does the timing and extent (exit velocity) of the jet penetration into the main chamber affect air utilisation in the main chamber at high loads? How is this affected by throat area?
- How does the position of the glow plug affect fuel vapour distribution before ignition, and flame development after ignition?
- Could the improvement observed in the downstream glow plug case be due, not to the change in glow plug position, but to the change in angle of fuel injection?

2. Modelling DI combustion

All the results presented in this thesis have been taken from IDI or auxiliary chamber diesel engines. This reflects their current and future widespread use in passenger car diesel engines. It is likely however that within the next decade, many motor manufacturers will move to the Direct Injection (DI) diesel combustion system. The

results obtained here relating to mesh density, differencing scheme selection and boundary conditions, all apply equally to numerical models of DI. Models of DI engines have the obvious advantage that the geometry is relatively simple to generate, when compared to the IDI design. As in the IDI case, extensive test results on DI engine performance have been published for comparison and validation.

3. Automated parametric studies

In Chapter 6, the application of numerical modelling to parametric studies of engine designs was discussed. Taking the variable throat area case as an example, for each throat area, a separate mesh was generated. Full automatic mesh generation will not be available in the short term, but with advanced modellers (such as Patran 3) and command languages (eg Patran's pcl), increasingly automated mesh generation is possible. For a more involved parametric study of an engine design, a package could be envisaged which required from the user, key parameters relating to the engine design (throat area, swirl chamber diameter, bore etc.), from which information, a suitable mesh would be automatically generated.

4. The interaction of flow and finite element modelling

Finite element (FE) methods of calculating thermal and structural stresses in engine components are widely used in engine design. In the same way that the flow model requires wall temperatures as a boundary condition for the head / gas or block / gas interfaces, the finite element model requires gas temperatures and heat transfer coefficients at the interface. Just as the wall temperatures must be approximated in the flow model, the heat transfer coefficients must be approximated for the FE model. By combining flow and structural modelling, both techniques can be enhanced, with heat transfer coefficients being fed straight from the flow modelling to the FE model, and wall temperatures fed into the flow predictions. Obviously the heat transfer coefficients and wall temperatures are coupled, and ideally would be solved for simultaneously. The fundamental differences between the finite element and finite volume (flow solver) numerical techniques present code developers with difficulties in implementing full interaction. However by breaking the heat transfer surface into

regions (piston crown, throat etc.) and averaging heat transfer coefficients over these regions, data from the flow modelling could be passed relatively easily into a FE model.

6 CONCLUSIONS

1. Flow modelling

Flow modelling techniques have been applied to Indirect Injection diesel engine cold flow, based on the geometry of the Ricardo Comet Vb swirl chamber, from a small production diesel engine.

Swirl number and average air turbulence have been calculated on a range of computational meshes and with standard / higher order differencing schemes. A study of mesh dependency shows that with a higher order differencing scheme, a cell length of less than 0.1mm is required for mesh independency. Solutions obtained from realistic meshes are therefore mesh dependent.

Peak swirl (mesh length 0.7mm, higher order differencing scheme) were calculated as 29.6. The mesh dependency study suggests that the swirl and turbulence values should be increased by 10% and 50% respectively.

For the Ricardo Comet V combustion chamber (figures quoted at 3000rpm)

Peak Swirl	33 x engine speed @ 13°btdc	adjusted for mesh dependency
Peak turbulence	$250m^2/s^2$ @ 16°btdc	adjusted for mesh dependency

removing the glow plug increases peak swirl by around 16% + (10% of this value to compensate for mesh dependency)

Throat discharge coefficient	varies from 0.5 to 0.6 (Figure 4.11)
Peak heat transfer coefficient	5500 W/m^2K (Figure 5.18)

2. Experimental measurement

Laser Doppler Anemometry measurements of swirl chamber air flow have been taken over the low swirl regions of the cycle, but the data rate in high swirl regions was

insufficient to measure gas velocity. It is likely that these difficulties can be overcome, and that full cycle measurement of velocity and turbulence will be feasible.

3. Validation

In the regions where direct comparisons between LDA and flow model data are possible, the model predicts significantly lower velocities than those measured experimentally. This error is likely to be due to a combination of defects in the modelling techniques, and the problems associated with the acquisition of LDA data.

4. Swirl chamber design

Having formulated the numerical model, the technique can be used to investigate the effect of design changes on the bulk air flow. By comparing cold-flow predictions with experimentally measured overall engine performance, an attempt can be made to link design change, air motion, combustion and engine performance. A study of the expansion stroke flow field suggests that pumping losses could be decreased without a significantly affecting compression stroke swirl levels.

5. Combustion

Multi-dimensional combustion modelling is complex, and the basic theory is far from complete. Existing models of diesel combustion can be applied to the IDI engine, and allow the main stages in the combustion process to be investigated. Without accurate predictions of the underlying air motion, the combustion models will not be able to *predict* the effects of combustion accurately, although by tuning the model constants, it will be possible to match experimental heat release rates.
The model of IDI combustion suggests that

- swirl controls the rate of mixing of fuel and air in the swirl chamber
- oxygen utilisation in the swirl chamber can be increased, by increasing swirl levels

REFERENCES

1 Fortnagel M, (1990) The Mercedes-Benz diesel engine range for passenger cars and light-duty trucks as viewed from emission aspects. In Proc IMechE Conference *Automotive Power Systems - Environment and Conservation.* September 1990.

2 Watson N, Kamel M (1979) Thermodynamic Efficiency Evaluation of an Indirect Injection Diesel Engine. *SAE* paper 790039

3 Dunne J M, Greening P J (1993) European emission standards to tye year 2000. In Proc IMechE Conference *Worldwide engine emission standards and how to meet them.*

4 Horrocks R W. (1993) Light duty diesels - an update of the emissions challenge. In Proc IMechE Conference *Worldwide engine emission standards and how to meet them.*

5 Lilly L R C. ed (1984) **The Diesel engine reference book.** London Butterworth and Co Ltd

6 Stone R. (1992) **Introduction to Internal Combustion Engines.** 2nd Ed. Macmillan.

7 Alcock J F, Scott W M, (1962) Some more light on diesel combustion. *Proc. IMechE.* Automotive Division. **No 5** 1962-1963

8 Broome D, (1966) The breathing and combustion requirements of the small high-speed diesel engine. In: *Proceedings of Symposium on diesel engines - breathing and combustion,* London. Proc IMechE. 1965-66 **180**

9 Nagao F, Ikegami, et al. (1967) Air motion and combustion in a swirl chamber type engine. *Bulletin of the JSME* Vol **10** No 41

10 Nakajima K, Kaijiya S, Nagao F, (1968) An experimental investigation of the air swirl motion and combustion in the swirl chamber of diesel engines. In: *Proceedings of the XXII FISITA Congress,* 1-02, Barcelona

11 Meintjes K, Alkidas A C, (1982) An experimental and computational investigation of the flow in diesel pre-chambers. *SAE* paper 820275.

12 Nakakita K, Nagaoka M, et al. Photographic and three dimensional numerical studies of diesel soot formation process. *SAE* paper 902081

13 Tanaka Y, Sugihara K, Ueda T, (1986) Improvement of IDI diesel engine combustion through dual-throat jet swirl chamber. *SAE* paper 861184.

14 Nishida, K., Hiroyasu, H. et al. (1986) Characterization of combustion processes in the pre-chamber and main chamber of an indirect injection diesel engine by high speed photography. *SAE* Paper No. 861181.

15 Hassan H, Dent J C, (1970) The measurement of air velocity in a motored internal combustion engine using a hot wire anemometer. *Proc. IMechE.*

185 50/71.

16 Tawfig M E, Charlton S J, Prest P H, (1991) An investigation of air motion and gas temperature in a motored indirect-injection diesel engine. *Proc of IMechE Conference: Internal Combustion Engine Research* London 1991 C433/002.

17 Subramaniya S, Ganesan V, An experimental investigation of the flow characteristics in the swirl chamber of a C.I. engine. *SAE* paper 910480

18 Charlton S J, Cox A, Somerville B J, et al. (1992) An investigation of the emission characteristics of the passenger car IDI diesel engine In *Combustion in Engines: Technology, Applications and the Environment.* Proc IMechE Conference. London C448/035

19 French G R, Scott W M, (1985) Giving the IDI diesel a fresh start. *SAE* paper 850452

20 Dicksee C B. (1944) *The High speed compression ignition engine.* Blackie & Son Ltd, London.

21 Aoyama T, Mizuta J, Oshima Y, (1990) NOx reduction by injection control. *SAE* paper 900637

22 Greeves G, Wang C H T et al. Improvements to indirect injection diesel combustion. *IMechE* paper No. C41/88

23 Lawrence R J, Evans R W. The Ford 1.8l four cylinder turbocharged diesel engine for passenger car application. *SAE* paper 901716

24 Wigley G, (1987) Laser anemometry measurement techniques in internal combustion engines. *Proc. 2nd International Conference on Laser Anemometry - Advances and Applications.* Strathclyde, Paper IP3

25 Rask R B, (1978) Velocity Measurements inside the cylinder of a motored internal combustion engine. In *Proc International Conference Workshop Laser Velocimetry.* July 1979 251-260

26 Wigley G, Patterson A C, Renshaw J, (1981) Swirl velocity measurements in a firing production diesel engine by laser anemometry. *ASME* Fluid Mechanics of Combustion Systems 1981 29-39

27 zur Loye A O, Siebers D L, et al. Cycle-resolved LDV measurements in a motored diesel engine and comparison with k-ε model predictions. *SAE* paper 900618

28 Fu H, Watkins A P, Tindal M J, Yianneskis M. (1991) Turbulent dividing flow in a branched duct. In *Proc of the fourth International Conference on Laser Anemometry - Advances and Applications.* August 1991. Clevland, Ohio.

29 Arcoumanis C (1991) In-cylinder flow measurements in motored internal combustion engines. In *Internal combustion engine research.* Proc IMechE Conference. London 1991. Paper No. C433/060

30 Kamimoto T, Yagita M, et al. (1988) An experimental study of in-cylinder air flow with a transparent cylinder engine. *JSME International Journal.* Series II, Vol **31**, No 1

31 Wigley G, Renshaw J. (1979) In-cylinder swirl measurement by laser anemometry in a production diesel engine. *AERE* - R 9651 (through Wigley, Patterson et al).

32 Arcoumanis C, Bicen A F, Whitelaw J H, (1982) Effect of inlet parameters on the flow characteristics in a four-stroke model engine. *SAE* paper 820750

33 Kamimoto T, Yagita M, et al. (1988) An experimental study of in-cylinder air flow with a transparent cylinder engine. *JSME International Journal.* Series II, Vol **31**, No 1

34 Arcoumanis C, Whitelaw J H, (1991) Measurements of the flow in a Hydra direct injection diesel engine. In *Internal combustion engine research.* Proc IMechE Conference. London 1991. Paper No. C433/019

35 Arcoumanis C (1991) In-cylinder flow measurements in motored internal combustion engines. In *Internal combustion engine research.* Proc IMechE Conference. London 1991. Paper No. C433/060

36 Zimmerman D R, (1983) Laser anemometer measurements of the air motion in the pre-chamber of an automotive diesel engine. *SAE* paper No. 830452.

37 Alcock, J. F. (1934) Air swirl in oil engines. *Proc. IMechE.* **128.**

38 Pinchon Ph, (1989) Three dimensional modelling of combustion in a pre-chamber diesel engine, *SAE* paper 890666

39 Kouremenos D A, Rakopoulos C D, Hountalas D. (1988) Thermodynamic Analysis of a Divided Combustion Chamber Diesel engine. *Forschung im Ingenieurwesen.* **54** No 3.

40 Kourememos D A, Rakopoulos C D, Hountalas D (1989). Themodynamic analysis of indirect injection diesel engines by two-zone modelling of combustion. *Trans ASME J Eng for Gas Turbines and Power* through (41)

41 Kouremenos D A, Rakopoulos C D, Hountalas D. (1990) A digital simulation of the exhaust nitric oxide and soot formation histories in the combustion chambers of a swirl chamber diesel engine. *Forschung im Ingenieurwesen.* **56** No 1.

42 Ahamidi-Befrui B, Gosman A D, Lockwood F C, Watkins A P, (1981) Multi-dimensional calculation of combustion in an idealised homogeneous charge engine: A progress report. *SAE* paper 810151.

43 Gosman A D, Harvey P S, (1982) Computer Analysis of fuel-air mixing and combustion in an axisymmetric D.I. Diesel engine, *SAE* paper 820036.

44 Cloutman L D, Dukowicz J K, et al. (1982) CONCHAS SPRAY: A computer code for reactive flows with fuel sprays. *Los Almos National Laboratory.* Report No. LA-9294-MS. (through Pinchon SAE 850186)

45 Amsden A A, Butler T D et al. (1985) KIVA - A comprehensive model for 2-d and 3-d engine simulations. *SAE* paper 850554

46 Taghavi R, (1992) CRI / TurboKIVA delivers the power of insight. Article in *Cray Channels*. CRI. Winter 1992

47 Pinchon Ph, Guillot B, (1985) Thermodynamic and flow analysis of an indirect injection diesel combustion chamber by modelling. *SAE* paper no 851686

48 Zellat M, Rolland Th, Poplow F. (1990) Three dimensional modelling of combustion and soot formation in an indirect injection diesel engine, *SAE* paper 900254

49 Gosman A D, Maroonet C J, Theodossopoulos P, (1992) Development strategies for diesel combustion simulation using the SPEED code. In *Combustion in Engines: Technology, Applications and the Environment.* Proc IMechE Conference. London C448/035

50 Boretti A A, Nebuloni P et al. (1992) Diesel engine combustion chamber design with three-dimensional flow computations. In *Combustion in Engines: Technology, Applications and the Environment.* Proc IMechE Conference. London C448/005

51 Nixon S W, (1930) The compression ignition automobile engine. *Proc I Auto E.* Volume **XXV**

52 Various. (1933) *The Modern Diesel.* 2nd Ed. Iliffe & Sons Limited, London

53 Glyde H S, Soar E N, (1936) Compression swirl oil engines. *Proc I Auto E.* Volume **XXXI**

54 Judge A. (1948) *High speed Diesel engines.* Chapman & Hall Ltd. 4th Ed.

55 Judge A. (1957) *High speed Diesel engines.* Chapman & Hall Ltd. 5th Ed.

56 Judge A. (1967) *High speed Diesel engines.* Chapman & Hall Ltd. 6th Ed.

57 Pounder C C, (1962) *Diesel engines: Principles and Practices.* George Newnes Ltd. 2nd Ed.

58 Article in *The oil engine and gas turbine.* September 1961

59 Rogers G F C and Mayhew Y R. (1980) *Engineering Thermodynamics Work and Heat Transfer.* 3rd Edition. London

60 Ealing Electro-optics Product Guide

64 Heywood J B. *Internal Combustion Engine Fundamentals.* McGraw-Hill. 1988.

65 JANAF Thermochemical tables, 2nd Ed. NSRDS-NB537. US National Bureau of Standards, 1971. (through Heywood).

66 Rogers G F C, Mayhew Y R. Thermodynamic and Transport Properties of Fluids. Blackwell.

67 Tawfig M (1991) *An investigation of air motion and heat transfer in a motored indirect injection diesel engine.* PhD thesis. University of Bath.

68 Lyn, W T. (1962) Study of burning rate and nature of combustion in diesel engines. In *Proceedings of Ninth International Symposium on Combustion* The Combustion Institute (through Heywood)

69 Halstead M P, Kirsch L J & Quinn C P. (1977) The autoignition of hydrocarbon fuels at high temperatures and pressures - fitting of a mathmatical model. *Combustion and Flame* **30**, 45 (through Gosman, Maroonet et al.)

70 Magnussen B F, Hjertager B H (1978) On mathematical modelling of turbulent combustion. 16th Symposium on combustion. *The Combustion Institute*

71 Ishiguro J, Kidoguchi Y, Ikegami M. (1988). Three-dimensional simulation of the diesel combustion process. *JSME International Journal.* Series II, **31** No 1.

72 Gosman A D, Private Communication. 31st August 1993

73 Gerhart P, (1992) **Fundamentals of Fluid Mechanics**, Addison-Wesley Publishing Company. 2nd Ed.

74 Gosman A D, Issa R I, Marquis A J. Computational Fluid Dynamics. Lecture Course given at Ford UK April 1992

75 Patankar S, (1980) **Numerical Heat Transfer and Fluid Flow**, McGraw Hill

76 Peric M, Kessler R, Comparison of Finite-Volume numerical methods with staggered and colocated grids. *Computers and Fluids* Vol 16 pp389-403

77 Schlicting, (1968) **Boundary Layer Theory**, McGraw Hill, 6th Ed

78 Shaw C T, (1992) **Using Computational Fluid Dynamics**, Prentice Hall

79 Wanik A, Schnell U, (1989) Some Remarks on the PISO and SIMPLE algorithms for steady turbulent flow problems. *Computers and Fluids* Vol 17 No 4 pp555-570

APPENDIX A
BASIC THEORY OF CFD

1 Introduction A-2

2 Formulation of the basic Navier-Stokes equations A-2

3 Formulating the discretised equations A-9
- 3.1 Diffusion A-9
- 3.2 Convection A-11
- 3.3 Upwind differencing A-12
- 3.4 Hybrid and higher order schemes A-13
- 3.5 Discretising the pressure term A-13
- 3.6 Numerical diffusion A-15
- 3.7 Temporal discretisation A-15
- 3.8 Discretisation of the complete momentum equations A-16
- 3.9 Boundary conditions and wall modelling A-17

4 Obtaining a solution A-17
- 4.1 Solving the scalar variables A-17
- 4.2 Solving for the flow A-19
- 4.3 SIMPLE A-20
- 4.4 PISO A-22
- 4.5 Implementation of SIMPLE and PISO in STAR-CD A-23

5 Turbulence modelling A-24
- 5.1 Introduction A-24
- 5.2 The k-ε model A-26
- 5.3 Further stress models A-28

1 Introduction

The engine flow predictions presented in this report have been calculated by the STAR-CD code, written by Computational Dynamics, London. STAR is one of a number of packages which offer the user a general tool for calculating many types of flow regime. Such packages represent many years of development and allow flow predictions to be made in complicated geometries and situations. Although it is sometimes possible to use a CFD package as a 'black-box', its application to complex engine flows demands an understanding of the techniques and algorithms used.

This section attempts to present the basic theory of CFD, from the fundamentals of the fluid flow, to the techniques used to solve the disecretized equations. Emphasis is placed on techniques used by STAR, and especially on issues discussed elsewhere in this report (eg differencing schemes, turbulence). No attempt is made to discuss the detail of the numerical algorithms or to present mathematically rigorous derivations and theory.

In general, one and two dimensional examples have been used to demonstrate the ideas behind three-dimensional finite volume discretisation.

2 Formulation of the basic Navier-Stokes equations

Computational Fluid Dynamics is based on finding the solution of a set of partial differential equations which govern fluid flow. These are commonly known as the Navier-Stokes equations. The main steps in the derivation of the 2-dimensional form of these equations are presented here. The details have been drawn from a number of Fluid Mechanics textbooks [73-79] which provide a more rigorous approach.

Consider a fluid particle P located at the point (x,y) in a flow described in Cartesian coordinates. From Newton's Second Law, in the x-direction (ignoring gravitational effects)

$$ma_x = \Sigma F_{Pressure} + \Sigma F_{Stresses} \tag{1}$$

With the flow described in Cartesian Coordinates, the particle's properties and velocity depend on its location and time (an Eulerian description). Thus for acceleration a, the rate of change of velocity of P is given by:

$$\begin{aligned} V_p &= V_p(x_p, y_p, t) \\ a_p &= \frac{d}{dt}(V_p) \\ &= \frac{d}{dt}(V(x_p, y_p, t)) \end{aligned} \tag{2}$$

In the x-direction

$$\begin{aligned} a_p &= \frac{\partial u_p}{\partial x_p}\left(\frac{dx_p}{dt}\right) + \frac{\partial u_p}{\partial y_p}\left(\frac{dy_p}{dt}\right) + \frac{\partial u_p}{\partial t} \\ &= u_p \frac{\partial u_p}{\partial x_p} + v_p \frac{\partial u_p}{\partial y_p} + \frac{\partial u_p}{\partial t} \end{aligned} \tag{3}$$

Similar expressions are easily derived for the y and z directions

The particle's mass is given by

$$m = \rho(\delta x)(\delta y)(\delta z) \tag{4}$$

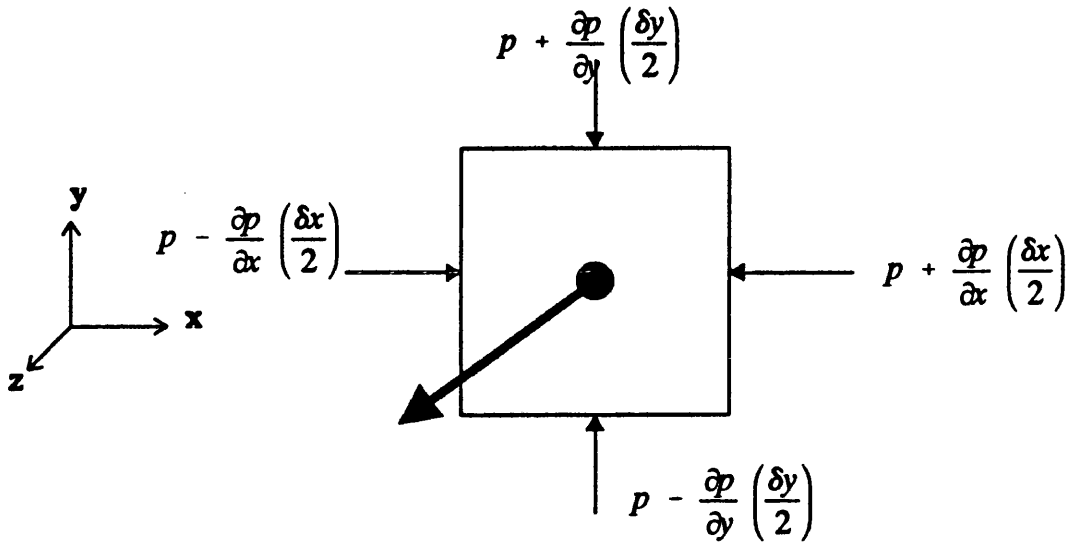

Figure A1. Pressures acting on fluid particle

Figure A1 (particle depth δz into paper) shows the pressure forces acting on the particle. The net pressure force in the x-direction is given by

$$\delta F_{x,pressure} = -\frac{\partial p}{\partial x}(\delta x)(\delta y)(\delta z) \qquad (5)$$

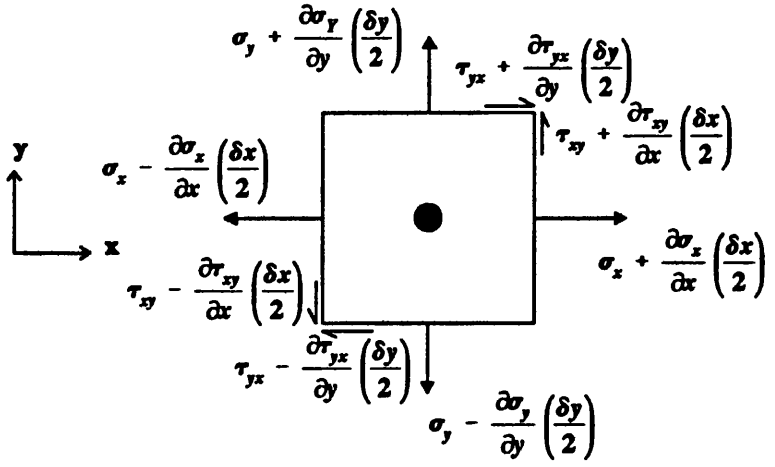

Figure A2. Stresses acting on fluid particle

Figure A2 shows the stress forces and shear stresses acting on the particle. The net stress in the x-direction is given by

$$\delta F_{x,stress} = \left(\frac{\partial \sigma_x}{\partial x} + \frac{\partial \tau_{yx}}{\partial y} \right) (\delta x)(\delta y)(\delta z) \qquad (6)$$

Substituting for the particle's mass, acceleration and forces into (1) (the 2nd Law equation), dividing by (δx)(δy)(δz), and taking the limit as the particle becomes a point, gives for the x-direction

$$\frac{\partial(\rho u)}{\partial t} + u\frac{\partial(\rho u)}{\partial x} + v\frac{\partial(\rho u)}{\partial y} = -\frac{\partial p}{\partial x} + \frac{\partial \sigma_x}{\partial x} + \frac{\partial \tau_{yx}}{\partial y} \qquad (7)$$

For the y-direction,

$$\frac{\partial(\rho v)}{\partial t} + u\frac{\partial(\rho v)}{\partial x} + v\frac{\partial(\rho v)}{\partial y} = -\frac{\partial p}{\partial x} + \frac{\partial \sigma_y}{\partial y} + \frac{\partial \tau_{xy}}{\partial x} \qquad (8)$$

These equations are known as the Cauchy equations (for two dimensional flow). The full equations for three-dimensional flow are similarly derived.
To obtain a closed set of equations, the fluid stresses must be related to the velocity field.

For an incompressible fluid[1], the stress-strain relationships for two-dimensions are

---

[1] In general for three-dimensional compressible flow, the stresses may be written as:

$$\sigma_{ij} = -p\delta_{ij} = \mu \left(\frac{\partial u_i}{\partial x_j} + \frac{\partial u_j}{\partial x_i} - \frac{2}{3}\delta_{ij}\frac{\partial u_k}{\partial x_k} \right)$$

where (i,j,k = 1,2,3)
and δ_{ij} is the Kronecker delta $\delta = 0$ when $i \neq j$ and $\delta_{ij} = 1$ for $i = j$

$$\tau_{xy} = \tau_{yx} = \mu\left(\frac{\partial u}{\partial y} + \frac{\partial v}{\partial x}\right)$$

$$\sigma_x = 2\mu\frac{\partial u}{\partial x} \tag{9}$$

$$\sigma_y = 2\mu\frac{\partial v}{\partial y}$$

Substituting these into the Cauchy equations, and assuming a constant viscosity gives

$$\rho\left(\frac{\partial u}{\partial t} + u\frac{\partial u}{\partial x} + v\frac{\partial u}{\partial y}\right) = -\frac{\partial p}{\partial x} + \mu\left(\frac{\partial^2 u}{\partial x^2} + \frac{\partial^2 u}{\partial y^2}\right) \tag{10}$$

$$\rho\left(\frac{\partial v}{\partial t} + u\frac{\partial v}{\partial x} + v\frac{\partial v}{\partial y}\right) = -\frac{\partial p}{\partial y} + \mu\left(\frac{\partial^2 v}{\partial x^2} + \frac{\partial^2 v}{\partial y^2}\right) \tag{11}$$

These are the two-dimensional Navier-Stokes equations which together with the continuity equation completely define an incompressible, constant viscosity flow.

The derivation for the three-dimensional equations is similar. The compressible form of the equations relating stress-strain to the velocity field is more complicated (footnote 1).

The three-dimensional compressible momentum equations may be written in tensor notation. For clarity, the viscous strain term is not substituted into the momentum equations.

$$\underbrace{\frac{\partial(\rho u_i)}{\partial t}}_{I} + \underbrace{\frac{\partial}{\partial x_j}(\rho u_j u_i - \tau_{ij})}_{II\quad III} = \underbrace{-\frac{\partial p}{\partial x_i}}_{IV} + \underbrace{S_{u_i}}_{V} \qquad (12)$$

$$\tau_{ij} = \mu\left(\frac{\partial u_i}{\partial x_j} + \frac{\partial u_j}{\partial x_i} - \frac{2}{3}\frac{\partial u_k}{\partial x_k}\delta_{ij}\right)$$

This set of equations will be referred to as the 'momentum equations'. The terms in the momentum equations are commonly referred to as the physical processes which they describe:

I Unsteady term (rate of change)

II Convection of fluid from one control volume to the next

III Viscous stresses

IV Pressure force

V Any source terms which affect the momentum equations (eg gravity, magnetic fields)

The three momentum equations (Eqns 12) have four unknowns: three components of velocity (u,v,w) and pressure. To obtain a solution for these variables, the continuity equation is required. In its unsteady, compressible form this is:

$$\frac{\partial \rho}{\partial t} + \frac{\partial(\rho u)}{\partial x} + \frac{\partial(\rho v)}{\partial y} + \frac{\partial(\rho w)}{\partial z} = 0 \qquad (13)$$

or in tensor notation

$$\frac{\partial \rho}{\partial t} + \frac{\partial}{\partial x_j}(\rho u_j) = 0 \qquad (14)$$

It is clear from (13) that the continuity equation does not contain a pressure term. One of the complications in solving the differential flow equations is arranging the continuity equation so that a solution may be obtained. The numerical technique

used to invoke the continuity equation differs between CFD schemes. This is discussed below in *Solving for Flow.*

Changes in pressure and density affect the fluid temperature. For a complete description of the fluid, three additional equations are required. The equation of state relates temperature to pressure and density.

$$p = \rho RT \tag{15}$$

If a process is not isothermal, an energy transport equation is required to relate heat and work (First Law of Thermodynamics), similar in general form to the momentum equations presented above.

$$\underset{I}{\frac{\partial(\rho h)}{\partial t}} + \underset{II}{\frac{\partial}{\partial x_j}(\sigma u_j h} - \underset{III}{\frac{k}{C_p}\frac{\partial h}{\partial x_j}}) = \underset{IV}{S_h} \tag{16}$$

where

I Unsteady term (rate of change of enthalpy)

II Convection of heat by the flow

III Diffusion of heat

IV Energy sources / sinks

Finally, an empirical viscosity law defines viscosity as a function of temperature $\mu(T)$.

In total there are seven equations (three momentum, continuity, energy, state, and viscosity) and seven variables (u,v,w,p,T,ρ,μ). Introducing additional variables (for instance turbulence, species concentration) generally requires the formulation of an additional transport equation in the general form of (16).

3 Formulating the discretised equations

To allow numeric computation of the partial differential equations derived above, the terms in the equations are 'discretised'. Many discretisation techniques exist, the examples listed here are intended to illustrate the basic principles behind the finite volume discretisation of the terms in the scalar and momentum transport equations. In general, one dimensional examples have been used.

3.1 Diffusion

The momentum equations (12) contain diffusion (viscous stress) terms of the basic form

$$\frac{\partial}{\partial x}\left(\Gamma\frac{\partial \phi}{\partial x}\right) = 0 \tag{17}$$

where in the momentum equation ϕ represents velocity u, but in general, any variable eg temperature, enthalpy, concentration.

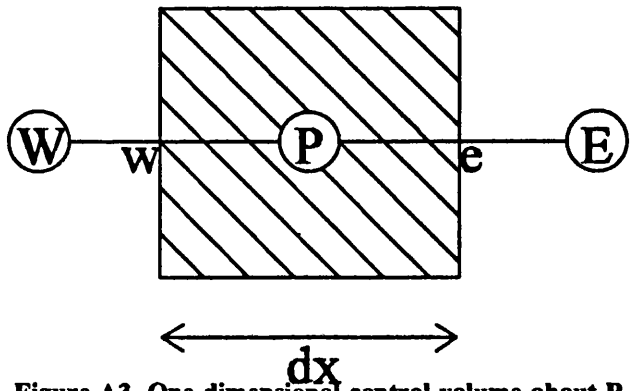

Figure A3, One dimensional control volume about P

Now integrating over the one-dimensional control volume around node P in Figure A3 gives

$$\left(\Gamma\frac{\partial \phi}{\partial x}\right)_e - \left(\Gamma\frac{\partial \phi}{\partial x}\right)_w + \int_w^e S\,dx = 0 \tag{18}$$

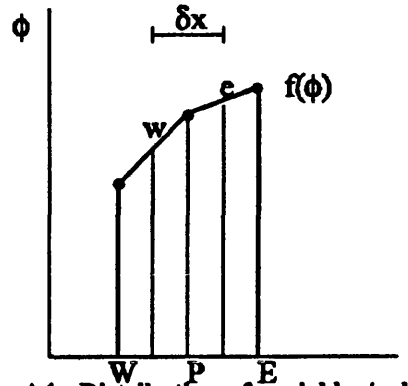

Figure A4. Distribution of variable ϕ about P

Figure A4 represents the distribution of ϕ. The gradient at (e), assuming a simple linear interpolation between E and P is:

$$\frac{\partial \Phi_e}{\partial x} = \frac{\Phi_E - \Phi_P}{\partial x} \tag{19}$$

a similar equation can be written for the gradient at (w).

Substituting the expressions for the gradient terms into (18).

$$\frac{\Gamma_E (\phi_E - \phi_P)}{(\partial x)_e} - \frac{\Gamma_W (\phi_P - \phi_W)}{(\partial x)_w} + \bar{S}\Delta x = 0 \tag{20}$$

which can be rearranged into the form

$$\begin{aligned} a_P\phi_P &= a_E\phi_E + a_W\phi_W + b \\ a_P\phi_P &= \Sigma\, a_{nb}\phi_{nb} + b \end{aligned} \tag{21}$$

where nb represents all neighbouring cells (2 in 1-d, 4 in 2-d, 6 in 3-d). In general, the discretisation of each term in Equations 17 leads to an equation of the form (21) for each cell in the mesh, with the appropriate modifications made for boundary conditions etc. The matrices formed from the equations are then solved simultaneously as discussed in a later section.

3.2 Convection

The diffusion term in the momentum equation can be combined with the convection term (term II in Equation 12), with the basic form

$$\frac{\partial}{\partial x}(\rho u\phi) = \frac{\partial}{\partial x}(\Gamma\frac{\partial \phi}{\partial x}) \tag{22}$$

Referring to Figures A3 and A4, assuming a linear profile for ϕ, and assuming that e is halfway between P and E, then the *central differencing* discretisation of the convection term gives

$$\phi_e = \frac{1}{2}(\phi_E+\phi_P) \qquad \phi_w = \frac{1}{2}(\phi_P+\phi_W) \tag{23}$$

Different interpolation factors would be necessary had the interfaces not been assumed to be midway between the nodes.
Thus integrating (22) over the control volume (Fig A4) gives

$$\frac{1}{2}(\rho u)_e(\phi_E+\phi_P) - \frac{1}{2}(\rho u)_w(\phi_P+\phi_W) = \frac{\Gamma_e(\phi_E-\phi_P)}{(\partial x)_e} - \frac{\Gamma_w(\phi_P-\phi_W)}{(\partial x)_w} \tag{24}$$

Defining symbols F for convection and D for diffusion

$$F \equiv \rho u \;;\; D \equiv \frac{\Gamma}{\partial x} \tag{25}$$

allows (25) to be reduced to the form

$$a_P\phi_P = a_E\phi_E + a_W\phi_W \tag{26}$$

where

$$a_E = D_e - \frac{F_e}{2}$$
$$a_W = D_w + \frac{F_w}{2} \qquad (27)$$
$$a_P = a_E + a_W + (F_e - F_w)$$

To satisfy continuity across the cell F_e -F_w must equal 0 (ie flux in must equal flux out of cell). Then

$$a_P = a_E + a_W \qquad (28)$$

A consequence of (26) is that if one of the coefficients a_E, or a_W is negative then given Equ 28, the value of ϕ_P could lie outside the range ϕ_E to ϕ_W. From a physical standpoint, this 'unbounded' solution is clearly impossible,[2] and can lead to the instabilities in the solution associated with central differencing formulations of the convective term discretisation. Provided that |F| is less than 2D, the coefficients will always be positive, a situation which however only applies to low Reynold's number flows

The Peclet number P_e is defined as the ratio of convection to diffusion:

$$P_e = \frac{convection}{diffusion} = \frac{\rho u l}{\tau} = \frac{F}{D}$$

The non-negative coefficient requirement may then be written as $|P_e| < 2$.

3.3 Upwind differencing

The stability restrictions of central differencing formulations of the convection terms have traditionally been overcome by use of *Upwind differencing*. The Upwind differencing scheme does not suffer from the stability restrictions of the central

---

[2] This would be equivalent to the situation where, for a given cell without energy source or sinks, temperatures of 80°C and 100°C in neighbouring cells define a cell temperature outside this range within the cell - a situation which is obviously impossible physically.

differencing scheme, but is less accurate than the central differencing scheme, especially on fine meshes. Using the same formulation for the diffusion term, the convection term is discretised as follows.

Consider two adjacent cells. In the central differencing scheme, the value of ϕ at the interface was assumed to be the average of the two adjacent cell centre values. In the upwind differencing scheme the interface value is taken to be the value at the upwind cell centre. Thus for ϕ_e in Figure A4

$$\begin{aligned} \phi_e &= \phi_P \quad \text{if } F_e > 0 \\ \phi_e &= \phi_E \quad \text{if } F_e < 0 \end{aligned} \tag{30}$$

This formulation is stable for all values of P_e.

3.4 Hybrid and higher order schemes

It can be shown (Patankar) that for $-2 < P_e < 2$, the upwind differencing scheme is a close approximation to a theoretical solution (which can be obtained if Γ is a constant). Thus a 'hybrid' scheme can be devised, with the central differencing scheme being used when $|P_e| < 2$ and the upwind scheme otherwise.

A number of higher order schemes have been devised which generally include a greater number of neighbouring cells (usually upwind) to calculate the convective fluxes at the cell. Such methods are often more accurate than Upwind or Central differences, at the expense of computational requirements. Some such higher order schemes are difficult to implement on non-cartesian meshes.

3.5 Discretising the pressure term

A method is required for discretising the $-\delta p/\delta x$ terms in the momentum equations. Using the one-dimensional case above, integrating across the control volume about P in Figure A5 (upper figure) and assuming, for simplicity, that the control-volume faces e and w are midway between cell centres gives

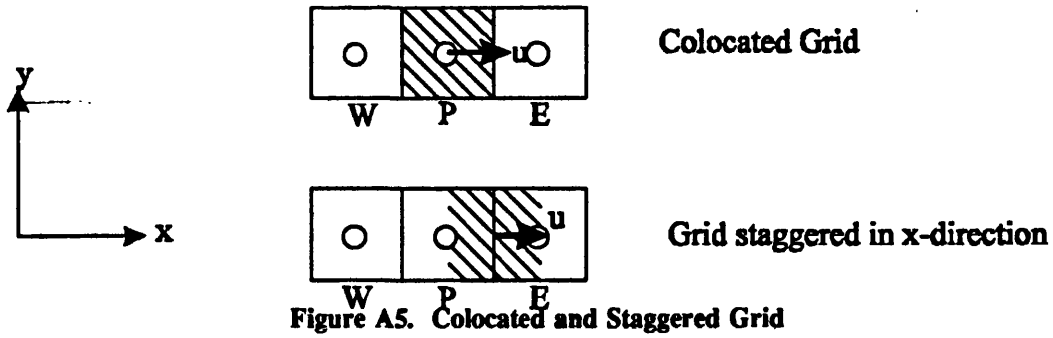

Figure A5. Colocated and Staggered Grid

$$P_w - P_e = \frac{P_E + P_P}{2} - \frac{P_P + P_E}{2} = \frac{P_W - P_E}{2} \qquad (31)$$

With this approach, where it is assumed that the pressure and velocities are stored at the same grid point (*colocated*), the contribution of the pressure term to the momentum equations will be the difference not between adjacent (E and P) cells but alternate cells (E and W). This can lead to the *checkerboard* effect where the pressure differences seen by any two adjacent cells are decoupled, leading to a 'wavy' pressure field. The traditional solution to the problem has been to use a *staggered* variable location scheme, where the velocities are stored at grid points mid-way between the pressures which drive them (eg between E and P) (Figure A5-lower).

The location of these staggered control volumes is different for each cartesian direction requiring additional sets of control volumes to be formulated. Such an arrangement is difficult to implement with unstructured or non-orthogonal grids, especially with higher order differencing schemes.

STAR-CD uses a *colocated* technique developed originally by Rhie and Chow which stores all variables at the cell centres, and uses interpolation to combine the original colocated and staggered approaches to overcome the checkerboard effect. The principal advantages of this technique are that it can easily be applied to complex geometries and that it simplifies the numerical scheme [76]. In general, either scheme (staggered or colocated grids) can be applied to any of the flow solution techniques discussed in the following sections.

3.6 Numerical diffusion

Numerical diffusion is the term given to a numerical error which leads to an effect similar to an additional diffusion term. Consider two parallel fluid streams of equal velocity, but with differing temperatures (Patankar). If the diffusion coefficient Γ is zero, then when these two streams come into contact, no mixing will occur, and the temperature discontinuity will persist along the flow streamline. When the numerical solution of this problem is attempted using the *upwind* scheme, and with the *mesh the aligned with the flow streamlines* the discontinuity is preserved. When however, a solution is obtained with the *mesh at 45° to the flow streamlines*, the upwind solution appears to *smear* the two flows, as if Γ were non-zero. This is numerical diffusion.

Numerical diffusion can be reduced by decreasing the cell size, and where possible aligning the mesh streamlines with the flow. Thus in the simulation of the swirl chamber flow, the mesh in the swirl chamber throat has been generated with the cells lying perpendicular to the throat walls. As real diffusion occurs in most flow situations, it is often acceptable to regard false diffusion as small in comparison to real diffusion. Higher order and thus blended schemes are less prone to numerical diffusion. In the IDI diesel case, the numerical diffusion (which acts as an additional 'artifical' viscosity) will tend to reduce the angular velocity of the swirling flow, calculated using the upwind differencing scheme. This leads to a lower swirl number throughout the cycle.

3.7 Temporal discretisation

Temporal discretisation refers to the techniques used to couple the numerical solutions at each time step. In an *explicit* formulation, the *new* solution is calculated as a function of the *old* flow field only (ie the old velocity, pressures are used, and coefficients calculated based on these values). A *fully-implicit* scheme calculates the *new* solution based on the (to be calculated) *new* values, leading to a set of simultaneous equations in which the only coupling between the two time steps is the unsteady term (Eq 12):

$$\frac{\partial(\rho u)}{\partial t} = \frac{(\rho u)^{new} - (\rho u)^{old}}{\delta t} \qquad (32)$$

Semi-implicit schemes combine implicit and explicit formulations. Explicit and semi-implicit schemes suffer severe time-step restrictions. STAR-CD uses a fully-implicit type formulation.

3.8 Discretisation of the complete momentum equations

Using a two-dimensional example, the x-direction Navier-Stokes equation (Eq 10) can be rearranged as

$$\frac{\partial}{\partial t}\rho u + \frac{\partial}{\partial x}\left(\rho uu - \mu\frac{\partial u}{\partial x}\right) + \frac{\partial}{\partial y}\left(\rho vu - \mu\frac{\partial u}{\partial y}\right) = -\frac{\partial P}{\partial x} + S$$

A source term has been introduced here.
In general, integrating across the control volume

$$\frac{\partial}{\partial t}\int \rho u\, dv + \int_S^N \left(\rho uu - \mu\frac{\partial u}{\partial x}\right)_W^E dy + \int_W^E \left(\rho vu - \mu\frac{\partial u}{\partial y}\right)_S^N dx - \int S dv = -\int\frac{\partial P}{\partial x}$$

Using the discretisation procedures presented above, (the coefficients depend on the geometry of the local grid and whether a staggered or colocated grid is used), this equation is reduced (using the staggered grid example for the pressure distribution,) to a 2-dimensional discretisation equation of the form:

$$a_e u_e = \Sigma\, a_{nb} u_{nb} + (P_P - P_E)A_e + b$$

where the sum is over the neighbouring cells, and the neighbour coefficients a_{nb} account for the influence of both convection and diffusion at the cell faces. In the two dimensional case. A_e is $\Delta y \times 1$.

3.9 Boundary conditions and wall modelling

The discretisation procedures outlined above must be modified to take account of boundary conditions. The main boundary conditions encountered are prescribed flow, pressure and wall. In almost all 'engine' flows, it is the *walls* that define and drive the flow. Turbulent wall flow is complicated (Schlicting) and a *Law of the Wall*, based on experimental observation is often used to reduce the computational effort. This approach divides the turbulent near wall flow into three regions. Nearest the wall, a *viscous sub-layer* exists where turbulence is effectively damped by the wall. In the next region, velocity varies as a function of the log distance from the wall. This is termed the *log-law* region. In the outer layer, the boundary layer and the core flow merge. *Law of the Wall* approaches assume that the near-wall node lies within the logarithmic transition region, thus avoiding the need for detailed near wall velocity calculations. Wall laws are not capable of accurately calculating wall heat transfer coefficients, which require specific knowledge of the flow very close to the wall.

4 Obtaining a solution

A wide range of techniques exist for obtaining a solution from the discretised transport equations. It is usual to split the procedure into two sections. Firstly, given a flow field (velocity and pressure), how are the transport equations for scalars such as temperature and concentration solved? Secondly, how is a flow field calculated that satisfies the momentum and continuity equations? As the techniques used to calculate scalars are also used in the flow calculation, this will be considered first.

4.1 Solving the scalar variables

The discretisation procedures described above present the basic principles behind the discretisation of the terms in the momentum equations (Eq 12). Similar techniques may be used to discretise the scalar equations (eg Eq 16 for energy). This leads to an equation set of the form

$$a_p^n \Phi_p^n = \Sigma a_j^n \Phi_j^n + \textit{Source terms}$$

where subscript $_p$ refers to the cell for which the equations are being formulated, superscript^n refers to the *new* value of the variable, and the summation is over the neighbours (generally j = 1 to 6 for a simple 3-d differencing scheme) of the cell. This form of the equation implies an *implicit* solution (the unsteady term is embedded in the coefficients). An *explicit* formulation would calculate the new values (left hand side) based only on old values (right hand side).

A technique is required to solve the set of (implicit) equations simultaneously.

Direct

The solution is obtained in one pass, by operating directly on all elements in the matrix. Typical techniques (Gosman) are matrix decomposition, Gaussian elimination and matrix inversion. Although this method has traditionally been used by finite element codes it has a number of disadvantages for CFD: The matrices are generally sparse, and the above methods introduce non-zero elements where previously only zero elements existed. The additional memory requirements are large compared with the memory needed to store the original matrix and the time to reach a solution varies as the cube of the number of unknowns.

Iterative

Most CFD schemes use iterative methods to solve the matrices. Techniques such as *Gauss-Seidel, Point Successive Over-relaxation* (PSOR) can be used on all matrices and generally are effective on coarse meshes. As mesh refinement increases, the time for solution increases rapidly. *Line Iteration Procedures* (LIP) find the direct solution along a line (or plane) of the matrix. LIP are faster than PSOR methods, but are restricted to regular banded matrices (and hence structured meshes). More advanced solution techniques include Stone's Strongly Implicit Procedure (SSIP) which again is restricted to banded matrices and *Preconditioned Conjugate Gradient* (CG) methods and their derivatives. Extensive research has been directed at CG methods as they can handle any (sparse) matrix and give superior performance to

SSIP and other methods. When selecting a matrix solver, the degree to which the technique can be vectorised, to run on machines such as CRAY, CONVEX may also be considered. CG vectorises better than SSIP. STAR-CD uses a pre-conditioned Conjugate Gradient scheme with different versions for vector and non-vector machines.

4.2 Solving for the flow

It is generally the algorithms that are used to calculate the velocity and pressure fields that distinguish different CFD methods. This section presents an overview of some of the schemes that have been developed. The SIMPLE and PISO schemes which form the basis of the STAR-CD code are discussed in greater detail.

Obtaining the flow field involves finding a solution to the three momentum equations which satisfy the continuity equation. The four coupled equations (three momentum and continuity) are explicitly non-linear as the convection terms are themselves functions of the fluid acceleration, and implicitly non-linear as many of the constants are functions of the evolving velocity solution (eg $\mu_{eff} = f\{\delta U/\delta x\}$).

It is usual to select pressure / velocity as the two dependent variables used to calculate the flow. Other approaches use density / velocity (restricted to compressible flow) or vector / vorticity sets (restricted to constant density flows). When using the pressure / velocity dependent variable set, the main difficulty in obtaining the velocity field is calculating the pressure field. The pressure term in the momentum equations (12) effectively forms a source term, ie pressure differences drive the flow, and given the pressure field, the velocity field can be easily obtained (using the techniques outlined above). There is however no obvious method to obtain the pressure field. When the correct pressure is substituted into the momentum equations, the resulting velocity field satisfies continuity, but without solving all four equations simultaneously (a direct solution) this feature cannot be used to obtain the pressure field. Different algorithms use different approaches to invoke the continuity equation in the solution of the flow field.

Obtaining a solution

Unsteady flows can, in general, be solved using either explicit, partly-implicit, or fully-implicit algorithms. Steady state flows are inherently implicit, but can be calculated as time-marching unsteady flows. Given that the pressure and velocity fields are coupled, a fully-implicit solution now implies coupling between both nodes (for a given variable) and variables (eg pressure and velocity). Gosman breaks the major solution algorithms into the following categories

Fully explicit schemes, where variables at the new time step are calculated directly from those of the previous time step. Explicit schemes suffer from severe time step restrictions and are only really useful for calculations in quickly evolving flows (eg shocks).

Semi-implicit schemes have less severe time step restrictions, but are still expensive because of the small time step required. Examples include the Marker and Cell method (MAC), ICE and the widely used ICED-ALE method.

Fully-implicit schemes have no restriction on δt in theory, but in practice are limited by the non-linear two way coupling. The schemes may be broken into two broad types: Iterative and Non-iterative. These terms are misleading, as they refer to the overall scheme for calculating the velocity / pressure field, and not the methods for calculating a particular variable within the time step. For any given time step *iterative* schemes cycle through improving pressure/velocity fields until the solution is reached, *non-iterative* schemes find the solution directly, although this will often involve the use of iteration to solve a particular implicit equations set.

Many iterative schemes are based on the *SIMPLE* algorithm (discussed below) developed at Imperial College, London. Block iteration schemes (eg *X VANKA*) may also be grouped in the iterative category. Non-iterative schemes dispense with high-level iteration (generally repeated calculation of pressure and flow fields at each time step). *PISO* (see below) uses a single predictor stage, and a number of corrector stages. Other non-iterative techniques include Block factored methods (eg *Briley-MacDonald, Beam & Warming, MacCormack methods*).

4.3 SIMPLE

In the *Formulation of the Navier-Stokes Equations* section above, an implicit discretisation equation was obtained for the momentum equations

$$a_e u_e = \Sigma a_{nb} u_{nb} + (P_P - P_E) A_e + b \qquad \text{I}$$

Predictor Step

The basis of the SIMPLE algorithm (Patankar) uses the concept of pressure and velocity corrections to iterate to a solution. Starting with the existing (or a guessed pressure field) p^{n*} (generally that from the previous iteration), a new velocity field u^* (which usually does not satisfy continuity) can be calculated directly from the momentum equations. Thus for the x-direction

$$a_e u_e^* = \sum a_{nb} u_{nb}^* + (P_P^{n*} - P_E^{n*}) A_e + S_u \qquad \text{II}$$

where the starred velocities represent the solution based on the guessed pressure field.

Corrector Step

The final velocity set u^{**}, and pressure field p^{**} must be determined by invoking the continuity equation.
The momentum equations are written as

$$a_e u_e^{**} = \sum a_{nb} u_{nb}^* + (P_P^{**} - P_E^{**}) A_e + S_u \qquad \text{III}$$

where u^{**} is now an explicit equation (ie based on u^* and not u^{**} - hence the method is only semi-implicit) and subtracted from II to give IV

$$a_e (u_e^{**} - u_e^*) = (p_P' - p_E') A_e + b \qquad \text{IV}$$

where the pressure corrector p' is given by

$$p' = p^{**} - p^* \qquad \text{V}$$

Thus expressions for the new velocities u^{**}, in terms of the pressure corrector p' can be written

$$u_e^{**} = u_e^{*} + d_e(p_P' - p_E') \qquad \text{VI}$$

where

$$d = \frac{A_e}{a_e} \qquad \text{VII}$$

Now integrating the continuity equation across the control volume around P (see Figure A3)

$$\frac{(\rho_P - \rho_P^{OLD})A}{\delta t} + (\rho u^{**}A)_e - (\rho u^{**}A)_w = 0 \qquad \text{VIII}$$

Substituting for the new velocities (Eq VI), allows a pressure correction equation to be derived, of the form

$$a_P p_P' = \sum a_{nb} p_{nb}' + b \qquad \text{IX}$$

where the 'source' term is the left hand side of the negative of Eq VIII, evaluated in terms of u^{*}.

Thus an improved pressure field P^{**} can be calculated from Eq IX and these values substituted into the velocity correction formulae to calculate a new continuity satisfying velocity field u^{**}. At this stage any further scalars can be calculated (temperature, turbulence). The complete process is repeated until convergence is reached.

4.4 PISO

Piso may be regarded as an extension of the SIMPLE algorithm outlined above (Wanik). At the end of the corrector stage, a pressure field p^{**}, and a velocity field u^{**} have been calculated. The velocity field after the first corrector stage does not

generally satisfy the momentum equations. The PISO algorithm developed by Issa, calculates a further velocity field u^{***}, and pressure field p^{***}.

Second Corrector Step

The momentum equations are now written as (VIII)

$$a_e u_e^{***} = \sum a_{nb} u_{nb}^{**} + (P_P^{***} - P_E^{***})A_e + S_u \qquad \text{X}$$

Subtracting this from III gives

$$a_e(u_e^{***} - u_e^{**}) = (p_P'' - p_E'')A_e + b \qquad \text{XI}$$

where the pressure corrector p'' is given by

$$p'' = p^{**} - p* \qquad \text{XII}$$

As in the first corrector step, expressions can now be written down for u^{***} but as a function of u^{**} and p^{*}. Substituting these values into the integrated continuity equation (VIII), a second pressure correction pressure is obtained

$$a_P p_P'' = \sum a_{nb} p_{nb}'' + b \qquad \text{XII}$$

where the source term b now contains terms in u^{*} and u^{**}.
This pressure correction equation is solved, and thus u^{***}, and p^{***} are obtained.

In the original formulation of the PISO algorithm, Issa noted that two correctors only were required. STAR performs further correctors along the same lines until a solution to the required degree of convergence is obtained.

4.5 Implementation of SIMPLE and PISO in STAR-CD

The outline of the SIMPLE and PISO above show the key features of the algorithms in one-dimension on the simplest of grids. The STAR-CD package has been

designed to solve the flow equations on unstructured three-dimensional grids. The efficient solution of the equations on a non-cartesian mesh requires extensive modifications to the algorithms as originally formulated, primarily due to additional pressure gradient terms in the momentum equations.

5 Turbulence Modelling

5.1 Introduction

One of the major areas of uncertainty in numerical predictions of flow is turbulence modelling. Turbulent flow is characterised by apparently random velocity fluctuations at a given point in the flow, and intense mixing of the fluid. When dealing with turbulent flows it is usual to define a bulk flow average velocity, onto which the turbulent fluctuations are superimposed. Much research has been undertaken into turbulence and its modelling, but the mechanisms of the phenomena are only partly understood.

Turbulence is of great importance to fluid modelling in engineering. The effect of the random flow fluctuations is to create local eddies in the flow. As these eddies possess mass, momentum and energy, local fluid mixing, shear stress and heat transfer are considerably greater than in a comparable laminar flow. Gerhart [73] gives as an example the rapid mixing of cream into coffee after stirring (a turbulent mixture) compared with the (laminar) mixing of two paints. Turbulence is of special interest in engine flow modelling as combustion processes are greatly influenced by localised mixing or turbulence. Turbulence is often said to be *random*. It is however, completely predicted by the momentum equations, provided a fine enough mesh, and small enough time step are used to resolve fully the turbulent eddies. Such a technique is known as *direct simulation* of turbulence (D.S.). The mesh and time step requirements put realistic solutions using direct simulation far beyond the capabilities of current computing resources. It may however be possible to use direct simulation of turbulence on simple flow cases to help develop and validate turbulence models.

The turbulent momentum equations can be derived as follows:

The instantaneous velocity at a point is decomposed into steady and fluctuations components. The overbar signifies a time average (or an ensemble average for an unsteady flow)

$$u = \bar{u} + u'$$
$$v = \bar{v} + v'$$
$$w = \bar{w} + w'$$

where $\bar{u}$ is the average (time or ensemble) velocity

u' is the fluctuating component of the velocity u

Now by definition the $\bar{u}' = 0$ (ie average of the fluctuating component)

Substituting these relationships into the Navier-Stokes equations, (ie for incompressible flow) and after considerable manipulation gives, for the u momentum equation:

$$\rho\left(\frac{\partial \bar{u}}{\partial t} + \frac{\partial \bar{u}}{\partial x}(\bar{u} - \mu\frac{\partial \bar{u}}{\partial x}) + \frac{\partial \bar{u}}{\partial y}(\bar{v} - \mu\frac{\partial \bar{v}}{\partial y}) + \frac{\partial \bar{u}}{\partial z}(\bar{w} - \mu\frac{\partial \bar{z}}{\partial z})\right) =$$
$$-\frac{\partial P}{\partial x} + \frac{\partial}{\partial x}\left(-\mu\overline{u'^2}\right) + \frac{\partial}{\partial y}\left(-\mu\overline{u'v'}\right) + \frac{\partial}{\partial z}\left(-\mu\overline{u'w'}\right)$$

This can be written more generally, for all three momentum equations with Cartesian tensors. Grouping the turbulent terms together gives:

$$\rho\frac{\partial \bar{u}_i}{\partial t} + \rho\frac{\partial}{\partial x_j}\left(\overline{u_j u_i} - \mu\frac{\partial \bar{u}_i}{\partial x_j}\right) = -\frac{\partial P}{\partial x_i} + \frac{\partial}{\partial x_j}(\rho\overline{u'_i u'_j}) \qquad (52)$$

When all three momentum equations are evaluated, six new terms are introduced to the momentum equations as a result of the turbulent component. The physical effect of the turbulence is to increase the apparent stress in the fluid, and the terms are

often collectively called *Reynolds Stresses*, after Reynolds who first introduced the concept of time averaged equations of motion (1895). It is these terms that turbulence models attempt to simulate.

5.2 The k-ϵ model

The 'standard k-ε' model is currently the most frequently used turbulence model. It attempts to relate turbulence to the local flow field (velocity, pressure etc), and solves scalar transport equations for turbulent kinetic energy (k) and its dissipation (ε). Modelling turbulence as an additional stress, for an incompressible flow:

$$-\rho\,\overline{u_i'u_j'} = \mu_t\left(\frac{\partial \bar{u}_i}{\partial x_j} + \frac{\partial \bar{u}_j}{\partial x_i}\right) \tag{53}$$

where μ_t = Turbulent viscosity

Thus given the flow field and an effective turbulent viscosity, an expression for the grouped Reynolds Stresses can be calculated.

Now from dimensional considerations where μ_t = f(density, velocity, a length scale)

$$\mu_t = C_\mu \rho \frac{K^2}{\epsilon} \tag{54}$$

To allow a turbulent viscosity to be calculated, transport equations (ie equations tracking the convection, diffusion, production etc) are solved for turbulent kinetic energy (k) and its dissipation (ε).

$$\rho\frac{\partial k}{\partial t} + \rho\frac{\partial \bar{u}_l k}{\partial x_l} = \frac{\partial}{\partial x_l}\left(\frac{\mu_t}{\sigma_k}\frac{\partial k}{\partial x_l}\right) + \rho(P-\epsilon) \tag{55}$$

$$\rho\frac{\partial \epsilon}{\partial t} + \rho\frac{\partial \overline{u_l}\epsilon}{\partial x_l} = \frac{\partial}{\partial x_l}\left(\frac{\mu_t}{\sigma_\epsilon}\frac{\partial \epsilon}{\partial x_l}\right) + \rho\frac{\epsilon}{k}(C_{\epsilon 1}P - C_{\epsilon 2}\epsilon) \tag{56}$$

where P is a turbulence production term based on action of shear in the fluid

$$P = \frac{\partial \overline{u_i}}{\partial x_j}\left(\frac{\partial \overline{u_i}}{\partial x_j} + \frac{\partial \overline{u_j}}{\partial x_i}\right) \tag{57}$$

C_μ, $C_{\epsilon 1}$, $C_{\epsilon 2}$, σ_k, σ_ϵ are constants. Originally determined by Launder and Spalding (1975) from experimental data, a number of researchers have varied the values for particular classes of flows. The formulation presented here calculates the Reynolds stresses used in the momentum equations. A similar method is used to determine the turbulence terms for the time-averaged (ensemble-averaged) scalar transport equations (eg temperature). The equations listed above must be modified slightly to deal with compressible flows. As with the general flow, assumptions are made for the near wall behaviour of k and ε according to *Law of the Wall* functions.

The transport equations above for k, and ε indicate that for any point in the flow, only one value of turbulence exists. This is known as isotropy, and is one of the serious drawbacks with this two equation model. Turbulence, even in simple flows, is a three-dimensional phenomenon (anisotropic), with different turbulent viscosities acting in each direction. The k-ε model is generally regarded as a compromise between simplicity and complexity. It has the advantage of being robust and straightforward to implement, but is however, known to predict incorrectly flow in a number of common flow situations, including swirling, separating and recirculating flows. In swirling flows there is a tendency to overpredict the degree of solid body rotation. Many researchers have attempted to improve the k-ε model, generally by modifying the constants, or attempting to add further terms. Such improvments are however often flow specific, and while improving the modelling of turbulence in a range of specific cases, do not increase its overall applicability.

5.3 Further stress models

A number of alternative turbulence models are available, and extensive research is continuing to produce new approaches to the study of turbulence. The most common alternatives to the k-ε model are:

Reynolds-Stress Models (RSM)

When the time-averaged momentum equations are derived (above) six additional non-zero terms representing turbulence are introduced. Reynolds Stress models solve a transport equation for each of these additional stresses. Together with the one equation for dissipation, seven differential equations must be solved, compared with two for the k-ε model. If scalar transport equations are being solved, then additional transport equations must be solved for the turbulence terms. Reynolds Stress models do not suffer from the same limitations as k-ε models when applied to complex flows, but impose a significant computing overhead.

Large-Eddy Simulation (LES) / Subgrid Scale Modelling (SGS)

This techniques uses a direct simulation approach to resolve large scale eddies in the flow, and a simple turbulence model for subgrid turbulence. The momentum transport equations are solved by decomposing the velocities into large scale motion and subgrid components. The advantages of LES / SGS are that the solution gives direct information on the most important features of the turbulence (the largest eddies) - for instance allowing pressure fluctuations to be calculated, without the need to use a mesh capable of resolving the smallest eddies. The principal disadvantages are that three dimensional unsteady calculations are required for all flow cases, and mesh requirements are still considerable

APPENDIX B
THE COMPUTATIONAL MESH

The computational meshes used in this study were generated using the PATRAN finite element modeller (release 2.5). Separate databases were used for each of the swirl chamber, main chamber and piston crown. Each section was then imported into the STAR pre-processor where the appropriate boundary conditions and control parameters were applied. Most of the mesh was created using standard PATRAN modelling techniques: geometry entities (lines, surfaces and volumes) are created from technical drawings. The volumes are then meshed in such a way as to ensure the mesh at the interface is coherent. To model the glow plug, the swirl chamber was meshed without the glow plug, and then a rectangular block of cells in the region of the glow plug removed and placed in a separate database. Within this database, a geometry volume was created from the shape of the removed block, and the glow plug formed within this block. The resulting geometry was then meshed, and re-inserted into the original mesh, replacing the removed block.

All the models used for comparison with experimental results are fully three-dimensional (but with the symmetry plane boundary). The models for the mesh density investigation, and the throat area parametric study are 2½ dimensional - the symmetry plane surface is geometrically accurate, but is given a uniform depth. The swirl chamber and main chamber depths vary, to maintain realistic compression and volume ratios. The use of a 2½ dimensional model greatly reduces mesh generation and solution phase time. The model is not however capable of fully resolving the 3-dimensional flow in the engine.

The following pages contain a selection of the computational meshes created during the study. Each is a symmetry plane model. Figures B4 and B5 show 2½ dimensional models.

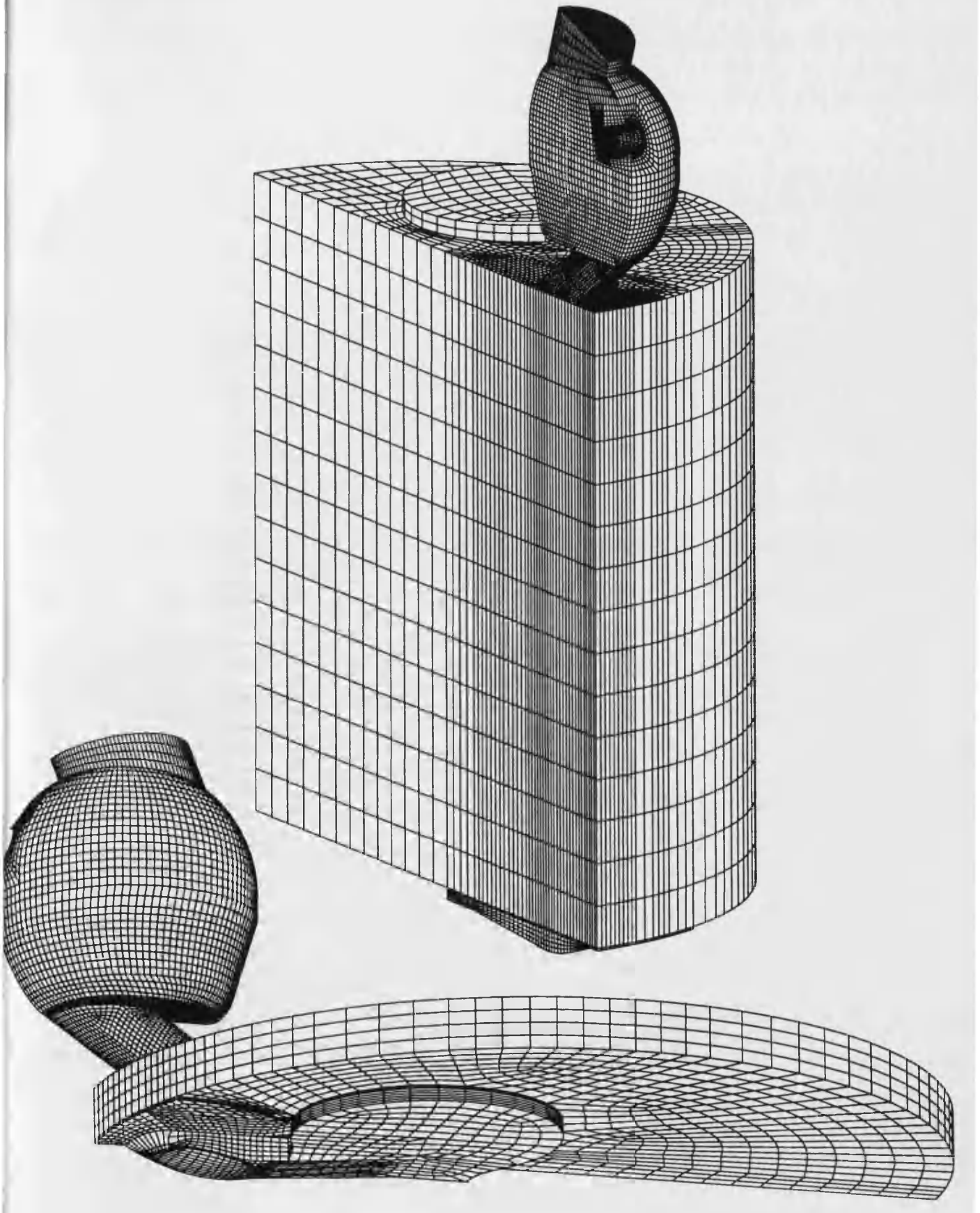

Figure B1
Complete computational mesh for Ricardo Comet Vb combustion system with standard glow plug and piston trough.
Lower view shows mesh near top dead centre after cell layer removal

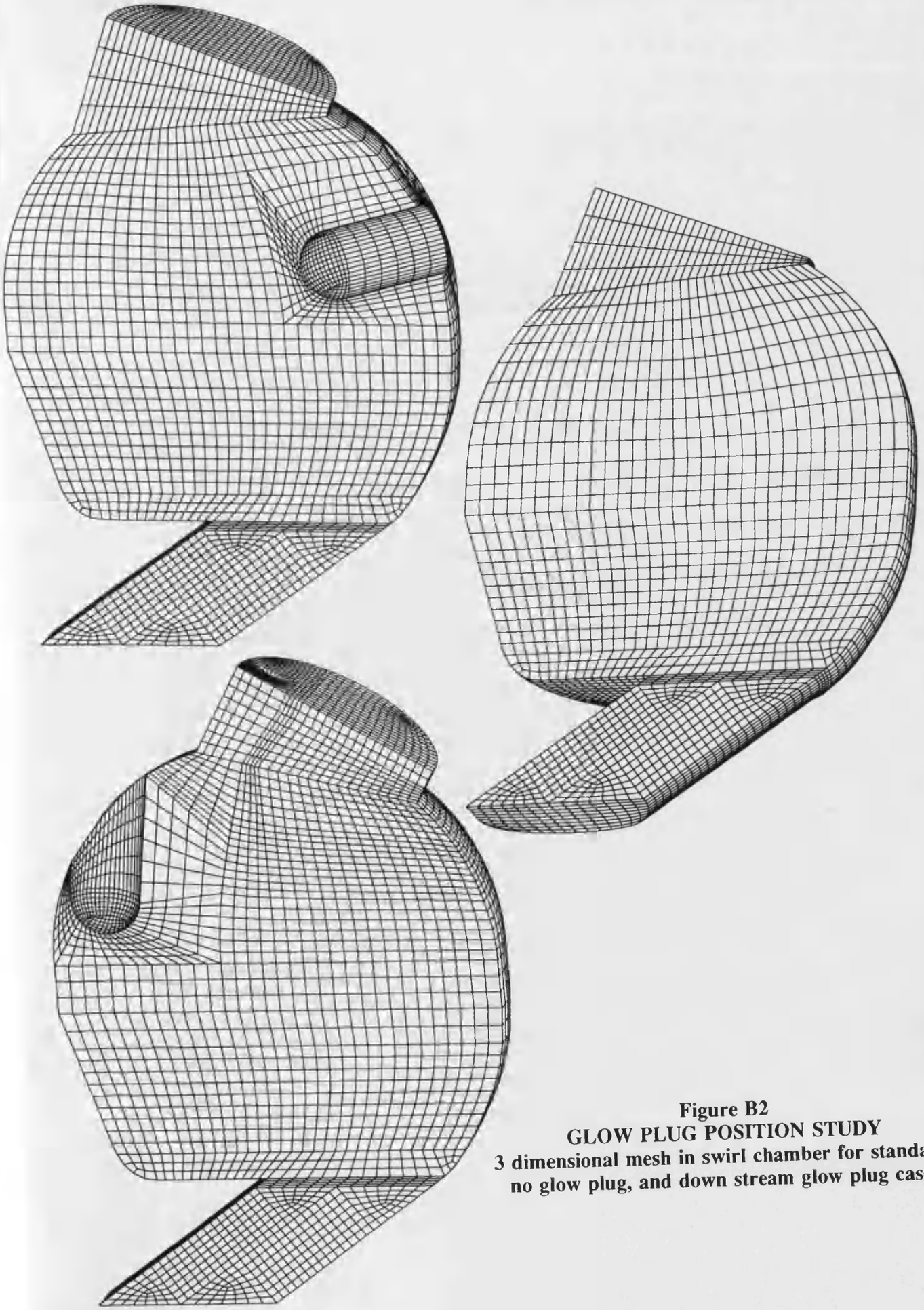

Figure B2
GLOW PLUG POSITION STUDY
3 dimensional mesh in swirl chamber for standard, no glow plug, and down stream glow plug cases

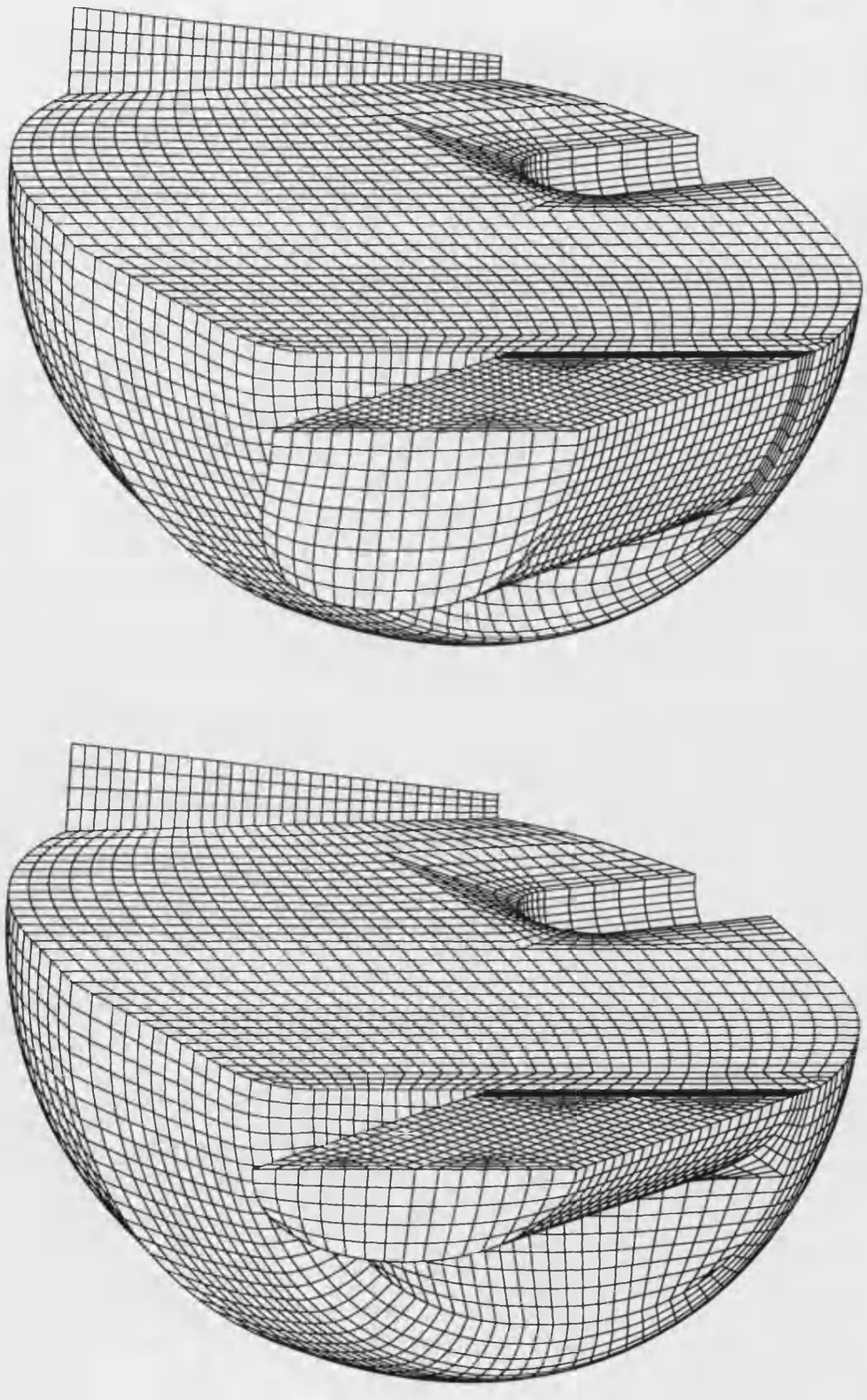

Figure B3
3 dimensional mesh for standard Ricardo Comet Vb combustion system and reduced throat area insert

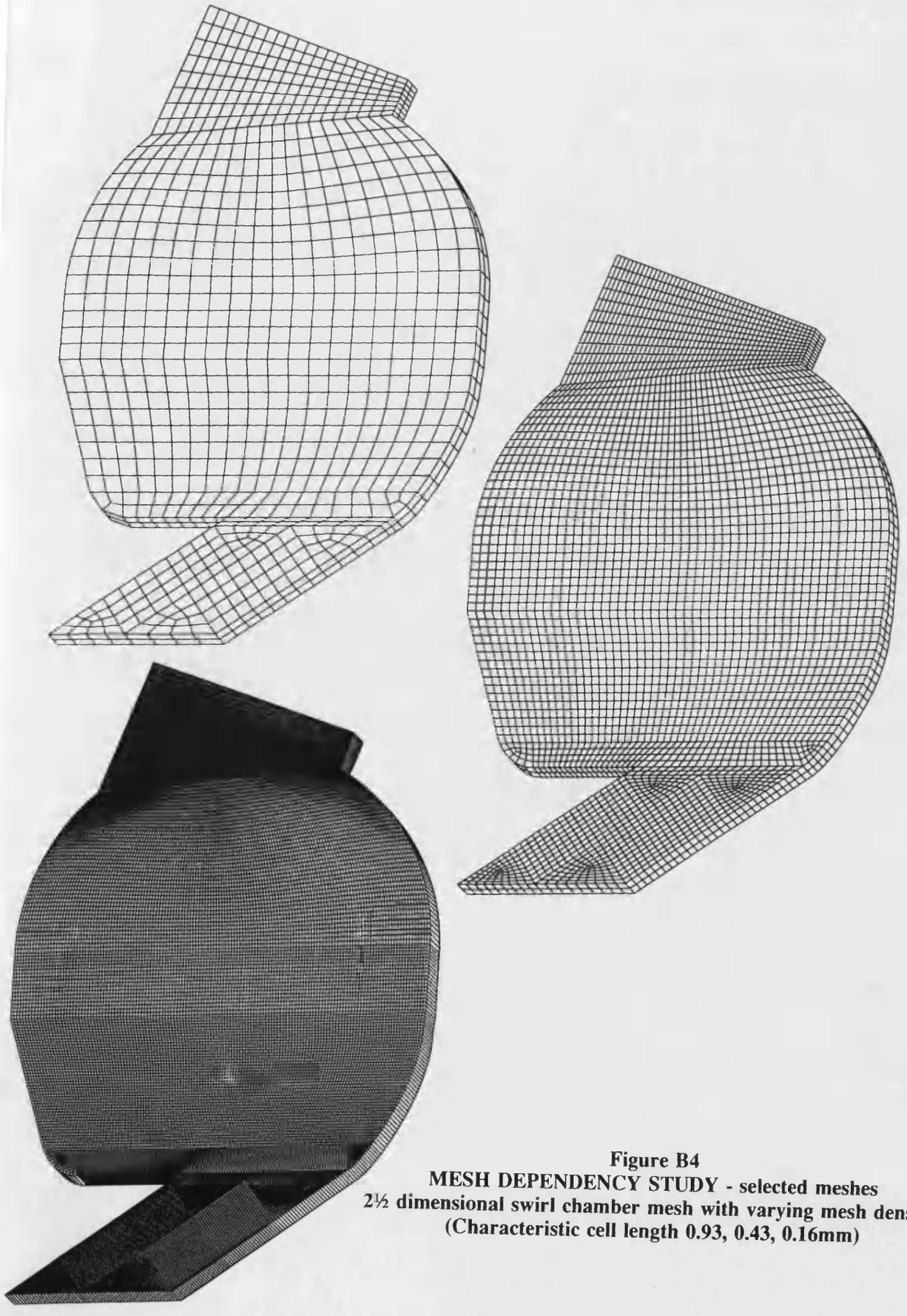

Figure B4
MESH DEPENDENCY STUDY - selected meshes
2½ dimensional swirl chamber mesh with varying mesh density.
(Characteristic cell length 0.93, 0.43, 0.16mm)

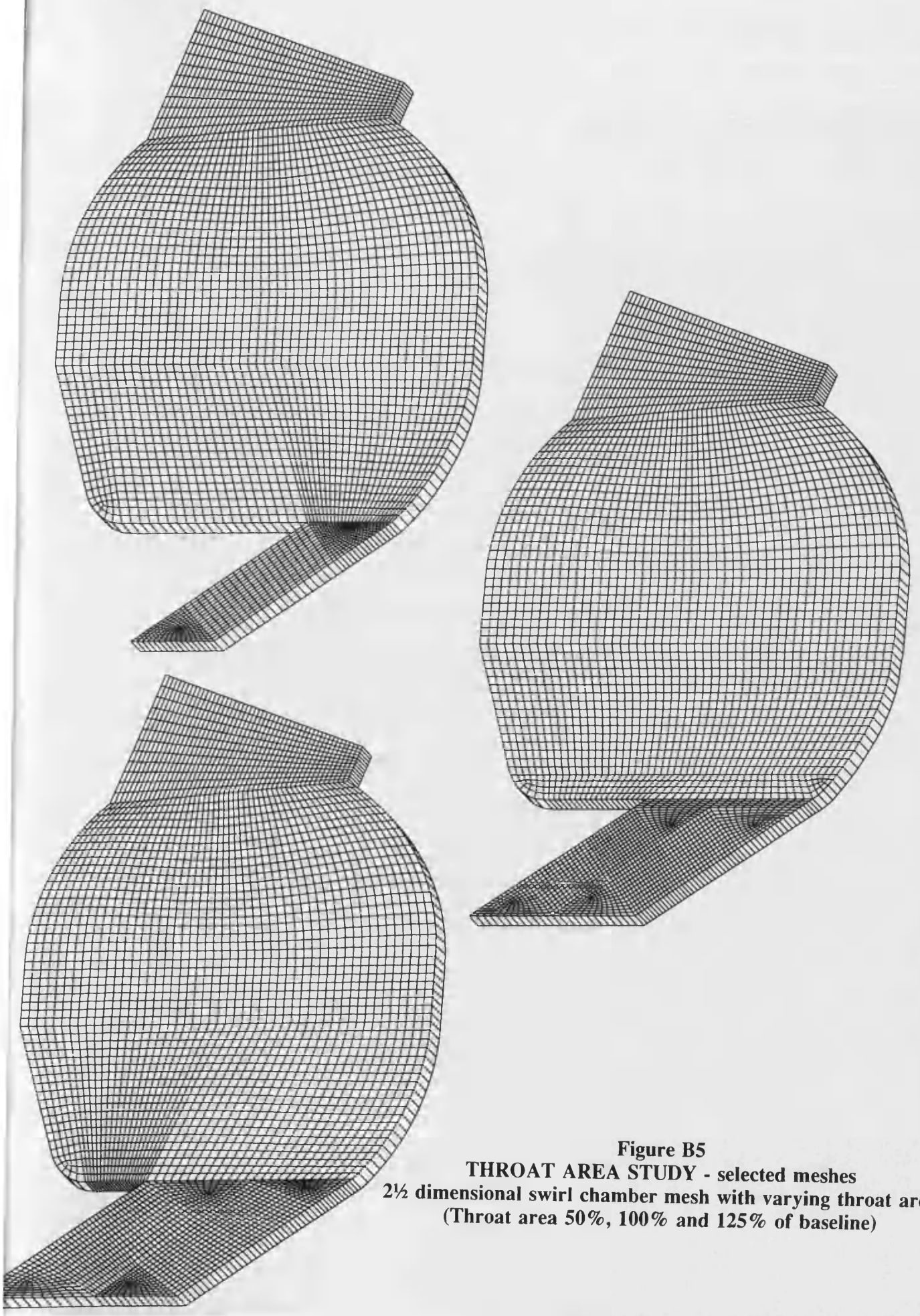

Figure B5
THROAT AREA STUDY - selected meshes
2½ dimensional swirl chamber mesh with varying throat area
(Throat area 50%, 100% and 125% of baseline)

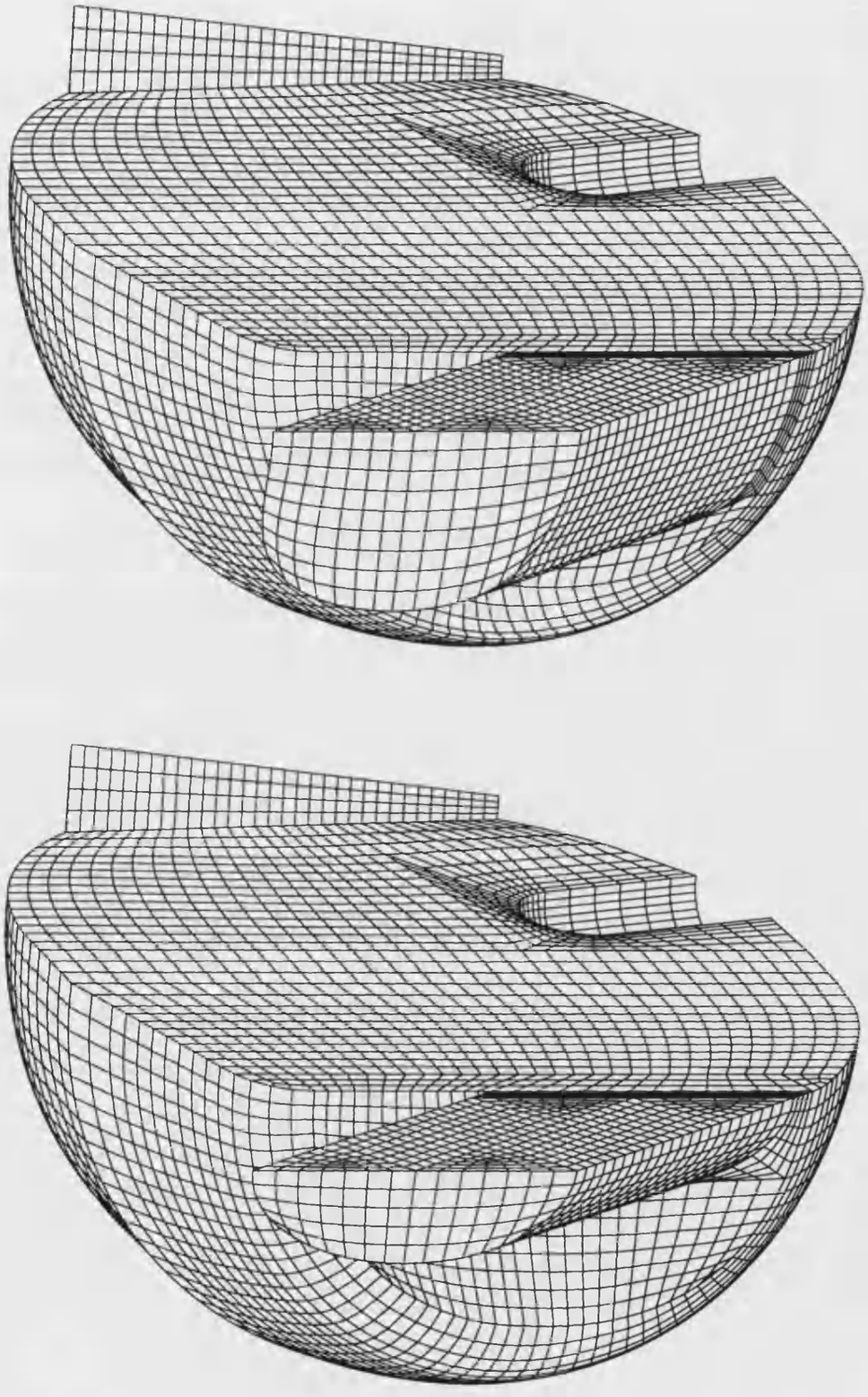

Figure B3
3 dimensional mesh for standard Ricardo Comet Vb combustion system and reduced throat area insert

APPENDIX C
SOLUTION PARAMETERS

The solution control parameters are set within the *prostar* environment. In general, very few of the default parameters needed to be changed. For each case, a parameter file similar to the following (for a 1000rpm validation run) was used to set up the run:

```
TITLE
FORD 1.8l IDI 40000 Cell  No glow p. SFCD 1000rpm (Var Cp /Wt = 80)

VERS UNSTRUCTURED
NUMF   0
ITER      400 0.100000E-02
SWIR   0.500
DSCH SFCD   UVW   1.000
DSCH SFCD   TURB  1.000
DSCH SFCD   T     1.000
DSCH SFCD   SC1   1.000
DSCH SFCD   SC2   1.000
DSCH SFCD   SC3   1.000
TIME TRANSIENT
PISO     20   0.2500   0.1500
SIMP OFF
SOLU VECTOR
RDAT NONE
WDAT POST    5
SOLV Y Y Y Y Y Y Y Y N N N
RELA   0.7000   0.8000   0.7000   1.0000   1.0000   1.0000   1.0000   1.0000   +
   1.0000
SWEE   100   100   100  1000   100   100   100   100   100   100
RESI   0.0100   0.0100   0.0100   0.0010   0.0100   0.0100   0.0100   0.0100   +
   0.0100   0.0100
RADI  OFF OFF
CONJ OFF
ALTS N N N N
!!    1 2 3 4 5 6 7 8 9 0 1 2 3 4 5 6 7 8 9 0
SWIT  F F F F F F F F F F F F Y F F F F Y F F
CPUT ON
PRFI NONE
PRWA   F  F  F  F  F  F  F  F  F  F  F  F  F
POWA   F  F  F  F  F  F  F  F  F  F  F  F  F
PRCH ON  OFF ON
RESD     2   10000
PMAT   1 FLUI
DENS IDEAL Y  28.9600
LVIS CONSTANT 0.181000E-04
!!!!!!!!!!!!!!!!!!   U S E R   S P E C I F I C   H E A T !!!!!!!!!!!!!!!!!!
SPEC USER  719.000
TDAT  273.000
PRAN 0.900000
TURB KE  1.00000
INIT STAN       0.          0.          0.          0.          0.          +
  293.000          0.          0.          0.
PRES  100000.          58267
COND CONSTANT 0.263700E-01
TNOR        0.
MONI     58267
COKE   0.0900   1.4400   1.9200   1.4400  -0.3300   0.4190   9.0000
SCHM 0.500000     0.500000     0.500000     0.900000     0.900000             +
 0.900000
REAC       0.          0.          0.
RSOU N N N N N N
HCOE STANDARD
ACCE       0.          0.          0.
SPIN       0.          0.          0.          0.          0.             +
      0.     1.00000
RTUR INLE KEPS
RTUR PRES MIXL
RDEF     0 WALL STAN
      0.          0.          0.          1       0.      9.00000
!
!!!!!!!!!!!     FIXED WALL TEMP     !!!!!!!!!!!
!
FIXED      353.          0.
RDEF     1 SYMP STAN
RDEF     5 PRESSURE
0. 0. 0. 0. 0.
MVGR ON
```

Flag 18 activates cell layer removal

Load Step data

```
TRFILE INIT 26 6

LSTE 1 20 25.0000E-5 N 0 20
CPOS Y Y Y N N N N N
VPOS N N N Y Y Y Y Y
WLPO   F  F  F  Y  F  F  F  F  F  Y  F  F  F
!!     FX FY FZ HT S1 S2 S3 YP SH HF S1 S2 S3
RDEF 5 PRESSURE
0. 0. 0. 0. 0.
LSSA 1

LSTE 2 60 25.0000E-5 N 0 30
CPOS Y Y Y N N N N N
VPOS N N N Y Y Y Y Y
WLPO   F  F  F  Y  F  F  F  F  F  Y  F  F  F
!!     FX FY FZ HT S1 S2 S3 YP SH HF S1 S2 S3
RDEF 5 WALL
0.
ADIAB
LSSA 2

LSTE 3 60 8.333333E-5 N 0 30
CPOS Y Y Y N N N N N
VPOS N N N Y Y Y Y Y
WLPO   F  F  F  Y  F  F  F  F  F  Y  F  F  F
!!     FX FY FZ HT S1 S2 S3 YP SH HF S1 S2 S3
RDEF 5 WALL
0 0 0
ADIAB
LSSA 3

LSTE 4 140 3.333333E-5 N 0 70
CPOS Y Y Y N N N N N
VPOS N N N Y Y Y Y Y
WLPO   F  F  F  Y  F  F  F  F  F  Y  F  F  F
!!     FX FY FZ HT S1 S2 S3 YP SH HF S1 S2 S3
RDEF 5 WALL
0 0 0
ADIAB
LSSA 4

LSTE 5 20 3.333333E-5 N 0 8
CPOS Y Y Y N N N N N
VPOS N N N Y Y Y Y Y
WLPO   F  F  F  Y  F  F  F  F  F  Y  F  F  F
!!     FX FY FZ HT S1 S2 S3 YP SH HF S1 S2 S3
RDEF 5 WALL
0 0 0
ADIAB
LSSA 5

LSTE 6 80 6.250000E-5 N 0 40
CPOS Y Y Y N N N N N
VPOS N N N Y Y Y Y Y
WLPO   F  F  F  Y  F  F  F  F  F  Y  F  F  F
!!     FX FY FZ HT S1 S2 S3 YP SH HF S1 S2 S3
RDEF 5 WALL
0 0 0
ADIAB
LSSA 6
LSRA 1 6
PROB 10 CODE
!!
!! Check monitor cell
```

The last set of commands (LSTE) define the time steps for the runs. The time steps were chosen based on the largest time step which maintained a stable solution. In very few cases were times steps greater than 1.5° crank angle used. The time steps are defined in seconds - the user subroutine NEWXYZ must be given the engine speed.

Engine Speed	1500 / 3000 rpm	4500 rpm
1	80 * 1.5°	80 * 1.5°
2	60 * 0.5°	30 * 1.125°
3	160 * 0.2°	32 * 0.6°
4	80 * 0.375°	30 * 1.125°

Time steps for numerical model

Solution stability

For most of the cases, the solution (code 2.112) remained stable with the above time steps. If difficulties were encountered (normally negative temperatures), the time step was reduced, and the solution re-run. In extreme cases (for instance the downstream glow plug case {case 4}, in which the mesh included a high proportion of distorted cells), underrelaxation of pressure was reduced from 0.8 to 0.6, and the tolerance on the PISO parameter to 0.1.

APPENDIX D
SUMMARY OF MODEL AND BOUNDARY CONDITIONS FOR NUMERICAL MODELS

This table lists the geometry, initial and boundary conditions used for each of the models for which results are presented in this thesis. A blank entry indicates the default case (underlined in the header).

Run	Case name	Geometry Ricardo Comet Vb or throat area	Full 3-d model or reduced 2½d	Glow plug ? ✓=cross-flow	Piston Crown ?	Valve Recess	Valve open until IVC (37° abdc)	Mesh Density (charac. length in mm) LOW = 1.0 MED = 0.7 HIGH = 0.4	Number of swirl chamber cells	Engine speed (rpm)	Wall boundary conditions adiabatic	Variable Cp ?	Differencing scheme
1	comp14			-	-	-	-	LOW	17047	3000	-	-	UD
2	comp14.sfcd			-	-	-	-	LOW	17047	3000	-	-	SFCD
3	noglow			-	-	-	-	MED		3000	-	-	UD
4	down.2			down stm.	-	-	-	MED		3000	-	-	UD
5	base			✓	-	-	-	MED	38088	3000	-	-	UD
6	hd.sfcd			-	-	-	-	HIGH		3000	-	-	SFCD
7	1500.ud			-	-	-	-	MED		1500	-	-	UD
8	shd3.ud			-	-	-	-	HIGH		3000	-	-	UD
9	nog.45.ud			-	-	-	-	MED		4500	-	-	UD
10	shd3.sfcd			-	-	-	-	HIGH		3000	-	-	SFCD
11	1500.sfcd			-	-	-	-	MED		1500	-	-	SFCD
12	comp14.varcp			-	-	-	-	LOW		3000	-	✓	UD
13	val1_2			✓	✓	✓	✓	MED		1500	77°C	✓	UD
14	6mmthr	50%		✓	✓	-	✓	MED		1500	77°C	✓	UD
15	6mmthr.1450sf	50%		✓	✓	-	✓	MED		1450	100°C	✓	SFCD
16	comp14.valve.15			-	-	-	✓	LOW	17047	1500	77°C	-	UD
17	valng			-	✓	-	✓	MED		1000	80°C	✓	SFCD
20	adiab			-	-	-	-	LOW		3000	adiabatic	-	UD
21	wt70			-	-	-	-	LOW		3000	70°C	-	UD
22	wt150			-	-	-	-	LOW		3000	150°C	-	UD
23	wt250			-	-	-	-	LOW		3000	250°C	-	UD
24	wt70 @ 1500			-	-	-	-	LOW		3000	70°C	-	UD
25	wt70 @ 4500			-	-	-	-	LOW		3000	70°C	-	UD

Run	Case name	Geometry Ricardo Comet Vb or throat area	Full 3-d model or reduced 2½d	Glow plug ? ✓=cross-flow	Piston Crown ?	Valve Recess	Valve open until IVC (37° abdc)	Mesh Density (charac. length in mm) LOW = 1.0 MED = 0.7 HIGH = 0.4	Number of swirl chamber cells	Engine speed (rpm)	Wall boundary con-ditions adiabatic	Variable Cp ?	Differ-encing scheme
31	twidth0b	100%	2½	-	-	-	-	MED		3000	-	-	UD
32	twidth1	50%	2½	-	-	-	-	MED		3000	-	-	UD
33	twidth2	75%	2½	-	-	-	-	MED		3000	-	-	UD
34	twidth3	95%	2½	-	-	-	-	MED		3000	-	-	UD
35	twidth4	105%	2½	-	-	-	-	MED		3000	-	-	UD
36	twidth5	115%	2½	-	-	-	-	MED		3000	-	-	UD
37	twidth6	125%	2½	-	-	-	-	MED		3000	-	-	UD
40	twod1b		2½	-	-	-	-	0.93		3000	-	-	UD
41	twod2b		2½	-	-	-	-	0.58		3000	-	-	UD
42	twod3b		2½	-	-	-	-	0.43		3000	-	-	UD
43	twod4b		2½	-	-	-	-	0.31		3000	-	-	UD
44	twod5b		2½	-	-	-	-	0.21		3000	-	-	UD
45	twod6		2½	-	-	-	-	0.16		3000	-	-	UD
50	twod1.sfcd		2½	-	-	-	-	0.93		3000	-	-	SFCD
51	twod2.sfcd		2½	-	-	-	-	0.58		3000	-	-	SFCD
52	twod3.sfcd		2½	-	-	-	-	0.43		3000	-	-	SFCD
53	twod4.sfcd		2½	-	-	-	-	0.31		3000	-	-	SFCD
54	twod5.sfcd		2½	-	-	-	-	0.21		3000	-	-	SFCD
55	twod6.sfcd		2½	-	-	-	-	0.16		3000	-	-	SFCD

APPENDIX E
COMPUTING REQUIREMENTS

The numerical models listed in Appendix D were mainly run on a CRAY ymp supercomputer. This machine is an 8 processor, shared memory computer capable of running vectorised code. Vectorisation is a technique that allows DO loop operations on large arrays to be processed more quickly than on a comparable *scalar* machine. If the source code is written to use the vectorisation, significant reductions in CPU times can be achieved. The STAR package does not currently use the parallel-processing capabilities of the ymp.

Computing requirements can be broken into three main components: processor time, memory requirements and disk space requirements.

Processor time

Processor time (CPU) is a function of a combination of factors:

number of cells in mesh: CPU varies as $N^{3/2}$ to N^{2}, although vectorisation efficiency improves greatly with larger arrays. Figure E1 plots the total CPU requirement for a series of meshes of varying number of cells {cases 40-45}.
number of time steps - CPU is directly proportional to the number of steps, BUT increasing the step may make the fluid mechanic solution more difficult within the time step - increasing CPU per time step.
submodels: CPU is a function of the degree of complexity of the solution. Adding models to calculate specific heat as a function of temperature, wall heat transfer etc increase the processor time. Although not investigated in this thesis, the turbulence model can greatly influence CPU. Advanced turbulence models such as Reynolds Stress modelling can add a further six variables for which solution must be obtained.
degree of mesh distortion. Excessive *mesh distortion* (ie deviance from cubic cells in the mesh) increases computation time, as the solver takes longer to converge. It may be necessary to reduce the solver tolerances to maintain numerical stability (see Appendix C) further increasing CPU.
differencing scheme Higher order difference schemes (eg the SFCD scheme) involve a greater degree of coupling between variables increasing CPU. The increased

coupling between variables reduces the extent to which the code can be vectorised, increasing overall CPU. The difference between the SFCD and the UD differencing schemes is greater therefore on a vector machine (eg the CRAY) than on a scalar computer (SUN workstation).

cell layer removal: the control code for the cell layer removal requires a small amount of CPU. The time step following a cell layer removal operation typically takes about twice the CPU of the previous time step. As subsequent layers of cells are removed from the solution, CPU/time step reduces because 1. the total number of cells is reduced and 2. the removal of cell layers reduces mesh distortion.

The following table lists some typical run times on the CRAY ymp8 (SN1712), using solver version 2.112c in vector mode. The figures assume 400 time steps per solution (bcd to 20°atdc). For some cases (eg the high density mesh, and the downstream glow plug case) a greater number of time steps is required.

The penultimate column lists run times for a 'simple' case - *upwind differencing, no wall heat transfer, constant Cp.*

The final column lists the corresponding time for the validation type case: *SFCD differencing scheme, wall heat transfer, variable Cp.*

Case number (Appendix C)	Notes	Number of cells	Run time CPU HOURS *Simple* case	Run time CPU HOURS *Validation* case
1		17000	1.0	
17	'Standard' mesh	41000	3.2	4.5
4	Downstream case - distorted mesh	44000	3.7	
8	high density mesh: 580 steps needed (times given for 400)	120000	11.2	

Memory

Memory requirements are dependent on the number of memory arrays required for the solution. Thus memory varies as a function of the number of variables for which a solution must be obtained, and the number of sub-models included in the solution. On workstations, memory requirements can present the limiting factor as to the size of model which can be run. The standard validation models required 6 MWords of memory. The high density (120 000 cell) model uses 10.8 MWords of memory (the ymp has 128 MWords of memory).

Disk Space

The major factor affecting disk space requirements for a in-cylinder model is the number of time steps at which the results must be stored. To reduce the size of the results files, the approach described in Chapter 4 of only storing essential data was used. A typical run with a 40000 cell mesh uses around 200MB of file space.

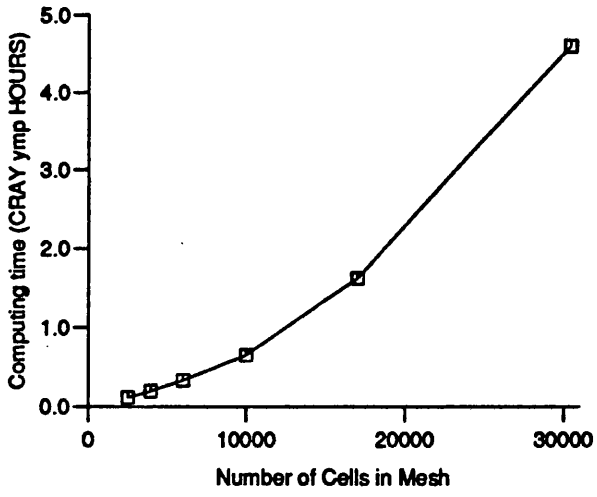

Figure E1
Variation of CPU time with model size

C448/025

An investigation of the emission characteristics of the passenger car IDI diesel engine

S J CHARLTON, BSc, PhD, CEng, MIMechE, MSAE, A COX, BEng, B J SOMERVILLE, BEng
School of Mechanical Engineering, University of Bath
M J WATTS, BSc, CEng, MIMechE and R W HORROCKS, MSc
Ford Motor Company Limited, Research & Engineering Centre, Basildon, Essex

SYNOPSIS The paper describes an investigation of the emission and fuel economy characteristics of a number of alternative indirect-injection (IDI) Diesel engine swirl chamber concepts. The alternative chambers evaluated cover glow plug location and throat area, as well as novel dual throat and air cell configurations. The experimental work was carried out on a steady-state emissions test bed and on a rolling road equipped for full drive-cycle assessment of emissions, fuel economy and real-time particulates. The emissions considered are those subject to forthcoming legislation within Europe, namely: oxides of nitrogen (NOx), unburned hydrocarbons (HC) and particulates.
The experimental study has shown that particulate emissions may be reduced by adopting a tangential glow plug arrangement. Such a configuration, with the glow plug located downstream of the injector, also gives a significant reduction of visible smoke, especially in the part load regions important for vehicle applications. Real-time measurement of particulate emission during the FTP 75 / German drive cycle show considerable reductions during periods of vehicle acceleration.
The results of a computational fluid dynamics (CFD) simulation of the air motion within the swirl chamber, with 'cross-flow' and 'tangential' glow plug locations are presented.

1.0 INTRODUCTION

The IDI Diesel engine was first developed by Ricardo as a means of achieving rapid combustion in small automotive engines. The IDI combustion system consists of a swirl chamber in the cylinder head, which connects with the chamber above the piston via a passageway, or throat. During the latter part of the compression stroke air is transferred into the swirl chamber at high velocity, thereby forming a more or less orderly air motion, or swirl. Swirl is required to provide the mixing energy necessary for rapid break-up of the injected fuel, prior to rapid and clean combustion. The rate of heat transfer resulting from the additional surface area and high gas velocity is such that a glow plug has to be used to give reliable starting in cold conditions. It is a tribute to the effectiveness of this system that today it is used in the great majority of passenger car Diesel engines in a form virtually unchanged for thirty years, in a climate of acute concern for the environment.

The object of this research study is to evaluate the effects of a number of design changes to the basic Ricardo Comet chamber with special emphasis on exhaust emissions. The study has focussed on the location of the glow plug and the cross-sectional area of the throat between the two chambers. In addition, the dual throat system described by Tanaka [1] is evaluated, as is a novel air cell chamber. The research was carried out on an experimental version of the Ford 1.8 litre engine [2], in which the glow plug protrudes into the swirl chamber in a radial direction upstream of the fuel injector. The glow plug and throat exert a significant influence over the air motion in the swirl chamber, not only determining the swirl but also the intensity and scale of turbulence. The relationship between swirl and turbulence for some of the geometries presented here is being studied at the University using the STAR-CD CFD package. Preliminary results for the datum 'cross-flow' glow

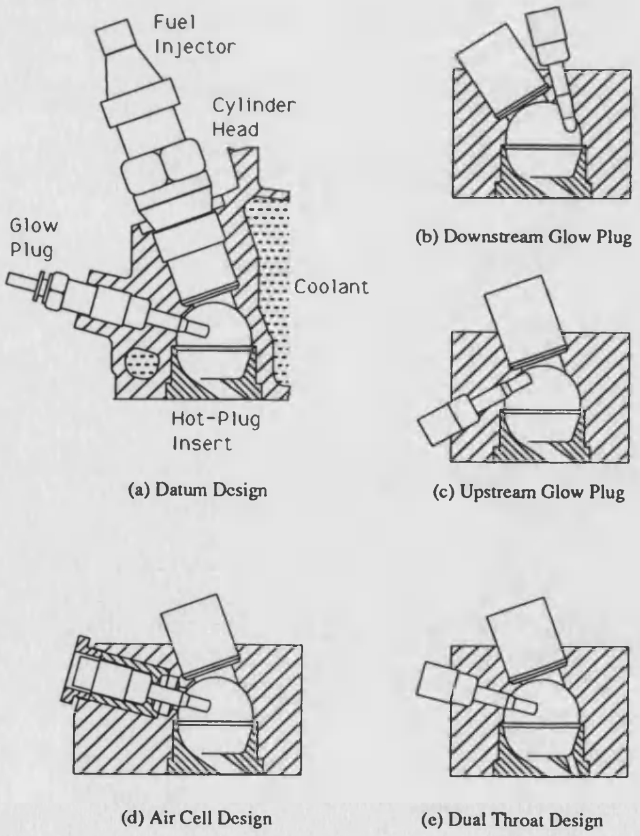

Figure 1 Details of the swirl chamber designs investigated

plug and 'tangential' glow plug arrangements are presented.

Growing concern for the environment has put pressure on manufacturers and governments to seek ways to reduce emissions from road vehicles. In Europe and North America new measures are being debated to limit further the emissions from passenger cars and trucks. In June 1991 the Council of the European Communities modified the test procedure for passenger vehicles by introducing a 400 second 'extra-urban' cycle to the existing urban cycle. The maximum speed during the test procedure was increased from 50 kph (31 mph) during the urban cycle to 120 kph (70 mph) in the extra-urban cycle. New limits for gaseous and particulate emissions were specified. This 'consolidated directive' is generally considered to be more severe than the 1987 US Federal limits for passenger cars. However, in the directive it was also stated that a further reduction in permissible levels will be proposed, to apply some time after 1st January 1996.

In the USA the Clean Air Act Amendments of 1990 introduce new Federal standards which will be phased-in over the period 1994 to 2003, with a 'Tier II' level proposed for 2004. From a Diesel perspective there is a NOx waiver at the current 1.0 g/mile (0.62 g/km) until 2003 and the particulate standard of 0.08 g/mile (0.05 g/km) is to be phased-in over the period 1994 to 2003 and remain at that level for 2004. The NOx proposal for 2004 is 0.2 g/mile, which is currently regarded as infeasible. The work reported here is a response to demands for a cleaner environment and tightening emission legislation.

2.0 SWIRL CHAMBER DESIGNS INVESTIGATED

The variations to the Ricardo Comet chamber investigated in the paper are as follows:

1. Datum design with conventional 'cross-flow' glow plug *Figure 1a*
2. Glow plug in a position downstream of the injector and tangential in orientation *Figure 1b*
3. Glow plug in a position upstream of the injector and tangential in orientation *Figure 1c*
4. Designs 1 to 3 but with enlarged throat area (5%, 10% and 20%)
5. Datum design with an air cell located around the glow plug in the head casting *Figure 1d*
6. Datum arrangement with dual throat *Figure 1e*

The object of the study is to examine the effects of these chamber designs on fuel consumption and emissions under steady-state conditions and under transient (drive cycle) conditions on a rolling road emission facility.

These configurations were chosen principally for their effects on the orderly air motion (swirl) and on the turbulence levels in the chamber. The throat area, glow plug penetration and attitude are known to influence the level of swirl and the formation of turbulence [3]. It has been assumed that the more 'streamlined' tangential configurations would be least detrimental to swirl. If a tangential glow plug is used with an enlarged throat the effect on swirl may be neutral, with the benefit of a reduction in the work needed to transfer the air into the swirl chamber, as expounded by Greeves et al [4].

The dual throat design is thought to enhance turbulence at the expense of swirl since some of the flow into the swirl chamber during compression is directed against the swirl. The secondary throat is aligned with the fuel spray, as in the research reported by Tanaka [1]. Tanaka suggested that such an arrangement would not only help to break up the fuel spray in the early part of combustion, but would allow some of the fuel to enter the main chamber at an early stage, thus reducing the inevitable overfuelling of the swirl chamber and the consequent particulate formation.

The air cell concept was inspired by the apparent benefits of conventional designs in which there is a clearance between the glow plug and the surrounding casting. It is believed that air is forced into such 'cells' during compression to be released later in the expansion process when combustion in the swirl chamber is starved of oxygen, thereby reducing soot formation in the otherwise fuel rich zones. In this research the concept was carried further by building in an enclosed volume around the glow plug, but separated from the swirl chamber by a small throat. The incorporation of the air cell reduced the compression ratio from 21.5 to 20.5.

3.0 STEADY-STEADY EXPERIMENTAL FACILITY

An engine research facility has been developed at Bath University for the investigation of exhaust emissions from passenger car Diesel engines under steady-state operation. The facility features electronic data acquisition for all experimental measurements and independent closed-loop control of engine speed and load. The engine 'environment' is carefully controlled to minimise the effects of variation in ambient conditions. Figure 2a shows the instrumentation system in outline. The heart of the data acquisition system is a PC computer with high-speed analogue to digital converter (ADC) and digital i/o cards. The ADC, which has a maximum acquisition rate of 1 MHz, has an integral multiplexer (MUX) which enables up to 16 channels of data to be read. Three of these channels are further multiplexed to increase the number of channels to 61. This configuration, under the control of software developed at the University, is capable of gathering all the data required for a thorough assessment of steady-state performance. The test procedure at a given operating point involves sampling each instrument a number of times, and taking an average for the calculation of performance and emissions. The data are corrected where relevant for ambient pressure, temperature and humidity.

according to the appropriate standards.

Figure 2b shows the control systems connected to the engine. These control torque, speed and the engine 'environment' in an attempt to obtain a high degree of repeatability, especially in emission measurements. To this end the controlled parameters are:

Intake air temperature
Fuel temperature
Lubricating oil temperature
Coolant temperature
Exhaust back pressure

In this paper the results are presented as maps of parameters of interest superimposed on load-speed axes. The maps were produced by collecting data at up to 80 load-speed points. This procedure takes up to three days to complete for each engine design, as the engine has to be allowed to stabilise thermally at each point and the calibration of exhaust analysers needs to be periodically checked.

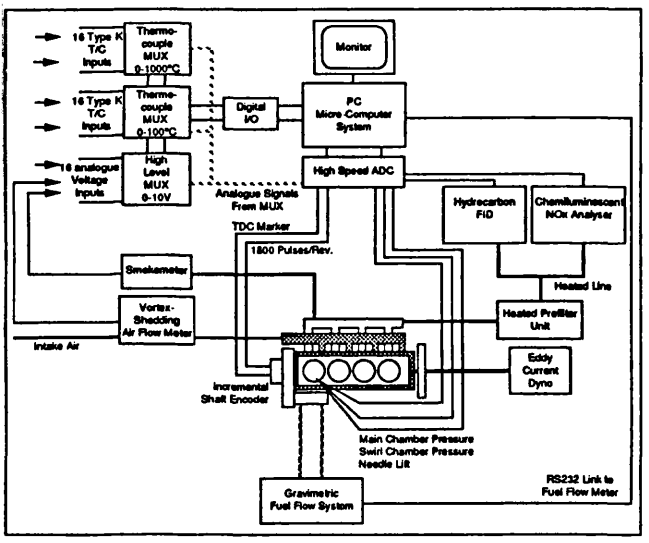

Figure 2a Data acquisition system and instrumentation

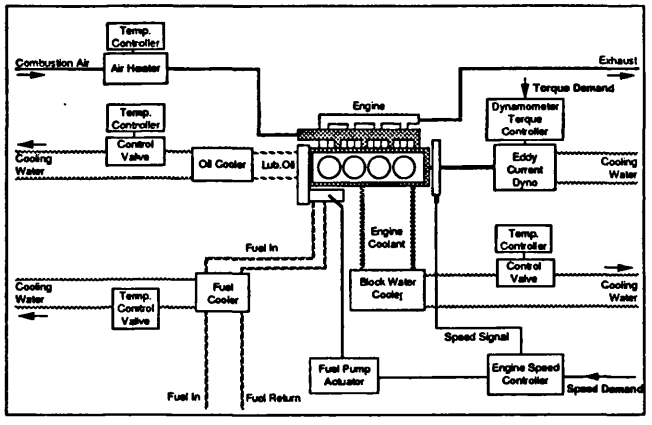

Figure 2b Control systems on the test facility

4.0 EXPERIMENTAL RESULTS

4.1 Steady-State Dynamometer Results

Glow Plug Position

Figure 3a compares the datum design with the downstream and upstream tangential glow plug designs on the basis of fuel economy, NOx, hydrocarbons (HC), smoke and calculated particulates. Each map is built up from data collected at speed intervals of 500 r/min and torque intervals of 10 Nm. The results for the datum design show a best fuel consumption of 260g/kWh at a bmep of 6.5 bar at a speed of 2500 r/min. As expected the NOx emission closely follows engine power. The highest levels occurring at maximum power and the lowest at idle. Maximum NOx has a value close to 150 g/h. The HC emission is very low at 4 to 10 g/h and is seen to increase with engine speed. The emission of visible smoke increases with load reaching values of 2.5 BSU at maximum bmep between 1500 and 4000 r/min. The particulate map has been derived from the HC and smoke results using the correlation of Greeves and Wang [5]. The calculated particulates are seen to increase with engine power from less than 5 g/h at idle to about 60 g/h at maximum power.

The results for the downstream glow plug design show a number of significant changes compared with the datum design. The best fuel consumption has improved to 250 g/kWh from 260 g/kWh (3.8%) and the consumption is generally improved over the entire map. The NOx emission has deteriorated somewhat, from 150 g/h to 170 g/h (13.3%) close to maximum power. The change in HC emission is quite small with some evidence of an increase at high loads and low speed. The most striking gain is in the emission of smoke, which has fallen by about 50% over the greater part of the low load, low speed region. As a consequence of reduced smoke , the particulates are also seen to be improved, at least over the greater part of the map.

The upstream glow plug design exhibits a similar characteristic to the downstream design. The fuel consumption is improved and the NOx emission is increased, although the upstream design has inferior NOx emission at light load. The upstream design has improved HC emission particularly at low speed. The smoke emission is improved over the datum but falls short of the improvement achieved by the downstream design. Particulates are improved over the datum, at least over the light load region, and the upstream design has a marginally better particulate emission.

Throat Cross-Sectional Area

Figure 3b shows the results of a study of the effects of swirl chamber throat cross-sectional area. Two cases were investigated : +10% and +20% cross-sectional area relative to the datum design. Results from a +5% area throat are presented later.

The trend with increased throat area is for the fuel consumption to increase slightly at higher loads with the global minimum almost unchanged,

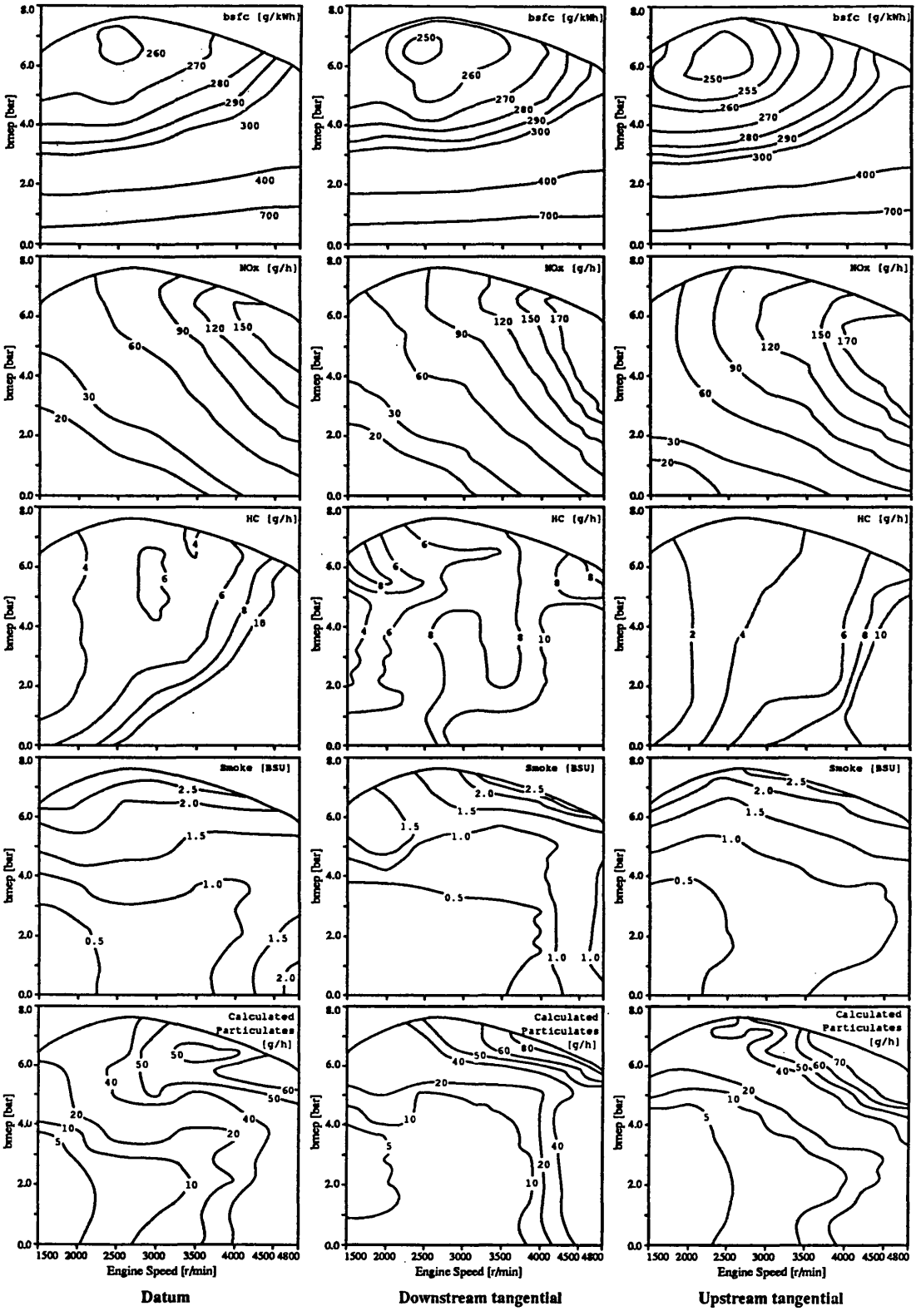

Figure 3a Experimental results for variation of glow plug location

whilst the NOx emission is decreased at maximum power. For both enlarged throat designs the NOx emission is seen to be reduced by about 25 g/h (16%) at maximum power. The HC emission is unchanged by throat area. The smoke emission is slightly increased at light load, but is significantly increased at loads above 50%. Smoke values of 3.5 BSU are seen, compared with 2.5 BSU for the datum design. Calculated particulates are slightly increased.

Tangential Glow Plug / Enlarged Throats

In Figures 3a and 3b it was shown that the enlarged throat swirl chambers produced lower NOx

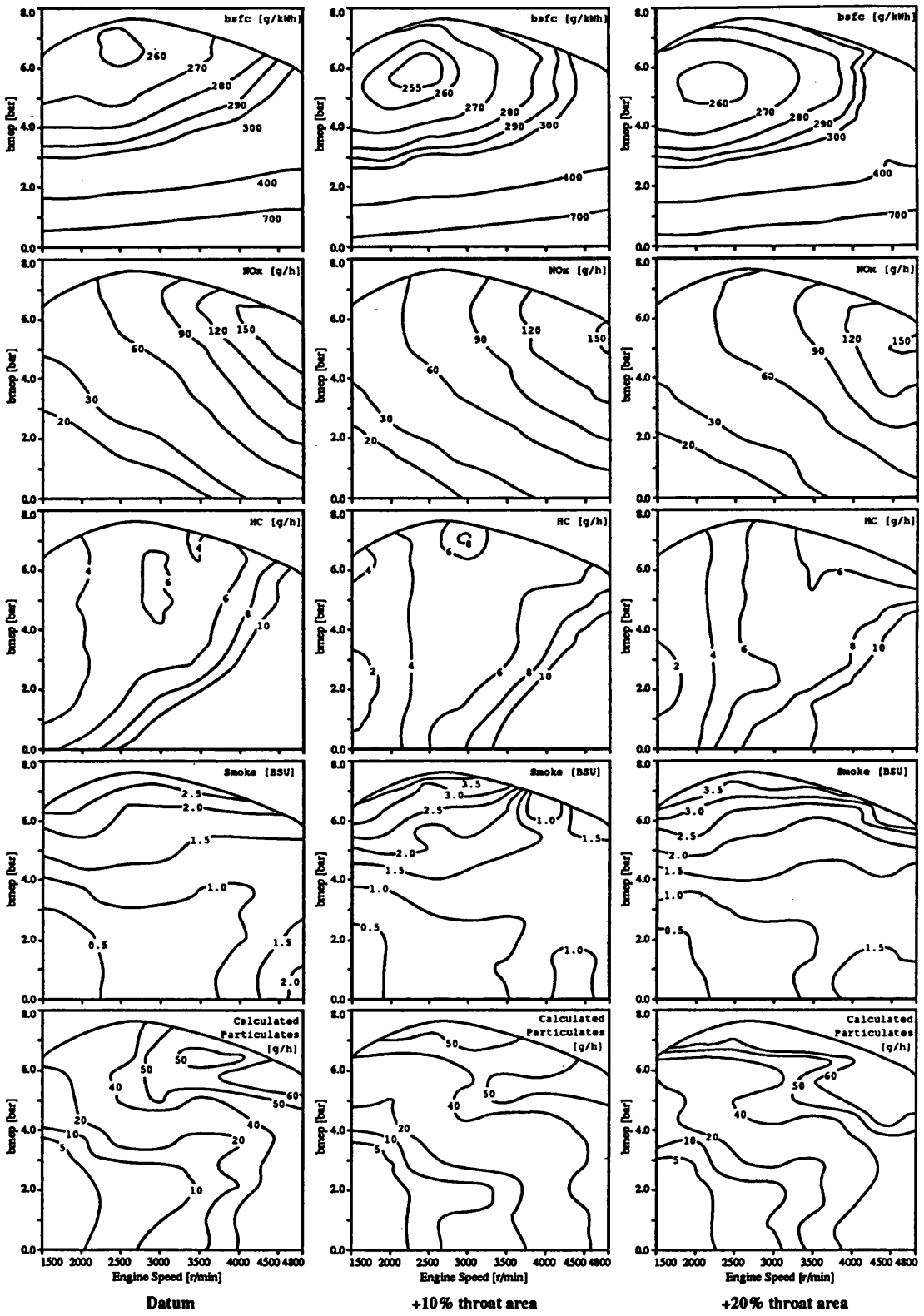

Figure 3b Experimental results for variation of throat area

emissions and inferior smoke and particulates, whilst the tangential glow plug arrangements produced the opposite effect - increased NOx and reduced smoke and particulates. Figure 3c shows experimental results from two combinations of tangential glow plug and enlarged throat compared with the datum chamber. The downstream chamber is combined with a throat increased by 5% over the datum design. This produces very significant improvements in smoke and particulates at part load, but the NOx emission is even worse than for the downstream tangential design shown in Figure 3a. Also shown in Figure 3c are results from the upstream glow plug

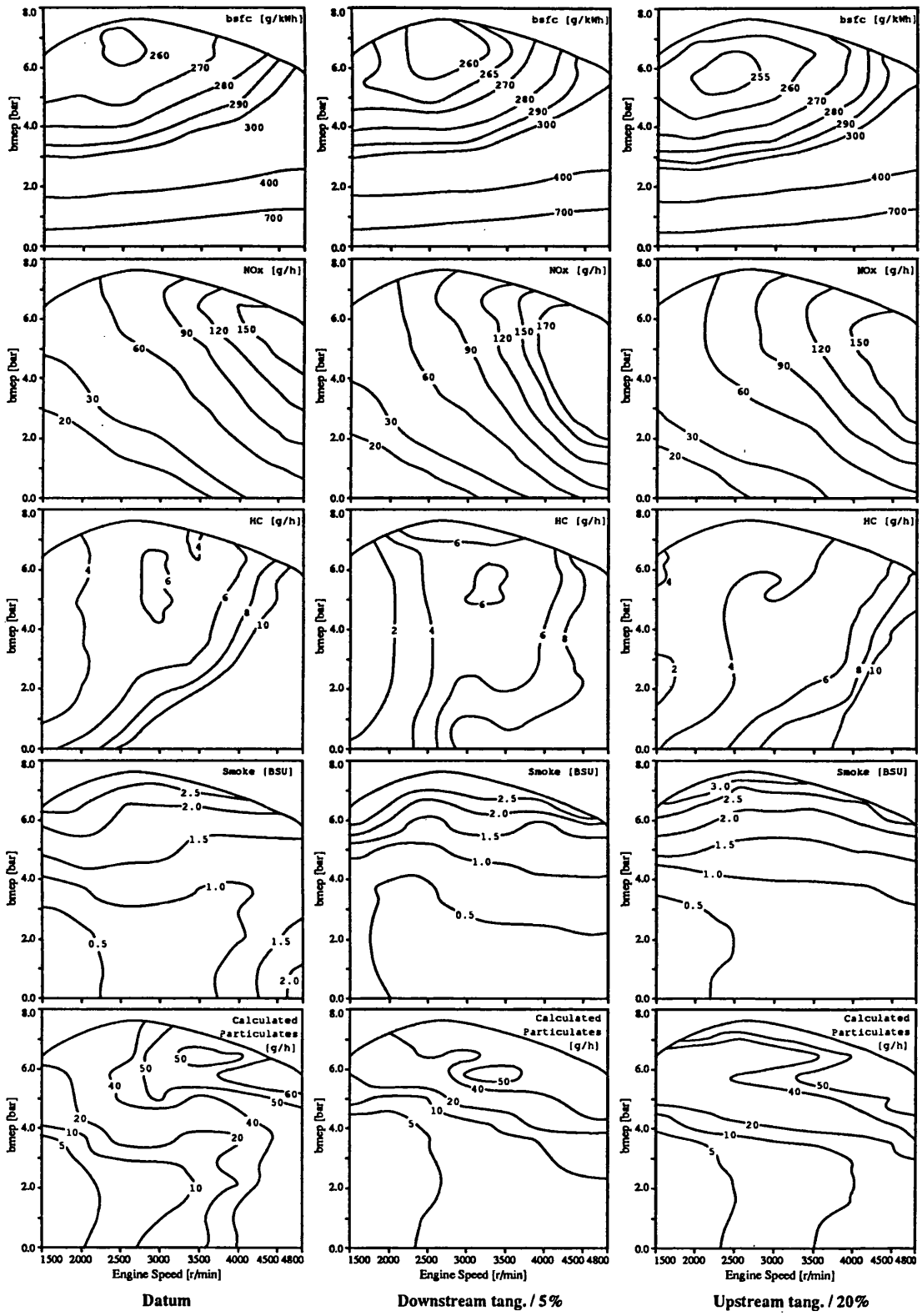

Figure 3c Experimental results for combination of glow plug and throat area

arrangement with a throat having a 20% increase in cross-sectional area. The fuel consumption is slightly improved over the datum design, whilst smoke and particulates are marginally improved. The NOx emission is slightly worse than the datum design.

Air Cell and Dual Throat Designs

Figure 3d shows the response of the engine to the dual throat and air cell designs.

The dual throat design has a fuel consumption characteristic which has a best value comparable with the datum build, but elsewhere on the map is

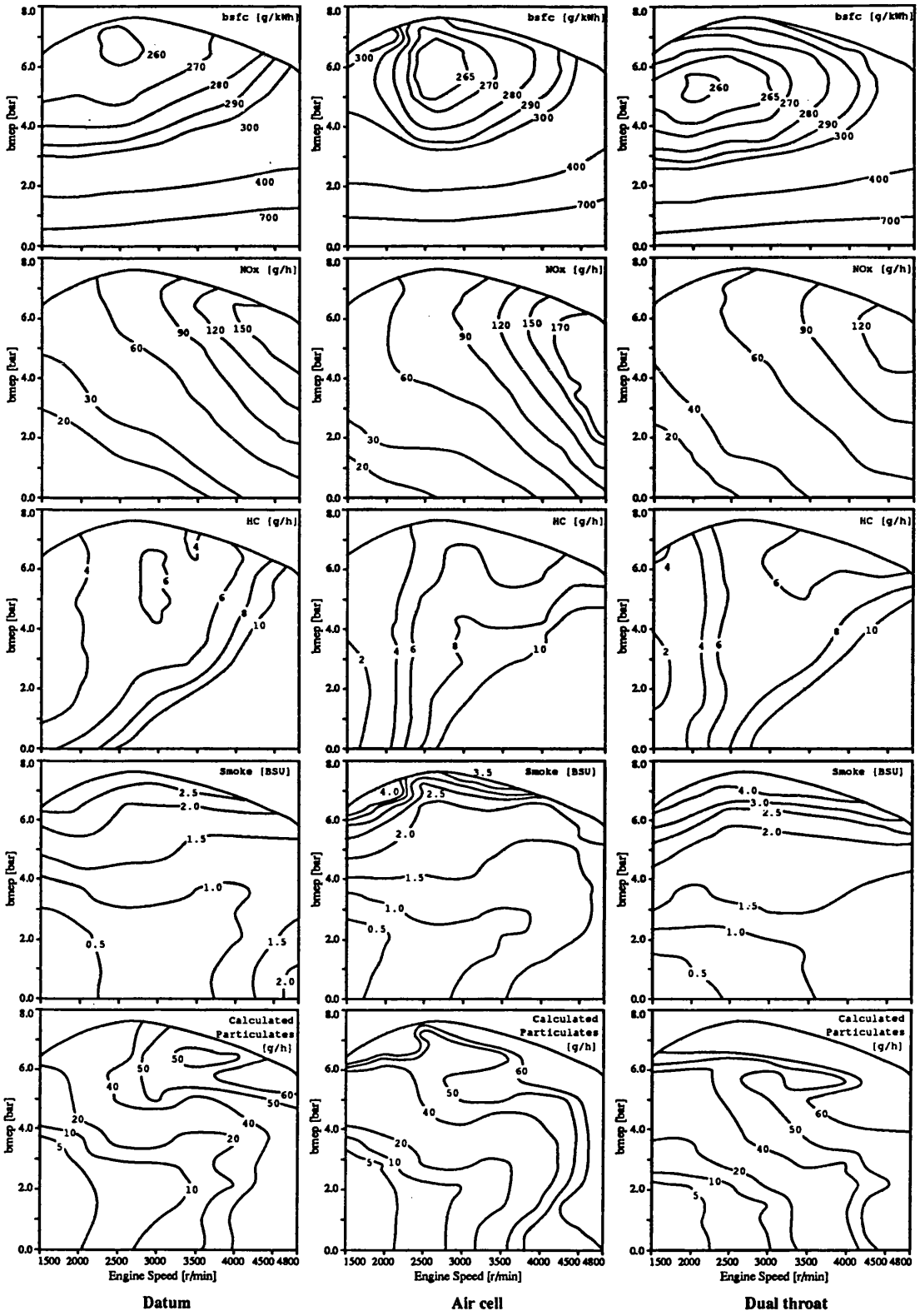

Figure 3d Experimental results for dual throat and air cell designs

considerably worse. The NOx emission is significantly reduced at high loads, from 150 g/h to 120 g/h (20%). The HC emission is little changed, however, the smoke characteristic is very much worse than the datum design. Smoke levels of more than 4 BSU are seen over most of the high load region. As a result of the higher visible smoke emission, the calculated particulates are seen to be increased, by as much as 50%.

The air cell design also has a fuel consumption characteristic which is somewhat worse than the datum. The best fuel consumption island being slightly higher at 265 g/kWh. The air cell design has

a higher NOx emission at high loads (150 g/h versus 170 g/h). The HC emission is little changed compared with the datum, whilst the visible smoke emission is significantly inferior at part loads and exhibits values in excess of 3.5 BSU at high bmep. Consequently, the calculated particulate emission is up to 50% higher than the datum.

4.2 Vehicle Testing

Having established that the downstream glow plug design gave the most encouraging results under steady-state dynamometer testing, this design was evaluated further by carrying out vehicle rolling road emission tests. Although a high degree of accuracy can be achieved from steady-state dynamometer testing by the close control of parameters such as water, oil and fuel temperature, there is an obvious difference with the transient nature of vehicle testing. This has become even more apparent recently as more and more emphasis is placed on exhaust emissions.

In order to obtain a direct comparison between the vehicle and dynamometer results, the fuel injection pump (FIP), cylinder head and injectors used on the dynamometer were transferred to the vehicle. Whilst on the dynamometer the FIP was set 3 degCA retarded, which earlier work had shown counteracted the increase in NOx seen with the downstream glow plug arrangement. This would most easily allow the advantage in the NOx-particulate trade-off to be seen. Vehicle testing was carried out on the rolling road facility at the Ford Research and Engineering Centre. The vehicle tested was a Ford Escort run with the chassis dynamometer set to simulate vehicle road load with vehicle inertia set to 1300 kg. Tests were run to the German emission cycle with the facility providing a second-by-second analysis of emissions throughout the drive cycle, including particulates, which were recorded in real-time using the Horiba TEOM analyser. Particulates were also measured in the traditional manner using a tunnel and weighed filter papers.

The vehicle was run with the datum cylinder head to establish a datum performance with which to compare the downstream glow plug design. The vehicle was finally returned to the datum build to enable the datum performance to be repeated in order to ensure the results were not subject to an underlying change in engine characteristics.

The vehicle emission and economy results are shown in Table 1, the datum results being an average of six tests, three run before the downstream design, three run after the downstream design. The results for the downstream design are the average of three tests. Figure 4a to c shows the real-time particulate measurement for the datum and the downstream designs, both being the average of three tests. The reduction of particulates predicted from the steady-state dynamometer testing is seen to have been confirmed in the vehicle although to a lesser

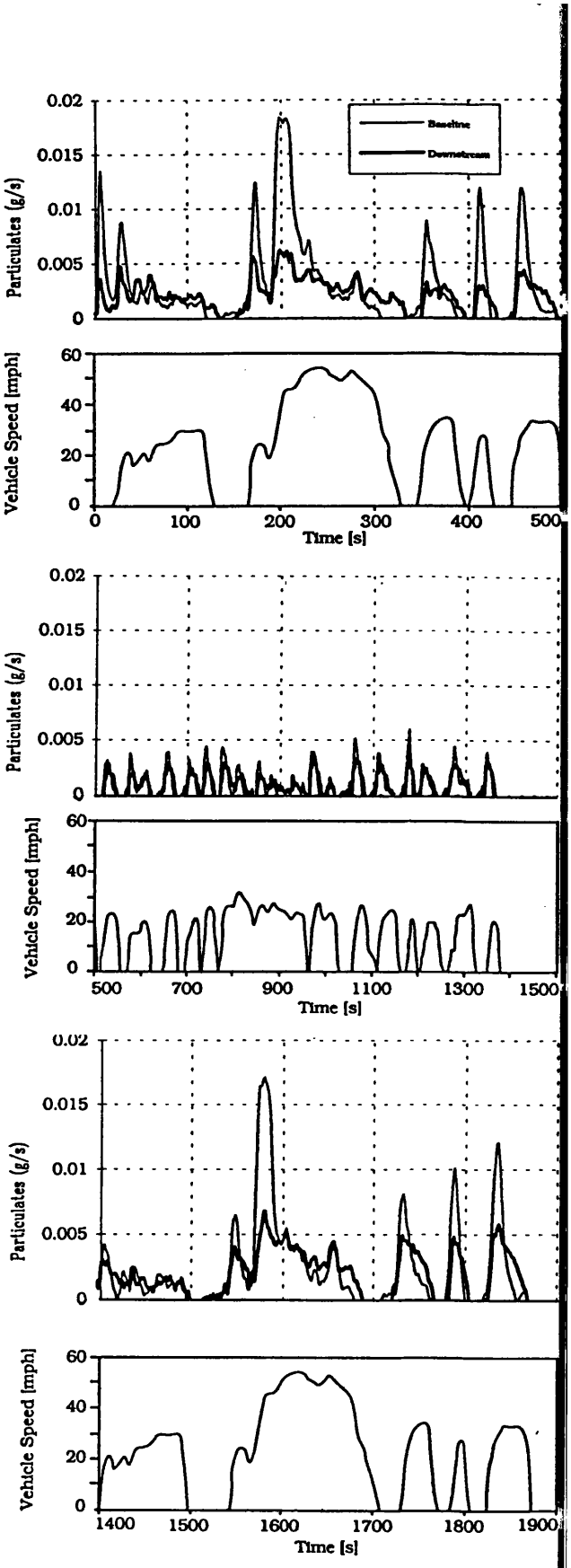

Figure 4 Real time particulate measurement during the FTP 75/German drive cycle.
Upper : Phase A (cold transient)
Centre : Phase C (stabilised)
Lower : Phase B (hot transient)

Table 1 Summary of results from the vehicle drive cycle tests - German Cycle

	HC	CO	CO2	NOx	Partics[1]	Partics[2]	Economy
Total	g/km	g/km	g/km	g/km	g/km	g/km	l/100km
Datum design	0.09	0.57	172	0.61	0.106	0.112	7.02
Downstream	0.18	0.61	174	0.53	0.077	0.083	7.14
Percentage gain	-100	-6.4	-1.5	+13	+27	+26	-1.7
Phase A (Cold 0-505 seconds Figure 4a)							
Datum design	0.14	0.76	183	0.67	0.174	0.222	
Downstream	0.27	0.74	183	0.57	0.106	0.134	
Percentage gain	-97	+1.8	+0.4	+15	+39	+40	
Phase C (Cruise 505-1372 seconds Figure 4b)							
Datum design	0.08	0.52	173	0.59	0.071	0.046	
Downstream	0.18	0.66	178	0.51	0.064	0.049	
Percentage gain	-124	-27	-2.8	+14	+9.8	-5.8	
Phase B (Hot 1372-1877 seconds Figure 4c)							
Datum design	0.08	0.53	159	0.60	0.120	0.154	
Downstream	0.12	0.42	161	0.56	0.079	0.110	
Percentage gain	-54.5	+21	-0.9	+7.7	+33.9	+28.6	

[1] Particulates measured by tunnel, [2] Particulates measured by TEOM real-time analyser.

extent, the vehicle averaging +27% against the test-bed +50%, compared with the datum. The most likely cause of the inferior particulates of the engine in the vehicle compared with the test-bed, is the increased hydrocarbon emissions seen in the vehicle results. This would appear to be a characteristic of the combustion system under transient conditions, particularly related to engine temperature. This latter point is borne out by the fact that the phase A hydrocarbons are much higher than the phase B hydrocarbons (0.14 g/km and 0.08 g/km), both phases being identical except that the engine is cold for phase A. This effect would be greatly reduced by the use of an oxidising catalyst, which would ameliorate the hydrocarbon contribution to the particulates, probably giving a gain over the datum design closer to the +50% seen on the steady-state test-bed. There was evidence of secondary injection occurring on this test which would have artificially increased the HC emission.

As with the particulate result the NOx result showed a different vehicle to test-bed relationship. Here the vehicle gave lower NOx levels than expected. The timing retard on the test-bed gave comparable results between the downstream and datum designs. The trend with engine temperature was, as expected, opposite to that of the hydrocarbons, the NOx being 13% less for phase A and 7.7% less for phase B. This reduction of NOx would indicate that a less retarded timing could be chosen if it was desirable to trade NOx for fuel economy.

Overall, the vehicle results confirmed the advantage of the downstream cylinder head design, showing the same improvement in the NOx-particulate trade-off as seen on the dynamometer. With the re-optimisation of injection timing for transient conditions and the addition of an oxidising catalyst it is predicted that a reduction of particulates of around 50% could be achieved with no increase in NOx or degradation of fuel economy.

5.0 CFD STUDY OF SWIRL AND TURBULENCE

CFD is now being used extensively by engine manufacturers in order to enhance understanding of mixing and combustion processes. Pinchon [9] reports work undertaken at the Institut Francais du Petrole on multi-dimensional modelling of combustion in an IDI Diesel engine. Zellat [10] reports on a similar investigation at Renault which included soot modelling. These studies used the KIVA code with the k-ε turbulence model, with other models added for ignition and combustion.

The CFD code STAR-CD was used to make a comparative study of the swirl and turbulence producing characteristics of the datum and downstream glow plug chambers. The program uses the finite volume numerical integration scheme to solve the Navier-Stokes equations for a wide range of flows. In this study the model requires a transient solution with compressibility, turbulence and a moving boundary to represent the piston crown. The simulation was run from a set of assumed initial conditions at the start of the compression stroke until the start of fuel injection close to top dead centre. The k-ε turbulence model was used in this study. This relates the Reynolds stresses and turbulent scalar fluxes to ensemble-averaged properties of the flow. k is the turbulent kinetic energy and ε is the dissipation rate. It is widely recognised that models of turbulence are inexact representations of the physical phenomena. The suitability of a particular model for a particular flow can only be established through experimental validation. Here, the CFD results are presented without validation and this should be borne in mind when considering the results presented. The

empirical coefficients used in the k-ε model for this work may be found in reference [7]. The mathematical models, numerical techniques and other details may be found in references [6-8].

The meshes used for the study are shown in Figure 5. It will be seen that advantage was taken of the vertical plane of symmetry through the combustion chamber in order to reduce the computer solution time. Each mesh consists of about 40,000 cells, which has been found to be a realistic compromise between accuracy of solution and computer solution time. The meshes are seen to include the swirl chamber, glow-plug, throat, cylinder and piston crown recess. The cylindrical portion on top of the swirl chamber is the bore into which the injector is located. The model not only provides for movement of the piston crown, in order to drive the flow, but a process of cell layer removal from the cylinder has to be used to prevent cells from becoming excessively misshapen as the piston approaches top dead centre. At the crank angle shown in Figure 5, the number of cell layers in the cylinder has been reduced to four in order to retain cell aspect ratio within acceptable limits for numerical accuracy.

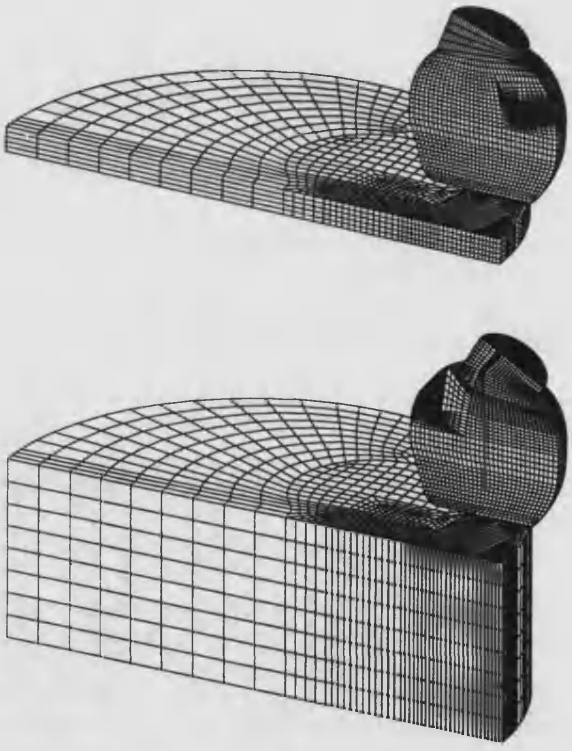

Figure 5 Computational meshes for the CFD study of air motion
Upper: cross flow glow plug
Lower: downstream tangential

Figure 6 compares the velocity distributions in the swirl chamber of the datum and downstream tangential designs, at 14 deg btdc and 3000 r/min. The velocity distributions are shown as contours for clarity of presentation. At this late stage in the compression stroke the velocity at exit from the throat exceeds 150 m/s, however, the velocity distribution is far from uniform and the highest velocities are concentrated on the throat side of the chamber. The velocity gradient in the direction of flow is steep, falling from 150 m/s to less than 100 m/s in about 180 deg of rotation about the swirl chamber centre. The cross flow glow plug is seen to obstruct the progress of the incoming flow and to redirect it slightly towards the centre of the chamber. This effect is, however, restricted to the relatively small area occupied by the glow plug. In both cases the flow takes up an approximately solid-body rotation, with a clearly defined swirl centre.

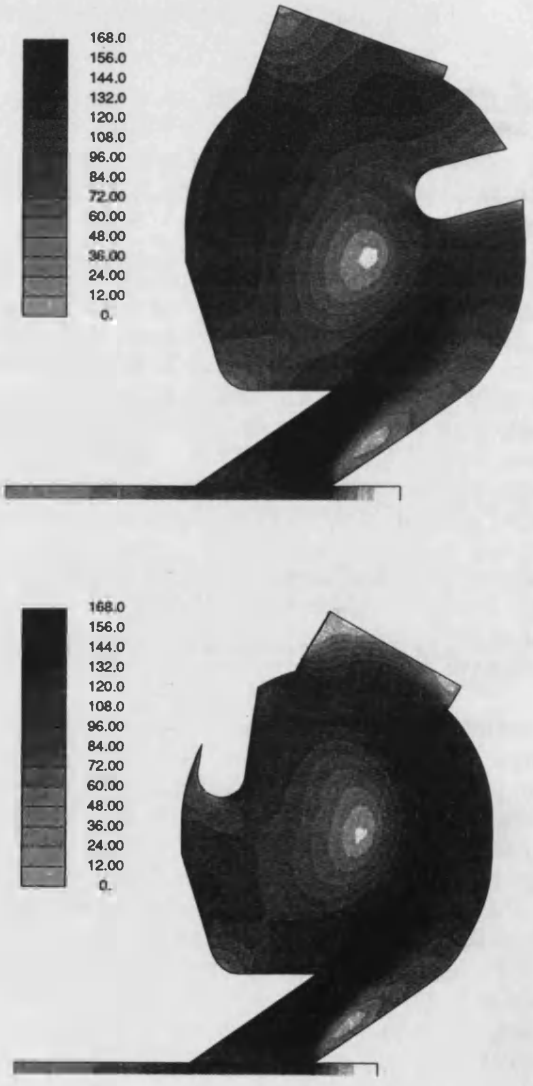

Figure 6 Calculated velocity distributions
Upper: cross flow glow plug
Lower: downstream tangential

Figure 7 shows contours of turbulent kinetic energy (k) calculated by the k-ε turbulence model. These show regions of high turbulence in the shear layers at the throat. The turbulence here will be convected into the chamber as the flow develops, as shown by the contours in the bowl. At this point in the compression stroke the turbulence distribution appears relatively unaffected by the glow plug location. There is some evidence that downstream of the cross flow glow plug the turbulence is of a slightly lower level, having been convected with a lower velocity due to the drag caused by the glow plug.

6.0 DISCUSSION

The experimental results show that the particulate emission may be reduced significantly by the adoption of a tangential glow plug arrangement, preferably in a location downstream of the injector, as shown in Figure 1c. The benefits observed during steady-state dynamometer tests were greater than the benefits seen during vehicle drive cycle tests. The steady-state results suggested particulate gains of up to 50%, whereas the actual drive cycle results showed a gain of only 27%. The differences were mainly due to the thermal lag of the engine, which ensures that much of the early part of the drive cycle is performed with chamber temperatures much lower than those obtained under steady-state tests. That this effect is real can be confirmed by comparing Figure 4a with Figure 4c. The former shows particulate emission from cold, whereas the latter shows particulate emission with the engine hot after more than 23 minutes of running. The integrated particulates for these parts of the drive cycle are 0.174 g/km and 0.120 g/km respectively for cold and hot phases, for the datum design, 0.106 g/km and 0.079 g/km for the downstream design. Particulate emissions would have been reduced even further but for the presence of secondary injection in the prototype FIE system.

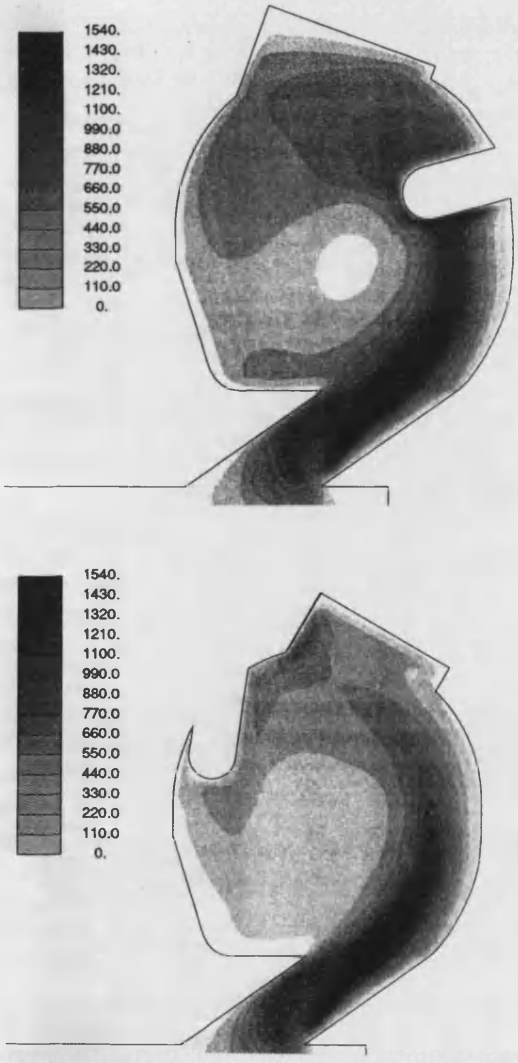

Figure 7 Turbulent kinetic energy distributions
Upper: cross flow glow plug
Lower: downstream tangential

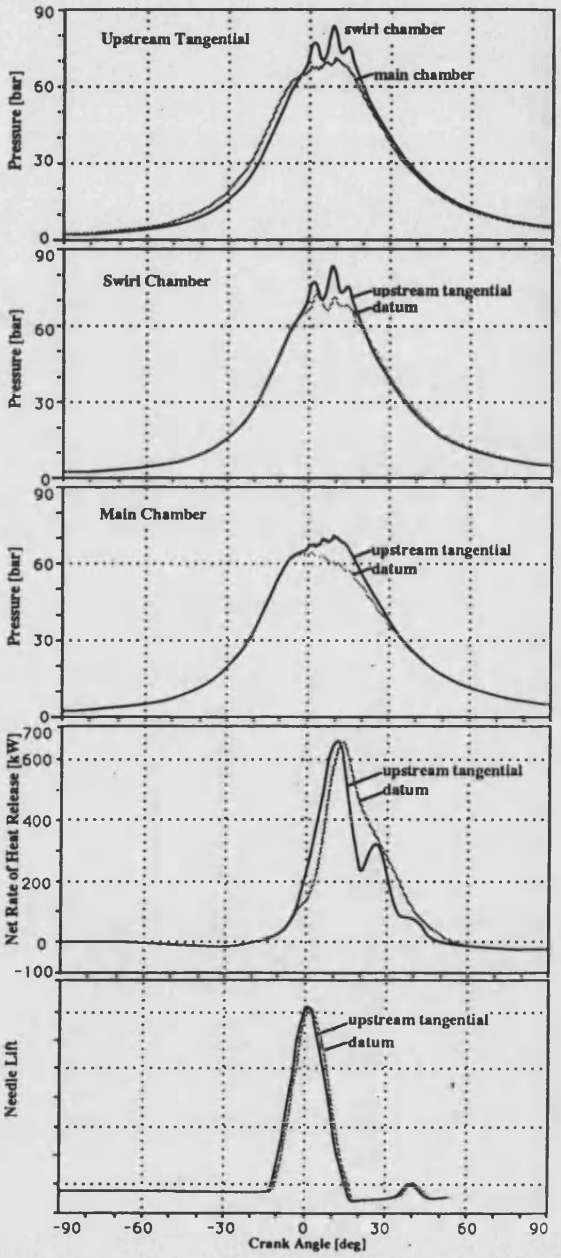

Figure 8 In-cylinder pressure, needle lift and heat release for the upstream tangential and baseline builds

It is evident from the marked change in emission performance between the datum and the tangential designs that combustion has been modified significantly. This is almost certainly due to an increase of swirl due to the less obstructive tangential design. Figure 8 shows pressure curves from the datum and upstream designs at a speed of 4000 r/min and a torque of 70 Nm (bmep = 5.0 bar). It may be seen that the swirl chamber and main chamber pressure curves are markedly different for the two cases. With the tangential glow plug the pressure in the swirl chamber rises both earlier and higher, indicating earlier, and possibly more rapid, combustion. This is confirmed by the rate of heat release, which was calculated by a single zone model based on swirl chamber pressure. The pressure development in the main chamber indicates that a higher proportion of combustion occurs in the main chamber with the tangential arrangement. This could explain the reduction of smoke and particulate emissions since the primary cause of those emissions is over-richness of the swirl chamber during combustion. It is possible that the early combustion seen in the swirl chamber, coupled with a changed swirl level, leads to the transfer of a larger proportion of the unburned fuel to the main chamber at an earlier stage. The assumed higher swirl level would be expected to provide better mixing in the swirl chamber, leading to a reduction of particulates and possibly earlier and faster combustion. Such a scenario is also consistent with the observed increase in NOx emission on two counts. Firstly, the change in combustion timing and rate would inevitably increase temperatures in the chamber. Secondly, the improved mixing characteristic would lead to less rich combustion giving higher flame temperatures.

The enlarged throat swirl chambers produced lower NOx emissions with increased particulates and smoke. From earlier work [3] it is clear that increasing the throat area will reduce swirl whilst also reducing pumping work.
In this case the reduced swirl appears to have made mixing worse, slowing down combustion and consequently reducing flame temperatures and NOx formation.

7.0 CONCLUSIONS

1. A number of alternative IDI Diesel engine swirl chamber concepts have been investigated in steady-state and transient experimental tests. The results show that particulate emissions may be significantly reduced by the adoption of a tangential glow plug, preferably downstream of the fuel injector. If injection timing is optimised for transient conditions and an oxidising catalyst is used, a reduction of particulates of around 50% could be achieved with no increase in NOx or degradation of fuel economy.

2. The downstream tangential glow plug arrangement appears to improve mixing, via its effect on swirl, such that combustion starts earlier. This leads to a more favourable distribution of combustion between the swirl chamber and the main chamber. Early transfer of fuel to the main chamber is thought to be important in reducing the formation of soot in the fuel rich regions of the swirl chamber.

3. The programme did not include evaluation of startability with the changed glow plug position, however, during experimental work the proposed arrangement did not appear to make starting any more difficult.

4. A CFD model has been used to study the generation of swirl and turbulence in the datum and downstream tangential swirl chambers. At 15 deg btdc, at an engine speed of 3000 r/min the differences between the two chambers are relatively small. On the central plane the cross flow glow plug deflects the incoming jet towards the centre of the chamber.

5. Novel dual throat and air cell chambers were investigated but gave relatively poor visible smoke emission, especially at higher loads. For the dual throat this was probably due to reduced swirl, for the air cell it may be due to the air in the cell being unavailable when needed for combustion.

ACKNOWLEDGEMENTS

The authors are grateful to the Ford Motor Company Limited for their support of this project and for permission to publish the research. The invaluable work of many others, in particular Ian Marsh and Martin Tanner at Bath University is acknowledged.

REFERENCES

(1) *Tanaka T, Sugihara K and Ueda T,* 'Improvement of IDI Diesel Engine Combustion Through Dual Throat Jet Swirl Chamber', SAE paper 861184, 1986.
(2) *Lawrence PJ, Knight D and Carnochan WA,* 'The Development of a 1.8 Litre Diesel Engine for Passenger Car Application' , IMechE Paper C382/070.
(3) *Tawfig M, Charlton SJ and Prest P,* 'An Investigation of Air Motion and Gas Temperature in a Motored Indirect-Injection Diesel Engine', Proc. IMechE, Conference on IC Engine Research in Universities, Polytechnics and Colleges, 30th-31st January 1991, pp143-150.
(4) *Greeves G, Wang C H T, Partridge I M and Black J R,* 'Improvements to Indirect Injection Diesel Combustion', IMechE Conference Publication C41/88, 1988.
(5) *Greeves G and Wang C H T,* 'Origins of Diesel Particulate Mass Emission', SAE Paper 810260, 1981.
(6) 'STAR-CD Version 2.1 User Guide', Computational Dynamics Limited, 1991.
(7) 'STAR-CD Version 2.1 Methodology - Part 1: Mathematical Modelling', Computational Dynamics Limited, 1991.
(8) 'STAR-CD Version 2.1 Methodology - Part 2: Numerical Solution Techniques', Computational Dynamics Limited, 1991.
(9) *Pinchon P,* 'Three Dimensional Modelling of Combustion in a Prechamber Diesel Engine', SAE Paper 890666, 1989.
(10) *Zellat M, Rolland Th and Poplow F,* ' Three dimensional Modelling of Combustion and Soot Formation in an Indirect Injection Diesel Engine', SAE Paper 900254, 1990.

APPENDIX - Basic Engine Data

Bore	82.5	mm
Stroke	82.0	mm
Swept volume	1.753	litres
Compression Ratio	21.5	
Firing order	1-3-4-2	
Nominal Datum Volume Ratio	0.50	
Nominal Throat Area / Piston Area	0.01	
Nominal Torque	110 Nm at 2500 r/min	
Nominal Power	44kW at 4800 r/min	
Injection timing	7 deg btdc at 1500 r/min 14 deg btdc at 4800 r/min	

C461/023/93

CFD study of air motion in a passenger car IDI diesel engine

B J SOMERVILLE, BEng, AMIMechE and S J CHARLTON, BSc, PhD, CEng, MIMechE
School of Mechanical Engineering, University of Bath
B NASSERI, PhD
Ford Motor Company, Basildon, Essex

SYNOPSIS

The paper describes a study of cold-flow air motion in a single cylinder of a small indirect-injection (IDI) Diesel engine during the compression and expansion strokes. Computational Fluid Dynamics is used to examine the effect of moving the cold-starting aid ('glow-plug'), and the effect of engine speed on swirl and turbulence. The sensitivity of the solution to the computational mesh-density, and numerical differencing scheme is investigated.
The study has shown that the predicted flow velocities and turbulence levels are sensitive to mesh density and differencing scheme.

1 INTRODUCTION

Since the introduction of the Diesel engine for automotive applications in the first decades of the century, designers have been steadily improving the engine. The result is that today's engines are clean, efficient power plants, that offer the user reliable and economical service over the life of the vehicle.

Since its inception, engine designers and manufacturers have conducted extensive research to improve the overall performance of the Diesel engine. A large percentage of this research expenditure has been directed towards engine testing: prototypes are built, tested and modified until a 'best' design is obtained.

Although development based on engine testing is an invaluable tool of the designer, it suffers a number of important drawbacks. Testing is time-consuming and expensive and often does not tell the engineer why a design change is having the observed effect on performance.

Computational Fluid Dynamic (CFD) techniques have the potential to allow the effect of a proposed design change to be evaluated relatively quickly, and to give the engineer a clear view of the effects of the design change on engine performance. The application of CFD to in-cylinder flows, however, is complex and the results obtained require careful evaluation. Validation of the results, either experimentally, or against some other theoretical or predictive technique increases confidence in the solution.

CFD is based on the numerical solution of the set of partial differential equations which govern fluid flow - the 'Navier Stokes' equations if the flow is incompressible. Although the solution of these equations defines the flow completely, it is usual to use empirically derived sub-models for a number of aspects of a calculation, most importantly the apparently random turbulent motion within the bulk flow, and combustion processes.

The purpose of this study is to apply CFD to the divided combustion chamber of the Indirect-Injection (IDI) Diesel engine, used in the majority of diesel passenger cars. This paper describes the investigation of 'cold-flow' in a single cylinder of a typical, small high-speed diesel engine during compression and part of the expansion stroke using the STAR-CD CFD package. To investigate the sensitivity of the solution to mesh density and numerical differencing scheme, the results on three mesh sizes and with Upwind and Central differencing have been compared.

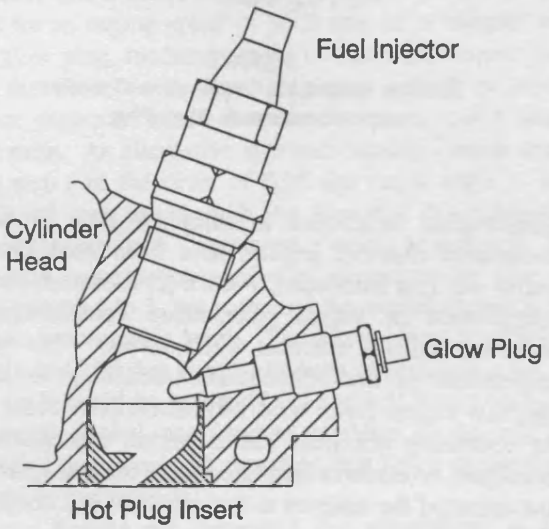

Figure 1
Ricardo Comet Vb Combustion Chamber

The widely used IDI Diesel combustion system developed by Ricardo (Figure 1), has remained largely unchanged for two decades. However, growing environmental awareness, and increasingly stringent exhaust emission legislation is forcing engine manufacturers to re-examine the combustion system, with a view to improving the fuel economy and exhaust emission levels, without sacrificing performance. To support experimental work undertaken at Bath University (1), CFD models are being used to examine the effects of various modifications to the standard Ricardo Comet Mk Vb combustion system. In this system, the piston moving in the main chamber forces air into an auxiliary or swirl chamber, creating a highly turbulent ordered swirling motion. The high air velocities, and the large surface area mean that even with the relatively high compression ratios, convective heat transfer losses are such that an electric cold-starting aid ('glow plug') is required in production engines.

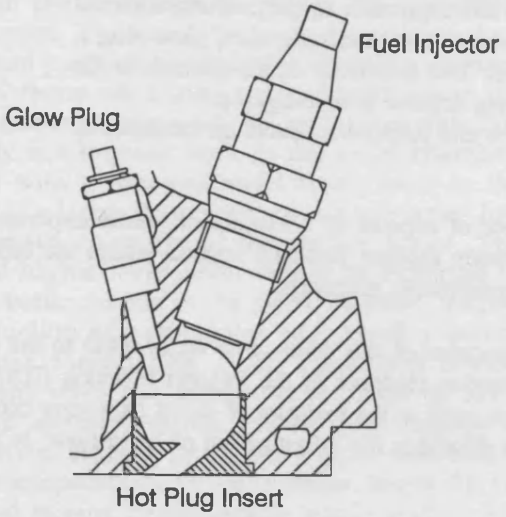

Figure 2
Ricardo Comet Vb Combustion Chamber with Downstream Glow Plug

Mathematical techniques to study air flow in divided combustion chamber engines have been used since the engine was first introduced. Alcock (2) used mass flow and conservation of angular momentum considerations to estimate auxiliary chamber swirl levels. The earliest applications of multi-dimensional modelling to indirect injection engine flows used two-dimensional codes (3,4). As computing resources and numerical algorithms have developed, researchers have used more realistic geometries and extended the analysis to fuel injection and combustion (5-8).

2 MESH AND DISCRETISATION

An accurate geometric model of a single cylinder of a Ford 1.8 litre IDI combustion system (Figure 1) was built using the PATRAN (release 2.5) mesh generator. The model includes the piston recess, main chamber, auxiliary chamber ('swirl chamber') and glow plug. Features of the engine that have not been modelled are the valve recesses, piston rings, the annulus of air between the glow plug and the cylinder head, and the surface details of the fuel injector. In the results presented here, to reduce computational time, the piston recess is not included in the mesh. To compensate for the valve recesses and the flat piston top, the top-dead-centre (tdc) clearance has been increased to maintain the correct compression ratio. As the valve recesses are not included in the model, the symmetry plane can be used to reduce the computational effort. Table 1 lists engine data and the corresponding model parameters.

	FORD 1.8 IDI Engine	CFD Model
Stroke mm	82	82
Bore mm	82.5	82.5
Compression ratio	21.5	22.4
Volume ratio	0.50	0.47
Throat Area / Cylinder Bore	0.01	0.01

Table 1
1.8l engine and CFD model parameters

The solution algorithm in STAR accepts an unstructured body-fitting mesh with a range of cell shapes. The meshes used in this study contain only hexahedral ('brick') elements.

For an investigation of the effect of mesh density and differencing schemes, three models of identical geometry, but with varying numbers of cells have been generated (Table 2). The geometry is that of the Ford 1.8

Mesh Density	Cells in Swirl Chamber	Total Number of Cells	Characteristic length of swirl chamber cell (mm)
Low	5 000	17 000	1.3
Medium	18 000	40 000	0.8
High	87 000	120 000	0.5

Table 2
Details of Computational Meshes

litre engine, but without the glow plug. The model without a glow plug is a useful datum case and allows results to be displayed on the central plane without the distraction of trying to visualise a three-dimensional flow (around the glow plug) in two-dimensions. The effect of increasing the mesh density is greatest in regions where high velocity gradients exist. In this study the mesh density has been

increased in the throat and swirl chamber, keeping the number of cells in the main chamber relatively constant.

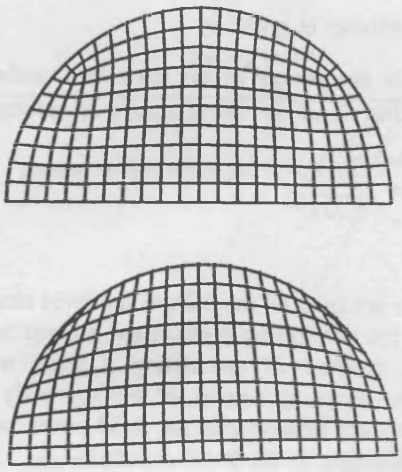

Figure 3
Swirl Chamber Mesh Structure

Early tests showed that the swirl chamber cross sectional area shown in the upper mesh in Fig 3 gave a considerably faster solution than in the lower. This mesh structure has been used for all meshes from which results are presented here.

In addition to the 'baseline' combustion chamber geometry and a case without a glow plug, results from a medium density model with a downstream (relative to the injector) glow plug are presented (Figure 2). An engine with this geometry has achieved good results experimentally (1).

Changing the engine geometry changes the engine volume and hence the compression ratio. To allow direct comparison of the results from models with different swirl chamber geometries, the volume of the passage adjacent to the fuel injector has been modified. This ensures that the swirl chamber volumes are identical in each model, thus maintaining the same compression and volume ratios for each geometry.

3 SOLUTION PARAMETERS

Starting at bottom-dead-centre (bdc), a subroutine defines the position of the cylinder mesh as a function of time - thus 'moving' the mesh. To maintain acceptable cell aspect ratios in the main chamber, the 15 layers of cells at bdc are reduced to 4 by successive removal of cell layers during the compression.

Table 3 shows the main parameters used for the cases presented here. Turbulence is modelled by the two equation k-ε model. It is generally accepted that the k-ε model is an inexact representation of the physical phenomenon it models, but is used in this study in the absence of a more suitable alternative.

INITIAL CONDITIONS	
Pressure	1 bar
Temperature	20 deg C
Turbulence	negligible
Air velocities	zero
BOUNDARY CONDITIONS	
Wall	Adiabatic
Symmetry plane	
SOLUTION PARAMETERS	
Solution algorithm	PISO
Solving for three components of velocity, pressure, temperature, turbulence energy and its dissipation	
Engine speed	3000 rpm
GAS PROPERTIES	
Dry Air, Perfect Gas	

Table 3
Computational parameters

The solution time steps were chosen on the basis of the largest time step that would give acceptable temporal accuracy and a stable solution. Table 4 lists the time steps used for an engine speed of 3000 rpm on a 'simple' mesh (no glow plug, medium density). The high density mesh, and the downstream glow plug case (which included a higher degree of mesh distortion) required much smaller time steps. An alternative approach: setting a much smaller time step (of the order of 0.05 deg crank angle (CA) at 3000rpm) was tested, with the idea that fewer iterations within the time step ('correctors') would be required. This approach reduced the number of correctors per time step from around 5 to 3, but increased the overall computational time to unacceptable levels. The solution was generally run until around 20 deg atdc. Although in principle a full 360 deg cycle could be modelled (adding cell layers during the expansion stroke), any features exhibited by the cold flow after this time would be swamped in a firing engine by the effects of combustion.

Results are presented for simulations at three engine speeds, 1500rpm, 3000rpm and 4500rpm. The comparisons of mesh density and differencing scheme have been run at 3000rpm.

Most computational fluid dynamic packages offer various differencing schemes, the most common being *Upwind* and *Central* differencing. The differencing scheme defines how the flow in a computational cell influences the flow in its neighbours. In the Upwind scheme, the major component of the flow in a cell is determined only by the flow in the cell immediately 'upstream'. In a high

	Cycle Crank Angle	Number of steps	Crank Angle step	Time step (micro-seconds)
1	-180 to -60	80	1.5	83
2	-60 to -30	60	0.75	28
3	-30 to 2	140	0.4	11
4	2 to 32	75	0.75	22

Table 4
Time steps for medium density model without a glow plug

Reynold's number flow with the flow streamlines aligned with the mesh, this has been shown to be a reasonable assumption. In a swirling flow however, where flow streamlines cross 'skew' to the mesh, the upwind scheme is known to underpredict angular velocity. In the Central differencing scheme the cell flow is influenced by the flow in cells both upstream and downstream. This leads to a more accurate representation of the flow, but the scheme suffers from the drawback that it can become numerically unstable. The STAR Self-Filtered Central Differencing scheme aims to overcome this restriction by detecting numerical instabilities and 'blending' in the Upwind scheme.

In comparison to traditional methods of engine testing, CFD presents the engineer with a considerable quantity of data. For each cell in the mesh, the values of each of the parameters being solved are available at each time step during the solution. Efficient use of computing resources demands that care is given to selecting the data to be stored and to the methods used for storing them. The technique adopted by the authors was to link a subroutine to the solver, to control data output to a binary results file stored for post-processing. This approach allowed only those data needed for post-processing to be stored (for instance all swirl chamber velocities, but not the main chamber values) and some data-reduction (for instance averaging of cylinder pressures) to be performed *during* the main solution phase. Although contour and velocity-vector plots provide an overview of the predicted flow, further data reduction is required to provide the engineer with more useful parameters for comparing results. For the results presented here, the parameters *swirl number* and *average turbulence* have been selected.

Swirl Number

Swirl number is a measure of the angular velocity of the air motion in the swirl chamber relative to engine speed, calculated as

$$N_s = \frac{\textit{Angular velocity of swirl } (\omega)}{\textit{Engine Speed}}$$

where angular velocity is given by

$$\omega = \frac{\textit{Angular momentum of air mass in chamber}}{\textit{Total inertia of air about centre of rotation}}$$

$$= \frac{\Sigma I\omega}{I} = \frac{\Sigma m V_r k}{\Sigma m k^2}$$

The summations are over all the cells in the swirl chamber, except those in the connecting passage and around the fuel injector. This method of calculating a swirl number assumes that the air mass rotates as a fixed body. All results presented here assume that the swirl centre is fixed in the geometric centre of the swirl chamber.

Turbulence

Turbulent kinetic energy is a measure of the size of the local fluctuations in fluid velocities imposed on the bulk flow. The results for turbulence are calculated as a mass weighted average for all the cells in the swirl chamber. The units are of velocity squared (m^2/s^2).

Swirl number and turbulence are both important parameters for flow and combustion modelling in the engine. The swirl levels determine how quickly vaporised fuel is carried away from the fuel injector and fresh air supplied to the burning gases. Turbulence levels affect the rate of localised air / fuel mixing and flame propagation rates.

4 RESULTS

4.1 Results overview

Figure 4 shows the results obtained from a medium density mesh at 3000rpm for the standard engine geometry with a glow plug. Vector plots of the flow field are presented at 120 deg and 16 deg before top-dead-centre (btdc) and at 10 deg after tdc. As the piston moves from the bottom of its stroke, air is forced through the connecting passage into the swirl chamber. At 120 deg btdc, an ordered swirling pattern is observed in the swirl chamber, with the centre of swirl near the exit of the connecting passage. The swirl number increases to a peak at 15 deg btdc with the swirl centre near the geometric centre of the swirl chamber, before decaying. The primary source of turbulence generation is the connecting passage. Turbulence generated by the velocity shear layers in this region is convected into the swirl chamber by the flow. The peak average turbulence level in the swirl chamber is at 15 deg btdc, slightly later than the point at which the velocity through the throat is highest (19 deg btdc). As the amount of air flowing through the connecting passage reduces, towards tdc, the rate of dissipation of turbulence in the swirl chamber, exceeds the rate of generation of turbulence (principally in the

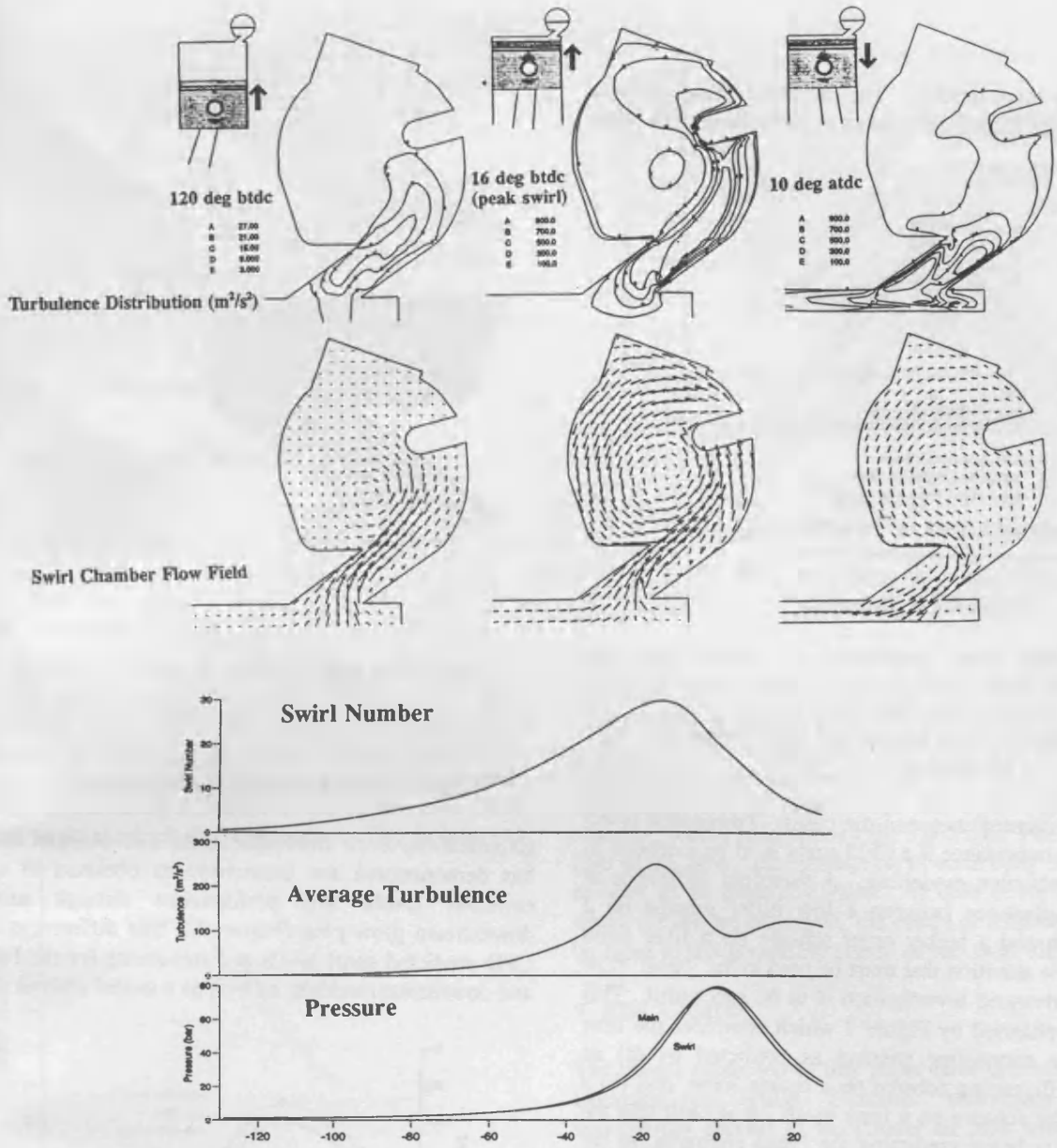

Figure 4

connecting passage), and the overall level of turbulence is reduced. The turbulence levels in this part of the cycle are of particular importance, as it is in the period following 15 deg btdc that, in a firing engine, fuel injection takes place.

The main and swirl chamber pressure traces in Figure 4 have been shown to be a close fit to the theoretical $pv^{1.4}$ = constant compression/expansion required of the adiabatic process being modelled. A pressure difference between the main and swirl chambers can clearly be seen. It is interesting to note that the swirl chamber pressure overtakes the main chamber pressure before the piston reaches the top of its stroke. Although the piston is moving more slowly, the momentum of the fluid in the connecting passage continues to transfer air into the swirl chamber, against the pressure gradient.

4.2 Effect of mesh density and differencing scheme

Figures 5 and 6 compare predicted swirl number and turbulence for a combustion chamber with no glow plug. The curves show the results from the three mesh densities, each with an upwind (UD), and a blended central differencing scheme (SFCD). The geometry and boundary conditions are identical for each case, so that every curve is an approximation to the **same** actual flow field. The filtered Central Differencing scheme predicts swirl levels 20% greater than the UD for the low density mesh, and 15% greater for the high density mesh, with the CD scheme predicting that the peak swirl will occur slightly later in the cycle. It is obvious from the swirl plot that the finer meshes and higher order schemes are resolving the flow better. During swirl generation, the UD scheme generates swirl at a slower rate than the CD scheme, and predicts that

it will decay more quickly. The increased velocities may explain the significant differences in turbulence (with units

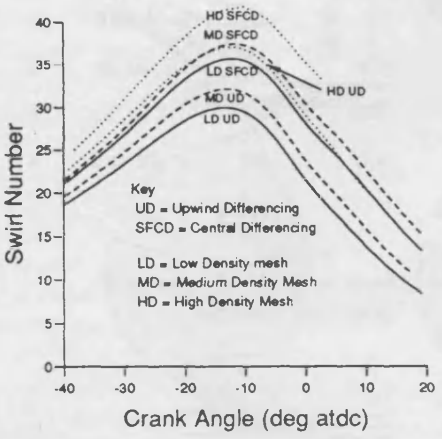

Figure 5
Effect of Mesh Density and Differencing Scheme on Swirl Number

of velocity squared) between the cases. Turbulence levels are of great importance if a CFD study is to be extended to include combustion modelling. A threefold difference in predicted turbulence between a low order scheme on a coarse mesh and a higher order scheme on a finer mesh illustrates the attention that must be paid to the 'basic' flow if a more advanced investigation is to be successful. This point is emphasised by Figure 7 which compares the flow field in the connecting passage as predicted by (a) an Upward Differencing scheme on a coarse mesh, and (b) a Higher Order scheme on a finer mesh. It is clear that the finer mesh is better predicting the 'vena contracta' in the throat.

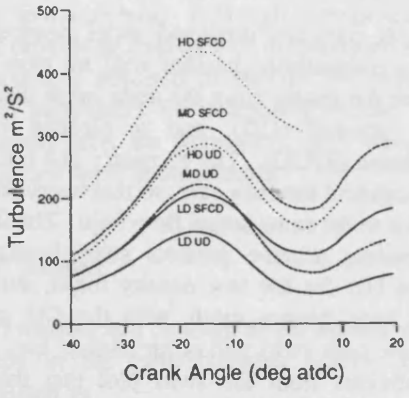

Figure 6
Effect of Mesh Density and Differencing Scheme on Swirl Number

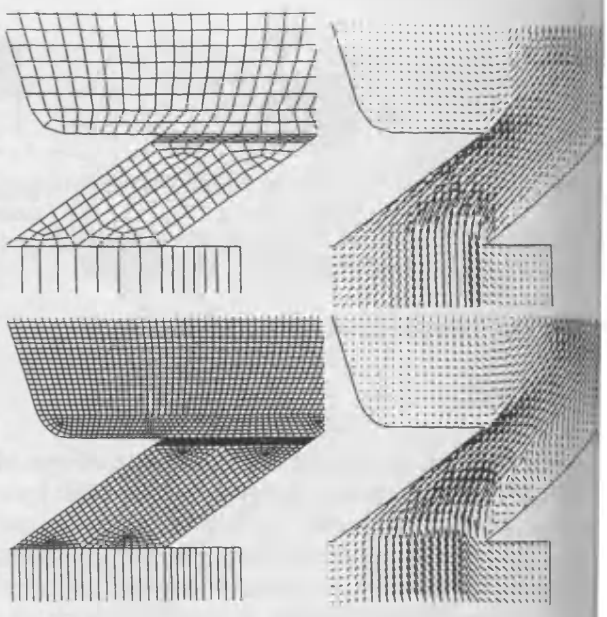

Figure 7
Throat flow field predicted by coarse and fine meshes

4.3 Effect of engine geometry modifications

Experimental work undertaken at the University of Bath (1) has demonstrated the improvements obtained in engine emission levels and performance through using a downstream glow plug (Figure 2). The differences in the CFD predicted swirl levels and turbulence for the baseline and downstream models, as well as a model without a glow

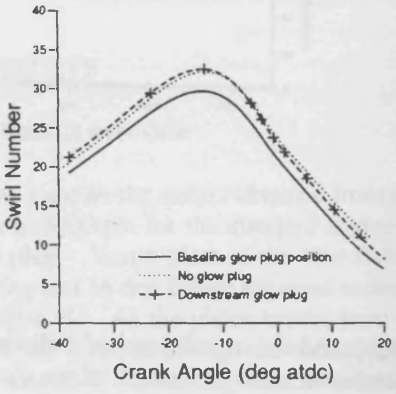

Figure 8
Effect of Glow Plug Position Swirl Number

plug are shown in Figures 8 and 9. Placing the glow plug downstream (into a region of lower mean velocity) appears to cause little reduction in swirl levels compared with a combustion chamber without a glow plug - the two lines are almost coincident. The standard cross-flow glow plug is seen to be obstructing the swirling flow, reducing swirl levels by over 10%, and increasing average turbulence by around 15%. Although the downstream glow plug does not significantly alter swirl levels, the average turbulence in the downstream case is significantly greater than that for the case without a glow plug.

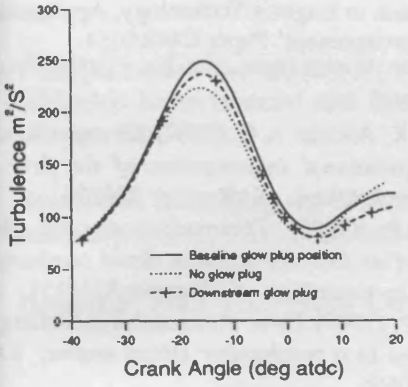

Figure 9
Effect of Glow Plug Position on Turbulence

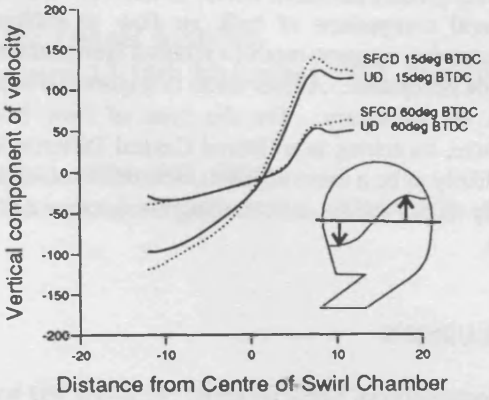

Figure 11
Velocity Profiles across Swirl Chamber

4.4 Effect of engine speed

Figure 10 shows predicted swirl levels for engine simulations at 1500, 3000, and 4500rpm, calculated on a medium density mesh with an upwind differencing scheme. The peak swirl values are very similar in all three cases. The effect of increasing the speed of the engine is to delay the crank angle at which the peak occurs. This is believed

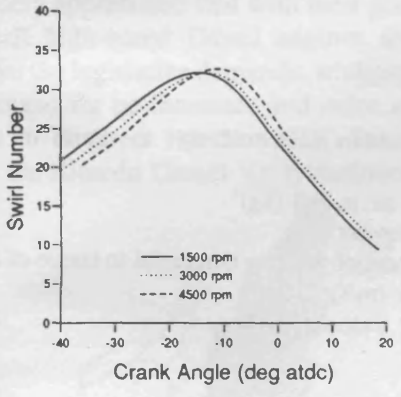

Figure 10
Effect of Engine Speed on Swirl Number

to be due to the 'vena contracta' effect in the connecting passage varying with air velocity. At higher engine speeds, the effective area of the passage is reduced, reducing the mass flow (per crank angle) through the throat, and leading to larger pressure differences between the two combustion chambers.

4.5 The assumption of solid body rotation

Velocity profiles along the horizontal axis through the geometric centre of the swirl chamber are shown in Figure 11. For crank angles 60deg and 15deg (peak swirl) before top dead centre, the predicted velocity profile for both the Upwind and Central Differencing schemes are presented.

When the method of calculating 'swirl number' was discussed above, the assumptions were made that the air mass rotated as a solid body, and that it rotated about the geometric centre of the swirl chamber. For perfect solid body rotation, each line on this figure would be expected to be straight, and if fixed about the centre of the swirl chamber, would pass through the 0,0 origin. For the central core of the flow, the assumption of solid body rotation can be seen to be generally valid. At both crank angles, for which results are displayed, the centre of rotation is seen to be close to the geometric centre of the swirl chamber.

5 DISCUSSION

The results presented in this paper have demonstrated that Computational Fluid Dynamic techniques can be successfully applied to in-cylinder air flow investigations. A detailed understanding of the basic processes occurring in an internal combustion engine is essential if the engine is to be improved substantially: CFD presents the engineer with information that would be difficult or impossible to obtain using experimental techniques and engine testing. The technology available, however, for in-cylinder CFD investigations is not yet sufficiently mature to allow the engineer to accept the results produced as 'correct' without further validation. Some validation is possible by comparing the results obtained with 'theoretical' or exact mathematical solutions. To support the computational work presented here, a Laser Doppler Anemometry (LDA) study of the auxiliary combustion chamber air-flow is being undertaken at Bath University, and results from this study will be published in the near future.

The differences in the predicted in-cylinder velocities presented above illustrate that computationally realistic models will not generate 'mesh independent' solutions: refining the computational mesh will change the results obtained. Although no validation data are available, the results suggest that CFD is generally underpredicting the angular velocity of the swirling air flow. The coarser mesh

does however predict the same trends as the finer meshes. For a general comparison of bulk air flow in different engine geometries, a coarse mesh (= reduced computational time) may be acceptable. A finer mesh is required, if better predictions are necessary. For the type of flow being modelled here, switching to a filtered Central Differencing scheme is likely to be a more efficient method of increasing the accuracy of the results, than running the solution with a finer mesh.

6 CONCLUSIONS

1 Computational Fluid Dynamic modelling has been successfully applied to an in-cylinder adiabatic compression / expansion and the results at different engine speeds compared. The numerical solution generates a large amount of output, which requires careful 'post-processing' if it is to provide a useful tool for detailed investigation of fluid flow.

2. Comparison of the results obtained from three meshes of varying cell density shows that the finer meshes better resolve the flow, and predict higher overall velocities, swirl levels and turbulence. It is likely that a 'mesh-independent' solution would require many more cells than the high density model used here.

3. For a given mesh, the filtered Central Differencing scheme predicts significantly higher velocity, swirl and turbulence levels when compared to a standard Upwind scheme. The CD scheme predicts a greater rate of production of swirl and a lower rate of swirl decay than the UD scheme.

4. An investigation of the air flow in three different combustion chamber geometries has shown that CFD is a useful tool with which to study the effect of geometry modifications on overall air flow.

5. The assumption that the swirl generated in an IDI Diesel engine rotates as a solid body about the geometric centre of the auxiliary chamber has been shown to be reasonable. Swirl number remains approximately constant at the three engines speeds investigated, but the crank angle at which the peak swirl occurs is retarded at higher speeds.

ACKNOWLEDGEMENTS

The authors are grateful to the Ford Motor Company and the SERC for their support of this project.

REFERENCES

1. Charlton S, Cox A, Somerville B, Watts M, Horrocks R, (1992) *An investigation of the emission characteristics of the passenger car IDI Diesel engine* **Proc IMechE** Conference 'Combustion in Engines Technology, Applications and the Environment' Paper C448/0251.
2. Alcock J F, (1934) *Air swirl in oil engines* **Proc IMechE** Vol 128
3. Meintjes K, Alkidas A C, (1982) *An experimental and computational investigation of the flow in diesel pre-chambers.* **SAE** paper 820275
4. Pinchon P, (1985) *Thermodynamic and flow analysis of an indirect injection diesel combustion chamber by modelling.* **SAE** paper 8510151
5. Pinchon P, (1989) *Three dimensional modelling of combustion in a prechamber Diesel engine.* SAE Paper 890666
6. Zellat M, Rolland Th, Poplow F. (1990) *Three dimensional modelling of combustion and soot formation in an indirect injection Diesel engine.* SAE paper 900254
7. Boretti A, Nebuloni P, Lisbona M, Milazzo P, (1992) *Diesel engine combustion chamber design with three-dimensional flow computations.* **Proc IMechE** Conference 'Combustion in Engines Technology, Applications and the Environment' Paper C448/005
8. Somerville, Charlton, MacGregor, Nasseri (1993) *A study of air motion in an IDI passenger car diesel engine. Proc IMechE Conference* 'Experimental and Predictive Methods in Engine Research and Development. Paper C465/029

NOMENCLATURE

k	distance from centre of cell to centre of swirl chamber (m)
m	mass of air in cell (kg)
N_s	Swirl Number
V_r	Component of velocity tangential to centre of swirl chamber (m/s)
ω	Angular Velocity (s^{-1})

A study of air motion in an IDI Passenger Car Diesel Engine

(IMechE Experimental and Predictive Methods Conference, 17-18th November 1993, Birmingham NEC)
Paper C465-002

Somerville B J, BEng, AMIMechE. Charlton S J, BSc, PhD, MIMechE, CEng.
MacGregor S A, BSc, PhD, MIMechE, CEng. School of Mechanical Engineering, University of Bath

Nasseri B, PhD Ford Motor Company Limited

SYNOPSIS

Predictive methods have been used to model the non-combusting air flow in the divided combustion chamber of an Indirect Injection (IDI) passenger car Diesel engine. The effect of engine design changes on the flow field are investigated with emphasis on the position of the cold starting aid.

1 INTRODUCTION

Faced with stringent exhaust-emission requirements, engine manufacturers are using increasingly advanced tools to improve passenger car engine design. It is widely appreciated that with their good fuel economy, small high-speed Diesel engines are well-placed to meet the legislative demands, whilst meeting consumer demand for performance and noise levels.

Indirect Injection (IDI) Diesel engines based on the Ricardo Comet Vb system are produced by the majority of Diesel passenger car manufacturers. Such engines use a divided combustion chamber with the two chambers connected by a narrow passage (throat) (Fig 1). During the compression stroke, air is forced through the connecting passage, forming a turbulent swirling air motion in the swirl chamber. Fuel is injected into this auxiliary chamber and the swirling air motion promotes the good air / fuel mixing needed for efficient combustion. Convective heat losses during compression are such that even with relatively high compression ratios, a cold-starting aid ('glow plug') is required.

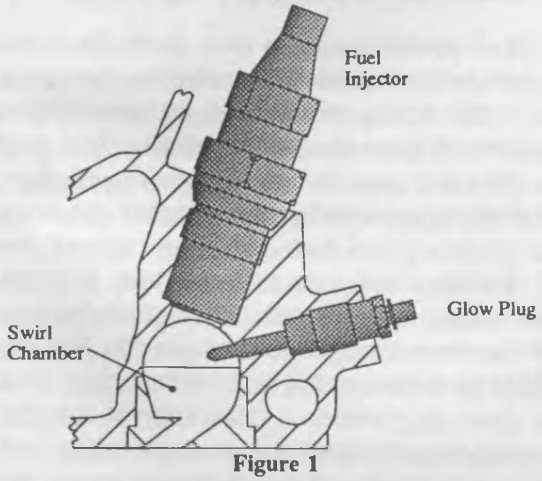

Figure 1
Ricardo Comet Vb Combustion Chamber with Crossflow Glow Plug

As part of an experimental and predictive investigation of non-combusting flow in a typical IDI Diesel engine, Computational Fluid Dynamic (CFD) techniques have been used to predict the compression and expansion flow fields in the FORD 1.8l IDI Diesel engine. This paper discusses the application of such predictive techniques to realistic in-cylinder engine flows, examines the flow in an IDI Diesel engine, and highlights the need for accurate experimental data to generate and validate the predicted data. The effects of a number of design changes on air flow are evaluated, with emphasis on the position within the auxiliary chamber of the cold-starting aid. Experimental studies undertaken at Bath University (1) have shown that moving the glow plug from its crossflow position (Figure 1) to a downstream (of the injector) position (Figure 2)

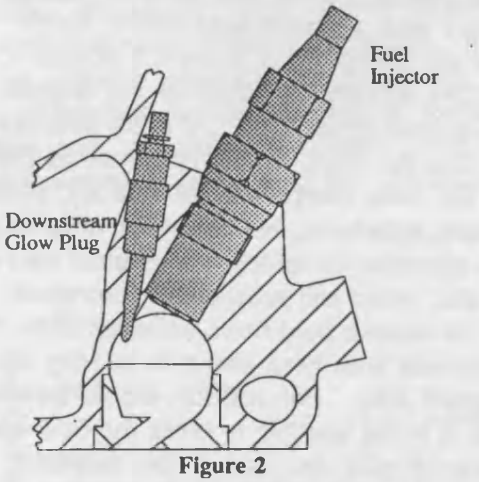

Figure 2
Ricardo Comet Vb Chamber with Downstream Glow Plug

significantly improves exhaust emissions and engine performance.

As the computing hardware and codes have become available in the last few years, a number of organisations have used predictive techniques to investigate auxiliary chamber non-combusting flows, air/fuel mixing and combustion (2)-(5). Due to the complicated geometry of a divided combustion chamber engine, there have been few experimental studies of auxiliary chamber air flow in production-type engines. Numerical prediction of in-cylinder flows is a relatively new technology and little has so far been published on realistic experimental in-cylinder investigations to validate predicted flow studies.

2 USING PREDICTIVE METHODS

Predictive models of engine flows are based on finding numerical solutions to a set of mathematical equations. The flow domain to be investigated is broken down into a series of straight-edged bricks, known as *cells* to form a mesh, and starting from assumed engine conditions at bottom-dead-centre (bdc) before compression, the equations are solved over a series of crank angles. For a given engine speed, at every time step the position of the piston defines the force driving the in-cylinder flow. Generally, the greater the number of cells, the more accurate the predicted flow will be. The results presented in this paper are computed using the STAR-CD package (6), on meshes with approximately 40000 Cells. The solutions are calculated at every 1.5 degrees Crank Angle (CA) initially, reducing to 0.4 degrees CA around top-dead-centre (tdc). At every time step, for every cell in the mesh, the numerical model predicts a value for three components of velocity, pressure, temperature, turbulence, and dissipation of turbulence. As with experimental testing, the required data must be recorded, stored and subsequently processed.

For laminar fluid flows, solutions of the fluid-flow equations have been shown to be very close to experimental data. For realistic engine geometries however, it is not possible to break the flow domain into enough cells to resolve the turbulent flow variations and modelling of turbulence is introduced. The results presented here are computed using the well-known two equation k-ε model which calculates values for turbulence (k) and its rate of dissipation (ε) as a function of the local velocity field. This turbulence model is known not to model recirculating and attaching flows accurately, but is widely used for many flow cases in the absence of a better alternative.

Results are presented for the air flow during the compression and part of the expansion stroke. In a firing engine, fuel injection takes place around 14° before tdc (btdc), and auto-ignition occurs a few degrees later. Although air flow can be predicted for a full 360° cycle, the effects of combustion dominate the flow during the expansion stroke, and the flow predictions have generally been terminated around 15° after tdc.

The initial and boundary conditions for the predictive model are listed in Table 1.

INITIAL CONDITIONS	
Pressure	1 bar
Temperature	20 deg C
Air Velocities	zero
BOUNDARY CONDITIONS	
Walls	Adiabatic
GAS PROPERTIES	
Perfect gas	
SOLUTION PARAMETERS	
Solving for three dimensional, compressible, viscous flow	
Solution algorithm	PISO
Turbulence modelling	Two equation k-ε
Differencing Scheme	Upwind

Table 1

Flow predictions have been made for three engine geometries: The standard crossflow glow plug position - the configuration used by most motor manufacturers (Figure 1); A downstream glow plug position (Figure 2); and for an engine without a glow plug. Modifying the combustion chamber geometry changes the compression and volume ratio of the engine. To allow comparisons to be made between the three cases, the volume of the fuel injector passage has been changed to compensate for any differences in volume in the downstream glow plug and no glow plug models. This ensures that the correct compression and volume ratios are maintained in each case. Details of the engine geometry are listed in Table 2.

Stroke	82 mm
Bore	82.5 mm
Compression ratio	22.4
Volume ratio	0.47

Table 2

3 RESULTS

3.1 Engine geometry comparison

Figure 3 shows the swirl number and average turbulence levels in the auxiliary chamber for each of the three engine geometries at 3000rpm. Swirl number is calculated as the *ratio of angular velocity of the swirling air motion in the chamber to crankshaft speed.* Although at any given time, the angular velocity of the air in the swirl chamber varies around

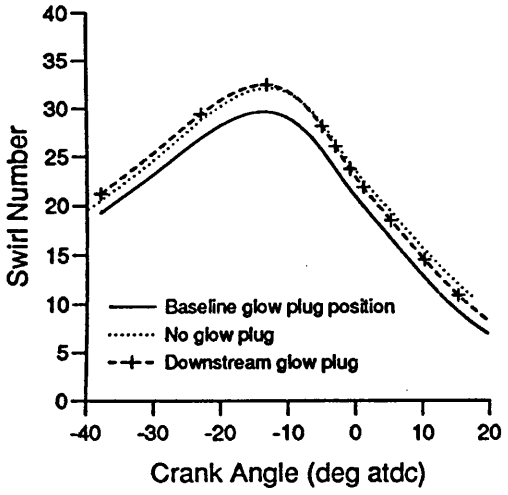

Figure 3
Effect of glow plug position on swirl number

the circumference, this definition of swirl number generates an equivalent solid body rotation based on flow around the geometric centre of the chamber. In a firing engine both swirl number and air turbulence are important parameters. During and after fuel injection, the swirling air motion supplies fresh air to the burning vaporised fuel and removes the combustion products. Air turbulence controls local mixing of air with fuel and influences the rate of pre-mixed and diffusion burning. It can be postulated that for efficient combustion high levels of both swirl and turbulence are desirable.

From Figure 3, the standard cross-flow glow plug can be seen to be acting as a significant restriction to the flow, giving a peak swirl of around 28 x engine speed, compared with around 32 x engine speed for the downstream and no glow plug cases. The downstream glow plug, situated in a region of lower average velocity than in the cross-flow position has only a small effect on swirl levels - the downstream and the no glow plug swirl lines are almost coincident. An average swirl number of 30 in the period between fuel injection and top dead centre indicates that the swirling air in the auxiliary chamber will complete one full revolution of the chamber in

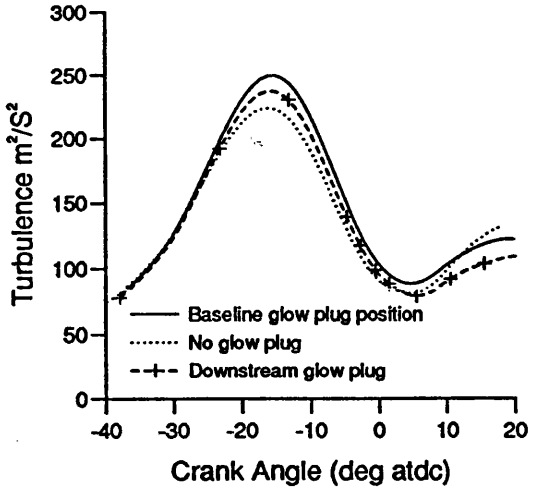

Figure 4
Effect of glow plug position on average turbulence

(360/30 = 12) degrees of crankshaft rotation. Figure 4 shows the average turbulence levels in the swirl chamber corresponding to the three geometries. The primary source of generation of turbulence is the connecting passage between the two combustion chambers. The generated turbulence is carried by the flow into the chamber and gradually dissipated into heat. The average throat velocity (Figure 5 - 3000 rpm) peaks around 18° btdc, shortly before the instance of peak swirl chamber turbulence. As the throat air velocity approaches zero (at top dead centre), turbulence dissipation exceeds turbulence generation and the global turbulence level falls, reaching a minimum shortly after tdc. As the piston

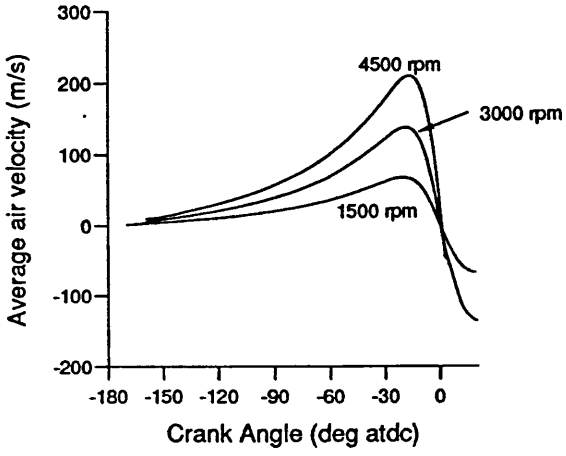

Figure 5
Average flow velocity through throat

changes direction, air is drawn out of the auxiliary chamber and turbulence generation increases in the throat. The cross-flow glow plug case, where the glow plug is placed in a region of high air velocity, generates the highest average turbulence. It is interesting to note that although the downstream case had a similar swirl number curve to the case without a glow plug, the associated turbulence levels are significantly higher.

3.2 Engine Speed

Figure 6 compares the predicted auxiliary chamber swirl levels in an engine without a glow plug for engine speeds of 1500, 3000 and 4500rpm. Turbulence is a function of overall velocity and increases with engine speed. The peak swirl level is approximately the same for each speed, but the peaks occur in different places - the crank angle at which the peak occurs is later at higher engine speeds. Figure 7 compares the pressure differences between the main and auxiliary chambers for the three engine speeds. The larger pressure differences between the chambers at higher engine speeds suggests that the connecting passage is offering greater resistance to the flow at higher air velocities. This is confirmed by considering the mass flow through the throat (Figure 8). The mass flow for the higher engine speeds lags behind that for the lower engine speeds. Referring to Figures 6 and 8, it can be seen that for each engine speed, the point of peak swirl occurs when the rate of mass flow into the swirl chamber reaches a maximum. As the cumulative mass flow into the swirl chamber at top dead centre will be equal for all engine speeds, air continues to flow into the swirl chamber for a longer

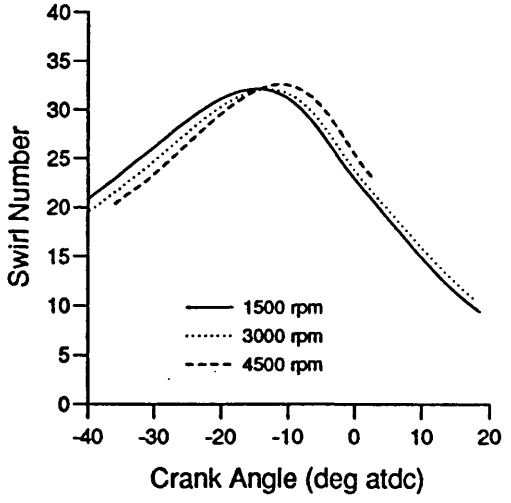

Figure 6
Effect of engine speed on swirl number

period (in terms of crank angle) for the higher engine velocities, having lagged behind the lower engine velocities during the earlier part of the cycle, thus delaying the point of peak swirl in the auxiliary chamber.

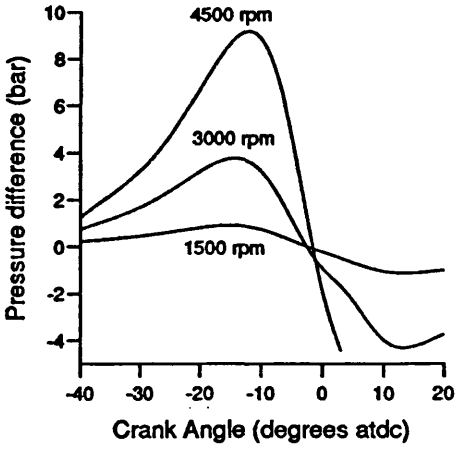

Figure 7
Variation of pressure drop across throat with engine speed

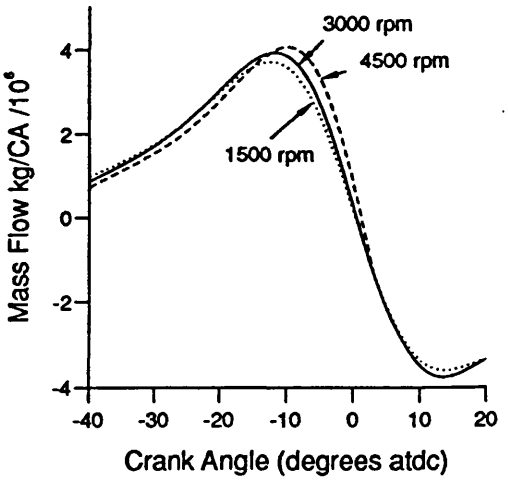

Figure 8
Variation of throat mass flow (per crank angle) with engine speed

Figure 8 shows that flow *into* the auxiliary chamber continues for a short period after top dead centre. The momentum of the flow into the chamber continues to force air into the swirl chamber against the pressure gradient (Figure 7). Comparing Figures 5 and 8 showing average connecting passage velocity and passage mass flow respectively, it can be seen that although the average velocity peaks shortly after 20° before top dead centre, mass flow into the swirl chamber continues to increase until shortly after 10° btdc. As the piston moves towards the top of its stroke, the charge continues to be compressed, and its

density increased: The mass flow through the connecting passage continues to increase, although the average velocity is decreasing.

3.3 Auxiliary chamber swirl

The data processing routine which calculates the auxiliary chamber swirl levels presented in this paper, converts the swirling air velocities to a solid body rotation that would have the same angular momentum. To perform this conversion, the algorithm calculates the total angular momentum about the geometric centre of the swirl chamber.

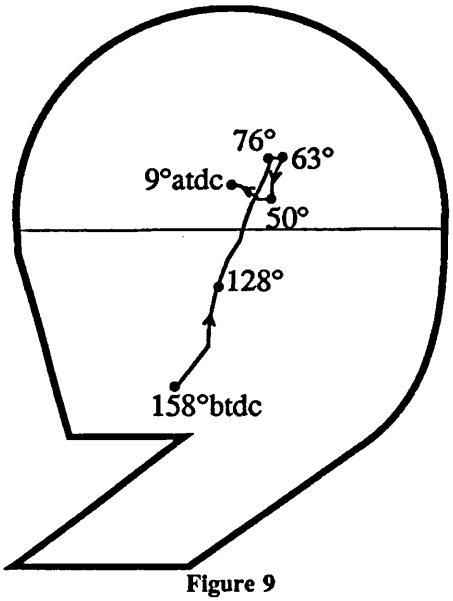

Figure 9
Location of centre of swirl through compression stroke

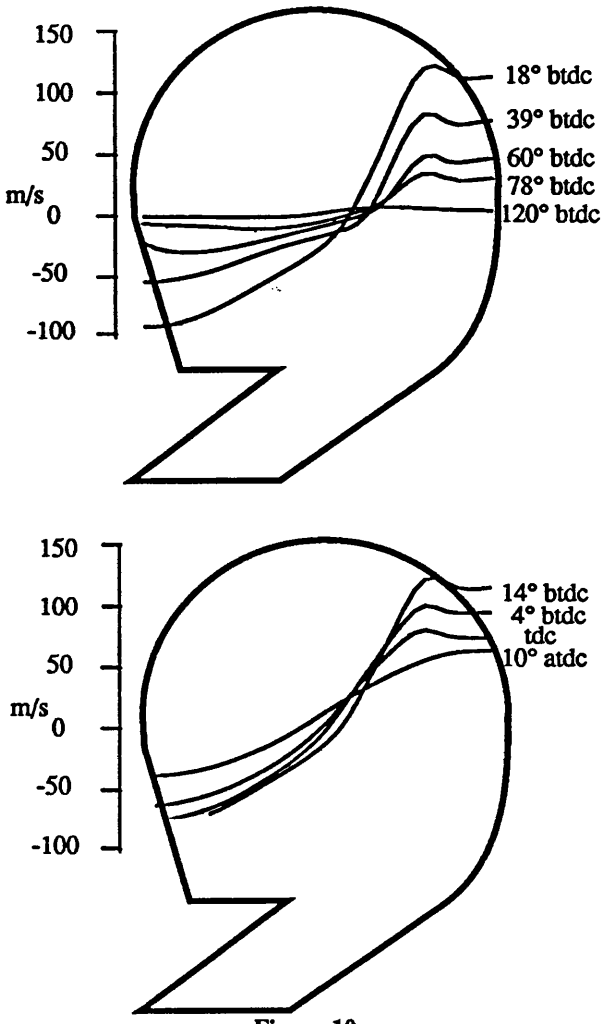

Figure 10
Velocity profiles across swirl chamber
a. Velocity increasing (before peak swirl)
b. Velocity decreasing (after peak swirl)

Figure 9 shows the locus of the instantaneous centre of swirl in the central plane during the cycle, for the engine without a glow plug. Shortly after bottom dead centre (158°btdc), an ordered swirling motion is formed in the auxiliary chamber, with a centre close to the throat exit. As the cycle progresses, the centre of the swirling motion moves towards the middle of the swirl chamber. The swirl centre passes to the right of the geometric centre of the chamber in a clockwise motion and remains slightly to the right of the centre until top dead centre. Calculation of swirl number based on the moving swirl centre gives very similar results to those calculated using the assumption of a fixed centre of swirl.

Figure 10 shows the velocity profile along the horizontal axis passing through the geometric centre of the swirl chamber central plane. If the air mass were rotating as a true solid body, the velocity profile at any point in the cycle would be a straight line. As previously shown, the centre of the swirling flow lies to the right of the geometric centre of the swirl chamber. On either side of the actual centre of swirl, the assumption of solid body rotation can be seen to be reasonable within the core of the flow, away from the chamber walls. The different gradients on either side of the swirl centre are due to the transient nature of the flow. At any given crank angle, the velocity profile to the left of the centre corresponds to an earlier profile to the right of the centre. As the flow through the connecting passage decreases (eg 10°btdc), the difference between the profiles on either side of the swirl centre diminishes. Considering the swirling mass as a whole, the assumption of solid body rotation may be considered a convenient method for calculating global swirl levels, but one which is only an approximate characterisation of the actual flow.

3.4 Comparing predicted and experimental results

The results presented in the preceding sections have been predicted by modelling an adiabatic compression of a perfect gas in a sealed combustion chamber. To compare the predicted results with results obtained from experimental in-cylinder measurements from a non-firing engine, the numerical technique must model a real gas, allow for convective heat losses during compression and take into account loss of charge during compression, primarily 'blowby' past the piston rings to the crankcase. Figure 11 compares experimental and predicted pressure in the main and swirl chambers of a small IDI diesel engine. The numerical model varies air properties (specific heat, Cp) as a function of temperature, and calculates rates of heat transfer to and from the cylinder walls. These two factors account for the 25 bar difference in peak pressure, compared with the adiabatic, constant Cp curve. The difference between the predicted and experimental measurements may be due to piston blowby, which has not been modelled and under-prediction of heat losses to the cylinder walls.

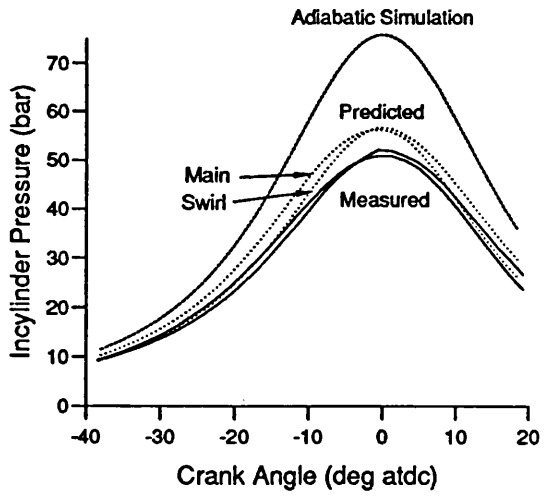

Figure 11
Comparison of experimental and predicted in-cylinder pressure

4 DISCUSSION

The results presented in this paper have shown that predictive techniques can successfully be used to model the effects of design changes and the engine speed on in-cylinder engine flows. Much of the data presented would have been difficult or impossible to measure experimentally using currently available techniques.

Although the predicted model has been shown to be an effective method for comparing the flow field between similar cases (design changes, engine speed), some validation of the results is required before the model can be used as a predictive design tool. Good agreement between predicted results and theoretical solutions, where they exist, is necessary. If the numerical model is to be validated against experimental data, a number of further inputs to the model are required. The need for these data arise from the isolated section of the complete engine which is being modelled. Without accurate initial and boundary conditions (cylinder wall temperatures, charge loss past the piston rings etc), good agreement between the predicted and experimental results is unlikely. The on-going experimental and predictive research programme being undertaken at Bath University into the small high speed Diesel engine aims to provide the necessary inputs to the predictive model. To provide validation data for the flow predictions, a Laser Doppler Anemometry (LDA) investigation of the auxiliary combustion chamber air motion in a motored engine is being undertaken, the results from which will be published shortly.

5 CONCLUSIONS

1. Numerical methods have been successfully used to investigate the effects of design changes on in-cylinder flow in an IDI passenger car Diesel engine. The techniques have been used to compare the combustion chamber flows at a range of engine speeds.
2. Validation of the numerical results is necessary if the technique is to be used as a truly predictive tool for engine design. Experimental data is required to define the initial and boundary conditions required as inputs to the model.
3. The assumption of the auxiliary chamber swirl rotating as a fixed body about the central axis of the chamber is a useful approximation to the actual flow field.

CKNOWLEDGEMENTS

he authors are grateful to the Ford Motor Company, nd the SERC for their support for this project.

EFERENCES

Charlton S, Cox A, Somerville B, Watts M, Horrocks R, (1992) *An investigation of the emission characteristics of the passenger car IDI Diesel engine* **Proc IMechE** Conference 'Combustion in Engines Technology, Applications and the Environment' Paper C448/025

Pinchon P, (1989) *Three dimensional modelling of combustion in a prechamber Diesel engine.* SAE Paper 890666

3. Zellat M, Rolland Th, Poplow F. (1990) *Three dimensional modelling of combustion and soot formation in an indirect injection Diesel engine.* SAE paper 9002544.

Boretti A, Nebuloni P, Lisbona M, Milazzo P, (1992) *Diesel engine combustion chamber design with three-dimensional flow computations.* **Proc IMechE** Conference 'Combustion in Engines Technology, Applications and the Environment' Paper C448/005

5. Somerville B, Charlton S, Nasseri B (1993) *CFD study of air motion in a passenger car IDI diesel engine.* **Proc IMechE** Conference 'Engineering Applications of Computational Fluid Dynamics'. Paper C461-023

6. STAR-CD - Computational Dynamics Limited, London.